

CONTENTS

Jan Górecki <i>Development of a Testing Station for Empirical Verification of the Algebraic Model of Dry Ice Piston Extrusion.....</i>	107
Anupam Bhandari <i>Mathematical Modeling of Water-Based Fe₃O₄ Nanofluid Due to Rotating Disk and Comparison with Similarity Solution.....</i>	113
Serhii Ternytskyi, Ivan Rehei, Nazar Kandiak, Ihor Radikhovskiy, Oksana Mlynko <i>Experimental Research of the Paperboard Cutting in Die-cutting Press with the Screw-nut Transmission in Drive Mechanism of Movable Pressure Plate.....</i>	122
Robert Skowronek, Józef Zawora, Krzysztof Kwiatkowski, Konstanty Skalski <i>Application of Statistical Analysis and Functional Assessment Tests in Patients after Trochanteric Fractures Treated Surgically in an Individual Rehabilitation Programme</i>	132
Dhotre Pavan Kumar, Chikkol V. Srinivasa <i>Modal Characterization of Sandwich Skew Plates</i>	143
Mohamed Arab, Abederezak Lachouri, Mohamed Kerikeb, Lamine Mehennaoui, Faouzi Bouchareb <i>Backlash Fault Suppression Using LQ-RST Controller in Wind Turbine System using Bond Graphs and MATLAB/Simulink</i>	154
Stanimir Karapetkov, Hristo Uzunov, Liliana Indrie, Zlatin Zlatev <i>Driving Comfort Assistance System Considering Two Sensors Data.....</i>	164
Volodymyr Morkun, Olha Kravchenko <i>Three-Dimensional Fuzzy Control of Ultrasonic Cleaning</i>	169
Radovan Gregor, Andrej Babinec, František Duchoň, Michal Dobiš <i>Hand Guiding a Virtual Robot Using a Force Sensor</i>	177
<i>Abstracts.....</i>	XVII

ABSTRACTS

Jan Górecki

Development of a Testing Station for Empirical Verification of the Algebraic Model of Dry Ice Piston Extrusion

Efficient use of resources is a very important consideration for every production process, especially where waste materials are being used as raw materials. One example of these kinds of processes is dry ice extrusion. Based on subject literature, it can be observed that the machines available on the market used to compress dry ice are characterized by high working force value. This leads to low efficiency of resource consumption, both in regards to electrical energy and carbon dioxide. This paper presents a proposed design of a test stand used for measuring compression force as a function of piston displacement in the course of the dry ice extrusion. The first part of the article presents the testing methodology and test stand design. The second part presents results of measurement of compression force as a function of piston displacement with three different die types. The results of the study allowed to establish the difference between values of measured limit force and values calculated with an analytical model. The test stand design as well as the results present in the paper are important for further research and development works in the area of efficient extrusion and compaction of dry ice.

Anupam Bhandari

Mathematical Modeling of Water-Based Fe₃O₄ Nanofluid Due to Rotating Disk and Comparison with Similarity Solution

The current research demonstrates the revolving flow of water-based Fe₃O₄ nanofluid due to the uniform rotation of the disc. This flow of nanofluid is investigated using CFD Module in COMSOL Multiphysics. However, the similarity solution for this flow is also obtained after transforming the given equation into a non-dimensional form. In the CFD Module, streamlines and surface plots are compared with the similarity solution for the magnitude of the velocity, radial velocity, tangential velocity, and axial velocity. The results from the direct simulation in the CFD Module and the solution of dimensionless equations represent a similar solution of velocity distribution. The derived results show that increasing the volume concentration of nanoparticles and effective magnetic parameters decrease the velocity distribution in the flow. Results in the CFD Module are important for monitoring the real-time particle tracing in the flow and, on the other hand, the dimensionless solution is also significant for the physical interpretation of the problem. Both methods of solution empower each other and present the physical model without sacrificing the relevant physical phenomena.

Serhii Ternytskyi, Ivan Rehei, Nazar Kandiak, Ihor Radikhovskiy, Oksana Mlynko

Experimental Research of the Paperboard Cutting in Die-cutting Press with the Screw-nut Transmission in Drive Mechanism of Movable Pressure Plate

This paper reports experimental research of torques during paperboard cutting in the die cutting press with the screw–nut transmission in the drive mechanism of the movable pressure plate. The purpose of the study is to substantiate the practical implementation of the pressure plate drive mechanism with the use of screw–nut transmission for the production of cartons of paperboard blanks. The manufactured experimental bench for the research of paperboard blanks provides the possibility of getting dependencies of loads on different parameters of the die cutting process. The developed method of the experimental research envisages the use of the strain gauge method and the wireless module for data measurement and software for its processing that allow getting trustworthy results with minimum faults. As a result of experimental research studies, the impact of paperboard thickness and cutting velocity on torque values has been established. Results of experimental research allow getting trustworthy and systematised information about torque values depending on the thickness of the paperboard, the paperboard fibre direction and pressure plate displacement velocity. It is established that torque values on drive shaft during die cutting of paperboard blanks made of folding boxboard with thickness that lay in range of 0.3–0.7 mm. Experimental research studies show the impact of rotation speed of a drive shaft of the pressure plate drive mechanism on the torque value. The article shows the workability of the designed device with screw–nut transmission in the drive mechanism of a movable pressure plate.

Robert Skowronek, Józef Zawora, Krzysztof Kwiatkowski, Konstanty Skalski

Application of Statistical Analysis and Functional Assessment Tests in Patients after Trochanteric Fractures Treated Surgically in an Individual Rehabilitation Programme

Physiotherapeutic procedures after surgical treatment of trochanteric fractures of femurs are a very important element of a post-operative management because they have a significant influence on the final result of physiotherapy. This is due to the nature of the fracture and the frequency of its occurrence. The aim of the work is, in particular, to determine the relationship between functional assessment scales in patients after trochanteric fractures treated surgically using extended statistical analysis including regression equations. Statistical analysis included a group of patients, which participated in a specialized programme of a post-operative procedure, called the 'Individual' Group. The matrix of research results, calculations of basic statistical measures, such as position, variability, interdependence, asymmetry and concentration were presented for this group. Regression equations representing the relationships between the considered variables, in particular concerning the applied scales and post-operative tests, were presented. Their purpose, mathematical interpretation, results of calculations and statistical tests were discussed. Attention was paid to the high correlation between the Parker and Mobility tests. The extended statistical analysis makes it possible to create an own system for assessing the treatment results of patients after trochanteric fractures are treated surgically.

Dhotre Pavan Kumar, Chikkol V. Srinivasa
Modal Characterization of Sandwich Skew Plates

The current work focuses on the experimental and finite element free vibration studies of laminated composite sandwich skew plates. The comparison was made between the experimental values obtained by the Fast Fourier transform (FFT) analyzer and a finite element solution obtained from CQUAD8 finite element of The MacNeal-Schwendler Corporation (MSC) / NASA STRucture Analysis (NASTRAN) software. The influence of parameters such as aspect ratio (AR) (a/b), skew angle (α), edge condition, laminate stacking sequence, and fiber orientation angle (θ°) on the natural frequencies of sandwich skew plates was studied. The values obtained by both the finite element and experiment approaches are in good agreement. The natural frequencies increase with an increase in the skew angle for all given ARs.

Mohamed Arab, Abederezak Lachouri, Mohamed Kerikeb, Lamine Mehennaoui, Faouzi Bouchareb
Backlash Fault Suppression Using LQ-RST Controller in Wind Turbine System using Bond Graphs and MATLAB/Simulink

The presence of backlash in wind turbines is a source of limitations as it introduces nonlinearities that reduce their efficiency in speed/torque control which affect the performance of the power quality. Because of production tolerances during rotation, the teeth contact is lost for a small angle; until it is re-established, it produces a backlash phenomenon. The desire to eliminate this phenomenon is often hard to realise due to the nonlinear dynamic behaviour, which arises with the presence of backlash fault in a system. Therefore, the goal of this study is to develop an LQ optimal control structure in a form of an R-S-T controller in order to reduce the disturbing torque transmitted inside the dead zone of a gearbox in the wind turbine system. The actual system is also developed to be used as a demonstration model at lectures or presentations. The efficacy of the proposed control is illustrated via simulations.

Stanimir Karapetkov, Hristo Uzunov, Liliana Indrie, Zlatin Zlatev
Driving Comfort Assistance System Considering Two Sensors Data

In the present work, a system using data from two sensors located next to the driver and to the mass centre of the bus is pro-posed. Three degrees of discomfort have been used – comfortable, moderately uncomfortable and very uncomfortable. These levels are set out in the questionnaire. A survey was conducted. Respondents were selected between the ages of 14 and 65 and were divided into three age groups – adults, middle-aged and young. Accelerometer systems with MPU-6500 (TDK InvenSense Corp.) sensors are used. A correlation method (CORR) and sequentially improving estimation methods are used for feature selection, which significantly reduce the number of combinations of features obtained. Selected sensor data is entered into feature vectors. These vectors are reduced by principal component analysis. Predictive models have been created that take into account the age of passengers. The use of data from two sensors and separation of the passengers according their age, leads to an increase in the accuracy of predicting passengers discomfort level (DL) of up to 98%. These results can be used to evaluate and guide the vehicle driver in order to improve his driving style. In addition, the simplified interface does not distract the driver from the road conditions. The results obtained can lead to an improvement in the parameters of the transport process, which covers the interest of the carrier related to the efficient use of vehicles, and hence the reduction of fuel consumption and harmful emissions. However, it should be recommended that, when developing systems to ensure comfort of travel, adjustments should be made to suit the age group of passengers carried on public transport buses.

Volodymyr Morkun, Olha Kravchenko
Three-Dimensional Fuzzy Control of Ultrasonic Cleaning

Consideration of ultrasonic cleaning as a process with distributed parameters enables reduction of power consumption. This approach is based on establishment of control over the process depending on fixed values of ultrasonic responses in set points. The initial intensity of radiators is determined using a three-dimensional (3D) interval type-2 fuzzy logic controller essentially created for processes with distributed parameters, as well as complex expert evaluation of the input data. The interval membership functions for the input and output data consider the space heterogeneity of ultrasonic cleaning. A rule base is formed, which is 2D and not dependent upon the number of input and output parameters. A model illustrating ultrasonic cleaning with a 3D interval type-2 fuzzy logic controller is designed. Comparative analysis of the output parameters of the proposed model and the traditional method indicates an increase in the energy efficiency by 41.17% due to application of only those ultrasonic radiators that are located next to the contamination.

Radovan Gregor, Andrej Babinec, František Duchoň, Michal Dobiš
Hand Guiding a Virtual Robot Using a Force Sensor

The research behind this paper arose out of a need to use an open-source system that enables hand guiding of the robot effector using a force sensor. The paper deals with some existing solutions, including the solution based on the open-source framework Robot Operating System (ROS), in which the built-in motion planner MoveIt is used. The proposed concept of a hand-guiding system utilizes the output of the force–torque sensor mounted at the robot effector to obtain the desired motion, which is thereafter used for planning consequential motion trajectories. Some advantages and disadvantages of the built-in planner are discussed, and then the custom motion planning solution is proposed to overcome the identified drawbacks. Our planning algorithm uses polynomial interpolation and is suitable for continuous replanning of the consequential motion trajectories, which is necessary because the output from the sensor changes due to the hand action during robot motion. The resulting system is verified using a virtual robot in the ROS environment, which acts on the real Optoforce force–torque sensor HEX-70-CE-2000N. Furthermore, the workspace and the motion of the robot are restricted to a greater extent to achieve more realistic simulation.

DEVELOPMENT OF A TESTING STATION FOR EMPIRICAL VERIFICATION OF THE ALGEBRAIC MODEL OF DRY ICE PISTON EXTRUSION

Jan GÓRECKI^{*}

^{*}Faculty of Mechanical Engineering, Poznan University of Technology, 3 Piotrowo Street, 61-138 Poznan, Poland

jan.gorecki@put.poznan.pl

received 8 June 2020, revised 8 June 2021, accepted 15 June 2021

Abstract: Efficient use of resources is a very important consideration for every production process, especially where waste materials are used as raw materials. One example of these kinds of processes is dry ice extrusion. Based on the subject literature, it can be observed that the machines available in the market that are used to compress dry ice are characterized by high working force value. This leads to low efficiency of resource consumption, in regards to both electrical energy and carbon dioxide. This paper presents a proposed design of a test stand used for measuring compression force as a function of piston displacement in the course of the dry ice extrusion. The first part of the article presents the testing methodology and test stand design. The second part presents the results of measurement of compression force as a function of piston displacement with three different die types. The results of the study allowed to establish the difference between the values of the measured limit force and the values calculated with an analytical model. The test stand design and the results presented in this paper are important for further research and development works in the area of efficient extrusion and compaction of dry ice.

Key words: dry ice, carbon dioxide, agglomeration, extrusion, compaction

1. INTRODUCTION

The use of waste products from manufacturing processes is very often economically justified as it contributes to waste recovery and allows to reuse of production waste as raw material. A review of the available subject literature demonstrates the availability of insufficient information on the description of various processes applied to non-classic materials, including waste material (Wałęsa et al., 2018; Wojtkowiak et al., 2018). An example of such waste product is carbon dioxide obtained, e.g. from the manufacturing of ammonia compounds (Fig. 1); due to the large amounts of generation, factories are often unable to utilize the entire material for their needs. Consequently, liquefied carbon dioxide (LCO₂) is often sold off to interested third parties (Górecki et al., 2018; 2019a; 2019b; Uhlmann et al., 2010).

Possible applications of LCO₂ include the production of dry ice. This material is obtained in solid form through decompression of the liquid. As a result of an adiabatic process, approximately 50% of the decompressed liquid gets crystallized. The resultant product's temperature is -78.4°C, which sublimates under normal ambient conditions (Górecki et al., 2017; Dzido et al., 2019a; Liu et al., 2012; Mazzoldi et al., 2008; Mikołajczak et al., 2018). Based on these characteristics, the material received its common name of dry ice. It is used mostly in product transportation where low temperatures are required (Dong et al., 2012; Li et al., 2016; Liu et al., 2010; Liu et al., 2017; Masa et al., 2016; Mazzoldi et al., 2008; Otto et al., 2011; Spur et al., 1999; Witte et al., 2017) and for surface cleaning (Dong et al., 2013; Dzido et al., 2019b, Dzido et al. 2021, Masa et al., 2014, Mikołajczak et al., 2018; Muckenaupt et al., 2019).

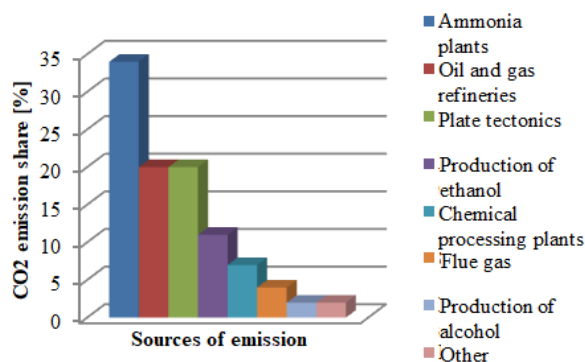


Fig. 1. Main sources of carbon dioxide emissions by percentage share (Górecki et al., 2017)

Extrusion of agglomerated, crystallized carbon dioxide serves to reduce the surface of phase transition, which slows down sublimation and extends the time for which the material stays in solid form (Górecki et al., 2020; Liu et al., 2012).

Various equipment for dry ice extrusion are available in the machine market. The majority of offered solutions utilise piston technology with hydraulic or crank-piston drives. However, there are few sources covering the methods of extrusion or agglomeration of dry ice available in the subject literature (Górecki et al., 2019b; 2020).

Due to the identified deficiency of information regarding extrusion and agglomeration of dry ice as well as considering the peculiar characteristics of the material, it is necessary to carry out scientific works to develop an algebraic model for establishing the resistance force value in multichannel dies (Gorecki et al., 2020b).

The model provided in this paper is verified only in the laboratory conditions. Therefore, with the intention of employing the model in an industrial environment, it is necessary to develop a suitable testing station to facilitate the study of this kind of environmental condition.

Available subject literature demonstrates a high degree of interest in works aiming to study and develop the shape of the tools used in the process with view of improving product quality as well as the energy efficiency of the process (Dudziak et al., 2017; Dzido et al., 2019a; Górecki et al. 2020a; 2020b; Ishiguro et al., 2020; Kukla et al. 2017; Malujda et al., 2016; Talaška, 2017; Wałęsa et al., 2019a; 2019b; 2020a; 2020b; Wilczyński et al. 2018; Wilczyński et al., 2019a; 2019b; 2019c; 2020; Wojtkowiak et al. 2019; 2021).

2. BUILDING OF THE TESTING STAND

Fig. 2 provides an overview drawing of the testing station developed by the authors. A vessel with LCO₂ kept at the pressure of 20 bar is attached to the machine. After its decompression in working chamber 2, the material crystallises in fragmented form (Górecki et al., 2017; 2019a). Afterwards, the pneumatic actuator 1 is powered by compressed air and its piston rod 1 moves together with the piston 3. The reduction of volume of the working chamber 2, which contains the crystallised carbon dioxide, leads to the agglomeration of the material. The compaction process continues until the force available on the piston F_T becomes equal to the resistance force F_{OP} associated with the extrusion of the material through the die channel 4 installed at the end of the working chamber 2. After withdrawing the piston to starting position, the device is ready to begin the next work cycle.

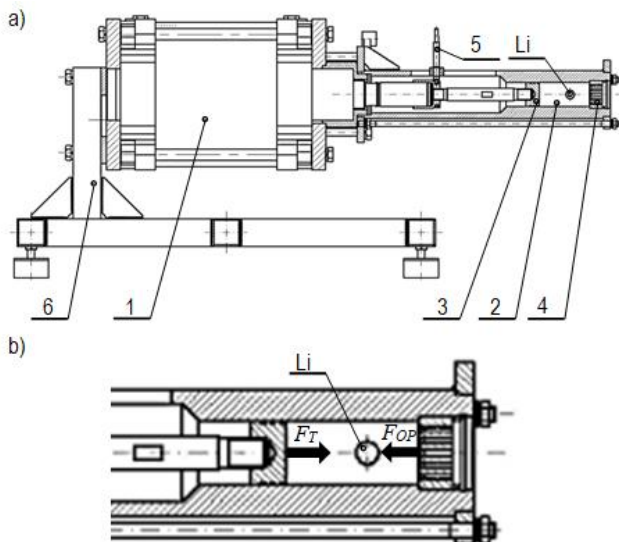


Fig. 2. The working unit of dry ice agglomeration. (a) test stand and (b) compaction assembly: 1 – pneumatic piston, 2 – working chamber, 3 – compacting piston, 4 – multi-channel die, 5 – displacement sensor grip, 6 – frame. Li, —liquid inlet

The components necessary to carry out the above process that are not provided in Fig. 2 include the unit responsible for the preparation and injection of the LCO₂ as well as the control and measurement instrumentation. Fig. 3 illustrates the interconnections between the indicated components.

3. METHODOLOGY

The testing station is equipped with suitable instrumentation to determine the change of force value applied on the piston F_T as a function of its displacement. Fig. 3 illustrates the schematic view of the station.

The F_T value is determined based on the signal from pressure transducers 12 and 13 placed on both sides of the actuator piston. The measurement of displacement of the compacting piston 3 is achieved by the displacement sensor 5. The transducers are connected to the data acquisition system that includes a data amplifier 19, the signal measurement board 20 and the PC 21.

Fig. 3 presents the automated control system for the testing station. It governs the operation of electrovalve 6, which controls the direction of movement of actuator 1 as well as the LCO₂ injection system electrovalves 11 and 7. The programmable logic controller (PLC) 18 operates the indicated components based on the developed algorithm and signals from limit switches 16 and 17 and the vibrating level sensor 10 controlling the LCO₂ level.

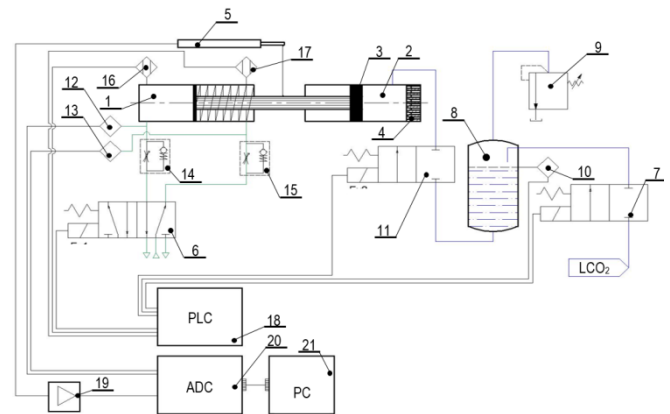


Fig. 3. Schematic view of the carbon dioxide agglomeration station: 1 – pneumatic actuator, 2 – working chamber, 3 – compacting piston, 4 – multi-channel die, 5 – WA-100 displacement sensor, 6 – type 5/2 distributing electrovalve, 7 – refill electrovalve, 8 – liquid CO₂ buffer container, 9 – pressure adjustment valve, 10 – vibrating level sensor for liquid presence, 11 – liquid injection electrovalve, 12, 13 – pressure transducer, 14 and 15 – throttle check valve, 16 and 17 – piston end position sensor, 18 – PLC controller, 19 – measurement amplifier, 20 – signal measurement board, 21 – data acquisition PC

For the purpose of the study, three types of multichannel dies (MCD) with conical-cylindrical channels are used. Each die is characterized by different geometric parameters as provided in Tab. 1 and illustrated in Fig. 4. The die dimensions match the design features of the device, enabling the testing station to be re-tooled. This allows to compare results with an identical error of measurement resulting from the inaccuracy of pressure transducers equal to 0.01% of the measurement range, i.e. 10 bar. Based on the above factors, it is determined that the pressure measurement error is equal to $|\delta p| = \pm 10$ kPa.

The following expression was used to determine the value of available force on the piston,

$$F_T = \frac{(p_1 - p_2) \cdot \pi \cdot (2 \cdot R_k)^2}{4}, \quad (1)$$

where: R_k – radius of the compacting piston, $R_k = 18$ mm.

Based on the formula 1, the measurement error value for force F_T was determined using the expression as given below,

$$|\delta_F| = \frac{(|\delta p_1| + |\delta p_2|) \cdot \pi \cdot (2 \cdot R_K)^2}{4} = 20.36 \text{ N.} \quad (2)$$

The established error value for force measurement is deemed sufficiently accurate for employing type A method for result analysis, based on statistical analysis (Arendarski, 2006).

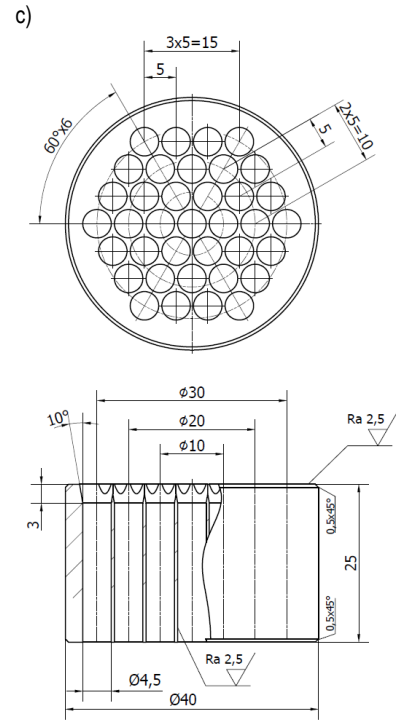
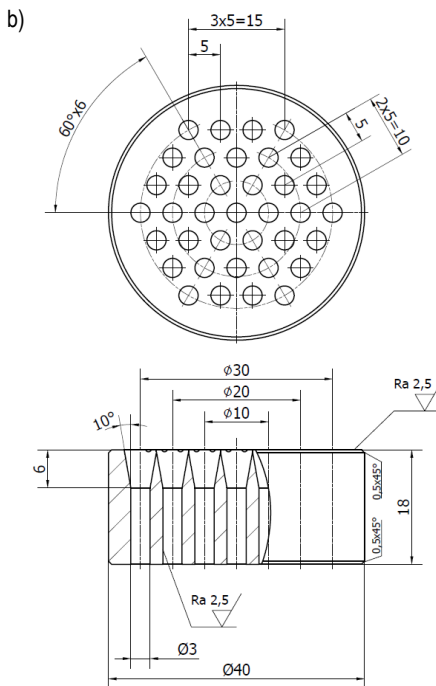
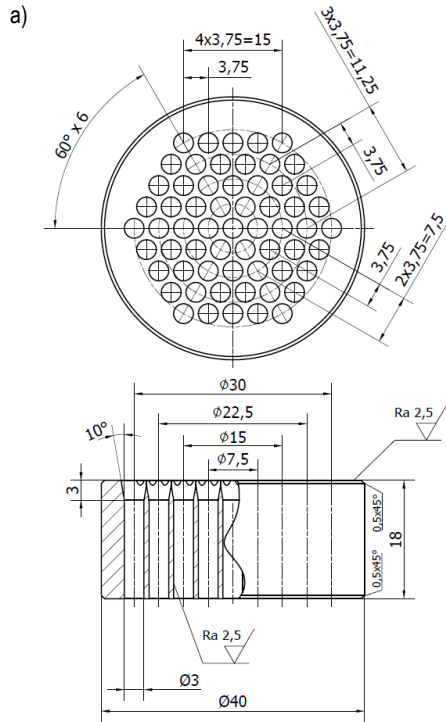


Fig. 4. Multichannel forming dies, a – MCD-0, b – MCD-1, c – MCD-2

Tab. 1. Geometric parameters of the multichannel forming dies, D_{out} – diameter of the channel outlet, n – number of channels

	n	D_{out} [mm]	α [°]	A [mm]	b [mm]	R_K [mm]	E [mm]	n_G
MCD-0	61	3	10	15	3	18	15	24
MCD-1	37	3		12	6		15	18
MCD-2	37	4.5		15	3		15	18

4. RESULTS

During the examination, results are recorded from 10 consecutive dry ice extrusion process cycles. The results of the example for the die MCD-0 are provided in Fig. 5 in the form of a line graph presenting the variation of piston force F_T as a function of displacement value x .

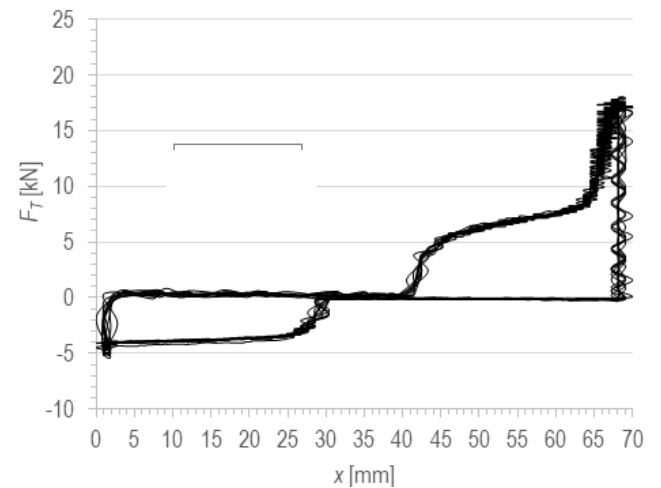


Fig. 5. Results of measuring the force applied to the piston F_T in the course of the extrusion process using MCD-0 die

The piston withdrawal part of the cycle is excluded from the registered measurements. The results are then averaged in each of the three cases. This allows to identify the characteristics of piston force variability F_T for each die as a function of piston displacement x , which are illustrated in Figs. 6–8.

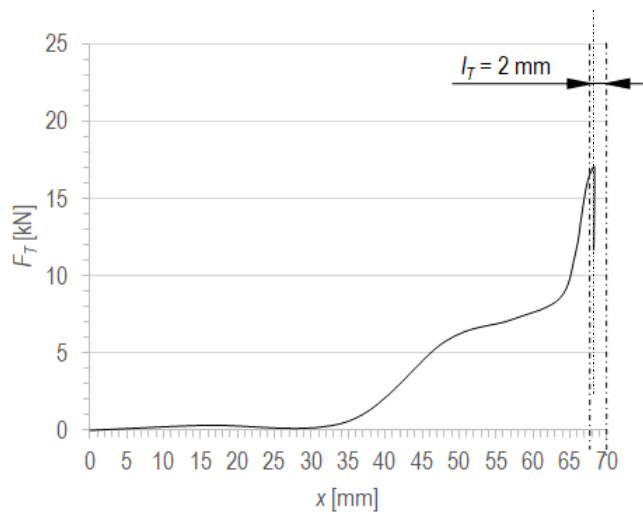


Fig. 6. The characteristic curve for force variation available on the piston F_T as a function of piston displacement x in the process of extrusion with MCD-0 die.

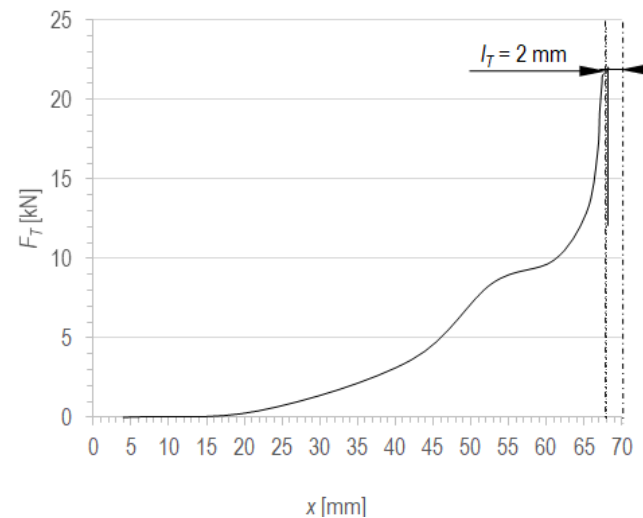


Fig. 7. The characteristic curve of the variation of force available on the piston F_T as a function of piston displacement x in the process of extrusion with MCD-1 die.

Based on the developed characteristics, the length of section l_T in the moment of extrusion of the agglomerated material through the die is determined. This parameter has a significant influence on the F_{OP} value and describes the length of agglomerated material along the axis of rotation of the compaction chamber. The influence of this parameter is described in the available literature (Górecki et al. 2017b). The value of limit force during the process utilising MCD-1 die is much higher than that in the processes employing MCD-0 and MCD-2 dies. One of the differences between MCD-0, MCD-1, and MCD-2 die types is the value of parameter b , which influences the shearing stress value as provided in the subject literature (Górecki et al. 2017b; Górecki 2020; Górecki et al. 2020b). Furthermore, the channel outlet diameter

D_{out} influences the value of the limit force. The D_{out} parameter relates to the value of cutting edge on the die inlet as well as the force of extrusion resistance. At the beginning of the product formation part of the process, each die channel will shear the agglomerated block of dry ice. The cutting edge parameters relate to the number of channels and the value of D_{out} .

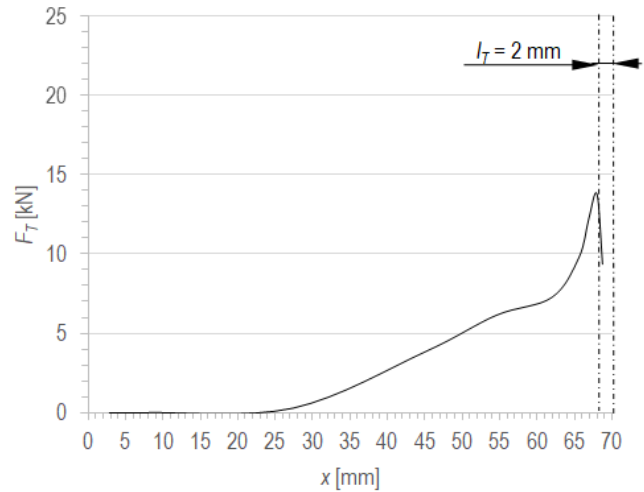


Fig. 8. The characteristic curve of the variation of force available on the piston F_T as a function of piston displacement x in the process of extrusion with MCD-2 die.

Test results allowed for comparison of the average limit force value on the piston F_T^{avr} measured during the examination and the results obtained from the algebraic model available in subject literature (Górecki, 2020), which describes the variance of F_{OP} as a function of the geometric parameters of multi-channel dies. See Table 2 for the calculated results together with the maximum measured force value on the piston F_T^{avr} . The information regarding the percentage difference in the force value determined via the algebraic method F_{OP} , and the limit value F_T^{avr} is also provided therein. The value of the difference is calculated using the formula below.

$$\delta = \frac{F_T^{avr} - F_{OP}}{F_T^{avr}} \cdot 100\% \quad (3)$$

Tab. 2. Results of measurement and analytic calculations

Die model	MCD-0	MCD-1	MCD-2
F_{OP} [kN]	14.2	16	10.6
F_T^{avr} [kN]	17.2	21.9	14.2
l_T [mm]	2	2	2
δ [%]	17.4	26.94	25.35

For all three dies, the value does not exceed 27%.

5. SUMMARY

The article presents the results of design works on the testing station, the developed methodology and study results. The examination focussed on identifying the characteristics of force variation on the agglomerating piston as a function of its displacement.

The obtained characteristics are used to determine the limit value of compacting force in industrial conditions. Consequently, the test results could be compared with the results derived from the algebraic model available in the subject literature (Górecki, 2020), which is used to determine the indicated force limit value based on the geometric parameters of multi-channel dies. This allows to determine the difference between results achieved in empirical testing and results derived from the algebraic model available in subject literature, the difference is expressed as a percentage value.

The difference between the calculated and the actual value of the resistance force F_{OP} is affected by the dosing accuracy of the LCO_2 , the efficiency of the crystallisation process as well as the resistances effected by the displacement of the agglomerating piston in the device working chamber. According to published studies, the difference in the value derived from the model and the verification tests in laboratory conditions is up to 12.9%. The differences between the algebraic calculation and measurement results obtained from the author's prototype carbon dioxide agglomeration machine are therefore justified. The test result analysis allows to demonstrate that the geometrical parameters of dies influence the limit force during the extrusion process.

The paper presented basic observations regarding the influence of geometrical parameters of multichannel dies on the limit force, which are in line with the conclusion of previous research (Górecki et al, 2019a; Górecki, 2020; Górecki et al. 2020b).

REFERENCES

- Arendarski J (2006), Measurement uncertainty (in Polish), Warsaw University of Technology Publisher.
- Dudziak M, Kołodziej A, Domek G., et al. (2017), Multi-angularity – identification of parameters and compatibility conditions of the axisymmetric connection with form deviations *Procedia Engineering*, vol. 177 431-438.
- Dong S., Song B., Hansz B., et al. (2012), Modeling of dry ice blasting and its application in thermal spray, *Material Research Innovations*, Vol. 16, 61-66.
- Dong S., Song B., Hansz B., et al., (2013), Combination Effect of Dry-Ice Blasting and Substrate Preheating on Plasma-Sprayed CoNiCrAlY Splats, *Journal of Thermal Spray Technology*, Vol. 22, No. 1, <https://doi.org/10.1007/s11666-012-9845-z>.
- Dzido A., Krawczyk P., Kurkus-Gruszecka M., et al. (2019) Analysis of the Liquid Natural Gas Energy Storage basing on the mathematical model, *Energy Procedia*, Vol. 159, 231-236.
- Dzido A., Krawczyk P., Kurkus-Gruszecka M. (2019), Numerical Analysis of Dry Ice Blasting Convergent-Divergent Supersonic Nozzle, *Energies*, Vol. 12, 4787.
- Dzido A., Krawczyk., Badyda K., Chondrokostas, (2021), Operational parameters impact on the performance of dry-ice blasting nozzle, *Energy*, Vol. 214, <https://doi.org/10.1016/j.energy.2020.118847>.
- Górecki J., Malujda I., Talaśka K., et al. (2015) Static compression tests of concentrated crystallized carbon dioxide, *Applied Mechanics and Materials*, Vol. 816, 490-495.
- Górecki J., Malujda I., Talaśka K., et al. (2017), Dry ice compaction in piston extrusion process, *Acta mechanica et automatic*, Vol. 11, no. 4, 313-316.
- Górecki J., Malujda I., Talaśka K., et al. (2017), Influence of the compression length on the ultimate stress in the process of mechanical agglomeration of dry ice, *Procedia Engineering*, vol. 177, 363-368.
- Górecki J., Malujda I., Wilczyński D. (2019), The influence of geometrical parameters of the forming channel on the boundary value of the axial force in the agglomeration process of dry ice, *Matec Web of Conferences*, Vol.254, 05001.
- Górecki J., Malujda I., Wilczyński D., Wojtkiak D. (2019), Influence of the face surface shape of the piston on the limit value of compaction stress in the process of dry ice agglomeration, *Matec Web of Conferences*, Vol.254, 2019, 06001.
- Górecki J., (2020), Preliminary analysis of the sensitivity of the algebraic dry ice agglomeration model using multi-channel dies to change their geometrical parameters, *IOP Conference Series: Materials Science and Engineering*, 776, 012030.
- Górecki J., Fierek A., Talaśka K., et al., (2020), The influence of the limit stress value on the sublimation rate during the dry ice densification process, *IOP Conference Series: Materials Science and Engineering*, 776, 012072.
- Górecki J., Talaśka K., Wałęsa K., et al., (2020), Mathematical Model Describing the Influence of Geometrical Parameters of Multichannel Dies on the Limit Force of Dry Ice Extrusion Process, *Materials*, vol. 13(15), 3317-1 – 3317-11.
- Ishiguro M., Dan K., Kaneko S., et al. (2020) Snow Consolidation Properties by using Mechanical Press Machine, *Journal of the Institute of Industrial Applications Engineers*, Vol. 7(3), 83-90.
- Kukla M, Górecki J, Malujda I, et al. (2017) The determination of mechanical properties of magnetorheological elastomers (MREs) *Procedia Engineering*, vol. 177 324-330.
- Li M., Liu W., Qing X., et al. (2016), Feasibility study of a new approach to removal of paint coatings in remanufacturing, *Journal of Materials Processing Technology*, Vol. 234, 102-112.
- Liu Y., Calvert G., Hare C., et al. (2012), Size measurement of dry ice particles produced from liquid carbon dioxide, *Journal of Aerosol Science*, Vol. 48, 1-9.
- Liu Y., Hiram D., Matusaka S. (2017), Particle removal process during application of impinging dry ice jet, *Powder Technology*, 607-613.
- Liu Y., Maruyama H., Matusaka S. (2010), Agglomeration process of dry ice particles produced by expanding liquid carbon dioxide, *Advanced Powder Technology*, Vol. 21, 652-657.
- Malujda I., Wilczyński D., (2016) Mechanical Properties Investigation of Natural Polymers, *Procedia Engineering* vol. 136, 263-268.
- Masa V., Kuba P., Perilak D., Lokaj J., (2014), Decrease in Consumption of Compressed Air in Dry Ice Blasting Machine, *Chemical Engineering Transactions*, 39, 805-810, <https://doi.org/10.3303/CET1439135>.
- Masa V., Kuba P. (2016), Efficient use of compressed air for dry ice blasting, *Journal of Cleaner Production*, Vol. 111, 76-84.
- Mazzoldi A., Hill T., Colls J. (2008), CO2 transportation for carbon capture and storage: Sublimation of carbon dioxide from a dry ice bank, *International Journal of Greenhouse Gas Control*, Vol. 2, 210-218.
- Mikolajczak A., Krawczyk P., Stępień M., et al. (2018), Preliminary specification of the dry ice blasting converging-divergent nozzle parameters basing on the standard (analytical) methods, *Rynek Energii*, Vol. 4, 91-96.
- Muckenaupt D., Zutzmann T., Rudek A., Russ G., (2019), An Experimental and Numerical Procedure for Energetic and Acoustic Optimization of Dry-ice Blasting Processes, *Chemical Engineering Transactions*, Vol. 74, 967-972, <https://doi.org/10.3303/CET1974162>.
- Otto C., Zahn S., Rost F., et al. (2011), Physical Methods of cleaning And Disinfection of Surfaces, *Food Engineering Review*, Vol. 3, 171-188.
- Talaśka K., (2017), Analysis of the energy efficiency of the shredded wood material densification process *Procedia Engineering* 177 352-357.
- Spur G., Uhlmann E., Elbing F. (1999), Dry-ice blasting for cleaning: process, optimization and application, *Wear*, Vol. 233–235, 402–411.
- Uhlmann E., Kretschmar M., Elbing F., et al. (2010), Deburring with CO2 Snow Blasting. In: J. Aurich, D. Dornfeld (eds) *Burrs - Analysis, Control and Removal*. Springer, Berlin, Heidelberg.

32. **Wałęsa K., Malujda I., Talaśka K.** (2018), Butt welding of round drive belts, *Acta Mechanica et Automatica*, Vol. 12, no. 2, s. 115-126
33. **Wałęsa K., Malujda M., Górecki J., et al.** (2019), The temperature distribution during heating in hot plate welding process, *MATEC Web of Conferences*, Vol. 254, 0233-1 - 02033-11.
34. **Wałęsa K., Malujda I., Wilczyński D.** (2019), Shaping the parameters of cylindrical belt surface in the joint area, *Acta Mechanica et Automatica*, vol. 13, 255-261.
35. **Wałęsa K., Malujda I., Wilczyński D.** (2020), Experimental research of the thermoplastic belt plasticizing process in the hot plate welding, *IOP Conference Series: Materials Science and Engineering*, 776, 012011.
36. **Wałęsa K., Malujda I., Górecki J.** (2020), Experimental research of the mechanical properties of the round drive belts made of thermoplastic elastomer, *IOP Conference Series: Materials Science and Engineering*, 776, 012107.
37. **Wilczyński D., Talaśka K., Malujda I., et al.** (2018) Experimental research on biomass cutting process MATEC Web of Conferences vol. 157 07016.
38. **Wilczyński D., Berdychowski M., Wojtkowiak D., et al.** (2019) Experimental and numerical tests of the compaction process of loose material in the form of sawdust, MATEC Web of Conferences, vol. 254 02042.
39. **Wilczyński D., Malujda I., Górecki J. et al.** (2019) Experimental research on the process of cutting transport belts, MATEC Web of Conferences, vol. 254 05014.
40. **Wilczyński D., Malujda I., Górecki J., et al.,** (2019) Research on the process of biomass compaction in the form of straw, MATEC Web of Conferences, vol. 254 05015.
41. **Wilczyński D., Wałęsa K., Berdychowski M., et al.,** (2020) Biomass cutting tests to determine the lowest value of the process force, *IOP Conf. Series: Materials Science and Engineering* vol. 776 012014.
42. **Witte A., Bobal M., David R., et al.** (2017), Investigation of the potential of dry ice blasting for cleaning and disinfection in the food production environment, *LWT - Food Science and Technology*, Vol. 75, 735-741.
43. **Wojtkowiak D., Talaśka K., Malujda I., et al.** (2018), Estimation of the perforation force for polymer composite conveyor belts taking into consideration the shape of the piercing punch. *The International Journal of Advanced Manufacturing Technology* <https://doi.org/10.1007/s00170-018-2381-3>.
44. **Wojtkowiak D. and Talaśka K.** (2019) Determination of the effective geometrical features of the piercing punch for polymer composite belts *The International Journal of Advanced Manufacturing Technology*, vol. 104, 315-332.
45. **Wojtkowiak D., Talaśka K., Wilczyński D., et al.** (2021), Determining the Power Consumption of the Automatic Device for Belt Perforation Based on the Dynamic Model. *Energies*, Vol. 14, No. 1, <http://dx.doi.org/10.3390/en14020317>.

Jan Górecki:  <https://orcid.org/0000-0002-4640-7418>

MATHEMATICAL MODELLING OF WATER-BASED Fe_3O_4 NANOFUID DUE TO ROTATING DISC AND COMPARISON WITH SIMILARITY SOLUTION

Anupam BHANDARI^{*} 

^{*}Department of Mathematics, School of Engineering, University of Petroleum & Energy Studies (UPES), Energy Acres Building, Bidholi, Dehradun- 248007, Uttarakhand, India

pankaj.anupam6@gmail.com

received 8 July 2020, revised 6 June 2021, accepted 15 June 2021

Abstract: The current research demonstrates the revolving flow of water-based Fe_3O_4 nanofluid due to the uniform rotation of the disc. This flow of nanofluid is investigated using CFD Module in COMSOL Multiphysics. However, the similarity solution for this flow is also obtained after transforming the given equation into a non-dimensional form. In the CFD Module, streamlines and surface plots are compared with the similarity solution for the magnitude of the velocity, radial velocity, tangential velocity, and axial velocity. The results from the direct simulation in the CFD Module and the solution of dimensionless equations represent a similar solution of velocity distribution. The derived results show that increasing the volume concentration of nanoparticles and effective magnetic parameters decrease the velocity distribution in the flow. Results in the CFD Module are important for monitoring the real-time particle tracing in the flow and, on the other hand, the dimensionless solution is also significant for the physical interpretation of the problem. Both methods of solution empower each other and present the physical model without sacrificing the relevant physical phenomena.

Keywords: nanofluid, velocity, CFD Module, dimensionless analysis

1. INTRODUCTION

Ferrofluids are colloidal suspensions of magnetic nanoparticles. These types of fluid are not present in nature. Ferrofluids are synthesised by different methods based on their application. One of the important properties of ferrofluids is that they work in a zero-gravity region. Ferrofluids have numerous applications in the field of engineering and medicine. Heat control loudspeaker and frictionless sealing are important applications of ferrofluids. However, in the field of medicine, ferrofluid is used in the treatment of cancer through magnetohyperthermia.

The rotational flow of viscous fluid over a rotating disc has been examined by researchers using similarity transformations (Cochran, 1934; Benton, 1966; Schlichting and Gersten, 2017). Based on the models of the rotational flow of viscous fluid, researchers have developed the models for magnetohydrodynamic flow due to rotating disc (Attia, 1998, 2007; Turkyilmazoglu, 2012). Using Rosensweig and Shliomis models, the researchers have demonstrated the flow of ferrofluid due to rotating disc (Ram et al., 2010; 2013a,b). The researchers have investigated the flow over a rotating disc to measure the irreversibility of the system and for heat transfer encampment applications (Qayyum et al., 2018; Rashihi et al., 2013; Hayat et al., 2018). For more practical applications of rotational flow, the researchers have classified the problems pertaining to specific types of nanofluid (Ijaz Khan et al., 2020; Hayay et al., 2017; Mustafa, 2017). Rotating boundary layer flow, flow over a wedge, plate and stagnation point, flow of an electrically conducting fluid along with a vertical plate, and flow over an exponentially accelerated plate have been investigated by researchers and they have presented the similarity solution using numerical techniques (Veera Krishna et al., 2020; Chamkha,

1997; Thameem Basha et al., 2019; Veera Krishna and Chamkha, 2019). However, researchers have demonstrated the perturbation technique to investigate the nanoparticles in blood flow and thermal transport of Williamson nanofluid flow (Bhatti et al., 2020a,b). Abo-Elkhair et al. (2021) used Adomain decomposition method to investigate hybrid bio-nanofluid flow in a peristaltic channel. The researchers have been working continuously to improve the numerical solution of a set of non-dimensional coupled differential of flow over a rotating disc problem (Chaturani and Narasimman, 1991; Rahman, 1978; Schultz and Shah, 1979; Hayat et al., 2018).

Reddy et al. (2017) investigated the flow of Ag-water and Cu-water nanofluids flow due to rotating disc. Takhar et al. (2003) studied the flow of electrically conducting fluid due to a vertical rotating cone and obtained the similarity solution through the finite difference method. Krishana and Chamkha (2020) obtained the analytic solution of the magnetohydrodynamic rotating flow of elastic-viscous fluid. Numerical solutions for the convective flow of nanofluids over a rotating cylinder have been obtained by researchers (Alsabery et al., 2020; Selimefendigil and Chamkha, 2019). Hybrid nanofluid flow in a rotating system, convective flow in a vertical moving cylinder, thin fluid over a vertical plate and conductive fluid over a vertical cone, have been investigated (Kumar et al., 2019; Chmkha et al., 2019; Takhar et al., 2002; Chemkha, 1996). Arain et al. (2020) investigated the multiphase flow between the rotating plates and obtained the numerical solution of similarity equations using the differential transform method. Ali et al. (2021) studied the non-Newtonian Oldroyd-B fluid flow over a parabolic surface and obtained the numerical solution of similarity equations through Runge–Kutta Fehlberg method.

In the present work, the impact of volume concentration and magnetic torque on the swirling flow of water-carrying iron(III)

oxide nanofluid due to the rotating disc is investigated. This swirling flow is considered steady and axisymmetric; therefore, cylindrical equations of the flow are directly numerically solved using the two-dimensional CFD Module in COMSOL Multiphysics. Further, the governing equations are reduced into non-dimensional coupled differential equations using a similarity approach and compared with the results obtained through CFD Module. The similarity model is also validated with the previous theoretical models.

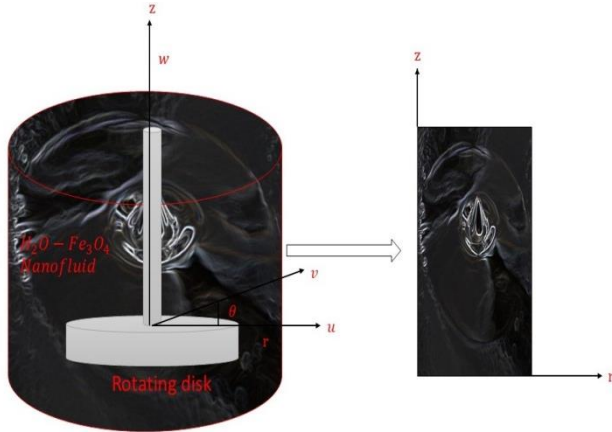


Fig. 1. Flow of axisymmetric nanofluid due to rotating disc and its two-dimensional CFD domain

2. MATHEMATICAL MODEL

The schematic diagram of the flow due to a rotating disc in a tank is shown in Fig. 1. The disc rotates uniformly about the z-axis and generates a three-dimensional boundary layer. The flow is axisymmetric; therefore, the three-dimensional flow has been considered over a two-dimensional region in the CFD Module. The velocities of the water-carrying iron(III) oxide nanofluid changes in the radial and axial directions. In the CFD Module, the computational domain is the two-dimensional geometry (Fig. 1). However, the similarity approach is used on the three-dimensional geometry in Fig. 1. These two approaches of rotational flow for velocity distributions are compared to each other. The flow of magnetic fluid is described by the following equations (Shliomis and Morozov, 1994; Odenbach and Thurm, 2002):

$$\nabla \cdot \mathbf{V} = 0 \quad (1)$$

$$\rho_n \left[\frac{\partial \mathbf{V}}{\partial t} + (\mathbf{V} \cdot \nabla) \mathbf{V} \right] = -\nabla p + \mu_0 M \nabla H + \mu_n \nabla^2 \mathbf{V} + \frac{I}{2\tau_s} \nabla \times (\boldsymbol{\omega}_p - \boldsymbol{\Omega}) \quad (2)$$

$$I \frac{d\boldsymbol{\omega}_p}{dt} = \mu_0 (\mathbf{M} \times \mathbf{H}) - \frac{I}{\tau_s} (\boldsymbol{\omega}_p - \boldsymbol{\Omega}) \quad (3)$$

The inertial term $I \frac{d\boldsymbol{\omega}_p}{dt}$ is negligible in comparison with the relaxation term $I \frac{\boldsymbol{\omega}_p}{\tau_s}$. Therefore the equation of rotational motion can be written as (Bacri et al., 1995; Bhabdari, 2020):

$$\boldsymbol{\omega}_p = \boldsymbol{\Omega} + \mu_0 \frac{\tau_s}{I} (\mathbf{M} \times \mathbf{H}) \quad (4)$$

Using Eq. (4), Eq. (2) can be written as (Shliomis and Morozov, 1994; Bacri et al., 1995):

$$\rho_n \left[\frac{\partial \mathbf{V}}{\partial t} + (\mathbf{V} \cdot \nabla) \mathbf{V} \right] = -\nabla \tilde{p} + \mu_n \nabla^2 \mathbf{V} + \frac{\mu_0}{2} \nabla \times (\mathbf{M} \times \mathbf{H}) \quad (5)$$

where $-\nabla \tilde{p} = -\nabla p + \mu_0 M \nabla H$ denotes the reduced pressure due to magnetisation force [43].

The equilibrium of the magnetic and viscous torque can be written from Eq. (5) as (Ram and Bhandari, 2013; Bacri et al., 1995):

$$\mu_0 (\mathbf{M} \times \mathbf{H}) = -6\mu_n \varphi_1 (\boldsymbol{\Omega} - \boldsymbol{\omega}_p) \quad (6)$$

The Eq. (6) can be written for mean magnetic torque as (Bacri et al., 1995):

$$\mu_0 (\overline{\mathbf{M} \times \mathbf{H}}) = -6\mu_n \varphi_1 m_1 \boldsymbol{\Omega} \quad (7)$$

where m_1 denotes the effective magnetic number due to the applied magnetic field. Using Eqs (6) and (7), the following relation is obtained (Shliomis and Morozov, 1994; Ram and Bhandari, 2013):

$$\begin{aligned} \frac{\mu_0}{2} \nabla \times (\overline{\mathbf{M} \times \mathbf{H}}) &= \frac{1}{2} \nabla \times -6\mu_n \varphi_1 m_1 \boldsymbol{\Omega} \\ &= -\frac{3}{2} \mu_n \varphi_1 m_1 \nabla (\nabla \cdot \mathbf{V}) + \frac{3}{2} \mu_n \varphi_1 m_1 \nabla^2 \mathbf{v} = \frac{3}{2} \mu_n \varphi_1 m_1 \nabla^2 \mathbf{V} \end{aligned} \quad (8)$$

In the above equation, $\frac{3}{2} \mu_n \varphi_1 m_1$ is the rotational viscosity due to the applied magnetic field. Using the result in Eq. (8), Eq. (6) can be written as:

$$\rho_n \left[\frac{\partial \mathbf{V}}{\partial t} + (\mathbf{V} \cdot \nabla) \mathbf{V} \right] = -\nabla \tilde{p} + \mu_n \left(1 + \frac{3}{2} \varphi_1 m_1 \right) \nabla^2 \mathbf{V} \quad (9)$$

The physical properties of the ferrofluid are as follows (Sheikholeslami and Shehzad, 2018):

$$\rho_n = (1 - \varphi_1) \rho_f + \varphi_1 \rho_s, \quad \mu_n = \frac{\mu_f}{(1 - \varphi_1)^{2.5}} \quad (10)$$

The density of the nanofluid depends on the density of the base fluid and volume concentration. Enhancing the concentration of iron(III) oxide increases the density of the nanofluid. Similarly, it changes the viscosity of nanofluids.

Since the flow is considered steady and axisymmetric, Eqs (1) and (9) can be written in cylindrical coordinates as (Shliomis and Morozov, 1994; Bhandari, 2020):

$$\frac{\partial u}{\partial r} + \frac{u}{r} + \frac{\partial w}{\partial z} = 0 \quad (11)$$

$$\begin{aligned} \rho_n \left[u \frac{\partial u}{\partial r} + w \frac{\partial u}{\partial z} - \frac{v^2}{r} \right] &= -\frac{\partial \tilde{p}}{\partial r} + \mu_n \left(1 + \frac{3}{2} \varphi_1 m_1 \right) \left\{ \frac{\partial^2 u}{\partial z^2} + \right. \\ &\left. \frac{1}{r} \frac{\partial u}{\partial r} - \frac{u}{r^2} + \frac{\partial^2 u}{\partial r^2} \right\} \end{aligned} \quad (12)$$

$$\begin{aligned} \rho_n \left[u \frac{\partial v}{\partial r} + w \frac{\partial v}{\partial z} + \frac{uv}{r} \right] &= \mu_n \left(1 + \frac{3}{2} \varphi_1 m_1 \right) \left\{ \frac{\partial^2 v}{\partial z^2} + \frac{1}{r} \frac{\partial v}{\partial r} + \right. \\ &\left. \frac{\partial^2 v}{\partial r^2} - \frac{v}{r^2} \right\} \end{aligned} \quad (13)$$

$$\begin{aligned} \rho_n \left[u \frac{\partial w}{\partial r} + w \frac{\partial w}{\partial z} \right] &= -\frac{\partial \tilde{p}}{\partial z} + \mu_n \left(1 + \frac{3}{2} \varphi_1 m_1 \right) \left\{ \frac{\partial^2 w}{\partial z^2} + \frac{1}{r} \frac{\partial w}{\partial r} + \right. \\ &\left. \frac{\partial^2 w}{\partial r^2} \right\} \end{aligned} \quad (14)$$

The boundary conditions for the considered flow are as follows:

$$z = 0; \quad u = 0, \quad v = r\omega, \quad w = 0; \quad z \rightarrow \infty; \quad u \rightarrow 0, \quad v \rightarrow 0 \quad (15)$$

In this case, the disc rotates with the uniform angular velocity ω about the axis perpendicular to its plane. No-slip boundary conditions are considered in the flow. The layer of the nanofluid is at the disc which is carried along with the disc. This layer of nanofluid is driven outwards by the centrifugal force. Then new fluid particles are coming towards the disc in the axial direction and these particles are ejected due to centrifugal force. The centrifugal force and radial pressure gradient have an important role in circulating the nanoparticles at a sufficient distance from the wall.

3. NUMERICAL SOLUTION

In the present problem, the swirling flow of water-based Fe_3O_4 nanofluid has been simulated in the CFD 2D axisymmetric module of COMSOL Multiphysics. The following physical parameter has been used in the solution:

Tab. 1. Values of parameters

Parameter	values
ρ_f	997.1[kg m ⁻³]
ρ_s	5500 [kg m ⁻³]
φ_1	0.1
μ_f	0.001[Pa s]
m_1	2
ω	0.5π [rad s ⁻¹]

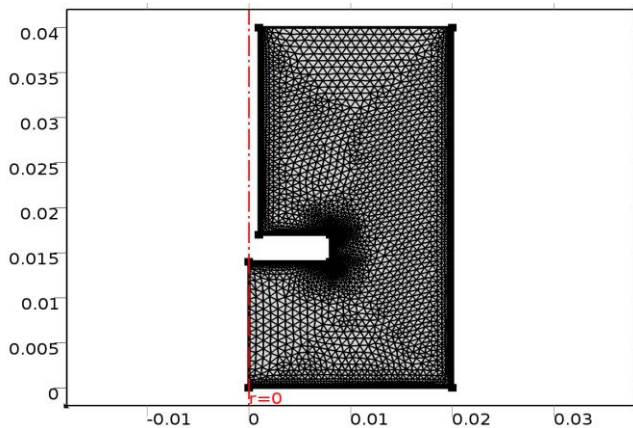


Fig. 2. Mesh selection on the geometry

There are a total of eight boundaries of the domain as shown in Fig. 2. The maximum element size taken is 9×10^{-4} and the minimum size of the element is 4×10^{-5} . The curvature factor selected is 0.3 and the maximum element growth rate is 1.15. The surface plots for the magnitude of the velocity, radial velocity, tangential velocity, axial velocity, and pressure on the nanofluid

are presented for different volume fractions and effective magnetic parameters. The values of the parameter used in the solution are given in Tab. 1. In the CFD Module, quadratic interpolation functions are used in the approximation of the solutions. The triangular and quadrilateral elements are used during the solution of the problem. The mesh description of the elements and their properties are shown in Tab. 2. The maximum number of iterations is taken as 300 and the error in the solution is of the order 10^{-5} .

Tab. 2. Mesh description during the finite element method over the domain of the flow

Property	Value
Minimum element quality	0.07274
Average element quality	0.794
Triangular elements	4679
Quadrilateral elements	984
Edge elements	265
Vertex elements	8

Eqs (11)–(15) can also be solved by using similarity transformation. The following similarity transformation has been used to obtain non-dimensional coupled differential equations:

$$u = r\omega E(\alpha), \quad v = r\omega F(\alpha), \quad w = \sqrt{v_f \omega} G(\alpha), \quad \tilde{p} - p_\infty = -\rho v \omega P(\alpha), \quad \alpha = \sqrt{\frac{\omega}{v_f}} z \quad (16)$$

The transformed equations are as follows:

$$\frac{dG}{d\alpha} + 2E = 0 \quad (17)$$

$$\left(1 + \frac{3}{2}\varphi_1 m_1\right) \left[\frac{1}{(1-\varphi_1)^{2.5} \left(1 - \varphi_1 + \varphi_1 \frac{\rho_s}{\rho_f}\right)} \right] \frac{d^2 E}{d\alpha^2} - G \frac{dE}{d\alpha} - E^2 + F^2 = 0 \quad (18)$$

$$\left(1 + \frac{3}{2}\varphi_1 m_1\right) \left[\frac{1}{(1-\varphi_1)^{2.5} \left(1 - \varphi_1 + \varphi_1 \frac{\rho_s}{\rho_f}\right)} \right] \frac{d^2 F}{d\alpha^2} - G \frac{dF}{d\alpha} - 2EF = 0 \quad (19)$$

$$\left(1 + \frac{3}{2}\varphi_1 m_1\right) \left[\frac{1}{(1-\varphi_1)^{2.5} \left(1 - \varphi_1 + \varphi_1 \frac{\rho_s}{\rho_f}\right)} \right] \frac{d^2 G}{d\alpha^2} - G \frac{dG}{d\alpha} - \frac{dP}{d\alpha} = 0 \quad (20)$$

The boundary conditions are as follows:

$$E(0) = 0, \quad F(0) = 1, \quad G(0) = 0, \quad E(\infty) = 0, \quad F(\infty) = 0 \quad (21)$$

The reduced pressure can be calculated as:

$$P(\alpha) = P_0 + \left(1 + \frac{3}{2}\varphi_1 m_1\right) \left[\frac{1}{(1-\varphi_1)^{2.5} \left(1 - \varphi_1 + \varphi_1 \frac{\rho_s}{\rho_f}\right)} \right] \frac{dG}{d\alpha} - \frac{1}{2} G^2 \quad (22)$$

4. RESULTS AND DISCUSSIONS

In this section, the results for radial tangential and axial velocity distribution are presented for different values of volume fraction and effective magnetic parameters. 2D surface plots are

obtained from the CFD Module in COMSOL Multiphysics, and for the same problem, a system of nonlinear coupled differential equations has been solved numerically. A brief discussion of the results is presented here.

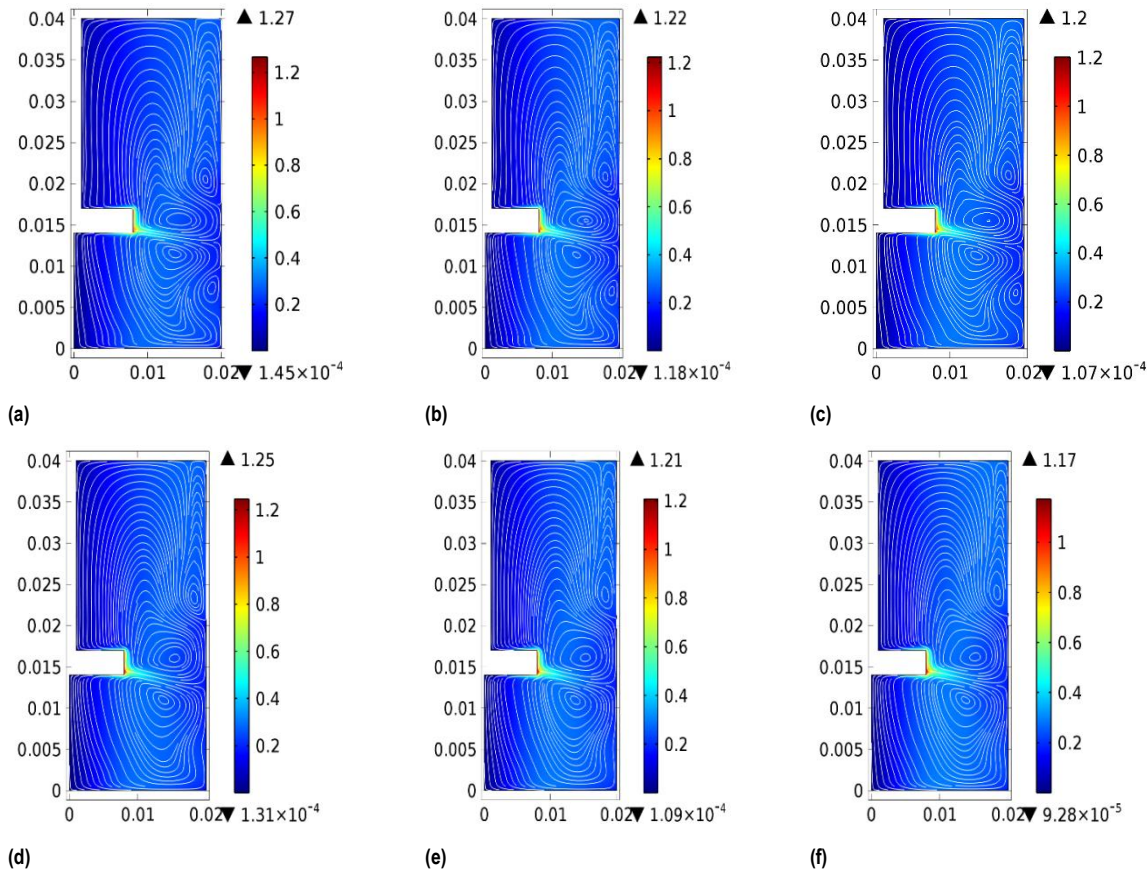


Fig. 3. Surface plot for the magnitude of the velocity (a) $\varphi_1 = 0, m_1 = 2$ (b) $\varphi_1 = 0.2, m_1 = 2$ (c) $\varphi_1 = 0.3, m_1 = 2$ (d) $\varphi_1 = 0.1, m_1 = 2$ (e) $\varphi_1 = 0.1, m_1 = 4$ (f) $\varphi_1 = 0.1, m_1 = 6$

Figs 3(a)–(f) show the magnitude of the velocity for different values of volume concentration and the effective magnetic parameter. Fig. 3(a) shows the magnitude of the velocity of the carrier liquid. Figs 3(b) and 3(c) are obtained for $\varphi_1 = 0.2$ and $\varphi_1 = 0.3$, respectively. It has been shown that for $\varphi_1 = 0.2$ the maximum value of the velocity is 1.22 m/s and for $\varphi_1 = 0.3$ the velocity is 1.20 m/s. Increasing the volume concentration reduces the velocity distribution in the flow. Fig. 3(d) shows the magnitude of the velocity for $m_1 = 2$ and $\varphi_1 = 0.1$. Increasing values of m_1 increases the viscosity of the fluid and therefore reduces the magnitude of the velocity. The velocity is maximum near the rotation of the disc. Similarly, Figs 3(e) and 3(f) are presented for $m_1 = 4$ and $m_1 = 6$, respectively.

Figs 4(a)–(f) show the radial velocity distribution for different values of volume concentration and the effective magnetic parameter. The streamline in the surface plot shows the tangent of the velocity distribution. The radial velocity decreases the increasing values of volume concentration and magnetic parameter. Swirling of the disc in the presence of the magnetic field enhances the difference between the rotation of the particles and fluid. This difference enhances the viscosity of water conveying iron(III) oxide nanofluid. Near the rotating equipment, the velocity is

higher than that in other places. Increasing these parameters changes the pattern of streamlines. The velocity changes Fe₃O₄ to become closer than the base fluid. Figs 5(a)–(f) show the tangential velocity distribution for different values of volume concentration and the effective magnetic parameter. The speed of tangential velocity distribution is higher than the radial velocity distribution. When increasing volume concentration and magnetic parameter, the streamlines become closer to each other than in ordinary cases. This situation arises due to the difference in the rotation between the nanoparticles and fluid. The magnetic field increases this misalignment between the rotation of the particles and fluid. Therefore, the viscosity of the nanofluid increases. Figs 6(a)–(f) show the axial velocity distribution for different values of volume concentration and the effective magnetic parameter. Some of the values of the axial velocity are negative. The negative values of the axial velocity show that the flow is directed towards the container.

Fig. 7 shows the magnitude of the dimensionless velocity distribution for different values of φ_1 . The magnitude for the velocity in dimensionless form is obtained from the expression $\sqrt{E^2 + F^2 + G^2}$. The velocity distribution is presented on dimensionless axial distance. It is seen that when increasing values of

φ_1 , the magnitude of the velocity decreases. The magnitude of the velocity also decreases for increasing values of m_1 , as shown in Fig. 8. The results in Figs 7 and 8 represent a similar character as presented in Figs 3(a)–(f). Figs 9 and 10 show the radial velocity distribution for different values of φ_1 and m_1 . A case $\varphi_1 = 0$ shows the velocity distribution of the base fluid. Adding Fe_3O_4 nanoparticles with suiTab. surfactants decreases the radial velocity distribution. In the presence of the magnetic field, a decrease in the radial velocity distribution is observed. Figs 11 and 12 show the tangential velocity distribution for different values of φ_1 and m_1 . The impact of the volume concentration and rotational viscosity on the tangential velocity distribution is less as compared to radial and axial velocity distributions. Near the surface of the container, the tangential velocity decreases for in-

creasing values of φ_1 and m_1 , and far from the surface, these parameters enhance the tangential velocity distribution. Near the surface, the flow of the nanofluid is influenced by the rotating cylinder. Figs 13 and 14 show the axial velocity distribution for different values of φ_1 and m_1 . In the absence of magnetic field and iron(III) oxide nanoparticles, the problem reduces to the previous theoretical models of rotational flow. The comparative results with previous theoretical models are shown in Tab. 3. Increasing the values of the volume concentration and effective magnetic parameter decreases the axial velocity. It is noticeable that the physical interpretation of the flow dimensionless approach is very useful and aligned with the results obtained through the CFD Module. However, the CFD Module can provide the problem imagination and more regions for the velocity distribution.

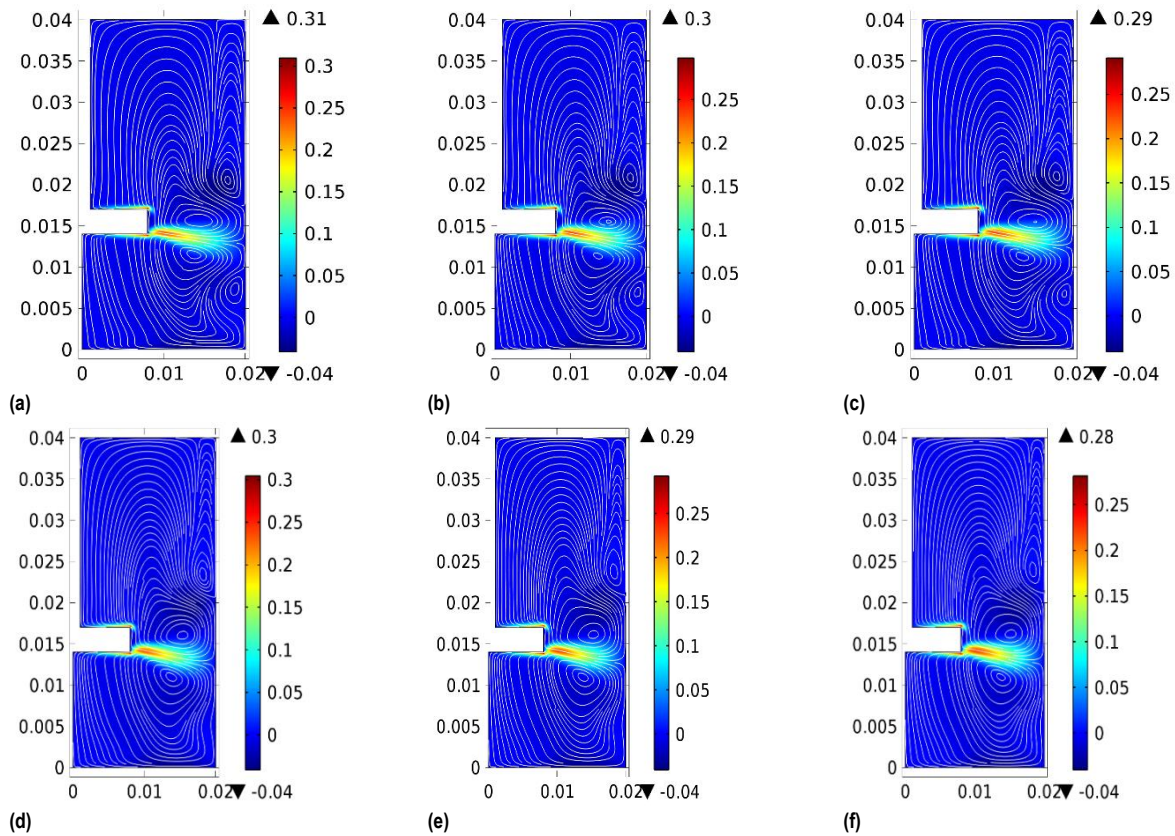
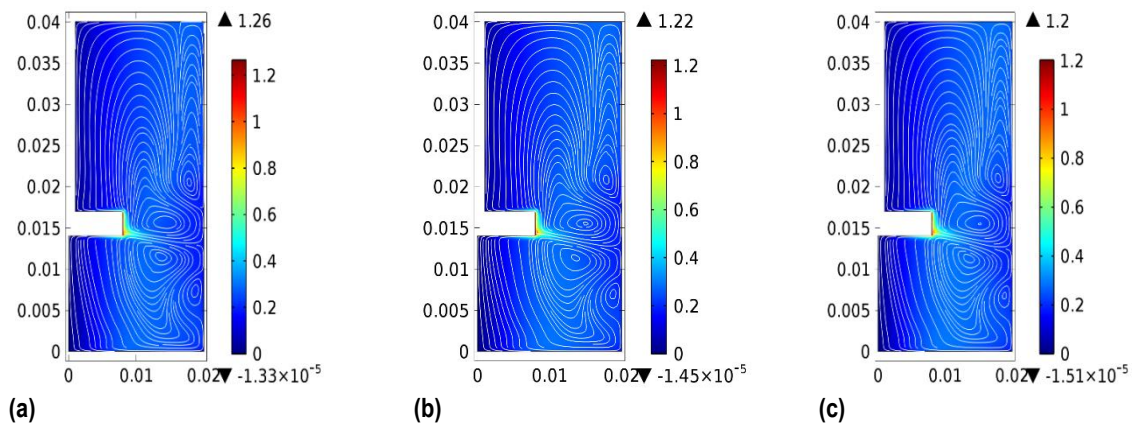


Fig. 4. Surface plot for the radial velocity (a) $\varphi_1 = 0, m_1 = 2$ (b) $\varphi_1 = 0.2, m_1 = 2$ (c) $\varphi_1 = 0.3, m_1 = 2$ (d) $\varphi_1 = 0.1, m_1 = 2$ (e) $\varphi_1 = 0.1, m_1 = 4$ (f) $\varphi_1 = 0.1, m_1 = 6$



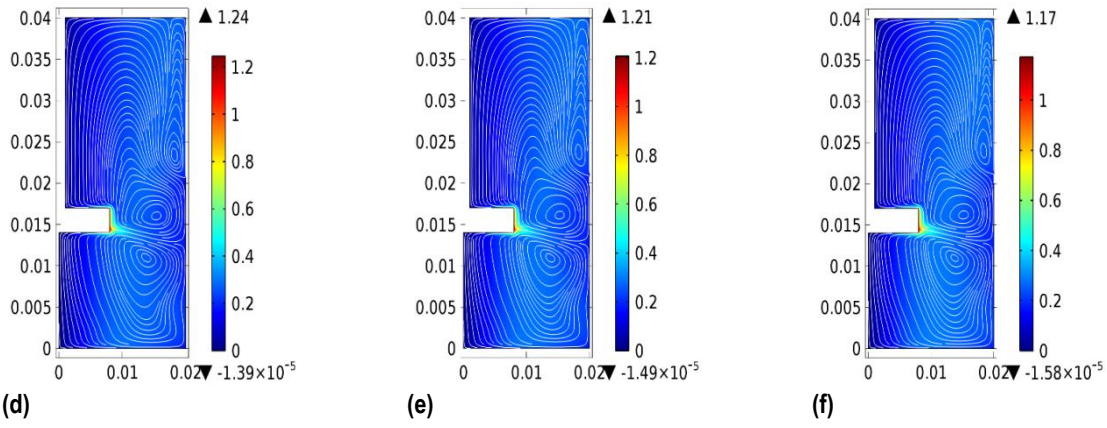


Fig. 5. Surface plot for the tangential velocity (a) $\phi_1 = 0, m_1 = 2$ (b) $\phi_1 = 0.2, m_1 = 2$ (c) $\phi_1 = 0.3, m_1 = 2$ (d) $\phi_1 = 0.1, m_1 = 2$ (e) $\phi_1 = 0.1, m_1 = 4$ (f) $\phi_1 = 0.1, m_1 = 6$

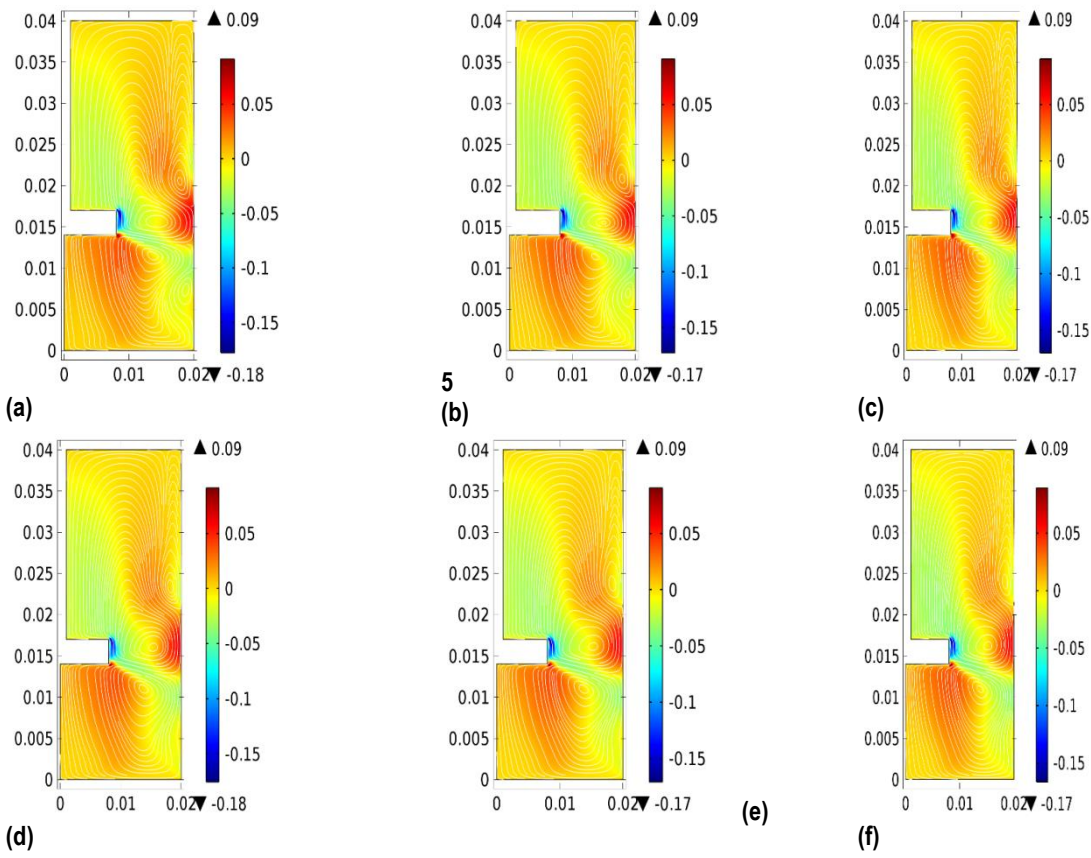


Fig. 6. Surface plot for the axial velocity (a) $\phi_1 = 0, m_1 = 2$ (b) $\phi_1 = 0.2, m_1 = 2$ (c) $\phi_1 = 0.3, m_1 = 2$ (d) $\phi_1 = 0.1, m_1 = 2$ (e) $\phi_1 = 0.1, m_1 = 4$ (f) $\phi_1 = 0.1, m_1 = 6$

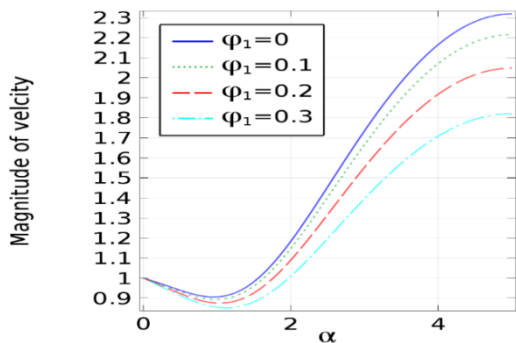


Fig. 7. Magnitude of the velocity for different values of ϕ_1 at $m_1 = 2$

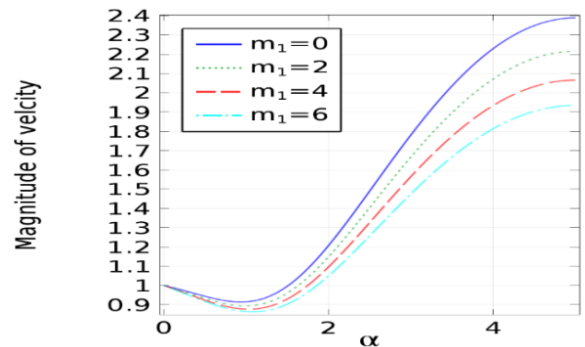


Fig. 8. Magnitude of the velocity for different values of m_1 at $\phi_1 = 0.1$

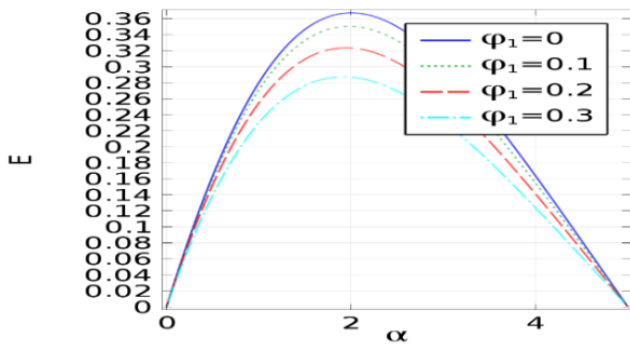


Fig. 9. Radial velocity distribution for different values of φ_1 at $m_1 = 2$

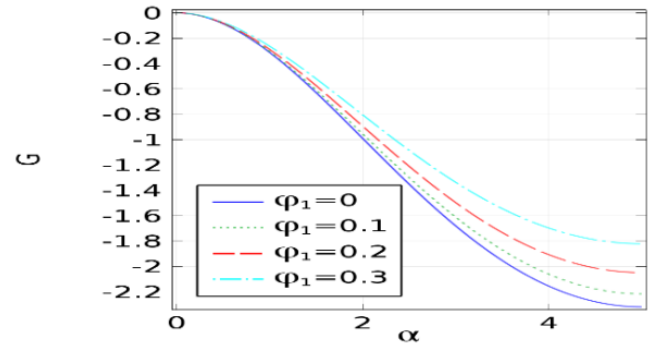


Fig. 13. Axial velocity distribution for different values of φ_1 at $m_1 = 2$

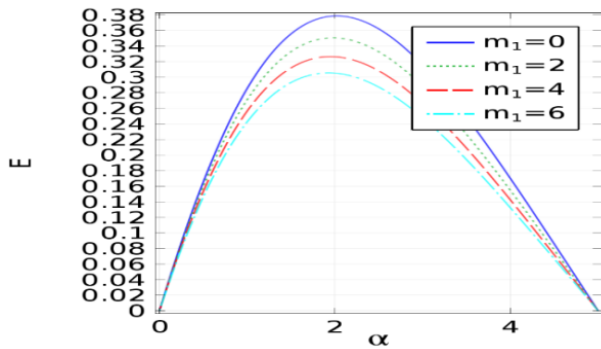


Fig. 10. Radial velocity distribution for different values of m_1 at $\varphi_1 = 0.1$

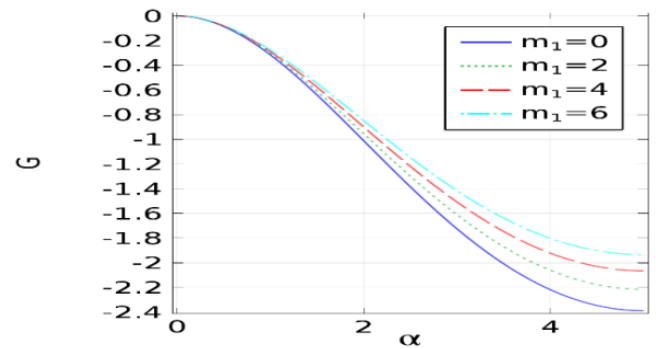


Fig. 14: Axial velocity distribution for different values of m_1 at $\varphi_1 = 0.1$

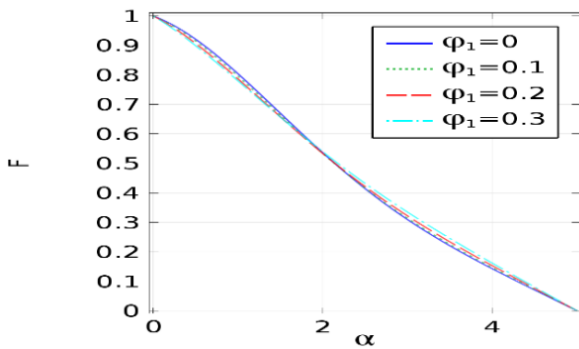


Fig. 11. Tangential velocity distribution for different values of φ_1 at $m_1 = 2$

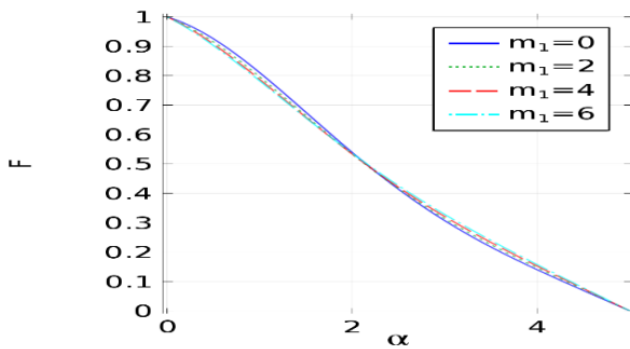


Fig. 12. Tangential distribution for different values of m_1 at $\varphi_1 = 0.1$

Tab. 3. Comparison of similarity solution with previous theoretical models for $\varphi_1 = m_1 = 0$

	$E'(0)$	$F'(0)$
Kelson and Desseaux [47]	0.510233	-0.615922
Bachok et al. [48]	0.5102	-0.6159
Turkylmazoglu [49]	0.51023262	-0.61592201
Present Result	0.5102337	-0.6159241

5. CONCLUSIONS

The swirling flow of water-based Fe_3O_4 nanofluid with different volume concentrations and rotational viscosity has been studied. The results for the velocity distribution have been obtained through the CFD Module and dimensional analysis. These results indicate that increasing the volume concentration and rotational viscosity decreases the velocity distribution. These results show the comparative results between the CFD Module and dimensionless analysis. Both techniques favour the findings of each other. For the physical interpretation of the results, dimensionless analysis is important. However, for real-time particle tracing CFD Module is important. These results show that both types of studies are relevant to the development of swirling flow analysis. These results might be useful in bringing about an improvement in the sealing of hard disc drives.

Nomenclature:

- E Dimensionless component of radial velocity
- F Dimensionless component of tangential velocity
- G Dimensionless component of axial velocity
- H Magnetic field intensity (A/m)

I	Sum of the particles moment of inertia (kg/m ²)
M	Magnetization (A/m)
m_1	Effective magnetic parameter
p	Fluid Pressure (kg/m/s ²)
\tilde{p}	Reduced fluid pressure (kg/m/s ²)
r	Radial direction (m)
t	Time (s)
u	Radial velocity (m/s)
v	Tangential velocity (m/s)
V	Velocity of ferrofluid (m/s)
w	Axial velocity (m/s)
z	Axial direction (m)
ρ_n	Nanofluid density (kg/m ³)
ρ_f	Carrier liquid density (kg/m ³)
ρ_s	Nanoparticles density (kg/m ³)
μ_0	The magnetic permeability of free space (H/m)
μ_n	Reference viscosity of nanofluid (kg/m/s ²)
μ_n	Reference viscosity of carrier liquid (kg/m/s ²)
ν_f	Kinematic viscosity of the base fluid (m ² /s)
∇	Gradient operator (/m)
τ_s	Rotational relaxation time (/s)
ω_p	Angular velocity of particles (rad/s)
Ω	Vorticity (rad/s)
ω	Angular velocity (rad/s)
θ	Tangential direction (rad)
φ_1	Volume concentration
ν_n	Kinematic viscosity without magnetic field (m ² /2)
α	Dimensionless distance parameter

REFERENCES

1. **Abo-Elkhair R.E., Bhatti M.M., Mekheimer K.S.** (2021), Magnetic force effects on peristaltic transport of hybrid bio-nanofluid (Au–Cu nanoparticles) with moderate Reynolds number: An expanding horizon, *Int. Commun. Heat Mass Transf.*, 123, 105228.
2. **Ali Z., Zeeshan A, Bhatti M.M., Hobiny A., Saeed T.** (2021), Insight into the Dynamics of Oldroyd-B Fluid Over an Upper Horizontal Surface of a Paraboloid of Revolution Subject to Chemical Reaction Dependent on the First-Order Activation Energy, *Arab. J. Sci. Eng.*, 1–10.
3. **Alsabery A.I., Ghalambaz M., Armaghani T., Chamkha, I. Hashim I., Pour M.S.** (2020), Role of rotating cylinder toward mixed convection inside a wavy heated cavity via two-phase nanofluid concept, *Nanomaterials*, 10(6), 1–22.
4. **Arain M.B, Bhatti M.M., Zeeshan A., Saeed T., Hobiny A.** (2020), Analysis of arrhenius kinetics on multiphase flow between a pair of rotating circular plates, *Math. Probl. Eng.*, 2020.
5. **Attia H.A** (1998), Unsteady MHD flow near a rotating porous disk with uniform suction or injection, *Fluid Dyn. Res.*, 23(5), 283–290.
6. **Attia H.A.** (2007), On the effectiveness of ion slip and uniform suction or injection on steady MHD flow due to rotating disk with heat transfer ohmic heating, *Chem. Eng. Commun.*, 194(10), 1396–1407.
7. **Bachok N., Ishak A., Pop I.** (2011), Flow and heat transfer over a rotating porous disk in a nanofluid, *Phys. B Phys. Condens. Matter*, 406(9), 1767–1772.
8. **Bacri J.C., Perzynski R., Shliomis M.I., Burde G.I.** (1995), Negative-viscosity effect in a magnetic fluid, *Phys. Rev. Lett.*, 75(11), 2128–2131.
9. **Benton E.R.** (1966), On the flow due to a rotating disk, *J. Fluid Mech.*, 24(4), 781–800.
10. **Bhandari A.** (2020a), Study of ferrofluid flow in a rotating system through mathematical modeling, *Math. Comput. Simul.*, 178, 290–306.
11. **Bhandari A.** (2020b), Study of magnetoviscous effects on ferrofluid flow, *Eur. Phys. J. Plus*, 135(7), 537.
12. **Bhatti M.M., Marin M., Zeeshan A., Ellahi R., Abdelsalam S.I.** (2020a), Swimming of motile gyrotactic microorganisms and nanoparticles in blood flow through anisotropically tapered arteries, *Front. Phys.*, 8(95).
13. **Bhatti M.M., Riaz A., Zhang L., Sait S.M., Ellahi R.** (2020b), Biologically inspired thermal transport on the rheology of Williamson hydromagnetic nanofluid flow with convection: an entropy analysis, *J. Therm. Anal. Calorim.*, 1–16.
14. **Chamkha A.J.** (1996), Non-darcy hydromagnetic free convection from a cone and a wedge in porous media, *Int. Commun. Heat Mass Transf.*, 23(6), 875–887.
15. **Chamkha A.J.** (1997), MHD-free convection from a vertical plate embedded in a thermally stratified porous medium with Hall effects, *Appl. Math. Model.*, 21(10), 603–609.
16. **Chamkha A.J., Dogonchi A.S., Ganji D.D.** (2019), Magneto-hydrodynamic flow and heat transfer of a hybrid nanofluid in a rotating system among two surfaces in the presence of thermal radiation and Joule heating, *AIP Adv.*, 9(2), 025103.
17. **Chaturani P., Narasimman S.** (1991), Numerical solution of a micropolar fluid flow between two rotating coaxial disks, *Acta Mech.*, 89(1-4), 133–145.
18. **Cochran W.G.** (1934), The flow due to a rotating disc, *Math. Proc. Cambridge Philos. Soc.*, 30(3), 365–375.
19. **Hayat T., Aziz A., Muhammad T., Alsaedi A.** (2018a), Numerical treatment for Darcy–Forchheimer flow of nanofluid due to a rotating disk with convective heat and mass conditions, *Int. J. Numer. Methods Heat Fluid Flow*, 28(11), 2531–2550.
20. **Hayat T., Qayyum S., Khan M.I., Alsaedi A.** (2018b), Entropy generation in magnetohydrodynamic radiative flow due to rotating disk in presence of viscous dissipation and Joule heating, *Phys. Fluids*, 30(1), 017101.
21. **Hayat T., Rashid M., Imtiaz M., Alsaedi A.** (2017), Nanofluid flow due to rotating disk with variable thickness and homogeneous-heterogeneous reactions, *Int. J. Heat Mass Transf.*, 113, 96–105.
22. **Ijaz Khan M., Khan S.A., Hayat T., Imran Khan M., Alsaedi A.** (2020), Entropy optimization analysis in MHD nanomaterials (TiO₂-GO) flow with homogeneous and heterogeneous reactions, *Comput. Methods Programs Biomed.*, 184.
23. **Kelson N., Desseaux A.** (2000), Note on porous rotating disk flow, *ANZIAM J.*, 42, 837.
24. **Krishna M.V., Chamkha A.J.** (2020), Hall and ion slip effects on MHD rotating flow of elastico-viscous fluid through porous medium, *Int. Commun. Heat Mass Transf.*, 113, 104494.
25. **Kumar B., Seth G.D., Nandkeolyar R., Chamkha A.J.** (2019), Outlining the impact of induced magnetic field and thermal radiation on magneto-convection flow of dissipative fluid, *Int. J. Therm. Sci.*, 146, 106101.
26. **Mustafa M.** (2017), MHD nanofluid flow over a rotating disk with partial slip effects: Buongiorno model, *Int. J. Heat Mass Transf.*, 108, 1910–1916.
27. **Odenbach S., Thurm S.** (2002), *Magnetoviscous Effects in Ferrofluids*, 185–201.
28. **Qayyum S., Hayat T., Khan M.I., Alsaedi A.** (2018), Optimization of entropy generation and dissipative nonlinear radiative Von Karman's swirling flow with Soret and Dufour effects, *J. Mol. Liq.*, 262, 261–274.
29. **Rahman M.** (1978), On the numerical solution of the flow between a rotating and a stationary disk, *J. Comput. Appl. Math.*, 4(4), 289–293.
30. **Ram P., Bhandari A.** (2013a), Effect of phase difference between highly oscillating magnetic field and magnetization on the unsteady ferrofluid flow due to a rotating disk, *Results Phys.*, 3, 55–60.
31. **Ram P., Bhandari A.** (2013b), Effect of phase difference between highly oscillating magnetic field and magnetization on the unsteady ferrofluid flow due to a rotating disk, *Results Phys.*, 3, 55–60.
32. **Ram P., Bhandari A.** (2013c), Negative viscosity effects on ferrofluid flow due to a rotating disk, *Int. J. Appl. Electromagn. Mech.*, 41(4), 467–478.

33. **Ram P., Sharma K., Bhandari A.** (2010), Effect of Porosity on Ferrofluid Flow With Rotating Disk, *6(16)*, 67–76.
34. **Rashidi M.M., Abelman S., Mehr N.F.** (2013), Entropy generation in steady MHD flow due to a rotating porous disk in a nanofluid, *Int. J. Heat Mass Transf.*, *62(1)*, 515–525.
35. **Reddy P.S., Sreedevi P., Chamkha A.J.** (2017), MHD boundary layer flow, heat and mass transfer analysis over a rotating disk through porous medium saturated by Cu-water and Ag-water nanofluid with chemical reaction, *Powder Technol.*, *307*, 46–55.
36. **Rosensweig R.E.** (1997), *Ferrohydrodynamics*, Dover Publications.
37. **Schlichting H., Gersten K.** (2017), *Boundary-Layer Theor.*, Berlin, Heidelberg: Springer Berlin Heidelberg.
38. **Schultz D.H., Shah V.L.** (1979), Numerical solution of laminar recirculating flow between shrouded rotating disks, *Comput. Fluids*, *7(2)*, 137–144.
39. **Selimefendigil F., Chamkha A.J.** (2019), MHD mixed convection of nanofluid in a three-dimensional vented cavity with surface corrugation and inner rotating cylinder, *Int. J. Numer. Methods Heat Fluid Flow*, *30(4)*, 1637–1660.
40. **Sheikholeslami M., Shehzad S.A.** (2018), Numerical analysis of Fe₃O₄-H₂O nanofluid flow in permeable media under the effect of external magnetic source, *Int. J. Heat Mass Transf.*, *118*, 182–192.
41. **Shliomis M.I., Morozov K.I.** (1994), Negative viscosity of ferrofluid under alternating magnetic field, *Phys. Fluids*, *6(8)*, 2855–2861.
42. **Takhar H.S., Chamkha A.J., Nath G.** (2002), Combined heat and mass transfer along a vertical moving cylinder with a free stream, *Heat Mass Transf.*, *36(3)*, 237–246.
43. **Takhar H.S., Chamkha A.J., Nath G.** (2003), Unsteady mixed convection flow from a rotating vertical cone with a magnetic field, *Heat Mass Transf. und Stoffuebertragung*, *39(4)*, 297–304.
44. **Thameem Basha H., Sivaraj R., Subramanyam Reddy A., Chamkha A.J.** (2019), SWCNH/diamond-ethylene glycol nanofluid flow over a wedge, plate and stagnation point with induced magnetic field and nonlinear radiation – solar energy application, *Eur. Phys. J. Spec. Top.*, *228(12)*, 2531–2551.
45. **Turkyilmazoglu M.** (2012), MHD fluid flow and heat transfer due to a stretching rotating disk, *Int. J. Therm. Sci.*, *51(1)*, 195–201.
46. **Turkyilmazoglu M.** (2014), Nanofluid flow and heat transfer due to a rotating disk, *Comput. Fluids*, *94*, 139–146.
47. **Veera Krishna M., Ameer Ahamad N., Chamkha A.J.** (2020), Hall and ion slip effects on unsteady MHD free convective rotating flow through a saturated porous medium over an exponential accelerated plate, *Alexandria Eng. J.*, *59(2)*, 565–577.
48. **Veera Krishna M., Chamkha A.J.** (2019), Hall and ion slip effects on MHD rotating boundary layer flow of nanofluid past an infinite vertical plate embedded in a porous medium, *Results Phys.*, *15*, 102652.

Anupam Bhandari:  <https://orcid.org/0000-0002-2881-0078>

EXPERIMENTAL RESEARCH OF PAPERBOARD CUTTING IN DIE CUTTING PRESS WITH THE SCREW–NUT TRANSMISSION OF DRIVE MECHANISM OF A MOVABLE PRESSURE PLATE

Serhii TERNYTSKYI¹, IVAN REHEI², Nazar KANDIAK¹, Ihor RADIKHOVSKYI¹, Oksana MLYNKO^{2*}

¹Faculty of Computer Printing Engineering, Department of Computerized Complexes of Printing and Packaging Industries, Ukrainian Academy of Printing, Lviv, 79020, Pid Goloskom street, 19, Ukraine.

²Institute of Applied Mathematics and Fundamental Sciences, Department of Mathematics, Lviv Polytechnic National University, Lviv, 79013, Bandera street, 12, Ukraine.

serhij86@gmail.com, regey.ivan@gmail.com, kandyak.nazar@gmail.com, radikhovskiy@gmail.com, r_oxanne@ukr.net

received 14 February 2021, revised 22 June 2021, accepted 25 June 2021

Abstract: This paper reports experimental research of torques during paperboard cutting in the die cutting press with the screw–nut transmission in the drive mechanism of the movable pressure plate. The purpose of the study is to substantiate the practical implementation of the pressure plate drive mechanism with the use of screw–nut transmission for the production of cartons of paperboard blanks. The manufactured experimental bench for the research of paperboard blanks provides the possibility of getting dependencies of loads on different parameters of the die cutting process. The developed method of the experimental research envisages the use of the strain gauge method and the wireless module for data measurement and software for its processing that allow getting trustworthy results with minimum faults. As a result of experimental research studies, the impact of paperboard thickness and cutting velocity on torque values has been established. Results of experimental research allow getting trustworthy and systematised information about torque values depending on the thickness of the paperboard, the paperboard fibre direction and pressure plate displacement velocity. It is established that torque values on drive shaft during die cutting of paperboard blanks made of folding boxboard with thickness that lay in range of 0.3–0.7 mm. Experimental research studies show the impact of rotation speed of a drive shaft of the pressure plate drive mechanism on the torque value. The article shows the workability of the designed device with screw–nut transmission in the drive mechanism of a movable pressure plate.

Key words: die cutting press, pressure plate, screw–nut transmission, leadscrew, ball screw, cutting knife, die cutting forme, paperboard blank, torque

1. INTRODUCTION

Today, the growth of the global packaging industry can be observed. In 2012, as it has been described by Emblem A. and Emblem H. (2012), it was valued at over \$400 billion, roughly constituting 36% of paper and paperboard, 34% plastics, 17% metals and 10% glass; the remainder being made up of materials such as wood and textiles. Today, the global packaging market value is approximately \$860 billion, of which paperboard packaging accounts for roughly a third. The packaging market will grow by \$280 billion during 2020–2024 according to World Packaging Organisation.

As it was proved by Kirwan (2013), the main features that made paper and paperboard a significant part of the total packaging market are raw material properties, principles of manufacture and environmental and waste management. Paper and paperboard packaging has good appearance and performance properties that allow using it in a wide range of packaging.

Paper is usually defined as the substrate, made from vegetable fibres, which has a grammage of <250 grams per square metre (gsm), and paperboard has a grammage of 250 gsm or more. This definitive difference, however, is not widely used within

the industry, with different countries using varying terminologies. In Germany, paperboard has a grammage of 150 gsm or more.

The main method of manufacturing paperboard packaging is die cutting. Due to this method, cutting and creasing is carried out using a flat die for sheet-fed materials or a rotary die for reel-fed materials. According to the book of Emblem A. and Emblem H. (2012), the use of a flat die cutting forme allows packaging and manufacturing paperboard of different sizes and shapes. The forme is made from plywood, with steel cutting knives and creasing rulers inserted into grooves that are cut using a laser. On both sides of cutting knives are placed special foam rubber pillows that remove paperboard sheets from blades of cutting knives. The cutting and creasing operation manufactures paperboard packaging cartons.

Manufacturing paperboard packaging requires the performance of some technological operations. As it has been established by Rehei (2011), the chain of technological operations is accomplished automatically at paperboard blank stops during its periodical transportation through sections of equipment. Modern die cutting equipment is built on a section principle. The most important section is the press, which accomplishes the technological operation of die cutting. In die cutting presses, for pressure plate drive, special lever mechanisms are used. Khvedchyn and

Zelenyi (2014) have carried out the analysis of existing mechanism designs of pressure plate drive in die cutting equipment and equipment from other industries, which perform operations that require overcoming a significant technological load at the end of the movement of the executive link. As it has been noted by the authors, the work of such mechanisms bases on wedging effect, which provides sufficient effort value of the pressure plate with comparatively little loads on driving links. Building such mechanisms causes asymmetry of the right and left part of the pressure plate during the movement cycle. The symmetry of plate movement can be seen only at the final stage of its displacement when the work surface of the pressure plate becomes parallel to the surface of the base plate and begins die cutting of paperboard blanks. This asymmetry causes unevenness of load distribution and shows oscillations in the press, which reduces the quality of paperboard packaging and production efficiency. The analytical research of different mechanisms of pressure plate drive conducted by authors allows evaluation of the quality level of compliant mechanisms to set parameters. However, detailed kinematic and kinetostatic analysis of mechanisms has not been carried out. Such analysis is important because of the complicated build of mechanisms and needs to overcome significant technological loads.

In the paper by Kuznetsov et al. (2012), analytical research studies of flatbed die cutting press with the pressure plate drive are conducted, which are built on the wedging effect. Analytical research studies have proven the occurrence of unevenness in the pressure plate movement during the press cycle. Such unevenness of plate displacement negatively affects load dispersion of the drive during the kinematic cycle. It also causes occurrence of loads oscillating in the drive. The method proposed by authors to eliminate unevenness of plate displacement by the ratio of the movement of the component slider change does not allow full elimination of plate movement unevenness during the press cycle.

Lin W. et al. (2015) have carried out research studies of die cutting press with dual-elbow-bar mechanisms. The authors have proved design complexity of such mechanisms of the pressure plate drive. The pressure plate drive that is built by such schemes has ten links that makes the mechanism complicated during operation. The analysis made by authors has shown high values of inertia force of the pressure plate during its movement. It has a significant impact on the drive mechanism of the die cutting press and its kinematic precision. Moreover, the mechanism causes a decrease in press productivity. Also, when the peak acceleration is reached, a shock load will occur. In view of existing drawbacks, the authors have proposed an optimised mechanism for the pressure plate drive. The main aim of the proposed mechanism is the improvement of pressure plate movement characteristics with maximum simplicity. It was proposed to use a cam mechanism in the drive of the pressure plate. However, such a mechanism design is characterised by the complexity of drive cams manufacturing that have two contacting profiles because of the requirement manufacturing high-accuracy drive cams. Besides, such drive cams occupy a significant part of the die cutting press. Shakhbazov et al. (2020) have proposed a new design of wedging cam mechanisms of the lower pressure plate drive in die cutting press. Authors have conducted theoretical computations of technological loads that arise during cutting and creasing of paperboard blanks and of the size of the driving force which arises in the proposed wedging cam mechanism. Despite some simplification of design, the mechanism remains complicated in set-up and exploitation. Furthermore, the authors have not

conducted experimental research studies of the proposed mechanism. Presses that will be built by such schemes would have complication in set-up and exploitation.

Vlakh and Pasika (2016) have created a methodology for main shaft work optimisation of the die cutting machine in the press. This methodology allows increasing productivity and production quality of die cutting machines with a decrease in its power assumption. The authors have derived analytical dependencies that provide mechanisms of synthesis conduction. To avoid the oscillating movement of the pressure plate of the die cutting press, the authors have proposed the use of a dual-crank four-bar linkage or coulisse mechanism for the drive of a dual-elbow crank instead of a direct electric motor. This helps to avoid quality deterioration of paperboard cutouts and increase production quality. However, the use of additional mechanisms causes complication in the design and set-up process of the die cutting press.

Kuznetsov et al. (2017) have proposed the use of a combined lever mechanism for the drive of the movable pressure plate of the die cutting press. It was made with an aim to minimise the drawbacks of existing equipment. The proposed mechanism consists of two pairs of crank–slider contours: leading and executive. The use of this mechanism decreases the total load and peak of kinetic power consumption. Nonetheless, besides the significant advantages of the proposed mechanism, it has a quite complicated design, and its dimensions are equal to existing mechanisms of the pressure plate drive of die cutting presses.

It was proposed by Happonen et al. (2015) to use laser cutting technology for paper and paperboard cutting. Potential and possible challenges of laser cutting of paper and paperboard-based materials have been discussed. The research aims to study the possibilities of laser cutting of paper material in the application area of complex low-volume geometry cutting. The authors have analysed the expediency of laser cutting according to the technique, quality and its realisation. Pinčjer et al. (2020) have researched the various parameters of laser in the cutting of paper. The results of this research show the perspective of laser use in paper and paperboard cutting. Also, the authors discovered the impact of different parameters of paper and paperboard on cutting power. However, the negative aspects of the use of lasers must also be investigated experimentally, especially the part related to environmental protection and safety at work. Besides that, laser cutting does not provide the necessary productivity of equipment, due to its low speed. The possible increase of laser cutting speed will significantly impact the cost of the process. Such a method of manufacturing paperboard packaging cartons is innovative and progressive.

Behen et al. (2020) have proposed a new design of the pressure plate drive of the die cutting press with an aim to avoid unevenness and provide strictly parallel movement during the pressure plate displacement. It can be achieved by the use of a screw–nut transmission in the drive mechanism of the pressure plate. The authors have researched kinematic parameters of the movable pressure plate of the die cutting press. The results of analytical research studies have shown the possibility and perspectives of the proposed mechanism use and the necessity of further research studies of the mechanism, especially its power parameters.

The screw–nut transmissions in press drive are mostly used in other areas that are not related to the production of paperboard packages. In the paper by Durand et al. (2018), it has been researched that screw presses are used for metal element pro-

cessing (forming presses). The authors have analysed the parameters of a screw press and proposed methods for determining the required rigidity of the press. The results of these research studies do not consider the properties of paperboard and its behaviour during cutting because of the focus on the formation of sheet metal products. However, the results of the research studies are interesting and can be used for calculation of the required rigidity of the die cutting press.

Zou et al. (2017) have investigated the impact of the screw-nut joint stiffness on the vibration characteristics of a vertical ball screw feed system without counterweight in the entire vertical position range through the development of a variable coefficient lumped parameter model. The created model is integrated with the modeling of the screw-nut joint stiffness under the preload and the weight of the spindle system. The preload weight model is compared with the preloaded model and the rigid model in predicting the dynamic characteristics of the system. The paper by Liu et al. (2015) has shown the method for modeling meshing behaviour of the roller screw accurately and has analysed the numerically calculated data which were used to evaluate the meshing characteristics. According to the results, it is possible to reach high loads by changing the parameters of the roller screw.

Rehei et al. (2020) have conducted an evaluation of components of the consumed kinetic power in the pressure plate drive with screw-nut transmission. The authors have created analytical dependencies that provide the evaluation of components of the consumed kinetic power that is spent on overcoming technological resistance during paperboard die cutting. It also considers inertia loads from moving masses of pressure drive elements and rolling friction of screw-nut transmission. The created method of the evaluation of the consumed kinetic power allows designing the pressure plate drive of die cutting presses with an application of the offered mechanism.

Because of the analysis of references, it can be concluded that the use of the drive mechanism of the pressure plate with screw-nut transmission allows avoiding drawbacks of existing die cutting presses in the area of pressure plate movement unevenness during the kinematic cycle. To confirm the reliability of ana-

lytical research studies and efficiency of the proposed mechanism of the pressure plate drive with the use of the screw-nut transmission, experimental research is necessary to be conducted. The aim of this research is the conduction of technological loads in the pressure plate drive and its dependence on several parameters that change during paperboard packaging production. Moreover, the experimental research makes it possible to study rational parameters of paperboard cartons in flatbed presses with the screw-nut transmission in the mechanism of the pressure plate drive during die cutting.

The purpose of the study is to substantiate the practical implementation of the pressure plate drive mechanism with the use of screw-nut transmission for the production of cartons of paperboard packaging.

To achieve the goal of the study, the following tasks during the experimental research need to be solved:

- to design and manufacture the experimental bench with the use of the screw-nut transmission in the combined mechanism of the movable pressure plate drive;
- to study parameters of die cutting that have a significant impact on the process;
- to develop the method of experimental research: the placement of measuring instruments and carrying out measurements of technological loads (torques) in the mechanism;
- to observe the impact of geometrical, kinematical and technological parameters on torques that arise on the input link of the drive mechanism of the pressure plate.

2. MATERIAL AND METHODS

For experimental research, the experimental bench which includes screw-nut transmission in the drive mechanism of the movable pressure plate had been designed and manufactured. This bench, shown in Fig. 1, provides strictly parallel displacement of the pressure plate during the working cycle of the press.

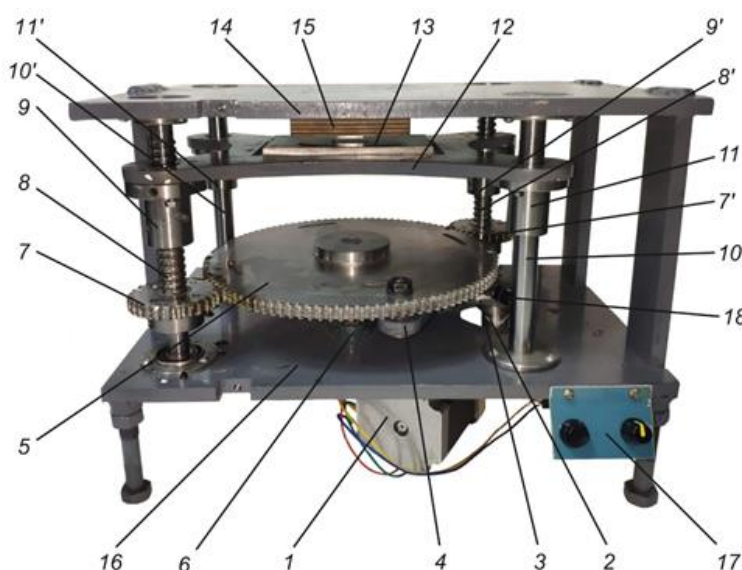


Fig. 1. Photo of the experimental bench for research on die cutting process with use of screw-nut transmission in the drive mechanism of the pressure plate: 1 – stepper motor, 2 – drive shaft, 3 – crank, 4 – connecting rod, 5 – gear wheel, 6 – thrust bearing, 7, 7' – gears, 8, 8' – vertical screws, 9, 9' – nuts, 10, 10' – cylindrical guides, 11, 11' – linear displacement bearings, 12 – movable pressure plate, 13 – adjustment plate, 14 – base plate, 15 – die cutting forme, 16 – mount

The experimental bench consists of a stepper motor 1 (Fig. 1) with a worm gearbox (not shown in figure), the connected drive shaft 2 of the experimental bench. On the drive shaft 2 is placed the crank 3 that is connected by a connecting rod 4 to a gear wheel 5. The gear wheel 5 is placed on a vertical shaft and installed into thrust bearings 6. The movement from the gear wheel 5 transfers to gears 7 and 7', which are fixed on vertical screws 8 and 8', respectively. On screws 8 and 8' are placed nuts 9 and 9' of the ball screw, and the movable pressure plate 12 is fixed to it. In nuts 9 and 9', the motion of screws transforms into the reciprocating motion of the pressure plate 12. To guarantee the strictly parallel movement of the pressure plate 12, cylindrical guides 10 and 10' with linear displacement bearings 11 and 11', respectively, are used. On the movable pressure plate 12 is fixed an adjustment plate 13 on which the paperboard blank (not shown) is placed. The adjustment plate 13 additionally provides high-quality cutting of the blank. A base plate 14 with die cutting forme 15 is fixed to a mount 16 of the experimental bench. The mount 16 of the experimental bench has the necessary rigidity to ensure high-quality cutting of paperboard packaging cartons. The use of a stepper motor for the pressure plate drive allows smooth adjustment of kinematic parameters of the pressure plate movement and setting of a specific law of periodic motion in case of necessity.

For experimental research, the paperboard blank was placed on the adjustment plate 13 that is fixed to the movable pressure plate 12. The paperboard blank has the necessary parameters for experimental research. The hardness of the adjustment plate 13 was optimised for ensuring the cutting of the paperboard blank and minimising the blunt of the cutting knife edges. The die cutting forme 15 with cutting knives and a foam rubber is placed on the immovable base plate 14 that is fixed to bench mount 16, which provides the necessary rigidity of the press. The pressure plate 12 performs reciprocating movement and brings the paperboard blank into the cutting zone. The experimental bench implements a flatbed scheme of a die cutting press design. The movable pressure plate 12 drive mechanism is carried out by the screw–nut transmission where the pressure plate 12 is fixed to nuts 9 and 9'. Screws 8 and 8' are driven from gears 7 and 7' which are fixed onto it, respectively. Gears 7 and 7' are driven by a gear wheel 5 which is placed on a vertical shaft with the use of thrust bearings 6. For the drive of the gear wheel 5, a four-bar linkage is used. The drive shaft 2 is driven from the stepper motor 1 through the worm gearbox. On the drive shaft 2 is placed the crank 3, and by the connecting rod 4, the movement is transferring to the gear wheel 5.

The experimental bench design shows the possible realisation of the pressure plate drive mechanism with the use of a screw–nut transmission with a leadscrew that provides the necessary displacement of the pressure plate. The use of such transmission has significant advantages: the possibility of obtaining a slow reciprocating motion of the pressure plate, providing relatively high power loads, high precision of plate displacement, design simplicity and small dimensions. To eliminate friction losses, a pair of screws and nuts and a ball screw which is characterized by low friction and fairly high efficiency (up to 0.9) are proposed to be used. The ball screw consists of a screw and a nut with helical cut grooves of a curvilinear profile serving as tracks for balls. The modern ball screws can provide the necessary load for the operation of die cutting.

In the experimental bench design, two ball screws with a leadscrew are used. They are placed on the diagonal of the

pressure plate and provide strictly parallel movement. To avoid the mismatch of the pressure plate during its movement, linear displacement bearings, which move along the vertically fixed cylindrical guides, are used. Such bearings make it possible to reduce the impact of friction forces during the pressure plate movement because of the low friction numbers.

The use of the worm gearbox with a gear ratio of 16 provides the desired speed range for the drive shaft of the drive mechanism of the pressure plate.

With the aim to get reliable load values that arise during die cutting of paperboard packaging by using the proposed drive mechanism of the pressure plate, a strain gauge method is used. This measurement method provides the needed precision of measurements. To measure torques in the researched mechanism on the drive shaft of the experimental bench, strain gauges are placed which change their resistance depending on values of loads according to recommendations of Schicher and Wegener (2002). When a conductor of the strain gauge is compressed such that it does not buckle, it will broaden and shorten, which decreases its end-to-end electrical resistance. From the measured electrical resistance of the strain gauge, the number of technological loads may be inferred. For reliable measurements of torques on the drive shaft of the mechanism, foil strain gauges N2A-06-T007R-350 with an electrical resistance of 350 Ohm and a base of 100 mm are used.

As it is recommended by Hilal Muftah M. et al. (2013), strain gauges are glued on the drive shaft 1 (Fig. 2) of the experimental bench (a mechanism) at an angle of 45° to the axis of the shaft and 90° relative to each other.

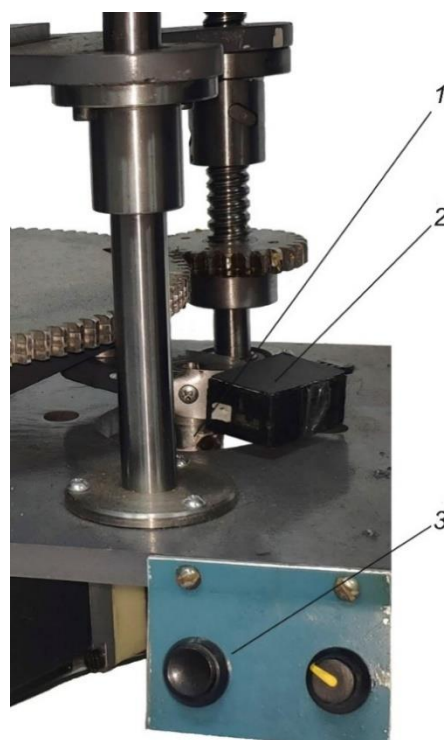


Fig. 2. Photo of strain gauge placement in the experimental bench: 1 – drive shaft, 2 – module of gathering, processing and transmission of the data, 3 – regulator

To prevent the influence of temperature fluctuations and reduce the influence of the bending of the drive shaft, four strain gauges are used for measurements, which are connected

according to the complete bridge circuit. Power was supplied to one of the diagonals of the bridge circuit, and the output signal that shows the value of the load was obtained from strain gauges on the other diagonal of the bridge circuit. The connection of the strain gauge bridge to the measuring equipment was provided by a specially designed module 2 for processing and wireless data transmission. This kind of module, for gathering, processing and wireless data transmission was used to measure the tractive effort of the chain conveyor during spine processing of book blocks by Knysh et al. (2019).

The module for wireless data transmission consists of three elements: a 24-bit analogue-to-digit converter (ADC) Hx711 with an integrated amplifier (gain 128 times), microcontroller ATmega328P and Bluetooth HC05 module. The module provides gathering, processing and transmission of the data from strain gauges to future processing. The microcontroller carries out the data processing from the ADC and its transfer by Universal Asynchronous Receiver-Transmitter (UART) protocol to the Bluetooth HC05 module, which provides wireless data transmission. For the wireless data reception by Bluetooth v2.0 + Enhanced Data Rate (EDR) protocol from the module, software IVT Bluesoleil is used, which receives the data and creates a virtual communication (COM) port, where the data are transferred. To receive and display real-time results in a spreadsheet editor, MS Excel has been developed with macros in Visual Basic for Applications that read the data from the microcontroller through the virtual COM port, which decrypts and writes it to the appropriate cell spreadsheet editor without the use of an additional piece of software. The final processing and visualisation of the data are carried out by built-in functions of MS Excel.

To establish the compliance of ADC data with the real torque values on the drive shaft of the drive mechanism of the pressure plate, the calibration of the measuring equipment has been done. For this purpose, the mechanism was stopped in one of the extreme positions; by measuring equipment with the needed value of load, the display of the ADC was fixed. The real values of torque on the drive shaft of the experimental bench are determined by known load values. However, during the calibration process, different loads have been used to convert the values of the ADC into the value of torque is used the dependence:

$$T = (n - n_0) \cdot K, \quad (1)$$

where n_0 – ADC starting value, n – ADC current value, K – coefficient for ADC values conversion into the torque values that has been determined by dependence:

$$K = \frac{T_1}{n_t}, \quad (2)$$

where n_t – the quantity of ADC values, that corresponds to the change of the applied load.

The experimental bench makes it possible to get torque values from cutting forces of paperboard blank. The design of the experimental bench provides displacement of the movable pressure plate for a distance of 80 mm by using geometric parameters of the gear and four-bar linkage mechanism. It used a ball screw and a lead screw of 5 mm. Therefore, to ensure the movement of the pressure plate on the 80-mm screws, it needs to make 1.6 turns, which is provided by the gear ratio between the gear wheel and gears. The gear wheel rotates by 100 deg. The use of a step motor for the experimental bench drive enables the smooth adjustment of the movement speed of the pressure plate

by controlling the stepper motor with the designed regulator 3 (Fig. 2). This gives an opportunity to measure the torque value on the drive shaft of the bench with crank speed control depending on operation time. The beginning of the die cutting process starts with a sharp increase of the torque value.

For experimental research, the die cutting process with use of the proposed experimental bench was performed for the most common material – paperboard. According to Emblem A. and Emblem H. (2012) and Kirwan (2013), the most common paperboard for packaging is the folding boxboard (FBB), which has inner plies of a mechanical pulp and outer plies of a chemical pulp. This provides a board with maximum stiffness at minimum grammage. Such a type of paperboard provides the needed protective properties of packaging along with the possibility of obtaining high-quality printed packaging. For experimental research, paperboard blanks of a local manufacturer with a thickness of 0.3 mm (250 gsm), 0.45 mm (350 gsm), 0.5 mm (370 gsm), 0.6 mm (440 gsm) and 0.7 mm (500 gsm) were chosen. The thickness of paperboard blanks was measured and controlled during the experiments according to the recommendations of ISO 3034:2011. For experimental research, paperboard blanks have been conditioned at a temperature of 23°C and relative humidity of 50% for 4 h.

The experimental research of torque on the drive shaft of the bench was conducted with the use of new cutting knives, made by Bohler, with the curvature radius with a cutting edge of 9 µm and a thickness of 2 pt (0.71 mm).. According to the classification, the line-type Universal 40 with a length of 25 mm was used. Cutting knives have been selected according to existing recommendations.

3. RESULTS OF EXPERIMENTAL RESEARCH

The record of torque values on the drive shaft of the drive mechanism of the pressure plate that arises during paperboard cutting is shown in Fig. 3 and 4. The abscissa shows the time equal to the division of the number of experimentally obtained values by the sampling frequency of the ADC. These diagrams have shown the results of torque value measurements during die cutting of the paperboard blanks with a width of 20 mm made of FBB and a thickness of 0.7 mm (500 gsm) in machine direction (MD) and cross direction (CD) at a rotation speed of 30 rpm.

Figs. 3 and 4 show two kinematic cycles of operation of the combined pressure plate drive mechanism of the die cutting press. The graphical dependencies can be conditionally divided into several segments. On segment A–G, the change of torque on the drive shaft of the mechanism is shown, which occurs during its operation without a paperboard blank and the cutting process. Segment G–N characterises the period of operation of the mechanism during the technological operation of paperboard blank cutting.

Comparing two kinematic cycles of the mechanism operation, it is seen that the operation of the mechanism is accompanied by the arise of significant inertial loads. Moreover, the gaps in the gearing, friction in the components of the combined mechanism, gaps in the kinematic pairs, the characteristics of the drive and the noise of electronic devices make a perceptible influence on torque value changes.

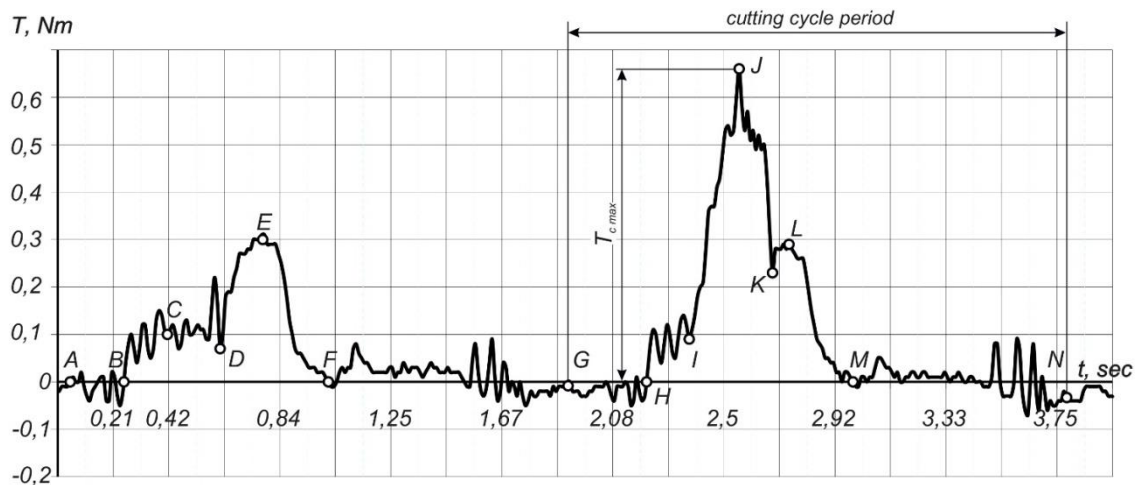


Fig. 3. Diagram of torque on the drive shaft of the drive mechanism of the pressure plate during die cutting of paperboard blank in MD and for paperboard FBB with a thickness of 0.7 mm. FBB, folding boxboard; MD, machine direction

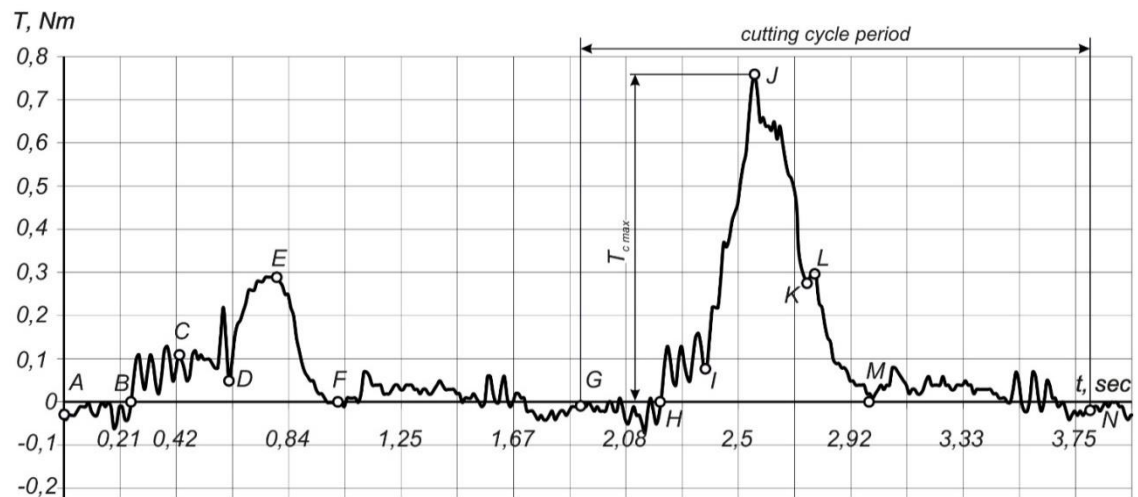


Fig. 4. Diagram of torque on the drive shaft of the drive mechanism of the pressure plate during die cutting of paperboard blank in CD and for paperboard FBB with a thickness of 0.7 mm. CD, cross direction; FBB, folding boxboard

At point A begins a kinematical cycle of the drive mechanism of the pressure plate operation, and the torque value on the drive shaft starts to increase. At point B, the rubber foam of die cutting forme starts to contact the surface of the base plate, and the pressure plate continues to move. On segment B–C, the impact of gaps on the gear wheel and gears and the further increase of torque from inertia forces can be seen. At point C, the maximum value of torque from inertia forces reached maximum and begins to gradually decrease, which is caused by the feature of the four-bar linkage mechanism. Segment C–D shows the continuing increase of the torques from rubber foam deformation with a simultaneous reduction of the torque values from the inertia forces. At point D, the cutting knife touches the surface of the adjustment plate and can be seen as the rapid increase of the torque value till reaching the maximum value at point E. This torque increase characterises the load from the incision of the cutting knife into the surface of the adjustment plate placed on the immovable base plate. The incision of the cutting knife into the surface of the adjustment plate is a necessary condition for ensuring the reliable cutting of paperboard blanks. Then, the

pressure plate changes the movement direction and begins to move away from the base plate that can be proof for the decrease in the level of torque on the segment E–F, reaching the minimum value at point F. On segment F–G, the drive mechanism of the pressure plate continues to return to the starting position. However, at this stage of the operation, the pressure plate moves downwards, and there is no significant load from the forces of inertia from components of the mechanism.

Then, the mechanism operation takes place in a logical sequence, but with the available paperboard blank, ie, the technological operation of cutting is carried out. The operation cycle of the drive mechanism of the pressure plate starts at point G where the increase of torque values can be seen. Segment G–H was characterised by slight changes in the torque value. At point H, the rubber foam of die cutting forme begins to contact the paperboard blank, and on segment H–I, the increase of the torque value from the deformation forces of the rubber foam is observed. This segment, as in the previous case, shows the impact of gear gaps. At the point I, the cutting knife touches the paperboard blank and begins the incision of the cutting knife into the

paperboard that is accompanied by the growth of the torque. The torque value increases to reach the maximum value which corresponds to point J. This will be the torque value ($T_c \max$) from the cutting of the paperboard blank. Next, there can be seen a sharp decrease of the torque value to reach some value at point K. This sharp decrease of the torque value is since the particles of the paperboard blank are separated before the contact of the cutting line with the surface of the adjustment plate. At point K, the cutting knife edge begins to contact with the surface of the adjustment plate that was accompanied by an increase in the torque value to reach the maximum at point L.

Then, the pressure plate of the experimental bench begins to move in the opposite direction, moving away from the base plate. The gradual decrease of the torque value from the deformation of the rubber foam is clearly visible in the area L–M. At point M, the contact of the rubber foam with the paperboard blank is completed. The further lowering of the pressure plate is accompanied by insignificant changes in the inertial loads (segment M–N).

During experimental research, it was found that the thickness of the cardboard blank does not impact the change character of the torque values, and for each paperboard thickness, there exists a certain torque value that arises during die cutting the blank. The significant impact on the torque amount has the placement of the cutting knife relatively to the directions of fibres in the paperboard blank.

During the experimental research, a certain data amount of torque values was obtained. Torque values are processed based on calibration dependencies in accordance with the experimental research program. With the aim to obtain valid results, the method of point estimation that consists of acceptance as the unknown true value of the distribution parameter has been used. Selective arithmetic mean (average) \bar{x} – the sum of random variable values that are got as a result of experimental sampling test divided by its volume:

$$\bar{x} = \frac{1}{n}(x_1 + x_2 + \dots + x_n) = \frac{1}{n} \sum_{i=1}^n x_i, \quad (3)$$

Gorvat et al. (2019), have considered methods of processing the experimental data according to mathematical statistics methods. In mathematical statistics, it has been proved that the selective arithmetic mean is the best (capable, irremovable and effective) estimate of the mathematical expectation of a random

value. The selective arithmetic mean method obeys the normal law of distribution.

The processed experimentally obtained data of the average value of seven measurements (minimal and maximum values have been neglected) that eventually give the value of the torque values that arise during paperboard blank die cutting for selected paperboard examples, as shown in Tab. 1.

Tab. 1. Results of experimental research of torque on the drive shaft of the mechanism that arise during die cutting of paperboard blanks

Crank speed, rpm		10		20		30	
Fibres direction		MD	CD	MD	CD	MD	CD
Torque values, Nm	0.3 mm, 230 gsm	0.52	0.58	0.48	0.56	0.44	0.52
	0.45 mm, 350 gsm	0.67	0.73	0.61	0.7	0.6	0.54
	0.5 mm, 370 gsm	0.72	0.79	0.62	0.66	0.59	0.6
	0.6 mm, 440 gsm	0.81	0.85	0.77	0.79	0.68	0.72
	0.7 mm, 500 gsm	0.79	0.96	0.76	0.82	0.67	0.71

According to the values that are shown in Tab. 1, graphical dependencies of torque values that arise during die cutting of paperboard blanks in the experimental bench have been built. These dependencies are shown in Fig. 5. The analysis of diagrams allows revealing the dependence of torque size on the thickness of a paperboard blank and epy direction of a cutting knife placement relative to the direction of the paperboard fibres.

Analysing the graphical dependencies of the torque values on the drive shaft that arise during die cutting of paperboard blanks has been established that the thickness of the paperboard blank causes an increase in the value of torque. However, it should be noted that there is no direct proportional dependence of the torque value on the thickness of the paperboard blank. The increase of the paperboard blank thickness, from 0.3 mm to 0.7 mm, causes the increase of the torque on the drive shaft of the experimental bench just in 1.52 time during paperboard cutting in MD (from 0.44 Nm to 0.67 Nm) and 1.36 time during paperboard cutting in CD (from 0.52 Nm to 0.71 Nm).

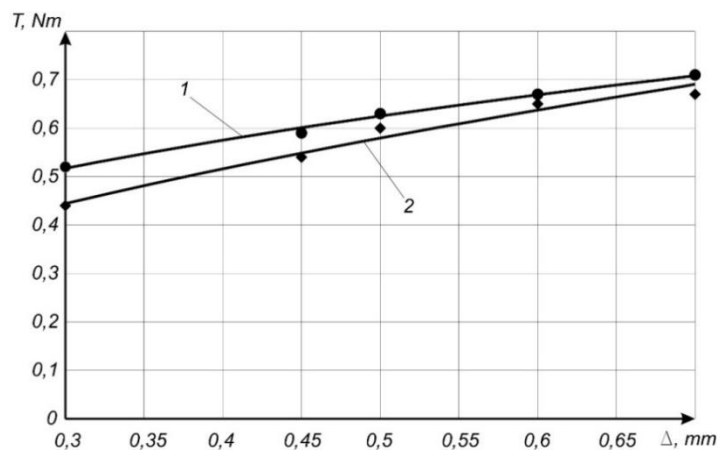


Fig. 5. Dependence of torque during die cutting on paperboard blank thickness measured on the drive shaft of the experimental bench: 1 – CD, 2 – MD. CD, cross direction; MD, machine direction

As it is known, the direction of paperboard fibres relatively to cutting knife placement has an impact on the torque value. Experimental research has allowed us obtain paperboard cutting in CD; the value of torque on the drive shaft on the average is 7.5% higher than the cutting in MD (for paperboard, with a thickness of 0.3 mm and 0.7 mm, 15% and 5% is obtained, respectively).

The change of the torque on the drive shaft of the drive mechanism of the pressure plate depends on the paperboard thickness can be described by empirical dependencies of the type:

$$T_c = A \cdot \Delta^n, \quad (4)$$

where A (N/mm^{n+1}) and n are characteristics of a certain type of paperboard, which are obtained using the software as a mathematical description of the average line.

For the researched paperboard blanks made of folding boxboard with rotation speed of drive shaft of 30 rpm:

– during paperboard cutting CD:

$$T_c = 0.83 \cdot \Delta^{0.52}, \quad (5)$$

– during paperboard cutting MD:

$$T_c = 0.8 \cdot \Delta^{0.37}. \quad (6)$$

The total dispersion S^2 (dispersion of the output parameter) characterises the scatter of the experimentally observed points relative to the average value. The closer the experimental data are to the diagram of empirical dependence, the closer the connection, the smaller the residual dispersion and the greater the correlation coefficient are. According to the results of experimental

research studies, its processing and the development of the empiric dependence of the torque on the thickness of the paperboard with the dispersion value of 0.97 is due to paperboard cutting in MD and 0.99 during cutting in CD. Thus, a functional dependence was developed that describes the experimental values of the variables and accurately reflects the general trend of change of this dependence with the exception of measurement faults and random deviations.

The program of experimental research has provided the dependence of the torque value on the drive shaft of the experimental bench on its speed parameters. As previous, for experimental research, the same examples of the paperboard (FBB) blanks have been chosen. The conditions of the research remained unchanged except for the change in the speed of the drive shaft of the experimental bench ($n_1 = 10$ rpm; $n_2 = 20$ rpm; $n_3 = 30$ rpm).

As it can be seen from the diagrams, the speed change of the experimental bench and therefore the cutting speed has little impact on the torque value. In the range of speeds that were studied (10–30 rpm), a decrease of the torque value on the drive shaft of the experimental bench while increasing its speed is observed. The triple increase of a rotation speed of the drive shaft and the crank of the bench cause the decrease of the torque value on the drive shaft on average by 15% during paperboard cutting in MD and by 20% during paperboard cutting in CD. For paperboard blanks with a thickness of 0.3 mm, there is a decrease by 10% and for 0.45 mm, 0.5 mm and 0.7 mm there is a decrease by 25%, and for blanks with a thickness of 0.6 mm, there is a decrease by 15%.

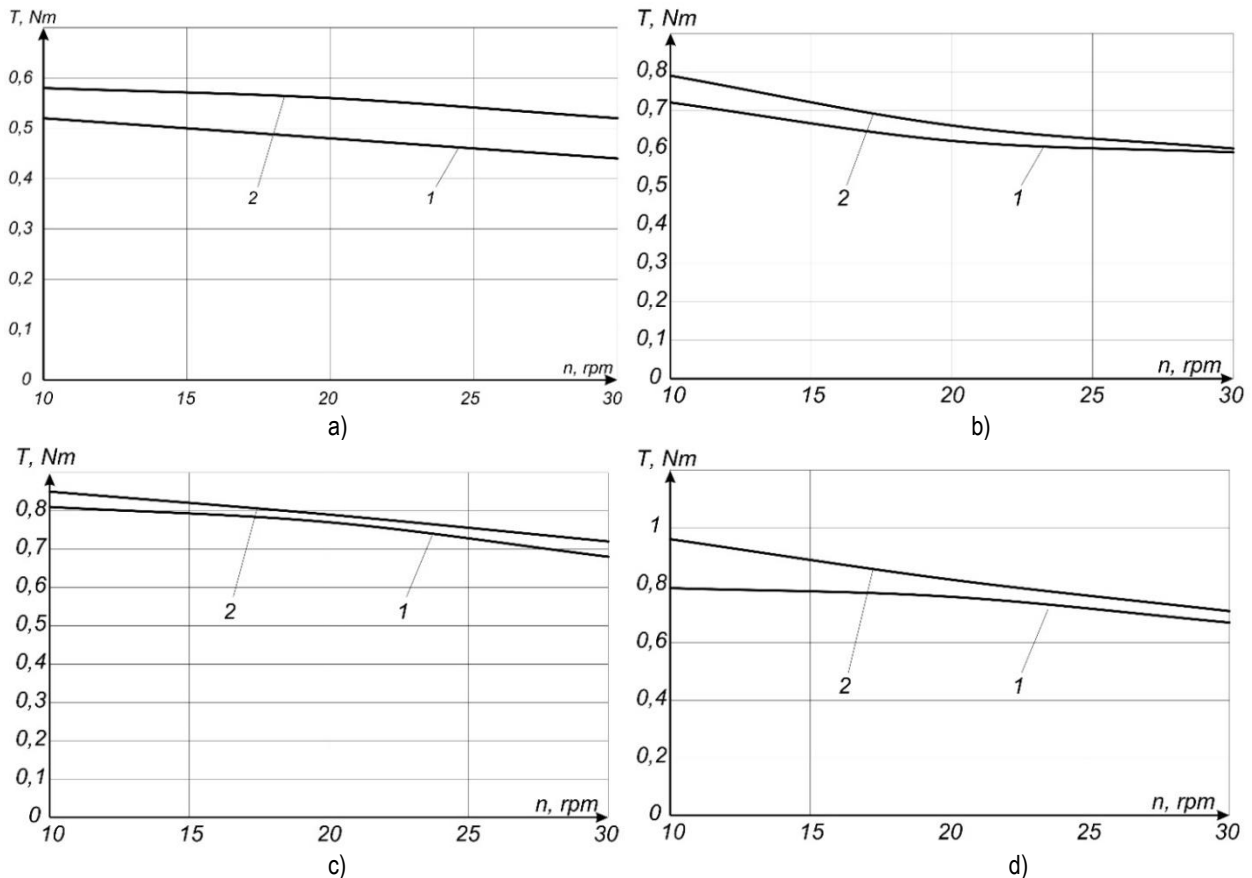


Fig. 6. Dependence of die cutting torque on drive shaft of experimental bench on crank speed during paperboard cutting MD (1) and CD (2) for paperboard blanks made of FBB with thickness: a – 0.3 mm, b – 0.5 mm, c – 0.6 mm, d – 0.7 mm

4. DISCUSSION

From the obtained results when determining the influence of the thickness of the paperboard blanks on the torque values, the drive shaft of the experimental bench is logical and can be explained by an increase of the contact area of the cutting knife with the paperboard. Also, fibres and their chemical connections influence torque. Increasing the paperboard thickness in diapason 0.3–0.7 mm causes the increase of the torque value, on average, 1.4 times. As for the force of paperboard cutting, it will vary in proportion to the embossing area, which will depend on the radius of curvature of the cutting edge of the cutting knife. The radius of curvature of the knife in the process of die cutting increases, which leads to a significant increase in force, which limits its suitability for further operation.

As it can be seen from Fig. 4, there is some difference between cutting in MD and CD of the paperboard blank. This pattern is due to the greater density in the CD of paperboard. Paperboard is a material that consists mainly of intertwined and interconnected plant fibres containing cellulose. The thickness of plant fibres is 100–1,000 times less than its length. Cellulose macromolecules in plant cells are placed parallel to each other forming fibrils, which are structural elements of cellulose fibre. Cutting a piece of paperboard in MD breaks the intermolecular bonds, which are much weaker than the bonds inside the cellulose fibre, and cutting in CD requires additional effort to break the fibre. This increase varies within 15–20%.

Mathematical models of torque value dependence on paperboard thickness provides the possibility to get physical characteristics that correlate the stress and strain of paperboard. This can be made based on experimental diagrams of the processed functional dependence of torque value on the thickness of the paperboard blank. These dependencies are useful for determining the cutting force from the degree of blunting of the cutting knife using certain characteristics of the paperboard.

During experimental research studies, the impact of the speed on the crank of the experimental bench on torque value has been evaluated. The increase of rotation speed of drive shaft of the experimental bench causes the decrease of torque. The tripple increase of rotation speed of drive shaft causes the decrease of torque on drive shaft in average by 15%. It can be explained by the plastic deformation during paperboard cutting that depends on time of the operation.

It is important to note that the obtained results of the experimental research studies of the torques during die cutting of the paperboard blanks and the proposed method confirm the theoretical assumptions. It also should be noted that the research shows the workability of the proposed device. The use of screw–nut transmission in the drive mechanism of the movable pressure plate of technological equipment for die cutting creates preconditions for high-quality manufacturing of paperboard packaging, simplifies equipment design and minimises power discharge.

5. SUMMARY AND CONCLUSIONS

The experimental bench with the screw–nut transmission in a combined drive mechanism of the pressure plate and a program of experimental research have been developed. The experimental bench allows a smooth change of the rotation speed of the drive

shaft. The developed program of experimental research of torque values on the drive shaft provides detection of the impact of different die cutting processes and equipment parameters on the loads that arise during its operation. Proposed methods of measurements and obtained data processing with the use of modern hardware and software provide the processing simplification of the measurement results and make it possible to obtain reliable values with minimal faults.

Values of torque on the drive shaft of the drive mechanism of the pressure plate that arise during paperboard blanks of die cutting are established. Moreover, the impact of paperboard blank thickness on torque values is revealed.

It is established that the torque values on the drive shaft that arise during die cutting for thick paperboard blanks made of FBB lay in range of 0.3–0.7 mm. It is found that the increase of the paperboard blank thickness from 0.3 mm to 0.7 mm causes the increase of torque on the drive shaft of drive mechanism of the pressure plate by 1.52 times during paperboard cutting in MD (from 0.44 Nm to 0.67 Nm) and by 1.36 times during cutting paperboard in CD (from 0.52 Nm to 0.71 Nm).

Mathematical models of torque value dependence on paperboard thickness are established. The total dispersion S_2 is 0.97 during cutting in MD and 0.99 during cutting in CD; the paperboard shows the exception of measurement faults and random deviations.


The increase of rotation speed of the drive shaft of the drive mechanism of the pressure plate causes the decrease of torque. The tripple increase of rotation speed of the drive shaft causes the decrease of torque on drive shaft in average by 15% during cutting in MD and by 20% during cutting in CD of the paperboard.

REFERENCES

1. Behen P. I., Radikhovskiy I. A., Mlynko O. I. (2020), Die-cutting Press wit Using a Lead Screw Transmission (Investigation of Pressure Plate Kinematic Parameters), *Upakovka*, 2020. № 1, 44–45 (in Ukrainian).
2. Durand C., Bigot R., Baudouin C. (2018), Contribution to characterization of metal forming machines: application to screw presses, *Procedia Manufacturing*, Volume 15, 1024–1032.
3. Emblem A., Emblem H. (2012), *Packaging technology Fundamentals, Materials and Processes*, Oxford: Woodhead Publishing.
4. Gorvat A. A., Molnar O. O., Minkovich V.V. (2019), *Metodiobrobkiesperimentalnihkdanikh z vikoristannyam MS Excel. VidavnictvoUzhNU «Goverla»* (in Ukrainian).
5. Happonen, A., Stepanov A., Piili H., Salminen A. (2015), Innovation Study for Laser Cutting of Complex Geometries with Paper Materials, *Physics Procedia*, № 78, 128–137.
6. Hilal Muftah M., Mohamed Haris S., Petroczki K., AwadKhidir E. (2013) An Improved Strain Gauge-Based Dynamic Torque Measurement Method. *International Journal of Circuits, Systems and Signal Processing*, Issue 1, Volume 7, 66–73.
7. Khvedchyn YU. Y., Zelenyi V. V. (2014) Analysis of The Mechanisms of Press in Die-cutting Automat, *Scientific Papers*, № 4 (49), 21–30 (in Ukrainian).
8. Kirwan, M. J. (2013), *Handbook of Paper and Paperboard Packaging Technology*, Oxford: John Wiley & Sons.
9. Knysh, O., Rehei, I., Kandiak, N., Ternytskiy, S. (2019), Experimental Evaluation of the Tractive Effort of the Chain Conveyor during Book Block Spine Processing by Cylindrical Milling Cutter at Perfect Binding, *Acta Mechanica et Automatica*, vol. 13 no. 2, 101–106.
10. Kuznetsov V. O., Kolomiets A. B., Dmitraschuk V. S. (2012), Parametric Researches of the Press Plate Drive in Die-cutting Automat, *Upakovka*, №6, 31–34 (in Ukrainian).

11. **Kuznetsov V. O., Rehei I. I., Vlach V. V.** (2017), Modification of a Drive Mechanism of a Press Plate in a Die-cutting, Press, *Printing and Publishing*, №1, 56–62 (in Ukrainian).
12. **Lin W., Zhou C., Huang W.** (2015), Optimum design for mechanical Structures and material Properties of the dual-elbow-bar mechanism, *Hindawi Advances in Materials Science and Engineering*.
13. **Liu Y., Wang J., Cheng H., Sun Y.** (2015), Kinematics Analysis of the Roller Screw Based on the Accuracy of Meshing Point Calculation, *Mathematical Problems in Engineering*, vol. 2015.
14. **Pinčjer I., Miketić N., Tomić I., Adamović S.** (2020). Exploring the Various Parameters of CO2 Laser in the Cutting of Paper. *Paper presented at the 10th International Symposium on Graphic Engineering and Design GRID 2020, Novi Sad, Serbia, November 12–14*.
15. **Rehei I.I., Knysch O. B., Behen P. I., Radikhovsky I. A., Mlynko O. I.** (2020). Drive of The Pressure Plate of the Die-cutting Press on The Basis of Using the Screw Nut Transmission (Method of Evaluation of Consumption Power Components), *Scientific Papers 1* (60), 98–107 (in Ukrainian).
16. **Rehei, I.** (2011), *Consumer Cardboard Packaging: Materials, Materials, Design, Manufacturing Equipment*, Lviv: Ukrainian Academy of Printing (in Ukrainian).
17. **Schicher R., Wegener G.** (2002). *Measuring Torque Correctly*, Hottinger Baldwin MesstechnikGmbH, Germany.
18. **Shakhbazov J., Cheterbukh O., Shyrovkov V., Palamar O.** (2020). The Drive Mechanism of a Pressure Plate of a Flat Die-cutting Press, *Printing and Publishing*, 1 (79), 112–120 (in Ukrainian).
19. **Vlach V., Pasika V.** (2016), Automated Synthesis of Mechanism of Press of Diecutting Machine, *Technological Complexes*, №1 (13), 57–63 (in Ukrainian).
20. **Zou C., Zhang H., Lu D., Zhang J., Zhao W.** (2017), Effect of the screw–nut joint stiffness on the position-dependent dynamics of a vertical ball screw feed system without counterweight, *Proceedings of the Institution of Mechanical Engineers, Part C: Journal of Mechanical Engineering Science*. 232.

Serhii Ternytskyi:  <https://orcid.org/0000-0002-3814-9762>

Ivan Rehei:  <https://orcid.org/0000-0002-3395-2994>

Nazar Kandiak:  <https://orcid.org/0000-0002-4720-3935>

Ihor Radikhovskyi:  <https://orcid.org/0000-0002-5036-3569>

Oksana Mlynko:  <https://orcid.org/0000-0001-9878-6846>

APPLICATION OF STATISTICAL ANALYSIS AND FUNCTIONAL ASSESSMENT TESTS IN PATIENTS AFTER TROCHANTERIC FRACTURES TREATED SURGICALLY IN AN INDIVIDUAL REHABILITATION PROGRAMME

Robert SKOWRONEK^{*}, Józef ZAWORA^{**}, Krzysztof KWIATKOWSKI^{*}, Konstanty SKALSKI^{***}

^{*}Department of Traumatology and Orthopaedics, Military Medical Institute, ul. Szaserów 128, 04-141 Warszawa, Poland

^{**}Warsaw University of Technology, Plac Politechniki 1, 00-661 Warszawa, Poland

^{***}The Institute of Precision Mechanics, ul. Duchnicka 3, 01-796 Warszawa, Poland

skowiuczelnia@wp.pl, jzawora@meil.pw.edu.pl, kwiatkowski@wim.mil.pl, konstanty.skalski@gmail.com

received 29 December 2019, revised 26 June 2021, accepted 1 July 2021

Abstract: Physiotherapeutic procedures after surgical treatment of trochanteric fractures of femurs are a very important element of a post-operative management because they have a significant influence on the final result of physiotherapy. This is due to the nature of the fracture and the frequency of its occurrence. The aim of the work is, in particular, to determine the relationship between functional assessment scales in patients after trochanteric fractures treated surgically using extended statistical analysis including regression equations. Statistical analysis included a group of patients, which participated in a specialized programme of a post-operative procedure, called the 'Individual' Group. The matrix of research results, calculations of basic statistical measures, such as position, variability, interdependence, asymmetry and concentration were presented for this group. Regression equations representing the relationships between the considered variables, in particular concerning the applied scales and post-operative tests, were presented. Their purpose, mathematical interpretation, results of calculations and statistical tests were discussed. Attention was paid to the high correlation between the Parker and Mobility tests. The extended statistical analysis makes it possible to create an own system for assessing the treatment results of patients after trochanteric fractures are treated surgically.

Key words: hip joint, rehabilitation, variance analysis, correlation of variables, variation measures

1. INTRODUCTION

The incidence of fractures of the proximal femur is increasing year by year. They account for 7% of all fractures in adults and 24% of fractures in the elderly (Zu-Sheng et al., 2018; Carulli et al., 2017). They mainly concern women over 60 years of age. After surgical treatment, mortality rates are 7–10% after 30 days, 10–20% after 90 days and 20–50% after 1 year (Borges et al., 2019; Lee et al., 2014; Rizk et al., 2016). The progressive age of patients is an independent mortality factor (Pincus et al., 2017).

Clinical analyses indicate that surgical treatment up to 48 h after an injury improves this index (Borges et al., 2019; Moja et al., 2012; Carulli et al., 2017; Forni et al., 2019). On this basis, guidelines were introduced in the USA and Canada to operate up to 48 h after an injury, and some authors even specify a threshold of 24 h as necessary for the procedure (Pincus et al., 2017). It is also indicated to quickly mobilise patients and then to verticalize them as early as possible to minimize the risk of complications associated with staying in a supine position, such as pneumonia, deep vein thrombosis, bleeding, pulmonary embolism, urinary tract infection and decubitus ulcers (Auron-Gomez and Michota, 2008; Bellebarba et al., 2000; Saarenpää et al., 2009; Huddleston and Whitford, 2001; Klestil et al., 2018).

A special group of fractures of the proximal femur are patients with trochanteric fractures. They constitute 31–51% fractures of the proximal femur. It is worth noting that patients with reduced

bone mineral density (BMD) are more susceptible to this type of fracture than to the fracture of the femoral neck (Bernstein et al., 2018). In patients with trochanteric fractures, the percentage of patients with concomitant age-related diseases increases, which can significantly worsen the state of health at the time of the injury. Comorbidities cause difficulties in treatment and influence post-operative prognosis (Zu-Shenk et al., 2018; Grau et al., 2018).

Patients with cognitive impairment (dementia) are a significant problem. 0.5% of the world's population suffers from dementia, and it is estimated that in 20 years this value will double. In this group, in addition to the typical factors that increase the risk of fracture (age, sex, comorbidities), we also observe limited physical fitness and a decrease in BMD in comparison to patients without cognitive impairment. This significantly limits the chances of returning to the fitness the patient had before the fracture and increases the risk of subsequent hospitalisations (Yli-Kyyny et al., 2019). Fig. 1 presents the risk factors for the fracture of the hip area (Friedman et al., 2010). It is emphasized that the early diagnosis of cognitive impairment and the treatment of osteoporosis in patients with dementia may reduce the incidence of hip fractures (Friedman et al., 2010; Hao-Kuang et al., 2014; Huang et al., 2015).

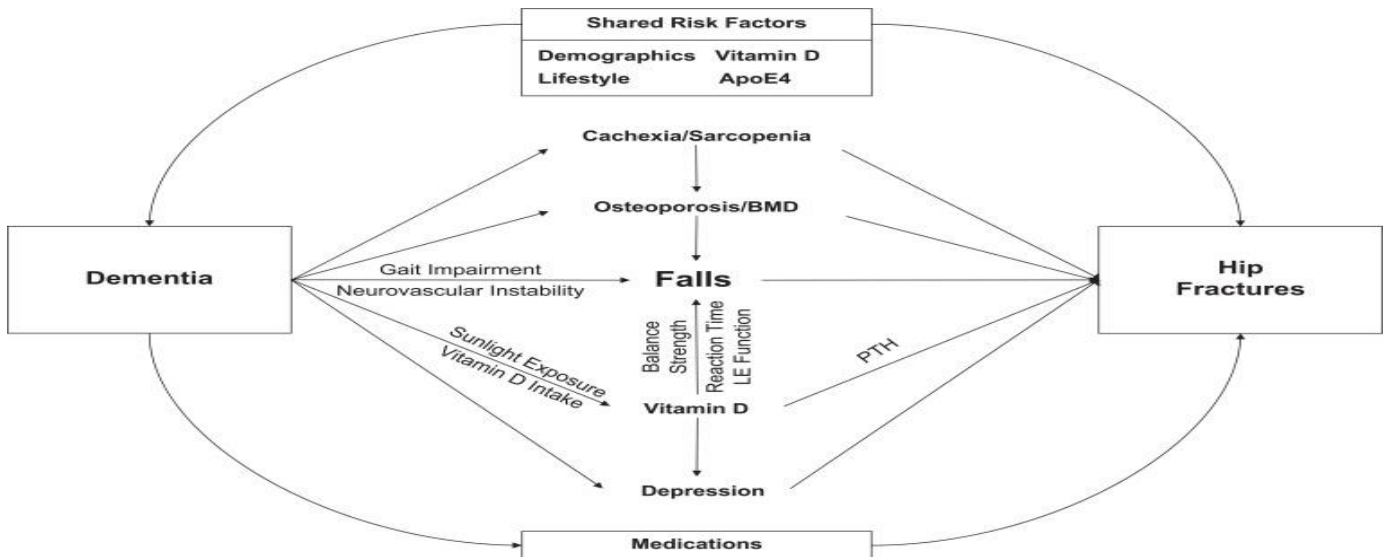


Fig. 1. Risk factors for dementia and hip fractures (Friedman et al., 2010)

Non-surgical treatment of this type of fracture is associated with mortality up to 60% during the year, therefore the surgical stabilisation of the fracture is an indication for life, except for terminally ill or incurable patients (Zhengan et al., 2018).

Operational goals include the anatomical reduction of fragments, sTab. anastomosis with minimal blood loss, and shortening the time of surgery (Yousry et al., 2015). Treatment is illustrated in Figs. 2a and 2b.

The most commonly used anastomoses are as follows: Gamma type intramedullary nails and DHS, DCS systems (Fig. 3, Zhengan et al., 2018; Ibrahim and Meleppuram, 2017; Carulli et al., 2017). The highest stability of the anastomosis can be obtained after the anastomosis with the Gamma type intramedullary nail.



Fig. 2. (a) Radiogram before the surgery, (b) Radiogram after the surgery

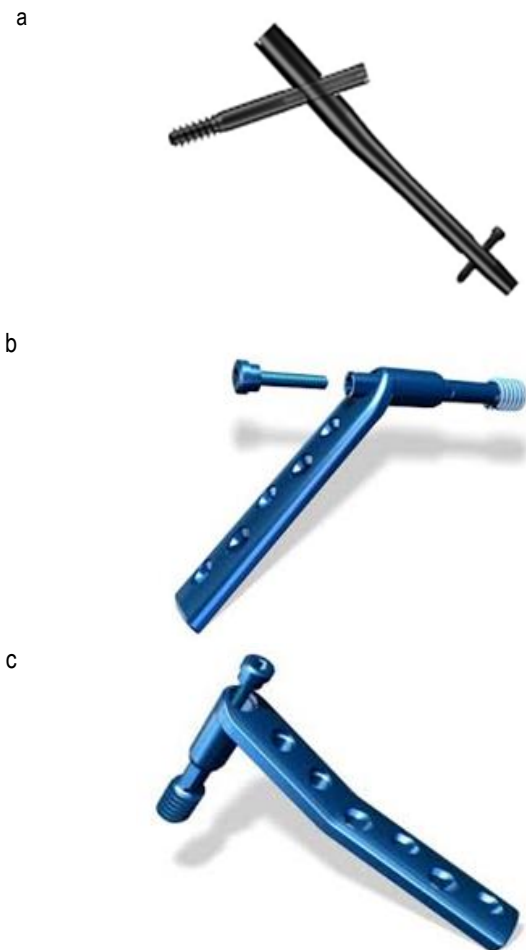


Fig. 3. Types of bone anastomoses in trochanteric fractures: a) Gamma type intramedullary nail, b) DHS System, c) DCS System [Stryker, Medgal]

Rehabilitation programmes in patients after surgical treatment of trochanteric fractures of the femurs are usually not described in detail. Most often the method and the programme of improvement depends on the skills and equipment of the centre. In addition to general improvement programmes, the element that the authors pay attention to is the quickest verticalisation of the patient with a partial limb loading, because only such a procedure limits the high mortality rate and minimizes disability (Baum Gaertner and Oetegen, 2009; Klestil et al., 2018; Nurul et al., 2019; Seitz et al., 2016; Shibasaki et al., 2018). The difficulty of the problem can be proved by the fact that only about 50% of patients with trochanteric fractures return to their pre-injury performance. In addition, the researchers jointly emphasize that in recent years, the stay of patients in hospitals has been shortened, while the role of long-term rehabilitation/care centres is growing (Tan et al., 2017).

Trying to find a compromise in the methodology of rehabilitation treatment, a research project entitled 'Comparative assessment of the effectiveness of physiotherapy in patients after surgical treatment of trochanteric fractures depending on the psychomotor state' was implemented at the Department of Traumatology and Orthopaedics at the Military Medical Institute in Warsaw in 2015. Many statistical variables resulting from the obtained information were subjected effectiveness assessment (demographic data and assessment of intellectual performance according to the modified Mini-Mental State Examination (MMSE.)) Analyzed variables are scales (tests) of the assessment of physical activity and clinical examination. It is worth noting that the authors interchangeably used the concept of tests or scales assuming that both of these properly reflect the meaning of the study (Friedman et al., 2010; Shibasaki et al., 2018; Skowronek et al., 2017). An important problem that was encountered was the statistical evaluation of the obtained results. The authors were aware that without the proper approach and analysis, the results may turn out to be incorrect and the conclusions unsuccessful. The problem of statistical analysis of research results was undertaken for the first time in the authors' work (Skowronek et al., 2017). The variance analysis used with constraints was a preliminary activity in the statistical evaluation of the presented research. At the current stage, an introduction of the regression analysis is planned, the equations of which will allow a quantitative assessment between variables. The presented calculations concern the patients from Group I, called the Individual Group. Statistical methods of describing the structure of the population were used for calculations. These results will allow characterisation of the examined group in terms of the influence of the examined variables on the results of the applied physiotherapy procedures in the examined group, and after the analysis on the comparison of the other groups involved in the mentioned research project, i.e. Norm (Group II) and Dementia (Group III) (Research project Military Medical Institute, 2015). Conducting the proposed research will allow to determine and select the best set of statistical variables in terms of tests and scales having the most important meanings to determine the relationship between the variables that determine the progress of physiotherapy. This analysis may also help find relationships representing a statistical mathematical model describing the output variables (e.g. time of survival) as a function of the input variables (e.g. functional tests) representing the results of physiotherapy, which will allow it to be improved and will help to indicate further directions of research.

Getting ready for the publication, very interesting statistical models regarding mechanical strength of the femur or prognosis

of fractures in the hip joint were found in the literature (Pottecher et al., 2016; Bredbenner et al., 2015; Bryan et al., 2010). Statistical models for the variables we discuss have been found in the literature only partially (Anunskys et al., 2008; Mizrahi et al., 2008).

The aim of the work is, in particular, to determine the relationship between functional assessment scales in patients after trochanteric fractures treated surgically using statistical analysis including regression equations. A mathematical model, that will allow to select the most crucial elements from the used functional assessment tests of patients, will be proposed, which may result in the creation in the future of the own system for the evaluation of treatment results of patients with trochanteric fractures.

2. MATERIAL AND METHOD

2.1. Material

A group consisting of patients operated on in the Traumatology and Orthopaedic Department of Military Medical Institute performing an individual rehabilitation programme without the control of the physiotherapist team according to the instructions received after the operative treatment. There was no division in this group due to the degree of mental state. The group is conventionally called 'Individual'. From the group originally consisting of 88 people, 26 people were analysed in full. The Individual Group was created as a test group being a reference for the Norm (II) and Dementia (III) Groups, for which the patients were qualified based on the intellectual efficiency assessment using the modified MMSE test.

The method of postoperative rehabilitation in the Individual Group is a typical model of physiotherapy currently functioning in the above-mentioned Department. In the Norm and Dementia Groups, apart from the assessment of the mental state, a rehabilitation consultation was introduced during the control visits at the Traumatology Department as a new element. Physiotherapy was additionally made dependent on the degree of mental state.

2.2. Method

To determine the descriptive characteristics in the form of the statistical measures of position, the calculations of average, mean and classical measures were used Zeliaś (2000), Aczel (2008); Korzyński (2006); Stwora (2019) and Stanisławek (2010). Classical average measures are calculated based on all values of the variable under examination. Average, positional measures are the most recurrent variables. Originally, we chose 13 statistical measures for the calculations (arithmetic mean, standard deviation (STD/ σ), coefficient of variation V , linear correlation coefficient $r(Y,X)$, coefficient of determination $r^2(Y,X)$, minimum value, maximum value, gap, average deviation V_{op} , coefficient of variation of the average deviation, asymmetry coefficient A_s , concentration coefficient K – kurtosis).

The description of statistical measures is additionally supplemented by a regression analysis which approximates the experimental data. For the available experimental data with the values of independent variables $x_{i,j}$ where: $i = 1, 2, \dots, N$ (number of experiments), $j = 1, 2, \dots, K$ (number of independent variables) and the corresponding values of dependent variables y_i , the re-

gression function, that best describes the considered phenomenon in physical terms, is searched. The significance of the fit of the function is evaluated for a given value of the significance level α .

The selection of the type of the regression function is very important for the identification of a given phenomenon. This selection is also very difficult due to the occurrence of disturbances in research as well as in some cases the lack of proper data collected over the years of observation, and which cannot be repeated or supplemented. Often the influence of disturbances is too high compared to the influence of the variation of input variables on the output variables. The significance of the obtained regression function indicates the existence of a correlation between the considered values but it does not have to contain a causal relationship, yet it does not exclude it. Establishing such a regression function that expresses the causal (physical) relationship of a given phenomenon (as far as it is possible with existing experimental data) is the main difficulty in this procedure. It should be emphasised that the determination of high-reliability conclusions based on the established regression equations is very difficult, especially in the assessment of medical problems due to the high variation of factors determining health state assessment. Conclusions obtained as a result of mathematical calculations support the work of the medical team to a large extent, but they cannot replace their knowledge and experience. In definite cases, they can only confirm or help in specifying the assessment of the validity of its constituent elements in the problem under consideration.

3. RESULTS

3.1. Results of calculations of population structure of group I 'individual' for statistical analysis

For the statistical calculations for the 'Individual' group, a measurement matrix of 23 variables characteristic for 26 patients of the studied group was used, and a set of appropriate tests was collected (Skowronek et al., 2017). The analysed variables are, among others: age, gender, range of hip joint motion and functional tests assessing the level of physical fitness of patients after the finished treatment. It is worth noting that the collected values represent the general and partial scores of the used tests. Medical examination with the above-mentioned tests was performed after treatment was completed (about 6 months after surgery). The medical examination took place in the Department or at patient's home.

The results of 26 measurements are presented in Tab. 2, the results of calculating statistical measures in Tab. 3. For a better insight into the research, a detailed description of 23 variables is included in Tab. 1.

Observing the matrix of experiments and the results of calculations of statistical measures, attention is drawn to a large number of data that requires evaluation and proper analysis, and which will be presented in further considerations.

Tab. 1. Physical names of variables considered in an individual improvement programme

Variable x_j	Symbol of variable	Name/Description
1	Y	Year of Patient's Birth
2	M / month	Month of Patient's Birth
3	A	Patient's Age
4	R / L	Operated Right / Left Limb L-1 pt., R – 2 pts.
5	M / W	Patient's Gender, Men / Woman K-1 pt. M-2 pts.
6	i	Indoor / Indoor Moving
7	o	Outdoor / Outdoor Moving
8	c	Community / Functioning in Community
9	P	Parker Scale (Parker Mobility Score): indoor moving + outdoor moving + functioning in community, e.g. shopping = Parker max. Maximum number of points 3 + 3 + 3 = 9 pts.
10	n	Walking Aid
11	m	Environmental Mobility
12	M	Mobility- Scale of dependence on walking aid and level of mobility 1. Walking aid: wheelchair (1 pt.), personal assistant (2 pts.), crutches (3 pts.), crutch/walking stick (4 pts.), without orthopedic help (5 pts.) 2. Environmental mobility: indoor moving (1 pt.), outdoor moving (2 pts.), functioning in the community, e.g. possibility of shopping (3 pts.) max. number of points 5 + 3 = 8 pts.
13	V	Scale of Pain Assessment (VAS) from 0 pts to 10 pts.
14	T	Trendelenburg Test 1 pt. - positive test result, 2 pts. - negative test result
15	f	Flexion in a Hip Joint in degrees
16	ex	Extention in a Hip Joint in degrees
17	ab	Abduction in a Hip Joint in degrees
18	ad	Adduction in a Hip Joint in degrees
19	ir	Internal Rotation in a Hip Joint in degrees
20	er	External Rotation in a Hip Joint in degrees
21	HHSm	HHS, score for the range of motion in a hip joint, 0–5 pts
22	HHS	HHS Scale max. number of pts to 100.
23	TI	Time of Life Since the Operation to the Day of Analysis in years

Tab. 2. Matrix (database) of experiments in an individual improvement programme (Results of medical research (N = 26) – Individual Group)

	Y	M	A	RL	WM	i	o	c	P	n	m	M	V	T	f	ex	ab	ad	ir	er	HHSm	HHS	TI
No.	1	2	3	4	5	6	7	8	9	10	11	12	13	14	15	16	17	18	19	20	21	22	23
1.	27.	3.	87.	1.	2.	2.	2.	2.	6.	4.	3.	7.	0.	1.	100.	-20.	30.	0.	0.	0.	4.40	86.40	2.475
2.	19.	1.	95.	1.	2.	1.0.	3.	3.	1.	4.	0.	2.	100.	-20.	20.	0.	0.	20.	4.70	71.70	2.491		
3.	36.	9.	78.	1.	1.	3.	3.	3.	9.	5.	3.	8.	0.	2.	100.	-20.	20.	0.	0.	20.	4.70	91.70	2.546
4.	37.	1.	77.	2.	1.	2.	2.	2.	6.	4.	2.	6.	1.	1.	100.	-15.	25.	0.	0.	20.	4.40	86.40	2.502
5.	41.	10.	73.	1.	1.	3.	3.	3.	9.	5.	3.	8.	0.	1.	100.	-20.	20.	0.	0.	20.	4.70	48.70	.457
6.	49.	4.	65.	1.	1.	3.	3.	3.	9.	5.	3.	8.	0.	2.	120.	0.	20.	15.	15.	30.	5.00	100.00	2.872
7.	24.	5.	90.	2.	1.	1.	1.	0.	2.	1.	1.	2.	1.	1.	100.	-20.	20.	15.	0.	0.	4.55	52.55	2.669
8.	26.	5.	88.	2.	1.	2.	2.	2.	6.	3.	1.	4.	2.	1.	100.	0.	20.	20.	-10.	10.	4.75	33.75	2.604
9.	34.	3.	80.	1.	1.	2.	2.	2.	6.	3.	3.	6.	2.	1.	100.	-30.	20.	0.	0.	30.	4.70	57.70	2.968
10.	30.	10.	84.	1.	2.	2.	2.	2.	6.	4.	2.	6.	0.	1.	100.	-20.	10.	5.	0.	0.	4.20	69.20	2.491
11.	35.	3.	79.	1.	1.	2.	2.	2.	6.	3.	2.	5.	0.	1.	100.	-20.	10.	5.	0.	0.	4.20	69.20	2.650
12.	38.	9.	76.	2.	1.	2.	2.	2.	6.	3.	1.	4.	0.	1.	100.	-20.	10.	5.	0.	0.	4.30	66.30	2.757
13.	52.	3.	62.	2.	2.	2.	2.	2.	6.	4.	3.	7.	1.	1.	70.	-20.	-20.	20.	0.	0.	3.15	68.15	2.880
14.	39.	3.	75.	2.	1.	2.	2.	2.	6.	4.	3.	7.	2.	1.	100.	-20.	20.	0.	0.	0.	4.40	69.40	2.869
15.	25.	5.	89.	1.	1.	3.	3.	3.	9.	5.	3.	8.	0.	2.	110.	0.	20.	10.	0.	0.	4.65	99.65	2.724
16.	22.	12.	92.	1.	1.	2.	2.	2.	6.	3.	2.	5.	1.	1.	100.	-20.	20.	15.	-10.	20.	4.85	67.85	2.645
17.	51.	4.	63.	1.	2.	0.	0.	1.	1.	2.	2.	2.	5.	1.	60.	-45.	-20.	20.	20.	20.	3.30	19.00	2.689
18.	48.	4.	66.	1.	2.	2.	2.	1.	5.	3.	1.	4.	5.	1.	100.	-20.	15.	0.	0.	0.	4.35	52.32	2.568
19.	33.	2.	81.	2.	2.	3.	2.	3.	8.	4.	3.	7.	1.	1.	110.	0.	30.	0.	0.	0.	4.55	81.55	3.042
20.	28.	4.	86.	2.	2.	2.	2.	2.	6.	3.	1.	4.	2.	1.	100.	-20.	20.	-20.	-10.	10.	4.75	50.75	2.601
21.	23.	9.	91.	2.	1.	0.	0.	0.	0.	1.	1.	2.	2.	1.	90.	-20.	20.	20.	20.	20.	4.70	6.70	.986
22.	45.	12.	69.	2.	1.	2.	2.	2.	6.	3.	3.	6.	0.	1.	90.	-20.	20.	20.	20.	20.	4.70	62.70	2.568
23.	40.	5.	74.	1.	1.	3.	2.	3.	9.	5.	3.	8.	0.	1.	120.	0.	20.	15.	15.	30.	5.00	88.00	2.905
24.	26.	3.	88.	1.	1.	3.	3.	3.	9.	5.	3.	8.	0.	2.	110.	-10.	30.	0.	0.	0.	4.55	99.55	2.667
25.	55.	11.	59.	2.	1.	3.	3.	3.	9.	5.	3.	8.	0.	2.	120.	0.	20.	0.	0.	0.	5.00	100.00	2.590

Tab. 3. Results of calculations for Group I (Individual) 7 statistical measures of 23 variables

No.	Name	\bar{X}	$V=(SDT/\bar{X})$	$r(y,x)$	$r(x,y)^2$	$Vop=(op/\bar{X})$	As	K
v.	v.		100[%]		100[%]	100[%]	asym.	coef. kurtosis
1	Y	35.34615	28.81796	0.125	1.570	23.395	0.287	1.912
2	m	5.53846	61.96632	-0.401	16.043	52.350	0.624	1.908
3	A	78.65385	12.95047	-0.125	1.570	10.513	-0.287	1.912
5	WM	1.30769	35.99324	0.193	3.741	32.579	0.786	1.567
6	i	2.15385	38.71671	0.212	4.482	27.198	-1.069	3.932
7	o	2.03846	40.40746	0.144	2.084	25.399	-0.892	3.580
8	c	2.03846	47.01392	0.191	3.659	32.656	-0.859	2.819
9	P	6.26923	40.49333	0.199	3.950	28.929	-0.798	2.981
10	n	3.65385	32.78952	0.137	1.879	27.044	-0.551	2.514
11	m	2.26923	38.53378	0.160	2.544	34.681	-0.515	1.459
12	M	5.846615	35.11952	0.128	1.632	29.555	-0.521	1.937
13	V	0.96154	148.48580	0.026	0.070	107.692	1.650	5.089
14	T	1.26923	35.64366	0.152	2.310	31.002	0.981	1.925
15	f	100.76920	13.43859	0.151	2.272	7.986	-1.062	4.866
16	ex	-15.38462	-72.33601	0.188	3.517	-56.731	-0.137	3.046
17	ab	16.92308	70.94695	-0.100	0.995	43.881	-2.088	7.066
18	ad	7.11538	142.17970	0.020	0.039	120.790	-0.338	2.753
19	ir	2.69231	320.50950	-0.133	1.773	239.560	0.791	2.752
20	er	10.76923	104.80300	-0.194	3.776	93.956	0.338	1.493
21	HHSm	4.52115	9.93199	-0.110	1.220	6.789	-1.678	5.692
22	HHS	69.20077	35.97741	0.464	21.551	27.116	-0.667	2.868
23	T	2.54185	22.18227	1.000	100.000	11.648	-2.662	9.482

3.2. Final characteristics of treatment results

The essence of the final assessment of the treatment of patients with trochanterian fractures in addition to radiological control

is the scale of pain assessment and the assessment of mobility (Skowronek et al., 2017; Tjun Huat Chya et al., 2013; Wamper et al., 2010). The latter one is performed in a clinical examination with functional tests.

For a physiotherapist, this is the basic measure of the outcome of treatment. Therefore, for the detailed statistical evaluation of 23 variables, 7 were selected. They include age, gender, Parker test/scale (Tab. 4) and VAS pain assessment scale, Trendelenburg test, the scale of dependence on walking aid and the mobility level – working name Mobility (Tab. 5) and the HHS scale. The scores of the tests were assessed as a whole without detailed evaluating of their components.

Tab. 4. Scoring of the Parker Test (Parker Mobility Score) and marking of its symbols (Skowronek et al., 2017; Tjun Huat Chya et al., 2013; Wamper et al., 2010)

Mobility	Without difficulty	With the help of orthopedic equipment	With the help of another person	Lack of activity
Indoor moving	3 pts.	2 pts.	1 pt.	0 pts.
Outdoor moving	3 pts.	2 pts.	1 pt.	0 pts.
Functioning in community e. g. shopping	3 pts.	2 pts.	1 pt.	0 pts.

Parker Test= indoor moving + outdoor moving + functioning in community e. g. shopping

Tab. 5. Scoring of the scale of dependence on walking aid and level of mobility (Skowronek et al., 2017; Tjun Huat Chya et al., 2013; Wamper et al., 2010)

System of scoring	Result
Walking aid	
Wheelchair	1 pt.
Personal assistant	2 pts.
Walking frame, crutches	3 pts.
Crutch, walking stick	4 pts.
Moving without help	5 pts.
Environmental mobility	
Indoor moving	1 pt.
Outdoor moving	2 pts.
Functioning in community, e.g. shopping	3 pts.

Scoring of the scale of dependence on walking aid and level of mobility= walking aid + environmental mobility

3.3. List of statistical measures

The results of the adopted statistical measures of the selected variables are summarised in Tab. 6. Each of the analysed variables and scales was subjected to the presented innovative statistical analysis. It facilitates the assessment of mutual links between variables. The applied test in the assessment of mutual correlations was first of all the linear correlation coefficient. The correlation was assessed according to the following assumptions (Skowronek et al., 2017; Zeliaś, 2000).

Correlation assessment:

- 0.0 – no correlation
- $0.0 < r(x, y) \leq 0.2$ – very small (practically no linear connection),
- $0.2 < r(x, y) \leq 0.4$ – clear but small,
- $0.4 < r(x, y) \leq 0.7$ – moderate,
- $0.7 < r(x, y) \leq 0.9$ – significant,
- $0.9 < r(x, y) \leq 1.0$ – very strong,
- $r(x, y) = 1.0$ – functional linear relationship between the variables y, x.







For a better insight into the assessment of the obtained results, coloured markings according to the attached legends were introduced. A list of the results of the calculations of statistical measures is shown in Tab. 6 and a list of correlation coefficients between the output values and the successive variables xi in regression equations for the specified medical tests is shown in Tab. 7. In order to determine the relationship between these tests, regression equations in the form of the third-degree polynomial were adopted. Finally, the form of regression equations and the results of their testing are given after presenting the statistical measures and the correlation coefficients.

Tab. 6. List of statistical measures in the Individual Group

Analyzed variables and scales	\bar{X}	V	Vop	As	K
Age	78.65385	12.95047	10.513	0.287	1.912
MW/Gender	1.30769	35.99324	32.579	0.786	1.567
Parker	6.26923	40.49333	28.929	0.798	2.981
"Mobility"	5.84615	35.11952	29.555	0.521	1.937
VAS	0.96154	148.48580	107.692	1.650	5.089
Trendelenburg	1.26923	35.64366	31.002	0.981	1.925
HHS	69.20077	35.97741	27.116	0.667	2.868

\bar{X} – arithmetic mean, V – coefficient of variation (differentiation), Vop – coefficient of variation of average, A – asymmetry coefficient, K – kurtosis)

Legend:

-  for v and vop, red means the most homogeneous result
-  for v and vop, blue means the least homogeneous result
-  for As, red means the right-sided asymmetry (As > 0)
-  for As, blue means the left-sided asymmetry (As < 0)
-  for K, red means values with higher concentration around averages (K > 3)
-  for K, blue means values with lower concentration around averages (K < 3)

Tab. 7. List of linear correlation coefficients between the used tests

Group/correlation	Variable x	Variable x ²	Variable X ³
Parker - HHS	0.79026	0.75639	0.72633
Mobility - HHS	0.81212	0.79995	0.77084
VAS - HHS	-0.65303	-0.62278	-0.57586
Trendelenburg -HHS	0.63291	0.73003	0.77755
Parker - Mobility	0.91384	0.88861	0.86245
VAS - Mobility	-0.58886	-0.57327	-0.55357
Trendelenburg - Mobility	0.47708	0.53140	0.57330
VAS - Parker	-0.55986	-0.55186	-0.52961
Parker - Trendelenburg	0.45685	0.45685	0.45685
VAS - Trendelenburg	-0.41687	-0.41687	-0.41687
Description of correlation		Graphic interpretation	
0.0 - no correlation			
0.0 < r(x, y) ≤ 0.2 – very small			
0.2 < r(x, y) ≤ 0.4 – clear but small			
0.4 < r(x, y) ≤ 0.7 – moderate			
0.7 < r(x, y) ≤ 0.9 – significant			
0.9 < r(x, y) < 1.0 – very strong			
when r(x, y) = 1.0 – linear function			

3.4. Models of regression equations, research observations

After analysing the linear correlation coefficients, the statistical models in the form of the third-order regression equations were

used in the next stage. The best ones were selected and presented. An additional goal of these activities was to improve research in the future by reducing the number of the currently performed tests which contain common features of elements related to physical and intellectual efficiency or other important features affecting the outcome of treatment.

In the exploratory research, the polynomial model was adopted in the following form:

$$\hat{y} = a_0 + a_1x + a_2x^2 + a_3x^3 \tag{1}$$

where: \hat{y} - output variable of the regression equation, a_i - regression coefficients, $i = 1, 2, 3$ x - input variable.

Below the selected calculation results, that were obtained using a standard IBM multiple-step regression programme, are presented. This programme was supplemented with the data necessary to select the best set of regression equations. This programme allows to match the assumed mathematical models to the experimental data according to the principle of the minimum sum of squares of deviations of differences between experimental points, and relevant points of the calculated mathematical models. The significance of the statistical fit of the mathematical model to the experimental data was tested with the F – Fischer Snedecor test, while the significance of individual coefficients of regression equations was tested with the t – Student test at the assumed significance level of $\alpha = 0.05$ in both cases. The significance level $\alpha = 0.05$ corresponds to the level of confidence (probability) $p = 1 - \alpha = 0.95$. The final form of regression equations was chosen by adopting the criterion of the execution of the applied tests at the significance level $\alpha \leq 0.05$. The test results are given in Tab. 8.

Tab. 8. Results of testing the significance of regression equations and regression coefficients regarding the dependences between the used tests

No.	Dependence of tests	Step of calculations	Multiple correlation coeff. R	No. of freed. deg.; no. & nam. n-k-1, k		Value of F – Fisher function F	Critical value F_{kr} (α, n-k-1, k)	$\frac{F}{F_{kr}}$	Value of t – Student function t	Critical value $t_{kr}(\alpha, n-1)$	$\frac{t}{t_{kr}}$
1	P-HHS	1	0.780	24	1	39.917	4.262	9.365	$t_1=6.318$	2.064	3.061
		2	0.791		2	19.244	3.430	5.610	$t_1=1.819$ $t_2=0.297$	2.064 2.069	0.879 0.135
		3	0.835	22	3	16.830	3.056	5.507	$t_1=2.770$ $t_2=2.884$ $t_3=2.262$	2.064 2.069 2.074	1.335 1.397 1.091
2	M-HHS	1	0.812	24	1	46.492	4.262	10.98	$t_1=6.819$	2.064	3.304
		2	0.814	23	2	22.615	3.430	6.598	$t_1=2.166$ $t_2=0.482$	2.064 2.069	0.483 0.233
		3	0.815	22	3	14.537	3.056	4.757	$t_1=0.758$ $t_2=-0.339$ $t_3=0.395$	2.064 2.069 2.074	0.365 0.163 0.190
3	V-HHS	1	0.653	24	1	17.845	4.262	4.422	$t_1=-4.224$	2.064	2.046
		2	0.656	23	2	8.707	3.430	2.538	$t_1=2.002$ $t_2=0.420$	2.064 2.069	0.968 0.203
		3	0.686	22	3	6.526	3.056	2.135	$t_1=0.857$ $t_2=1.334$ $t_3=-1.291$	2.064 2.069 2.074	0.413 0.622 0.643
4	T-HHS	1	0.778	24	1	36.696	4.262	8.610	$t_3=6.058$	2.064	2.935
		2	0.816	23	2	22.923	3.43	6.683	$t_3=3.026$ $t_2=-2.055$	2.064 2.069	1.462 0.993
		3	0.827	22	3	16.012	3,056	5.239	$t_3=2.080$	2.064	1.006

									$t_2 = -1.574$ $t_1 = 1.182$	2.069 2.074	0.759 0.570
5	P-M	1	0.914	24	1	121.947	4.262	28.519	$t_1 = 11.025$	2.064	5.341
		2	0.917	23	2	60.68	3.43	17.691	$t_1 = 2.715$ $t_2 = -0.897$	2.064 2.069	1.312 0.433
		3	0.961	22	3	88.509	3.056	28.962	$t_1 = 5.624$ $t_2 = -4.981$ $t_3 = 4.48$	2.064 2.069 2.074	2.712 2.402 2.160
6	V-M	1	0.589	24	1	12.74	4.262	2.989	$t_1 = -3.569$	2.064	1.729
		2	0.591	23	2	6.157	3.43	1.795	$t_1 = -0.8712$ $t_2 = -0.262$	2.064 2.069	0.421 0.127
		3	0.594	22	3	4.008	3.056	1.311	$t_1 = -0.578$ $t_2 = 0.424$ $t_3 = -0.401$	2.064 2.069 2.074	0.277 0.204 0.193
7	T-M	1	0.573	24	1	11.75	4.262	2.757	$T_3 = 3.428$	2.064	1.661
		2	0.647	23	2	8.294	3.43	2.418	$T_3 = 2.326$ $t_2 = -1.891$	2.064 2.069	1.124 0.914
		3	0.734	22	3	8.558	3.056	2.800	$T_3 = 2.905$ $t_2 = -2.641$ $t_1 = 2.387$	2.064 2.069 2.074	1.401 1.273 1.151
8	V-P	1	0.457	24	1	10.957	4.262	2.571	$t_1 = -3.310$	2.064	1.604
		2	0.457	23	2	3.033	3.43	0.884	$t_1 < 0.001$ $t_2 < 0.001$	2.064 2.069	$\ll 1.0$ $\ll 1.0$
		3	0.564	22	3	3.415	3.056	1.197	$t_1 = -0.398$ $t_2 = 0.194$ $t_3 = 0.227$	2.064 2.069 2.074	0.192 0.093 0.109
9	P-T	1	0.457	24	1	6.33	4.263	1.485	$t_1 = 2.516$	2.064	1.219
		2	0.457	23	2	3.033	3.43	0.884	$t_1 < 0.001$ $t_2 < 0.001$	2.064 2.069	$\ll 1.0$ $\ll 1.0$
		3	no solution in the field of real numbers								
10	V-T	1	0.417	24	1	5.048	4.263	1.84	$t_1 = -2.247$	2.064	1.089
		2	0.417	23	2	2.419	3.43	0.705	$t_1 < 0.001$ $t_3 < 0.001$	2.064 2.069	$\ll 1.0$ $\ll 1.0$
		3	no solution in the field of real numbers								

A set of the regression equations representing the effective mathematical models (linear/non-linear) describing the relationships between the selected tests significant in terms of model fit as well as the significance of individual regression coefficients are presented in Eqs. (2)–(11).

Dependence P - HHS $P = 0.69302 + 0.08058 \text{ HHS}$
or $P = -3.09728 + 0.42456 \text{ HHS} - 0.00706 \text{ HHS}^2 + 0.00004 \text{ HHS}^3$ (2)

Dependence M-HHS $M = 1.21159 + 0.06697 \text{ HHS}$ (3)

Dependence V-HHS $V = 3.55307 - 0.03745 \text{ HHS}$
or $V = 2.282 + 0.0975 \text{ HHS} - 0.00296 \text{ HHS}^2 + 0.00002 \text{ HHS}^3$ (4)

Dependence T-HHS $T = 0.73511 + 0.03284 \text{ HHS} - 0.00088 \text{ HHS}^2 + 0.00001 \text{ HHS}^3$ (5)

Dependence P-M $P = -0.33650 + 1.12993 \text{ M}$
or $P = -13.48795 + 10.80495 \text{ M} - 2.05105 \text{ M}^2 + 0.13140 \text{ M}^3$ (6)

Dependence V-M $V = 3.35547 - 0.40949 \text{ M}$ (7)

Dependence T-M $T = 0.91694 + 0.00132 \text{ M}^3$
or $T = -1.39013 + 2.00704 \text{ M} - 0.47591 \text{ M}^2 + 0.03424 \text{ M}^3$ (8)

Dependence V-P $V = 2.93555 - 0.31487 \text{ P}$ (9)

Dependence P-T $P = 3.01504 + 2.56391 \text{ T}$ (10)

Dependence V-T $V = 2.63158 - 1.1579 \text{ T}$ (11)

Statistical significance of the obtained results is a very important problem. One of the basic activities of statistical inference is verification which means making decisions about the truth or the falsity of statistical hypotheses. Most often it refers to the form of distributions or values of their parameters (Zeliaš, 2000). Here, the hypothesis is any assumption concerning an unknown distribution regarding the examined feature of the population, and about the truth or the falsity, which is deduced from the random test. When carrying out the significance tests, it is required to make such a hypothesis to which there is a greater guess about its falsity than its truth.

The measurement results contain a definite number of experiments of a given statistical measure, e.g.: mean value \bar{X} of the examined feature and coefficients of variation. In many cases there is a need to estimate the population confidence range at the assumed significance level, e.g. $\alpha = 0.05$ substantively justified. When estimating definite population measures based on the performed experiments in the test, the exact value of this measure is not given in this case, but the range is determined, which contains with the assumed probability the unknown missing measure

value of the parameter being tested. The most commonly accepted value is $p = 0.95$ (95%), in more detailed studies $p = 0.995$, and in very exact cases even 0.999 (99.9%).

To determine the confidence ranges for the selected statistical measures, which are characterised by possibly large correlation coefficients $r(y, x)$, a two-sided symmetric distribution of the significance level $\alpha = 0.05$ was adopted. The adoption of the two-sided distribution of the significance level is justified by the fact that disturbances may appear on the edges of the range of the definite statistical measures. The assumption was made that the tests have the t – Student distribution with $n-1$ degree of freedom. The mean values of random variables and STDs of the general population are not known.

The lower limit D and the upper limit G of the confidence range are defined by the dependences:

$$D = \bar{X} - t_{\left(\frac{\alpha}{2}, n-1\right)} \frac{\sigma}{\sqrt{n-1}};$$

$$G = \bar{X} + t_{\left(\frac{\alpha}{2}, n-1\right)} \frac{\sigma}{\sqrt{n-1}}, \dots \quad (12)$$

And the relative accuracy degree of the estimation v_i [%] of the chosen parameter is determined by the expression:

$$v_i = \frac{t_{\left(\frac{\alpha}{2}, n-1\right)} \sigma}{\bar{x} \sqrt{n-1}} 100 \text{ [%]}$$

The results of the calculations for the selected variables are given in Tab. 9.

Tab. 9. Results of calculations of statistical measures for the selected variables and scales

No.	Variable	Mean value, \bar{x}	Stand. deviations., σ	$t_{\left(\frac{\alpha}{2}, n-1\right)}$	Lower limit	Upper limit	Confiden. range	Range length	Estimation degree %
1	Age [years]	78.654	10.186	2.060	74.457	82.851	74.7÷82.8	8,394	5.28
2	MW/Gender	1.308	0.471	2.060	1.114	1.502	1 ÷ 2	1	14.78
3	Parker	6.269	2.539	2.060	5.224	7.312	5 ÷ 8	3	16.99
4	Mobility	5.846	2.053	2.060	5.001	6.698	5 ÷ 7	2	14.50
5	VAS	0.962	1.427	2.060	0.373	1.358	0 ÷ 2	2	61.11
6	Trendeleburg	1.269	0.452	2.060	1.085	1.549	1 ÷ 2	1	14.69
7	HHS	69.201	24.897	2.060	58.943	79.458	58.9÷79.4	20.515	14.78

Note: In Tab.9 the A - age variable is given in years, the remaining ranges and length of ranges for the variables are expressed in the appropriate units resulting from the tests and scales

It is worth noting that the best statistical results were obtained in the analysis of the third order regression equations. In order to additionally assess the significance of individual regression coefficients and the significance of mathematical model fit to the experimental data, the t - Student test and the F - Fischer test were analysed. In the analysed dependences, i.e. Parker on Mobility, Mobility on HHS and Parker on HHS, the fit of the mathematical model and the significance of individual regression coefficients were claimed at the significance level $\alpha \leq 0.05$. When analysing complex and difficult issues in research, this is a very good result. The F - Fischer and t - Student tests show that in the conducted analysis the best results are generally achieved in the first-order models.

When assessing the fit of regression equations using the multi correlation coefficient R , the best results are generally achieved in the third-order models. However, in such cases, the statistical analysis (the t - Student test) shows in most cases a considerable loss of significance level of individual regression coefficients at the required level of significance (regression coefficients become irrelevant at the assumed significance level), as well as the reduction of the parameters of the F – Fischer test while maintaining the condition of the specified significance level α .

4. DISCUSSION

The article presents a detailed analysis of the selected tests of functional assessment of patients after trochanteric fractures are treated surgically. Being aware of the time constraints in daily hospital work, a preliminary attempt was made to create an own

system that will allow to assess the recovery process quickly and reliably. For the assessment of pain, the Visual Analogue Scale (VAS) was chosen as a proven and easy to use scale, while the mobility test was chosen based on the applied statistical analysis and clinical experience.

Analysing the linear correlation between the applied tests, it was observed that a very strong correlation was obtained between the Parker test/scale and Mobility ($r = 0.91384$), and a significant correlation was obtained between Mobility and HHS ($r = 0.81212$). Also significant is the Parker and HHS correlation ($r = 0.79026$). The remaining relationships between the tests were moderate. Based on the variation coefficient V and the variation coefficient of the average deviation Vop , it was also found that the results of the above tests proved to be the most homogeneous (reaching the values close to the average) in the 'Individual' Group under study. Trying to confirm the results between the tests, the results of the calculations were compared with the resulting regression analysis. The multiple correlation coefficient R confirmed the high correlation between the tests: Parker and Mobility (0.961), Mobility and HHS (0.815) and Parker and HHS (0.835), which is conditioned by the form of the adopted mathematical model.

The obtained results and the implementation simplicity suggest that it is sufficient to use the Parker or the Mobility tests interchangeably in clinical practice for a full assessment of mobility. The performed analysis allowed to create a model of a fast assessment of the patient's condition. Physiotherapists and doctors are using our experience in the clinical assessment of the patient's condition after hip injuries. They use one functional test (Parker / Mobility interchangeably) and the VAS scale for pain assessment. Previously, 2–3 functional tests were performed,

which took twice as much time.

In the literature, we find the tests we used with various statistical calculations (Tjun Huat Chua et al., 2013; Wamper et al., 2010; Shin et al., 2020; Abdullah et al., 2018). However, we did not find any studies that would compare the described tests with the usage of the applied statistical model.

5. CONCLUSIONS

The results from the research on measures and regression equations give the following observations:

- The maximum correlation coefficient was obtained between the Parker and the Mobility tests/scales. Clinical experience confirms the possibility of using one of them in the examination of patients interchangeably.
- The results of the functional assessment regarding the Parker, Mobility, Trendelenburg and HHS tests are the most homogeneous.
- Multiple-step regression effectively supports the statistical analysis in the functional assessment of the 'Individual' Group, thus indicating its usefulness.
- The extended statistical analysis makes it possible to create an own system for assessing the treatment results of patients after trochanteric fractures are treated surgically. The application of the VAS pain assessment scale and the Parker / Mobility interchangeable tests based on clinical experience and statistical calculations allows to assess the patient's condition quickly and reliably.


REFERENCES


1. **Abdullah H.R., Tan S.R., Lee S.J., Razak H.R., Seet R.H., Ying H., Sethi E., Sim E.Y.P.** (2018), Protocol for a single-centre prospective observational study of postoperative delirium following total joint arthroplasties among South East Asians, *BMJ Open*, 8(3)
2. **Aczel A.D.** (2008), *Statistics in management*, Scientific Publisher PWN, Warsaw.
3. **Adunsky A., Arad M., Blumstein T., Weitzman A., Mizrahi E.Z.** (2008), Discharge hemoglobin and functional outcome of elderly hip fractured patients undergoing rehabilitation, *Eur J Phys Rehabil Med.*, 44(4), 417-22.
4. **Auron-Gomez M., Michota F.** (2008), Medical management of hip fracture, *Clin. Geriatr. Med.*, 24, 701-19.
5. **Baumgaertner M., Oetgen M.** (2009), Intertrochanteric Hip Fractures. Browner: Skeletal Trauma, *Philadelphia:Saunders*, 1913-52.
6. **Bellabarba C., Herscovici D., Jr., Ricci W.M.** (2000), Percutaneous treatment of peritrochanteric fractures using the Gamma nail, *Clin. Orthop. Relat. Res.*, 375: 30-42.
7. **Bernstein D.N., Davis J.T., Fairbanks C., McWilliams-Ross K., Ring D., Sanchez H.B.** (2018), Lower Bone Mineral Density is Associated with Intertrochanteric Hip Fracture, *Arch. Bone. Jt. Surg.*, 6(6), 517-522
8. **Borges F.K., Bhandari M., Patel A., Avram V.** (2019), Rationale and design of the HIP fracture Accelerated surgical Treatment And Care track (HIP ATTACK) Trial: a protocol for an international randomized controlled trial evaluating early surgery for hip fracture patients, *BMJ Open*, 9(4)
9. **Bredbenner T.L., Mason R.L., Havill L.M., Orwoll E.S., Nicoletta D.P.** (2015), Fracture risk predictions based on statistical shape and density modeling of the proximal femur, *J. Bone Miner. Res.*, 30(1), 197.
10. **Bryan R., Mohan P.S., Hopkins A., Galloway F., Taylor M., Nair P.B.** (2010), Statistical modeling of the whole human femur incorporating geometric and material properties, *Med. Eng. Phys.*, 32(1), 57-65.
11. **Carulli Ch F., Paoli T R M.** (2017), A comparison of two fixation methods for femoral trochanteric fractures: a new generation intramedullary system vs sliding hip screw, *Clin. Cases Miner. Bone. Metab.*, 14(1),40-47
12. **Forni C., Gazineo D., Fiorani A., Morri M., Sabattini T., Ambrosi E.** (2019), Predictive factors for thirty day mortality in geriatric patients with hip fractures: a prospective study, *Int. Orthop.*, 43(2), 275-281.
13. **Friedman S.M., Menzies I.B., Bukata S.V., Mendelson Kates S.L.** (2010), Dementia and Hip Fractures Development of a Pathogenic Framework for Understanding and Studying Risk, *Geriatr. Orthop. Surg. Rehabil.*, 1(2), 52-62.
14. **Grau L., Summers S., Massel D.H., Rosas S., Ong A., Hernandez V.H.** (2018), Operative Trends in the Treatment of Hip Fractures and the Role of Arthroplasty, *Geriatr. Orthop. Surg. Rehabil.*, 22, 9
15. **Hao-Kuang W., Chao-Ming H., Sheng-Hsiang L., Yi-Cheng T., Kang L., Po-Chou L., Chi-Wei L., Yi-Che L., Pei-Hsuan F., Li-Ching Ch., Ying-Chun L.** (2014), Increased risk of hip fractures in patients with dementia: a nationwide population-based study, *BMC Neurol.*, 14, 175.
16. **Huang S.W., Lin J.W., Liou T.H., Lin H.W.** (2015), Cohort study evaluating the risk of hip fracture among patients with dementia in Taiwan, *Int. J. Geriatr. Psychiatry*, 30(7), 695-701.
17. **Huddleston J.M., Whitford K.J.** (2001), Medical care of elderly patients with hip fractures, *Mayo Clin. Proc.*, 76, 295-8.
18. **Ibrahim S., Meleppuram J.J.** (2017), A retrospective analysis of surgically-treated complex proximal femur fractures with proximal femoral locking compression plate, *Rev. Bras. Ortop.*, 52(6), 644-650.
19. **Klestil T., Röder Ch., Stotter Ch., Winkler B., Nehrer S., Lutz M., Klerings I., Wagner G., Gartlehner G., Nussbaumer-Streit B.** (2018), *Impact of timing of surgery in elderly hip fracture patients: a systematic review and meta-analysis*, Scientific Reports.
20. **Korzyński M.** (2006), *Methodology of the experiment*, Scientific and Technical Publishers WNT, Warsaw.
21. **Lee Y.K., Lee Y.J., Ha Y.C., Koo K.H.** (2014), Five year relative survival of patients with osteoporotic hip fracture, *J. Clin. Endocrinol. Metab.*, 99, 97-100.
22. **Mizrahi E.H., Fleissig Y., Arad M., Blumstein T., Adunsky A.** (2008) Rehabilitation outcome of hip fracture patients: The importance of a positive albumin gain, *Archives of Gerontology and Geriatrics*, 47(3), 318-326.
23. **Moja L., Piatti A., Pecoraro V., Ricci C., Virgili G., Salanti G., Germagnoli L., Liberati A., Banfi G.** (2012), Timing Matters in Hip Fracture Surgery: Patients Operated within 48 Hours Have Better Outcomes. A Meta-Analysis and Meta-Regression of over 190,000 Patients, *PLoS One*, 7(10)
24. **Nurul 'Izzah I., Mohd Sharkawi A., Mohamed S.Z., Sharifah Nurul Aqilah Sayed Mohd Z., Zainal Abidin Nor A., Isa Naina M., Norazlina M., Sabarul Afian M., Ahmad Nazrun S.** (2019), Physical function assessment of older adults with lower body fractures at 3 months post-discharge, *Ther Clin Risk Manag.*, 15, 201-210.
25. **Pincus D., Ravi B., Wasserstein D., Huang A., Paterson J.M., Nathens A.B., Kreder H.J., Jenkinson R.J., Wodchis W.P.** (2017), Association Between Wait Time and 30-Day Mortality in Adults Undergoing Hip Fracture Surgery, *JAMA*, 318(20), 1994-2003
26. **Pottecher P., Engelke K., Duchemin L., Museyko O., Moser T., Mitton D., Vicaut E., Adams J., Skalli W., Laredo J.D., Bousson V.** (2016), Prediction of Hip Failure Load: In Vitro Study of 80 Femurs Using Three Imaging Methods and Finite Element Models - The European Fracture Study (EFFECT), *Radiology*, 280(3), 837-47.
27. **Research project Military Medical Institute** (2015), *Comparative assessment of the effectiveness of physiotherapy in patients after surgical treatment of trochanteric fractures depending on the psychomotor state*, MMI 14/MMI.


28. **Rizk P., Morris W., Oladeji P., Huo M.** (2016), Review of postoperative delirium in geriatric patients undergoing surgery, *Geriatr. Orthop. Surg. Rehabil.*, 7(2), 100-105.
29. **Saarenpää I., Heikkinen T., Ristiniemi J., Hyvönen P., Leppilähti J., Jalovaara P.** (2009), Functional comparison of the dynamic hip screw and the Gamma locking nail in trochanteric hip fractures: a matched-pair study of 268 patients, *Int. Orthop.*, 33(1), 255-60.
30. **Seitz D.P., Gill S.S., Austin P.C., Bell C.M., Anderson G.M., Gruneir A., Rochon P.A.** (2016), Rehaition of Older Adults with Dementia After Hip Fracture, *J. Am. Geriatr. Soc.*, 64(1), 47-54.
31. **Shibasaki K., Asahi T., Mizobuchi K., Akishita M., Ogawa S.** (2018), Rehabilitation strategy for hip fracture, focused on behavioral psychological symptoms of dementia for older people with cognitive impairment: A nationwide Japan rehabilitation database, *PLoS One.*, 13(7)
32. **Shin W.Ch., Jang J.H., Seo H.E., Suh K.T., Moon N.H.** (2020), Prevalence and clinical impact of sarcopenia in osteoporotic hip fracture: Single center retrospective cohort study, *Acta Ortop. Traumatol Turc.*, 54(1), 27-33
33. **Skowronek R., Zawora J., Kwiatkowski K., Skalski K.** (2017), Analysis of statistical calculations the factors deciding about physiotherapy progress in trochanteric fractures, *Surface Engineering, IMP 4*, 3-10.
34. **Stanisławek J.** (2010), Basics of statistics - Statistical description, Correlation and regression, Distributions random variable, Statistical inference, Publishing House of the Warsaw University of Technology, Warsaw.
35. **Stwora A.** (2019), Optimization of the manufacturing process by SLS / SLM incremental methods due to selected physical properties of the elements being made, Dissertation, Institute of Aviation, Warsaw.
36. **Tan S.T., Tan W.P., Jaipaul J., Chan S.P., Sathappan S.S.** (2017), Clinical outcomes and hospital length of stay in 2,756 elderly patients with hip fractures: a comparison of surgical and non-surgical management., *Singapore Med. J.*, 58(5), 253-257.
37. **Tjun Huat Chua I., Naidu Rajamoney G., Beng Kee Kwek E.** (2013), Cephalomedullary nail versus sliding hip screw for unstable intertrochanteric fractures in elderly patients, *Journal of Orthopedic Surgery*, 21(3), 308-12.
38. **Wamper K., Sierevelt I., Poolman R., Bhandari M, Haverkamp D.** (2010), The Harris hip score: Do ceiling effects limit its usefulness in orthopedics?, *Acta Orthop.*, 81(6), 703-707.
39. **Yli-Kyyny T.T., Sund R., Heinänen M., Malmivaara A., Kröger H.** (2019), Risk factors for early readmission due to surgical complications after treatment of proximal femoral fractures – A Finnish National Database study of 68,800 patients, *Injury*, 50(2), 403-408.
40. **Yousry A.H., Chotai P.N., Ghazaly S.E., Fayyad T.A., Abdelgawad A.A.** (2015), Outcomes of trochanteric external fixation for geriatric inter-trochanteric hip fractures, *J. Orthop.*, 12(4), 174-178.
41. **Zeliaś A.** (2000), *Statistical methods*, Polish Economic Publishing House, Warsaw.
42. **Zhengan H., Xifeng W., Xingqun** (2018), Comparing surgical interventions for intertrochanteric hip fracture by blood loss and operation time: a network meta-analysis, *J. Orthop. Surg. Res.*, 13(1), 157.
43. **Zu-Sheng H., Xian-Ling L., Ying-Ze Z.** (2018), Comparison of Proximal Femoral Geometry and Risk Factors between Femoral Neck Fractures and Femoral Intertrochanteric Fractures in an Elderly Chinese Population, *Chin. Med. J. (Engl.)*, 131(21), 2524-2530.

Acknowledgments: We would like to thank the patients and their families who opted to take part in the research project.

Robert Skowronek:  <https://orcid.org/0000-0003-0972-4390>

Józef Zawora:  <https://orcid.org/0000-0002-6305-2698>

Krzysztof Kwiatkowski:  <https://orcid.org/0000-0003-0898-1061>

Konstanty Skalski:  <https://orcid.org/0000-0001-6241-7475>

MODAL CHARACTERIZATION OF SANDWICH SKEW PLATES

Dhotre PAVAN KUMAR^{*} , Chikkol V. SRINIVASA^{**} 

^{*}Research Scholar, Department of Mechanical Engineering, GM Institute of Technology, Davangere, Visvesvaraya Technological University, Jnana Sangama, VTU Main Rd, Machhe, Belagavi, Karnataka 590018, India

^{**}Head, Department of Mechanical Engineering, GM Institute of Technology, Davangere, Visvesvaraya Technological University, Jnana Sangama, VTU Main Rd, Machhe, Belagavi, Karnataka 590018, India

pavankumar-gmitrs@gmit.ac.in, srinivasacv@gmit.ac.in

received 14 March 2021, revised 26 June 2021, accepted 1 July 2021

Abstract: The current work focuses on the experimental and finite element free vibration studies of laminated composite sandwich skew plates. The comparison was made between the experimental values obtained by the Fast Fourier transform (FFT) analyzer and a finite element solution obtained from CQUAD8 finite element of The MacNeal-Schwendler Corporation (MSC) / NASA STRucture Analysis (NAS-TRAN) software. The influence of parameters such as aspect ratio (AR) (a/b), skew angle (α), edge condition, laminate stacking sequence, and fiber orientation angle (θ°) on the natural frequencies of sandwich skew plates was studied. The values obtained by both the finite element and experiment approaches are in good agreement. The natural frequencies increase with an increase in the skew angle for all given ARs.

Keywords: natural frequency, non-dimensional frequency parameter (K_f), antisymmetric laminate, fiber orientation angle, skew angle

1. INTRODUCTION

Due to the reduced weight and high stiffness, sandwich structures have a wide area of applications in engineering science. With anisotropy and considering all parameters involved in the sandwich structure, it is difficult to evaluate the dynamic response analytically. In the literature review, various theories, methods, and techniques were cited (Pavan et al., 2021). However, with the evolution of technology in real engineering applications, it is possible to predict the dynamic response of any structure accurately.

First, an experimental approach to the determination of natural frequencies of sandwich plates was made (Raville et al., 1967). Verification was made (Barkanov et al., 2005) of the numerical results of laminated composite and different sandwich panels with pulse and noncontact laser techniques. Static deformation and free vibration study was conducted on sandwich plates with variable thickness using both numerical and experimental holographic interferometry techniques (Chang et al., 2006). A theoretical and experimental study was conducted on the vibration and acoustical properties of sandwich composite materials (Zhuang, 2006). The vibration testing approach was used to identify the material constants (Lee et al., 2007) and damping characteristics (Berthelot et al., 2008; Maheri et al., 2008; Andena et al., 2012; Petrone et al., 2014; Yang et al., 2014; Abdi et al., 2014) with the help of experimentally obtained natural frequency values of laminated composite sandwich plates. Dynamic behavior of honeycomb sandwich plates was investigated considering the effect of cell size (Adarsh Kumar et al., 2015) and other parameters (Mondal et al., 2015; Rezvani et al., 2018; Prasad et al., 2018; Benjeddou et al., 2019; Arunkumar et al., 2020; Zhicheng et al., 2020) of the honeycomb core. Free vibration and transient dynamic analyses of functionally graded sandwich plates are investigated (Jun Liu et al., 2021) using the scaled boundary finite element method (SBFEM). Nu-

merical studies were presented (Vinayak et al., 2020) on skew composite laminated and sandwich plates under temperature and moisture concentration effects; the laminated sandwich plate is subjected to hygrothermal conditions (Aman et al., 2020) and composite sandwich plates with three-dimensional stress recovery (Su Bin Lee et al., 2020). A review on the analysis of laminated composite and sandwich structures under hygrothermal conditions addressing bending, vibration, buckling, post-buckling, transient, dynamic, and impact studies were made (Aman et al., 2019). An extensive survey on the analysis of sandwich FGM structures under different loading conditions, effects of porosities, hygrothermal loadings, and structures resting on elastic foundations was made (Aman et al., 2020).

A vast amount of literature was reported in detail on free vibration studies for laminated composite skew sandwich plates using analytical and numerical approaches. Limited literature was found related to detailed experimental work on the dynamic response of laminated composite sandwich skew plates. Literature on finite element solutions validated by the experimental method is very scarce. The present paper is an attempt to address this issue in some detail. Fast Fourier transform (FFT) analyzer is an instrument best suited for dynamic applications. In the current work, an FFT analyzer is used for the prediction of natural frequencies of sandwich skew plates.

2. TEST SPECIMEN PREPARATION

The sandwich skew panels were prepared using glass/epoxy laminated composites as face sheets and aluminum honeycomb as core materials. Aluminum honeycomb (Al-3003) panels are

used as the core with a cell size of 6.35 mm, foil thickness of 50 microns, and height of 6 mm. Laminated glass/epoxy reinforced polymer composites are used as face sheets. Unidirectional glass fibers for $[\pm 0^\circ/\text{Core}/\pm 0^\circ]$, $[\pm 90^\circ/\text{Core}/\pm 90^\circ]$ and bidirectional glass fibers for $[\pm 45^\circ/\text{Core}/\pm 45^\circ]$, $[(0^\circ/90^\circ)_s/\text{Core}/(0^\circ/90^\circ)_s]$ of 220 gsm and Lapox L-12 (Epoxy) along with Lapox K-6 hardener were used in fabricating the laminates. Continuous hand lay-up technique was employed for fabricating the sandwich plates, during which the excess resin was removed from the laminate by steel roller. The sandwich laminates are cured at room temperature for a period of 48 h placing weights over them. The test specimens were prepared with fiber weight percentage 50:50 according to relevant American Society for Testing and Materials ASTM standards.

The material constants for aluminum honeycomb core are $E_x = E_y = 0.4043 \text{ MPa}$, $E_z = 941.0802 \text{ MPa}$, $G_{xy} = 0.0546 \text{ MPa}$, $G_{yz} = 110.3007 \text{ MPa}$, $G_{xz} = 73.5338 \text{ MPa}$, $\rho = 48.37 \text{ kg/m}^3$, $\nu_x = 0.994 \approx 1$, and $\nu_y = \nu_z = 0.001$ and evaluated using the formulae presented (Rajkumar S., et al., 2014). ASTM Standard D3039/D3039M (2006) are imposed while evaluating the material properties of laminated glass/epoxy composite panels. The material constants E_1 and E_2 were evaluated experimentally on an average of three trials using Instron Universal Testing Machine at the Central Institute of Plastics Engineering and Technology (CIPET), Mysore, Karnataka, India. Strain gauges were used for calculating strains in longitudinal (along the loading) and transverse (right angles to the loading) directions. The ratio of measured strains concludes the value of Poisson's ratio ν_{12} within the elastic range. The average of three experimental trials was made during the determination of the value of Poisson's ratio ν_{12} . The standard equation of shear modulus presented in Jones(1999) was implemented in calculations and the material properties imposed are given in Tab. 1. The aspect ratio (AR) of the test specimens varied from 1.0 to 2.5 and the skew angle varied from 0° to 45° .

Tab. 1. Material constants of E-glass fiber.

Parameter	Mean	Standard	%Error
E_1 [GPa]	38.07	1.205	0.048
E_2 [GPa]	8.1	0.271	0.033
G_{12} [GPa]	3.05	0.095	0.039
ν_{12}	0.22	0.036	0.015
ρ_{12} [kg/m ³]	2,200		

3. EXPERIMENTAL SETUP

The arrangement for conducting the experimentation is shown in Fig. 1. The test specimen was held in the fixtures, imposing Clamped-Free-Clamped-Free and Clamped-Free-Free-Free edge conditions. A piezoelectric accelerometer sensor was placed at the center of the test specimen using glue and was connected to the FFT analyzer (signal conditioning and amplifying unit). An impact hammer was also connected to the FFT analyzer, dedicated to exciting the test specimen on selected points five times. For each test specimen, five trials were made and an average value was adopted.

Soon, the impact hammer excites the test specimen with a strike (impact); the accelerometer sensor captures the vibration signals and exports them to the FFT analyzer for further pro-

cessing. The FFT analyzer gives the output in terms of Frequency Response Function (FRF) using the pulse lab software. It was ensured that the strike of the impact hammer was normal to the test specimen's surface and no other sources of excitations (surrounding and floor vibrations nearby) were present other than the impact hammer.

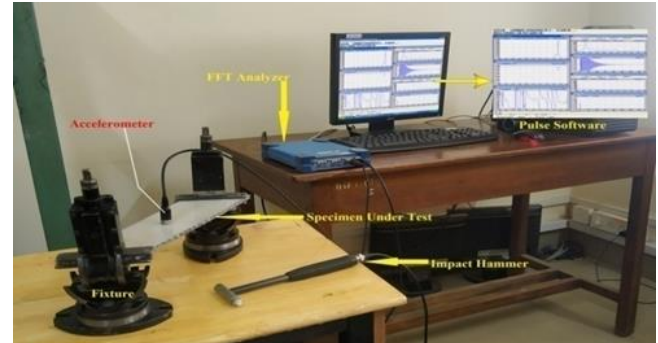


Fig. 1. Experimental Setup.

4. FINITE ELEMENT ANALYSIS

MSC/NASTRAN software package was employed for finite element analysis in obtaining the first three fundamental frequencies of skew sandwich plates. Eight-noded isoparametric curved shell elements, i.e., CQUAD8 and CQUAD4, are used in the analysis. A study (Pavan et al., 2020) disclosed that the CQUAD8 element produces more converging and accurate results than the CQUAD4 element. Accordingly, the CQUAD8 element was employed in the present study. To evaluate the real eigenvalues and eigenvectors, the Lanczos method of extraction was imposed for accurate results.

5. RESULTS AND DISCUSSION

The current work focuses on the influence of AR, skew angle, laminate stacking sequence, and edge conditions on the sandwich skew plates. To obtain higher natural frequencies of sandwich skew plates, considering the influence of t_c/t_f and a/h as discussed (Pavan et al., 2021) and minimizing the production cost, twenty-one layer, antisymmetric, angle-ply, and cross-ply laminated sandwich plates are designed and prepared. The thickness ratio of core to face sheet is kept constant in the whole study as $t_c/t_f=6$ and the ratio of length overall thickness a/h is varied to 12.5 ($a/b = 1.0$), 18.75 ($a/b = 1.5$), 25 ($a/b = 2.0$), and 31.25 ($a/b = 2.5$). Two types of edge conditions are implemented in the study i.e., Clamped-Free-Clamped-Free Edge Condition [C-F-C-F] and Clamped-Free-Free-Free Edge Condition [C-F-F-F]. The results from the current study are presented in non-dimensional form using Eq. (1).

$$K_f = 100 \omega a \sqrt{\left(\frac{\rho}{E_1}\right)_f} \tag{1}$$

First, three natural frequencies are extracted from experiments in non-dimensional form. The experimental values are compared with finite element values. The results are tabulated for the C-F-C-F edge condition in Tab. 2 and also graphically presented in Figs. 2–5. The mode shapes are presented in Tab. 3.

The results are tabulated for the C-F-F-F edge condition in Tab. 4 and also graphically presented in Figs. 6–9. The mode shapes are presented in Tab. 5.

Tab. 2. Natural frequencies of Clamped-Free-Clamped-Free laminated composite sandwich skew plates

Mo. No.	Skew Angle (α) 0°							
	Aspect Ratio (alb)							
	1.0		1.5		2.0		2.5	
	Exp	Num	Exp	Num	Exp	Num	Exp	Num
Angle ply $[(+0^\circ/-0^\circ)_s/\text{Core}/(+0^\circ/-0^\circ)_s]$								
1	7.334	7.408	5.539	5.594	4.372	4.415	3.579	3.623
2	9.783	9.892	9.156	9.262	8.759	8.886	8.482	8.628
3	26.069	26.439	22.973	23.283	20.185	20.572	17.862	18.239
Angle ply $[(+45^\circ/-45^\circ)_s/\text{Core}/(+45^\circ/-45^\circ)_s]$								
1	4.945	4.995	3.392	3.425	2.546	2.571	2.026	2.047
2	12.260	12.442	12.273	12.433	12.223	12.403	11.545	11.765
3	20.919	21.301	16.969	17.254	13.826	14.107	12.125	12.377
Angle ply $[(+90^\circ/-90^\circ)_s/\text{Core}/(+90^\circ/-90^\circ)_s]$								
1	4.082	4.123	3.183	3.214	2.139	2.160	1.721	1.738
2	8.569	8.678	8.288	8.390	7.989	8.086	7.837	7.945
3	19.468	19.764	16.398	16.699	12.944	12.376	10.077	10.259
Angle ply $[(0^\circ/90^\circ)_s/\text{Core}/(0^\circ/90^\circ)_s]$								
1	6.278	6.340	4.559	4.604	3.535	3.570	2.874	2.902
2	9.379	9.488	8.817	8.939	8.509	8.611	8.279	8.387
3	24.409	24.813	20.770	21.142	17.800	18.119	15.406	15.667
Skew Angle (α) 15°								
Angle ply $[(+0^\circ/-0^\circ)_s/\text{Core}/(+0^\circ/-0^\circ)_s]$								
1	21.863	22.083	20.491	20.693	18.155	18.338	16.270	16.431
2	23.488	23.777	23.040	23.301	21.665	21.931	20.979	21.226
3	36.405	36.956	41.862	42.451	38.500	39.087	35.901	36.428
Angle ply $[(+45^\circ/-45^\circ)_s/\text{Core}/(+45^\circ/-45^\circ)_s]$								
1	20.018	20.218	17.927	18.105	14.545	14.686	12.410	12.533
2	25.441	25.743	25.188	25.491	24.789	25.098	24.451	24.746
3	40.705	41.355	38.202	38.790	32.905	33.395	29.294	29.800
Angle ply $[(+90^\circ/-90^\circ)_s/\text{Core}/(+90^\circ/-90^\circ)_s]$								
1	18.285	18.461	15.445	15.598	12.193	12.313	10.215	10.315
2	21.183	21.438	20.218	20.463	18.650	18.868	18.013	18.221
3	38.597	39.159	34.982	35.533	29.253	29.663	25.479	25.859
Angle ply $[(0^\circ/90^\circ)_s/\text{Core}/(0^\circ/90^\circ)_s]$								
1	21.085	21.294	19.233	19.423	16.600	16.760	14.528	14.666
2	23.045	23.310	22.585	22.850	21.071	21.311	20.330	20.573
3	42.462	43.088	40.493	41.108	36.461	36.977	33.352	33.837
Skew Angle (α) 30°								
Angle ply $[(+0^\circ/-0^\circ)_s/\text{Core}/(+0^\circ/-0^\circ)_s]$								
1	23.634	23.867	21.080	21.287	18.290	18.470	15.668	15.823
2	25.448	25.747	24.739	25.020	24.381	24.657	24.150	24.440
3	39.264	39.849	43.512	44.141	40.348	40.924	36.453	36.981
Angle ply $[(+45^\circ/-45^\circ)_s/\text{Core}/(+45^\circ/-45^\circ)_s]$								
1	22.285	22.506	19.245	19.437	16.499	16.663	14.212	14.355
2	27.378	27.704	26.379	26.683	25.160	25.447	24.125	24.412
3	44.825	45.273	40.682	41.280	36.629	37.166	32.971	33.445
Angle ply $[(+90^\circ/-90^\circ)_s/\text{Core}/(+90^\circ/-90^\circ)_s]$								
1	20.342	20.545	16.410	16.576	13.315	13.446	11.012	11.122
2	23.465	23.738	22.200	22.459	21.485	21.714	20.930	21.165
3	42.851	43.474	37.288	37.821	32.200	32.680	27.998	28.403
Angle ply $[(0^\circ/90^\circ)_s/\text{Core}/(0^\circ/90^\circ)_s]$								
1	22.945	23.171	19.977	20.173	16.977	17.141	14.480	14.623
2	25.300	25.591	24.673	24.966	24.325	24.600	24.150	24.437
3	43.928	44.590	42.606	43.229	38.342	38.912	34.588	35.121
Skew Angle (α) 45°								
Angle ply $[(+0^\circ/-0^\circ)_s/\text{Core}/(+0^\circ/-0^\circ)_s]$								
1	27.555	27.829	23.435	23.670	19.112	19.300	13.043	13.172
2	29.865	30.221	29.968	30.330	30.210	30.551	26.945	27.262
3	44.752	45.393	47.852	48.553	44.097	44.786	34.248	34.745
Angle ply $[(+45^\circ/-45^\circ)_s/\text{Core}/(+45^\circ/-45^\circ)_s]$								
1	26.785	27.054	23.186	23.419	19.934	20.133	17.786	17.960
2	31.452	31.829	29.254	29.595	27.061	27.369	25.944	26.240
3	49.350	50.058	48.321	49.005	43.598	44.227	41.424	42.022
Angle ply $[(+90^\circ/-90^\circ)_s/\text{Core}/(+90^\circ/-90^\circ)_s]$								
1	24.688	24.930	19.634	19.829	15.678	15.833	16.158	16.319
2	28.255	28.571	27.559	27.862	27.185	27.492	31.001	31.374
3	48.711	49.425	44.562	45.197	38.088	38.638	39.955	40.556
Angle ply $[(0^\circ/90^\circ)_s/\text{Core}/(0^\circ/90^\circ)_s]$								
1	27.008	27.275	22.608	22.829	18.482	18.668	15.679	15.836
2	30.185	30.528	30.589	30.948	30.995	31.348	31.652	32.027
3	48.550	49.241	49.410	50.139	42.975	43.610	39.403	39.977

Tab. 3. Natural frequencies of Clamped-Free-Free-Free laminated composite sandwich skew plates

Mo. No.	Skew Angle (α) 0°							
	Aspect Ratio (alb)							
	1.0		1.5		2.0		2.5	
	Exp	Num	Exp	Num	Exp	Num	Exp	Num
Angle ply $[(+0^\circ/-0^\circ)_s/\text{Core}/(+0^\circ/-0^\circ)_s]$								
1	21.367	21.582	19.878	20.073	18.225	18.400	16.590	16.752
2	22.978	23.247	22.010	22.294	20.965	21.286	19.988	20.370
3	35.461	36.019	40.215	40.887	38.098	38.625	35.568	36.366
Angle ply $[(+45^\circ/-45^\circ)_s/\text{Core}/(+45^\circ/-45^\circ)_s]$								
1	19.336	19.526	16.445	16.609	13.870	14.010	11.789	11.905
2	24.832	25.164	24.810	25.126	24.729	25.042	24.681	24.969
3	39.419	39.997	35.436	36.001	31.550	32.107	28.063	28.530
Angle ply $[(+90^\circ/-90^\circ)_s/\text{Core}/(+90^\circ/-90^\circ)_s]$								
1	17.672	17.848	14.399	14.542	11.868	11.984	9.981	10.081
2	20.500	20.758	18.875	19.090	17.774	18.004	17.115	17.304
3	37.303	37.872	32.580	33.083	28.297	28.756	24.650	25.093
Angle ply $[(0^\circ/90^\circ)_s/\text{Core}/(0^\circ/90^\circ)_s]$								
1	20.728	20.934	18.624	18.810	16.518	16.684	14.631	14.774
2	22.532	22.826	21.249	21.528	20.091	20.339	19.142	19.378
3	41.579	42.210	38.541	39.293	35.829	36.377	33.050	33.537
Skew Angle (α) 15°								
Angle ply $[(+0^\circ/-0^\circ)_s/\text{Core}/(+0^\circ/-0^\circ)_s]$								
1	21.863	22.083	20.491	20.693	18.155	18.338	16.270	16.431
2	23.488	23.777	23.040	23.301	21.665	21.931	20.979	21.226
3	36.405	36.956	41.862	42.451	38.500	39.087	35.901	36.428
Angle ply $[(+45^\circ/-45^\circ)_s/\text{Core}/(+45^\circ/-45^\circ)_s]$								
1	20.018	20.218	17.927	18.105	14.545	14.686	12.410	12.533
2	25.441	25.743	25.188	25.491	24.789	25.098	24.451	24.746
3	40.705	41.355	38.202	38.790	32.905	33.395	29.294	29.800
Angle ply $[(+90^\circ/-90^\circ)_s/\text{Core}/(+90^\circ/-90^\circ)_s]$								
1	18.285	18.461	15.445	15.598	12.193	12.313	10.215	10.315
2	21.183	21.438	20.218	20.463	18.650	18.868	18.013	18.221
3	38.597	39.159	34.982	35.533	29.253	29.663	25.479	25.859
Angle ply $[(0^\circ/90^\circ)_s/\text{Core}/(0^\circ/90^\circ)_s]$								
1	21.085	21.294	19.233	19.423	16.600	16.760	14.528	14.666
2	23.045	23.310	22.585	22.850	21.071	21.311	20.330	20.573
3	42.462	43.088	40.493	41.108	36.461	36.977	33.352	33.837
Skew Angle (α) 30°								
Angle ply $[(+0^\circ/-0^\circ)_s/\text{Core}/(+0^\circ/-0^\circ)_s]$								
1	23.634	23.867	21.080	21.287	18.290	18.470	15.668	15.823
2	25.448	25.747	24.739	25.020	24.381	24.657	24.150	24.440
3	39.264	39.849	43.512	44.141	40.348	40.924	36.453	36.981
Angle ply $[(+45^\circ/-45^\circ)_s/\text{Core}/(+45^\circ/-45^\circ)_s]$								
1	22.285	22.506	19.245	19.437	16.499	16.663	14.212	14.355
2	27.378	27.704	26.379	26.683	25.160	25.447	24.125	24.412
3	44.825	45.273	40.682	41.280	36.629	37.166	32.971	33.445
Angle ply $[(+90^\circ/-90^\circ)_s/\text{Core}/(+90^\circ/-90^\circ)_s]$								
1	20.342	20.545	16.410	16.576	13.315	13.446	11.012	11.122
2	23.465	23.738	22.200	22.459	21.485	21.714	20.930	21.165
3	42.851	43.474	37.288	37.821	32.200	32.680	27.998	28.403
Angle ply $[(0^\circ/90^\circ)_s/\text{Core}/(0^\circ/90^\circ)_s]$								
1	22.945	23.171	19.977	20.173	16.977	17.141	14.480	14.623
2	25.300	25.591	24.673	24.966	24.325	24.600	24.150	24.437
3	43.928	44.590	42.606	43.229	38.342	38.912	34.588	35.121
Skew Angle (α) 45°								
Angle ply $[(+0^\circ/-0^\circ)_s/\text{Core}/(+0^\circ/-0^\circ)_s]$								
1	27.555	27.829	23.435	23.670	19.112	19.300	13.043	13.172
2	29.865	30.221	29.968	30.330	30.210	30.551	26.945	27.262
3	44.752	45.393	47.852	48.553	44.097	44.786	34.248	34.745
Angle ply $[(+45^\circ/-45^\circ)_s/\text{Core}/(+45^\circ/-45^\circ)_s]$								
1	26.785	27.054	23.186	23.419	19.934	20.133	17.786	17.960
2	31.452	31.829	29.254					

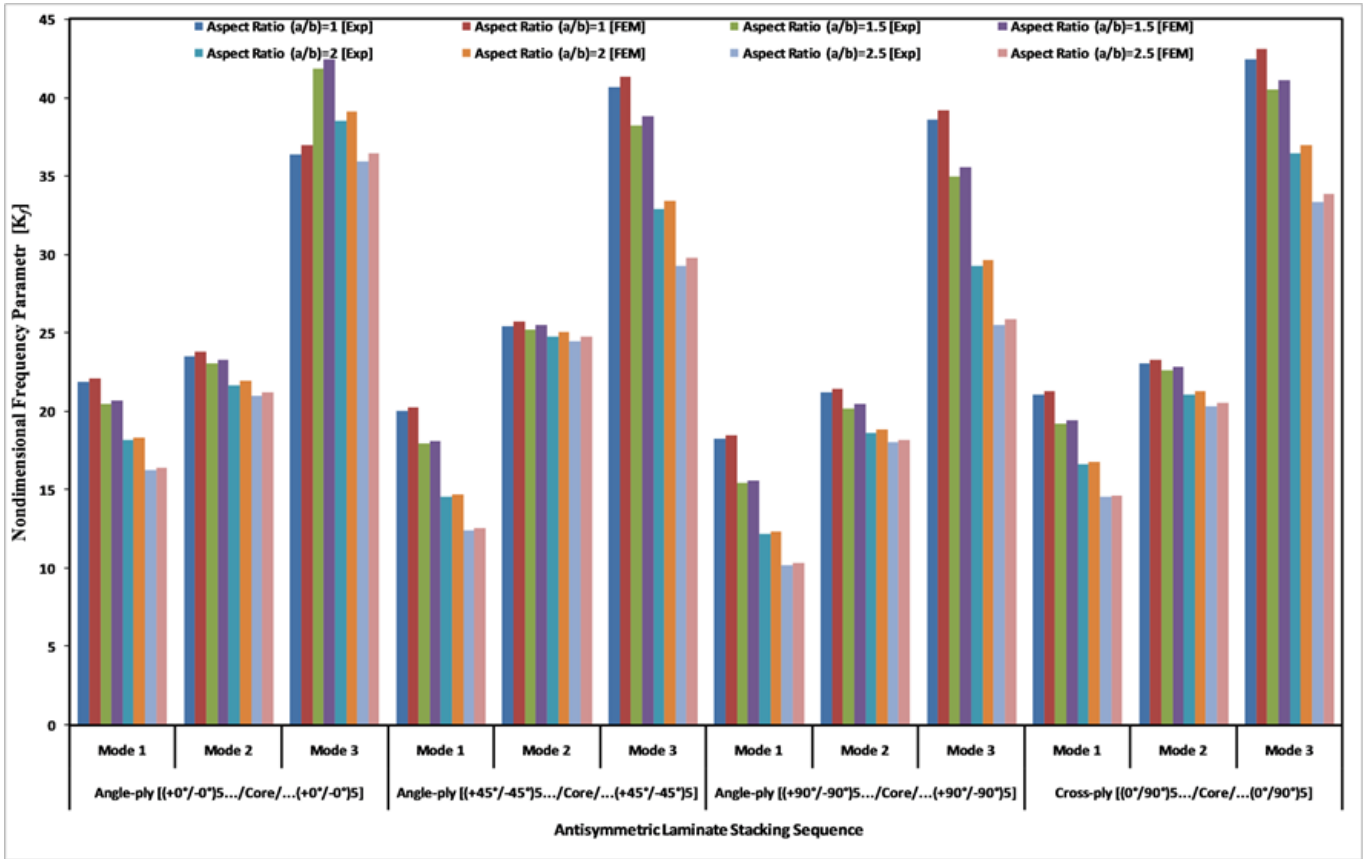


Fig. 2. Variation of K_f with AR (a/b) for C-F-C laminated composite sandwich skew plates with skew angle $\alpha = 0^\circ$.

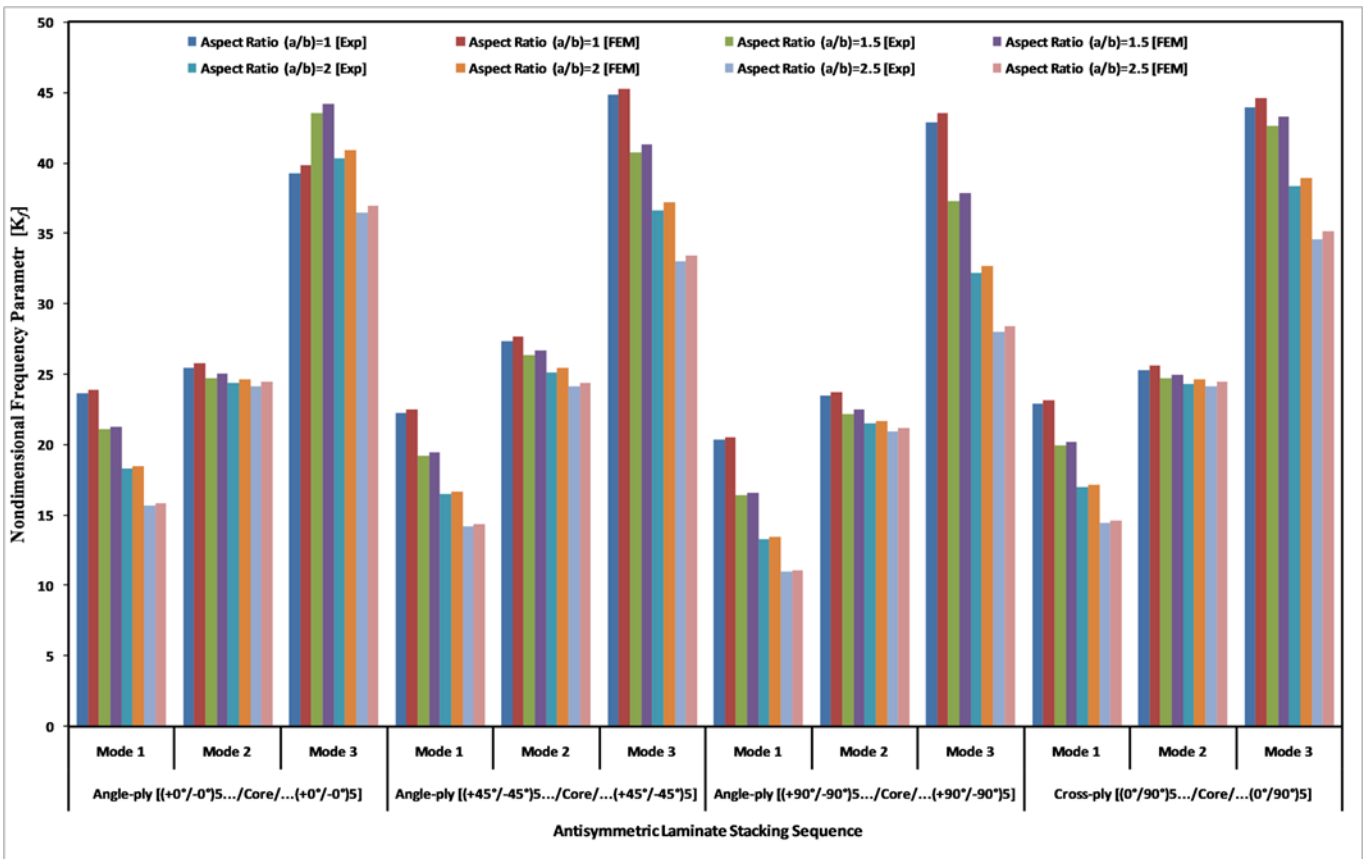


Fig. 3. Variation of K_f with AR (a/b) for C-F-C laminated composite sandwich skew plates with skew angle $\alpha = 15^\circ$.

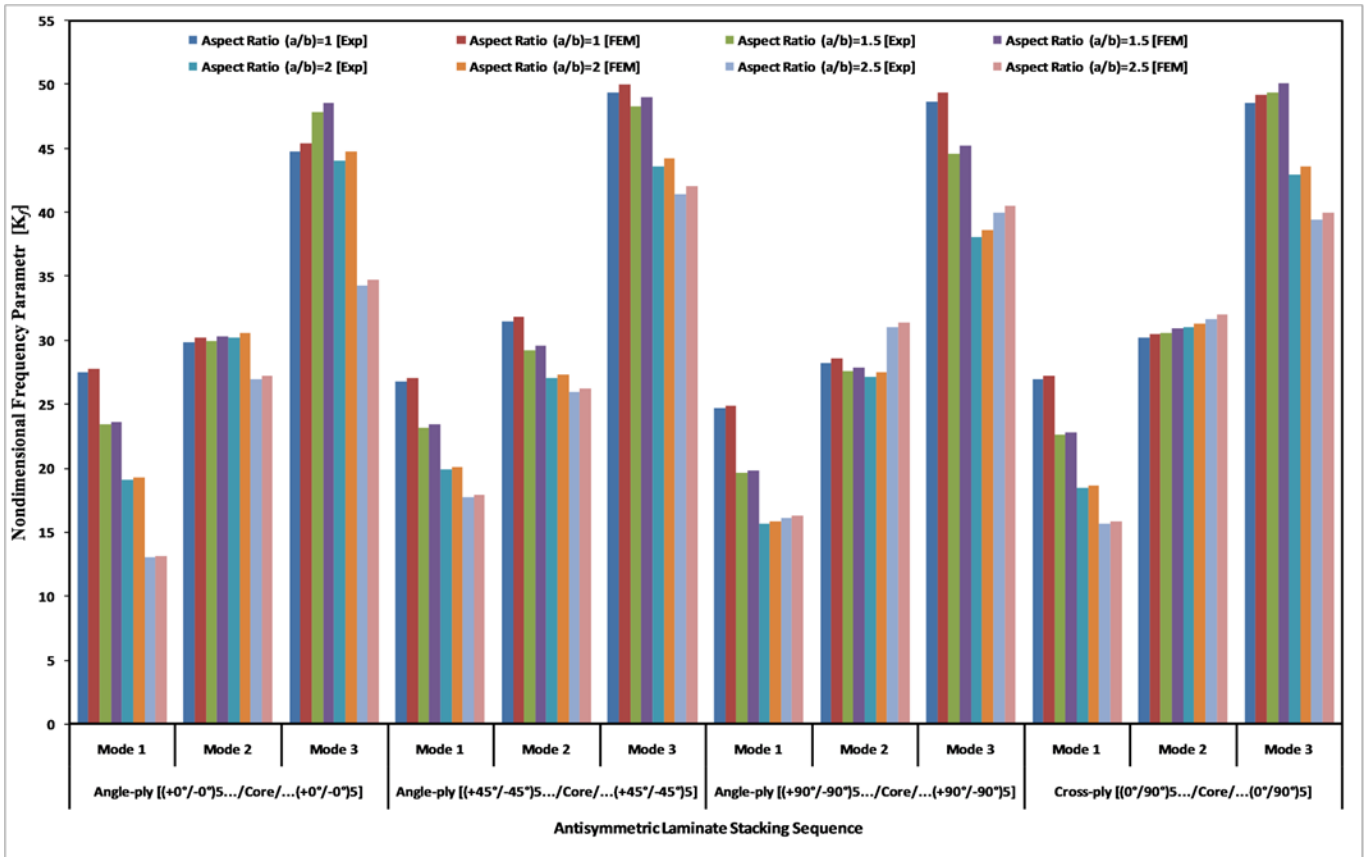


Fig. 4. Variation of K_f with AR (a/b) for C-F-C-F laminated composite sandwich skew plates with skew angle $\alpha = 30^\circ$.

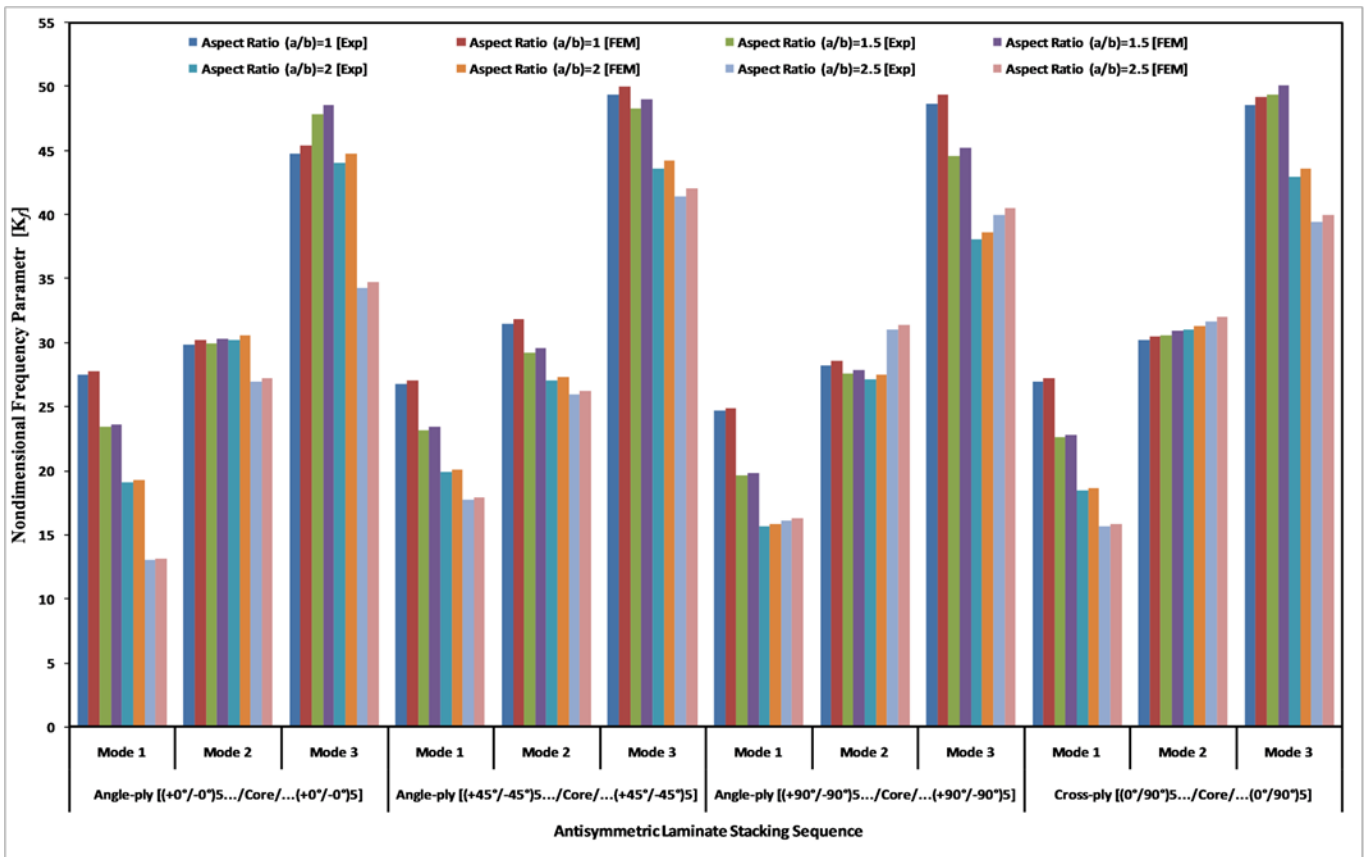


Fig. 5. Variation of K_f with AR (a/b) for C-F-C-F laminated composite sandwich skew plates with skew angle $\alpha = 45^\circ$.

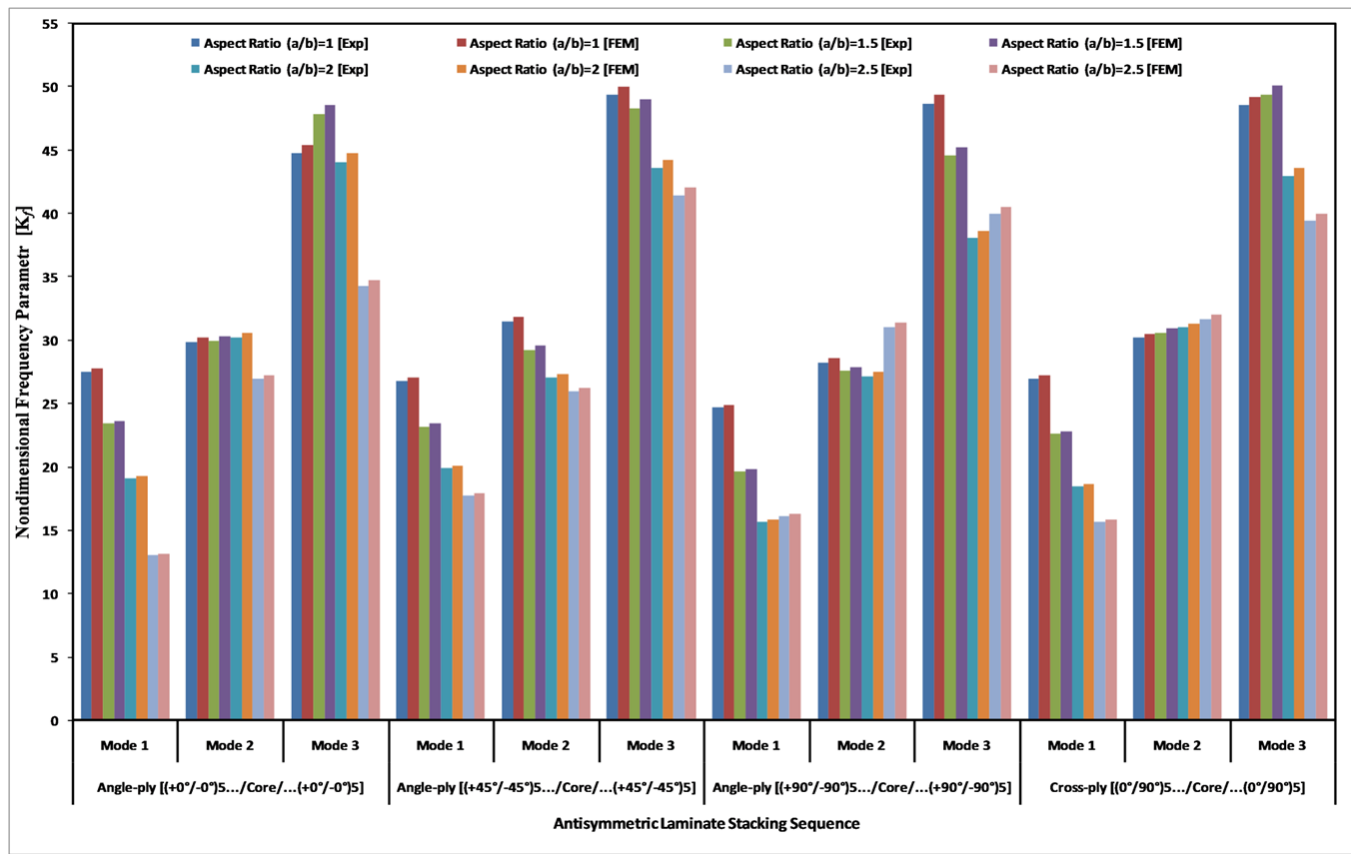


Fig. 6. Variation of K_f with AR (a/b) for C-F-F laminated composite sandwich skew plates with skew angle $\alpha = 0^\circ$.

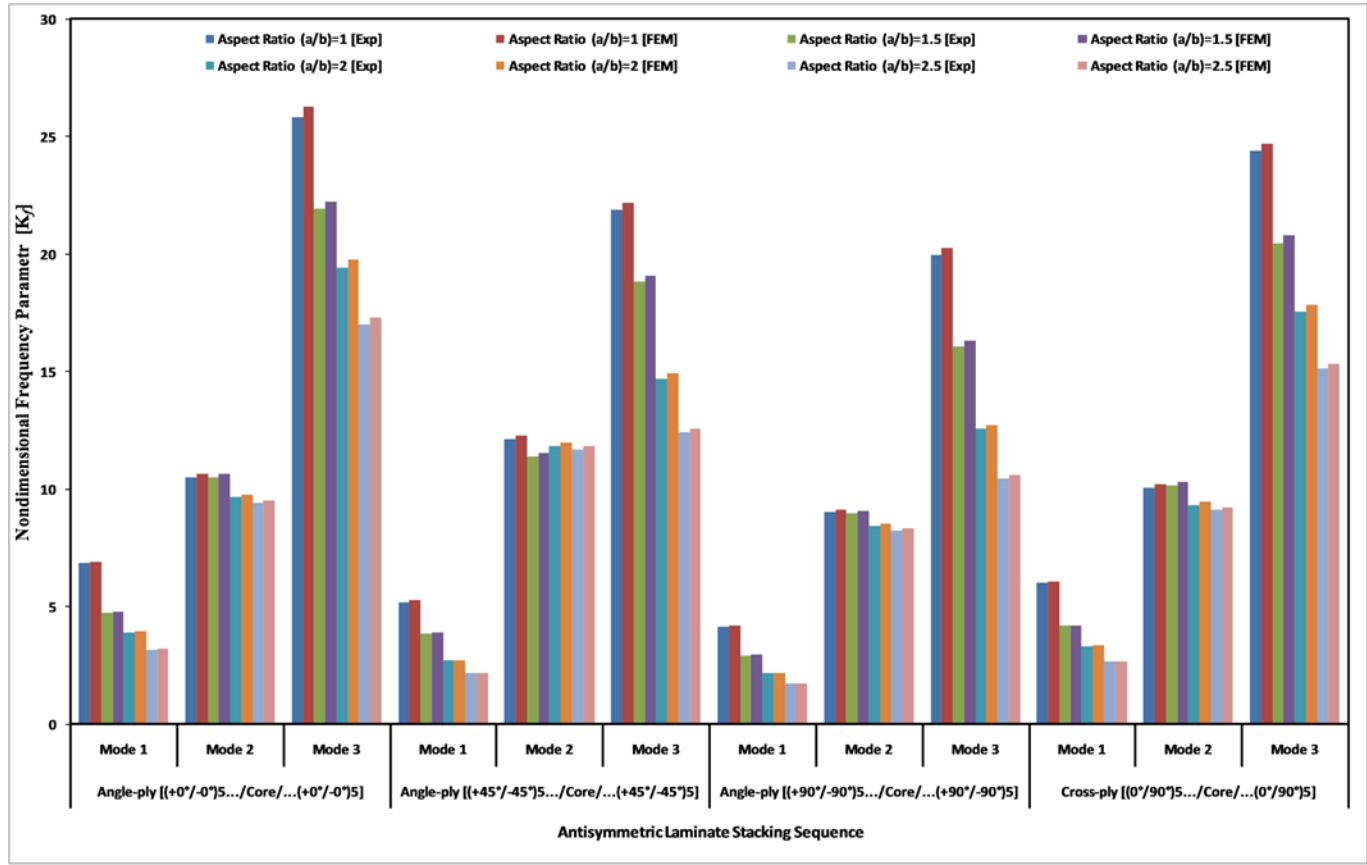


Fig. 7. Variation of K_f with AR (a/b) for C-F-F laminated composite sandwich skew plates with skew angle $\alpha = 15^\circ$.

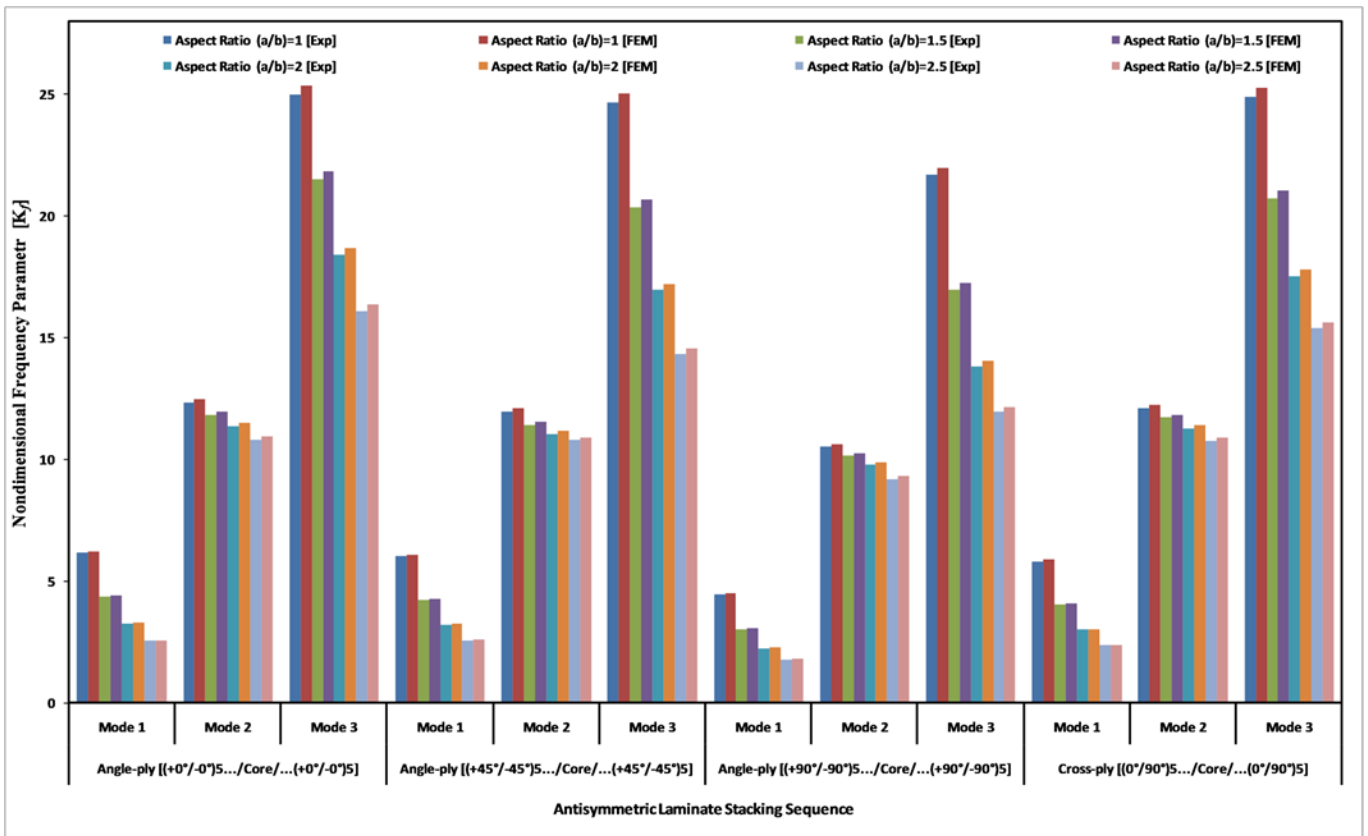


Fig. 8. Variation of K_f with AR (a/b) for C-F-F laminated composite sandwich skew plates with skew angle $\alpha = 30^\circ$.

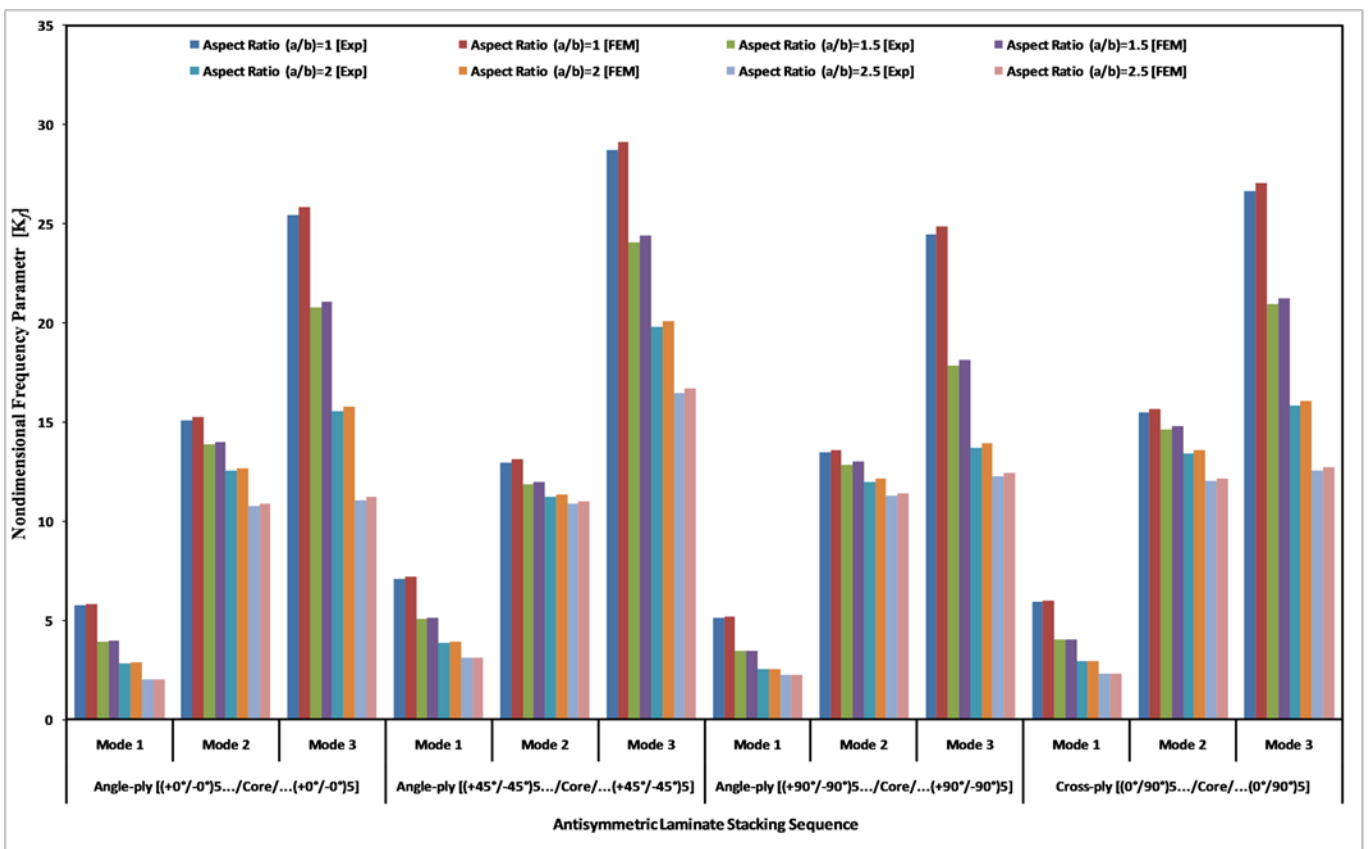
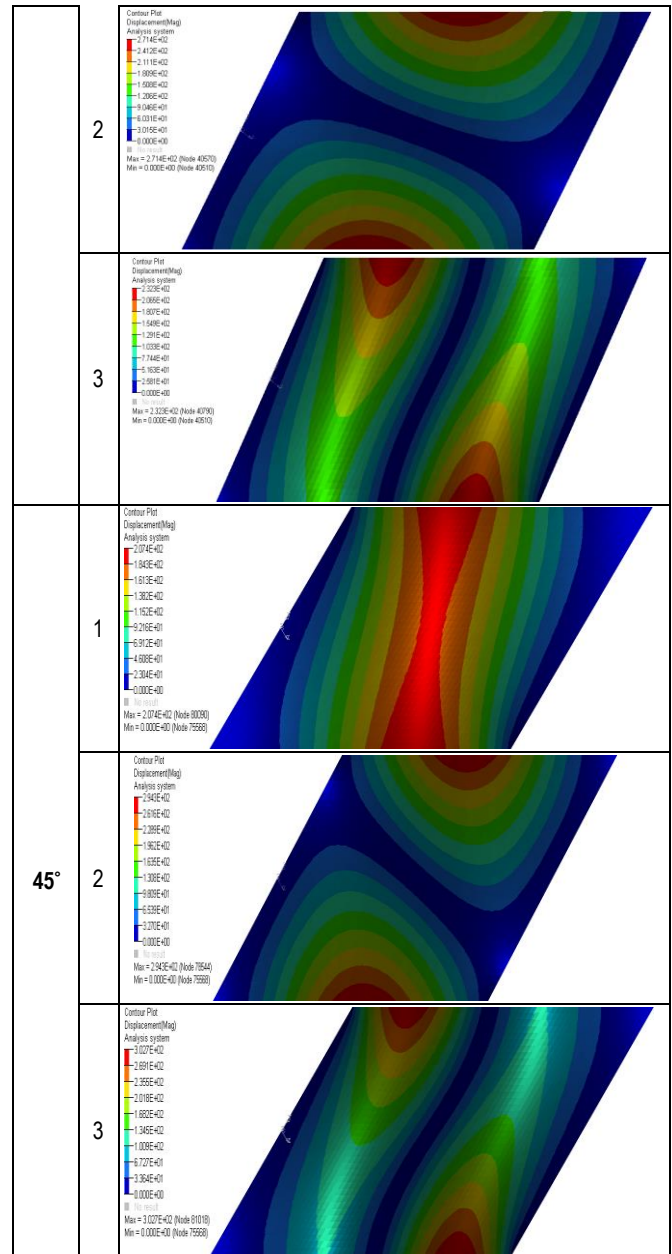


Fig. 9. Variation of K_f with AR (a/b) for C-F-F laminated composite sandwich skew plates with skew angle $\alpha = 45^\circ$.

Tab. 4. Mode shapes for C-F-C-F laminated composite sandwich skew plates ($a/b = 1.5$, $NL = 21$, antisymmetric cross-ply laminate)

Skew Angle	Mode Shapes [NL=21 AR=1.5]	
0°	1	
	2	
	3	
15°	1	
	2	
	3	
30°	1	



Figs. 2–5 clearly explain that:

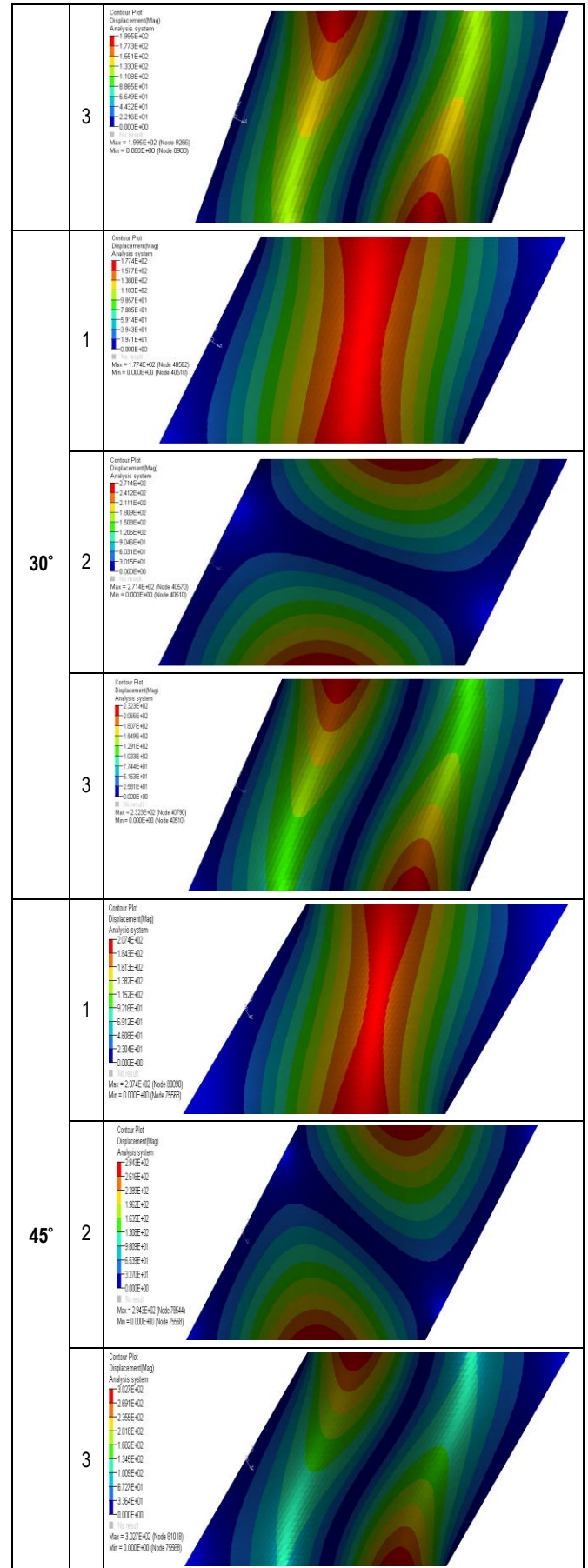
- For laminate stacking sequence angle ply $[(\pm\theta)_s/\text{Core}/(\pm\theta)_s]$, the first natural frequency decrease with an increase in the AR. AR is the ratio of length to width, where width is kept constant and only length is varied. As the AR increases, the length of the plate increases, which makes the plate less stiff, leading to a decrease in the natural frequency. For the second natural frequency, it decreases with an increase in AR except for skew = 45°. For skew 0° to 45°, as the skew angle increases, the width of the plate decreases due to the skew, and also the overall area of the plate goes on reducing. This makes the plate lighter and at the same time stiffer. For the third natural frequency, it increases from AR = 1 to AR = 1.5, then it decreases, it is due to the combined effect of fiber orientation, mode shape, mass density, and stiffness of the plate.
- For angle ply $[(\pm 45^\circ)_s/\text{Core}/(\pm 45^\circ)_s]$ the first and third natural frequencies decrease with an increase in the AR for a given skew angle. However, in the second natural frequency, variation is negligible for skew = 0°; it is considerable for other

skew angles. Here the plate produces more stiffness due to the fiber orientation and it overshadows the effect of plate stiffness due to the change in the AR compared to other skew angles.

- In angle ply $[(\pm 90^\circ)_s/\text{Core}/(\pm 90^\circ)_s]$ stacking sequence, for all three frequencies, the K_f value decreases as the increase in the AR except skew = 45° . For skew = 45° the K_f value decreases from AR = 1 to AR = 1.5 and then it increases. It is exactly opposite as in the case of angle ply $[(\pm 0^\circ)_s/\text{Core}/(\pm 0^\circ)_s]$.
- The K_f value decreases with an increase in the AR in all the three modes of cross-ply $[(0^\circ/90^\circ)_s/\text{Core}/(0^\circ/90^\circ)_s]$ stacking sequence from skew = 0° to 30° . The only exception is for skew = 45° in which the second natural frequency goes on increasing as the AR increased. The third natural frequency first increases from AR = 1 to AR = 1.5 and then decreases.

Tab. 5. Mode shapes for C-F-F laminated composite sandwich skew plates ($a/b = 1.5$, $NL = 21$, antisymmetric cross-ply laminate)

Skew Angle	Mode Shapes [NL=21, AR=1.5]
1	<p>Contour Plot (Displacement(Mag)) Analysis system Max = 1.462E+02 (Node 4522) Min = 0.000E+00 (Node 4492)</p>
	<p>Contour Plot (Displacement(Mag)) Analysis system Max = 2.413E+02 (Node 4521) Min = 0.000E+00 (Node 4492)</p>
	<p>Contour Plot (Displacement(Mag)) Analysis system Max = 2.605E+02 (Node 4548) Min = 0.000E+00 (Node 4492)</p>
15°	<p>Contour Plot (Displacement(Mag)) Analysis system Max = 1.639E+02 (Node 5245) Min = 0.000E+00 (Node 5825)</p>
	<p>Contour Plot (Displacement(Mag)) Analysis system Max = 2.581E+02 (Node 5043) Min = 0.000E+00 (Node 5853)</p>



And from Figs. 6–9, the following is observed:



- With skew = 15° for cross-ply $[(0^\circ/90^\circ)_5/\text{Core}/(0^\circ/90^\circ)_5]$ and Angle ply $[(\pm 45^\circ)_5/\text{Core}/(\pm 45^\circ)_5]$, the second natural frequency decreases then it increases and it increases then it decreases is the only change.
- The K_f value decreases in the order of laminate stacking sequence: angle ply $[(\pm 0^\circ)_5/\text{Core}/(\pm 0^\circ)_5]$, cross-ply $[(0^\circ/90^\circ)_5/\text{Core}/(0^\circ/90^\circ)_5]$, angle ply $[(\pm 45^\circ)_5/\text{Core}/(\pm 45^\circ)_5]$ angle ply $[(\pm 90^\circ)_5/\text{Core}/(\pm 90^\circ)_5]$.
- For a given value of AR, as the skew angle is increased, the value of K_f increases considerably (Pavan K., et al., 2021).
- The values of K_f are higher for C-F-C-F than C-F-F-F edge conditions for any given AR and skew angle.
- The experimental values in the form of the non-dimensional frequency coefficient K_f are very close to accurate and promising to those of the finite element solution.

6. CONCLUSION

Free vibration investigation was made on laminated sandwich skew plates adopting both experimental and finite element methods. Glass epoxy laminated composites are used as face sheets and aluminum honeycomb (Al3003) is used as the core in the current study. Two types of edge conditions were used. i.e., C-F-C-F and C-F-F-F. The experimentally obtained results were then validated by finite element values, and the experimental values are promising and close to the finite element values. Influences of various parameters, for instance, skew angle, AR, laminate stacking sequence, and edge conditions are studied. The thickness ratio of core to face sheet $t_c/t_f = 6$ was kept constant all through the study. As the AR increases for any skew angle, the K_f value decreases irrespective of the edge condition. When the AR increases, the length of the sandwich plate also increases. This reduces the stiffness of the sandwich skew plate. The skew angle plays a major role in the dynamic response of the sandwich skew plate. When the skew angle is increased, the K_f value increases for all ARs. The fiber orientation of the lamina plays a significant role in deciding the vibration response of the sandwich skew plates. When the fiber angle is 0° i.e., the fiber is placed parallel to the length of the plate, the plate produces higher natural frequency due to more stiffness in the longitudinal direction. In addition, the lowest natural frequency is observed when the fiber angle is 90° i.e., the fiber angle is perpendicular to the length of the plate. The natural frequencies for the other laminate stacking sequences lie in between these two extreme values. The sandwich skew plates with C-F-C-F edge conditions produce a higher natural frequency than plates with C-F-F-F edge conditions.

REFERENCES

1. **Abdi B., Azwan S., Ayob A., Rahman R.A., Abdullah R.A.** (2014), Experimental Investigation on Free Vibration of Foam-Core Sandwich Plate with and without Circular Polymer Columns, *Advanced Materials Research*, 845, 297-301.
2. **Adarsh K., Ramesh S.S.** (2015), Modal Analysis and Testing of Honeycomb Sandwich Composites, Topics in Modal Analysis, Volume 10, *Proceedings of the 33rd IMAC, A Conference and Exposition on Structural Dynamics*, Springer International Publishing, 237-241.
3. **Aman G., Chalak H.D.** (2019), A review on analysis of laminated composite and sandwich structures under hygrothermal conditions, *Thin-Walled Structures*, 142, <https://doi.org/10.1016/j.tws.2019.05.005>.
4. **Aman G., Chalak H.D.** (2020), Analysis of non-skew and skew laminated composite and sandwich plates under hygro-thermo mechanical conditions including transverse stress variations, *Journal of Sandwich Structures and Materials*, DOI: 10.1177/1099636220932782.
5. **Aman G., Mohamed O.B., Chalak H.D., Anupam C.** (2020), A review of the analysis of sandwich FGM structures, *Composite Structures*, <https://doi.org/10.1016/j.compstruct.2020.113427>.
6. **Andena L., Manconi E., Manzoni S., Moschini S., Vanali M.** (2012), Experimental tests and numerical modeling of a sandwich panel, *25th International Conference on Noise and Vibration engineering (ISMA2012), 4th International Conference on Uncertainty in Structural Dynamics (USD2012), Leuven*.
7. **Arun Kumar M.P., Jeyaraj P., Ganga Dharan K.V., Surya Narayana Reddy C.V.** (2020), Numerical and experimental study on dynamic characteristics of honeycomb core sandwich panel from equivalent 2D model, *Sadhana*, 45, 206, 1-6.
8. **Barkanov E., Chate A., Skukis E., Täger O., Kolsters H.** (2005), Finite element and experimental vibration analysis of viscoelastic composite structures, *Computational Methods and Experimental Measurements XII*, 41, 527-537.
9. **Benjeddou A., Guerich M.** (2019), Free vibration of actual aircraft and spacecraft hexagonal honeycomb sandwich panels: A practical detailed FE approach, *Advances in Aircraft and Spacecraft Science*, 6(2), 169-187.
10. **Berthelot J.M., Assarar M., Sefrani Y., Mahi A.E.** (2008), Damping analysis of composite materials and structures, *Composite Structures*, 85, 189-204.
11. **Chang J.S., Chen H.C., Lin H.T.** (2006), Numerical and experimental studies on aluminum sandwich plates of variable thickness, *Journal of the Chinese Institute of Engineers*, 29(5), 851-862.
12. **Jones R.M.** (1999), *Mechanics of Composite Materials*, Taylor and Francis.
13. **Jun L., Congkuan H., Wenbin Y., Fan Y., Gao L.** (2021), Free vibration and transient dynamic response of functionally graded sandwich plates with power-law nonhomogeneity by the scaled boundary finite element method, *Computer Methods in Applied Mechanics and Engineering*, 376, <https://doi.org/10.1016/j.cma.2021.113665>.
14. **Lee C.R., Kam T.Y., Sun S.J.** (2007), Free-Vibration Analysis and Material Constants Identification of Laminated Composite Sandwich Plates, *Journal of Engineering Mechanics*, 133 (8), 874-886.
15. **Maheri M.R., Adams R.D., Hugon J.** (2008), Vibration damping in sandwich panels, *Journal of Material Science*, 43, 6604-6618.
16. **Mondal S., Patra A.K., Chakraborty S., Mitra N.** (2015), Dynamic performance of sandwich composite plates with circular hole/cut-out: A mixed experimental-numerical study, *Composite Structures*, 131, 479-489.
17. **Pavan K., Srinivasa C.V.** (2020), Free vibration studies on skew sandwich plates by FEM, *IOP Conference Series: Materials Science and Engineering*, 925, 012024, Doi:10.1088/1757-899X/925/1/012024.
18. **Pavan K., Srinivasa C.V.** (2020), On buckling and free vibration studies of sandwich plates and cylindrical shells: A review, *Journal of thermoplastic composite materials*, 33 (5), 1-51.
19. **Pavan K.D., Srinivasa C.V.** (2021), On free vibration of laminated skew sandwich plates: A Finite element analysis, *Nonlinear Engineering*, <https://doi.org/10.1515/nleng-2021-0006>, 2021.
20. **Petrone G., Alessandro V.D., Franco F., Mace B., De Rosa S.** (2014), Modal characterisation of recyclable foam sandwich panels, *Composite Structures*, 113, 362-368.
21. **Prasad E.V., Sahu S.K.** (2018), Vibration Analysis of Woven Fiber Metal Laminated Plates — Experimental and Numerical Studies,

- International Journal of Structural Stability and Dynamics*, 18, 1850144-1-23.
22. **Rajkumar S., Ravindran D., Ramesh S.S., Raghupathy V.P.** (2014), Evaluation of elastic constants of A3003 honeycomb core with varying hexagonal cell geometries through finite element approach, *Proceedings of the Institution of Mechanical Engineers Part C Journal of Mechanical Engineering Science*, 203-210, DOI: 10.1177/0954406213510491.
 23. **Raville M.E., Ueng C.E.S.** (1967), Determination of Natural Frequencies of Vibration of a Sandwich Plate, *Experimental Mechanics*, 7, 490-493, <https://doi.org/10.1007/BF02326265>.
 24. **Rezvani S.S., Kiasat M.S.** (2018), Analytical and experimental investigation on the free vibration of a floating composite sandwich plate having viscoelastic core, *Archives of Civil and Mechanical Engineering*, 18, 1241-1258.
 25. **Su Bin L., Chang-Yong L., Dewey H.H.** (2020), On the mechanics of composite sandwich plates with three-dimensional stress recovery, *International Journal of Engineering Science*, 157.
 26. **Vinayak K., Balaji K., Kattimani S.C.** (2020), Effect of temperature and moisture on free vibration characteristics of skew laminated hybrid composite and sandwich plates, *Thin-Walled Structures*, 157, <https://doi.org/10.1016/j.tws.2020.107113>.
 27. **Yang J.S., Xiong J., Ma L., Wu L.Z.** (2014), Vibration and damping performances of carbon fiber composite pyramidal truss sandwich panels embedded with viscoelastic layers, *ECCM16 - 16TH European conference on composite materials*, Seville, Spain, 22-26.
 28. **Zhicheng H., Xingguo W., Nanxing W., Fulei C., Jing L.** (2020), The Finite Element Modeling and Experimental Study of Sandwich Plates with Frequency-Dependent Viscoelastic Material Model, *Materials*, 13, 2296, Doi:10.3390/ma13102296.
 29. **Zhuang L.** (2006), *Vibration and acoustical properties of sandwich composite*, Degree of Doctor of Philosophy, Auburn University, Auburn, Alabama.
- Acknowledgments: The authors would like to express gratitude to the Principal and Management of GM Institute of Technology, India, for their inspiration and support provided.
- Dhotre Pavan Kumar:  <https://orcid.org/0000-0002-7900-755X>
- Chikkol V. Srinivasa:  <https://orcid.org/0000-0002-9794-3886>

BACKLASH FAULT SUPPRESSION USING LQ OPTIMAL CONTROL BASED RST CONTROLLERS IN WIND TURBINE SYSTEMS USING BOND GRAPHS AND MATLAB/SIMULINK

Mohamed ARAB^{*}, Abederezak LACHOURI^{*}, Mohamed KERIKEB^{*}, Lamine MEHENNAOUI^{*}, Faouzi BOUCHARB^{*}

^{*}Automatic Laboratory, Electrical Engineering Departement, Faculty of Technology, 20 August 1955 University of Skikda, Algeria

mohelectron@yahoo.fr, alachouri@yahoo.fr, mohamedkerikeb@yahoo.com, me_lamine@yahoo.fr, bouchareb.fauzi@gmail.com

received 19 June 2020, revised 1 July 2021, accepted 5 July 2021

Abstract: The presence of backlash in wind turbines is a source of limitations as it introduces nonlinearities that reduce their efficiency in speed/torque control which affect the performance of the power quality. Because of production tolerances during rotation, the teeth contact is lost for a small angle; until it is re-established, it produces a backlash phenomenon. The desire to eliminate this phenomenon is often hard to realise due to the nonlinear dynamic behaviour, which arises with the presence of backlash fault in a system. Therefore, the goal of this study is to develop an LQ optimal control structure in a form of an R-S-T controller in order to reduce the disturbing torque transmitted inside the dead zone of a gearbox in the wind turbine system. The actual system is also developed to be used as a demonstration model at lectures or presentations. The efficacy of the proposed control is illustrated via simulations.

Key words: modeling, bond graph, wind turbine, backlash, quadratic linear control, RST controller

1. INTRODUCTION

Generally, the main problem with wind turbine installations is the quality of energy production, which is usually caused by voltage fluctuations measured from the generators. For this purpose, the wind turbines driven by stochastic wind disturbances, gravitational and gyroscopic loads, are perceived as fluctuating power sources (Tomonobu, 2018). Gearbox failure has been the main cause of many reliability defects for modern wind energy sources. The main gearbox elements subject of this failure are, mesh stiffness, bearing stiffness, damping and gear backlash.

Performance of gear transmission is bound to put forward higher requirements. In actual use, about 50% of wind generator fault occurs in the gear transmission system (Zhao et al., 2015). When the gear is at high speed, factors such as stiffness, processing and assembling error are prone to vibration, thus affecting the transmission system accuracy and stability, it even breaks the teeth destroying the machine and causes other major accidents (Zhao et al., 2015). The wind gust could result in unbalanced aerodynamic loads in the rotor, which leads to the non-torque bending moments that are fed into the gearbox. Large driving torques may lead to contact loss of the missing gear teeth. The bending moments applied on the main shaft could cause the loads on gear teeth to change dramatically.

Backlash or clearance exists in any gear system, either by design or due to manufacturing errors or wear. This backlash may induce vibro-impacts, leading to excessive vibration, noise, and dynamic loads (Amir et al., 2014). The clearance between gear pair teeth, or backlash, is considered to be a potential source of vibration in some research papers (Zhenxing et al., 2017; Ragheb and Ragheb, 2010). The influence of clearance occurs mainly in

cases when the torque's mean value is near zero or torque reversals are present in the system (Amir et al., 2014).

In the literature, many solutions have been developed to overcome backlash faults and reduce the impact on the life of the drivetrain in modern wind turbine systems (Yangshou et al., 2019). Control of systems with backlash is complicated for high-precision requirements and hence generally a mechanical solution with an anti-backlash arrangement is provided, introducing spring-loaded split gear assemblies, precision gear, inertias or other devices for attenuation. All of these solutions are satisfactory, but they aggravate modelling and system analysis which reduce the control accuracy. In this context, the control of systems with backlash has been the subject of study since the 1940s (Marton and Lantos, 2009; Yonezawa et al., 2019). The main analytical tool to describe the backlash has been the describing function technique. To anticipate these phenomena, there exist mechanical and automatic methods (Ruderman et al., 2018). Some control solutions have been proposed, like in Čulina (2011), Odgaard et al. (2013) and Mordian (2014), where they have studied the influence and the partial compensation of simultaneously acting backlash and coulomb friction in an elastic two-mass system with a speed and position controller.

Recker & al and Tao & Kokotovic have worked on the adaptive control of a system with backlash. On this subject, different mathematical models are proposed: Tao & Kokotovic have modelled the inverse backlash model based on a hysteresis cycle (Gang and Kokotović, 1992). Cadiou & M'Sirdi have developed a differentiable model based on the dead zone characteristics (Cadiou and M'Sirdi, 1995). An approximate inverse of the backlash has often been suggested as a backlash remedy, both in a non-adaptive and an adaptive setting. Modern digital controllers have been developed, such as, state space-

based controllers like a linear quadratic regulator (LQR) (Ruderman et al., 2008), a model reference adaptive controller (MRAC) (Guo-Qiang et al., 2013) and an applied heuristic based fuzzy control (Guo-Qiang et al., 2013; Qikun et al., 2019). The study of the impact of gear train backlash on performance of DFIG wind turbine system (Ganesh et al., 2018), partial offline fuzzy model-predictive pitch controller for large-scale wind-turbines model (Mohamed et al., 2020). The robust control is based on fractional- order controllers (et al., 2020). Another technique based on developing an estimator to periodically estimate the size of backlash in the gear of a wind turbine is established. Lagerberg and Egardt (2007) proposed a switched Kalman filter for estimating the backlash size in automobiles. Makosi et. al. (2017) developed an extended Kalman filter for automotive application by estimating the sum of the half shaft torques, the stiffness and damping of the drive shafts, and the size of the driveline backlash.

The purpose of this paper is to describe the characteristics of backlash, to investigate the drawbacks backlash imposes on the dynamics of wind energy conversion systems (WECSs) that contain backlash in a gearbox and to inquire possibilities of how to neutralise the effects of backlash and eliminate electrical pollution. This study was accomplished according this strategy:

- Using the bond graph as a modelling methodology, the dynamics of WECSs that contain backlash in a gearbox, which can be considered as a well tool, adapted for the analysis of these systems, is investigated. This study illustrates the importance of using a simplified bond graph model properly, which accounts for the reduction in simulation time in comparison with the available software package. The model was developed and simulations were obtained using the 20 sim software package environment.
- The linear quadratic (LQ) optimal control structure in the form of an RST controller for gearbox system's backlash vibration suppression in WECSs for an input-output approach of the optimal control is implemented. This structure has two degrees of freedom: the digital filters R and S are designed in order to achieve the desired regulation performances and the

digital filter T is designed afterwards in order to achieve the desired tracking performances. In this context, it is considered that the optimisation is achieved by means of a rotational speedtracking loop. The model was developed and simulations have been carried out using MATLAB/Simulink.

This article is organised as follows: let's start with a brief introduction and then a modelling of the wind turbine system with backlash in section 2. In section 3, a bondgraph model of the wind turbine system is proposed, and the section 4 is devoted to depict the LQR-RST controller for the reduction of the backlash phenomenon. The results of the simulation are presented in section 5. At the end, section 6 includes a short conclusion.

2. SYSTEM MODELING

In this section, the dynamic simulation model is described for the proposed wind turbine energy conversion. The block diagram of the integrated overall system is shown in Fig. 1. This system is adopted from Tao et al. (2014). The wind turbine consists of a rotor mounted to a nacelle and a tower with two or more blades mechanically connected to an electric generator. The gearbox in the mechanical assembly transforms slower rotational speeds of the wind turbine to higher rotational speeds on the electric generator. The rotation of the electric generator's shaft generates electricity whose output is maintained by a control system. Afterwards, each sub-model of the wind turbine system is presented and combined to obtain a complete model of the wind turbine.

The subsystem emphasised in this paper is the influence of the backlash fault in the gearbox part in order to reduce their efficiency in speed/torque control, which affects the performance of the power quality. Therefore, a control system of a wind turbine is developed using the LQ-RST algorithm to optimise the wind turbine energy conversion process in the presence of vibrations caused by the backlash fault. Fig. 1 shows the basic components of the controlled system.

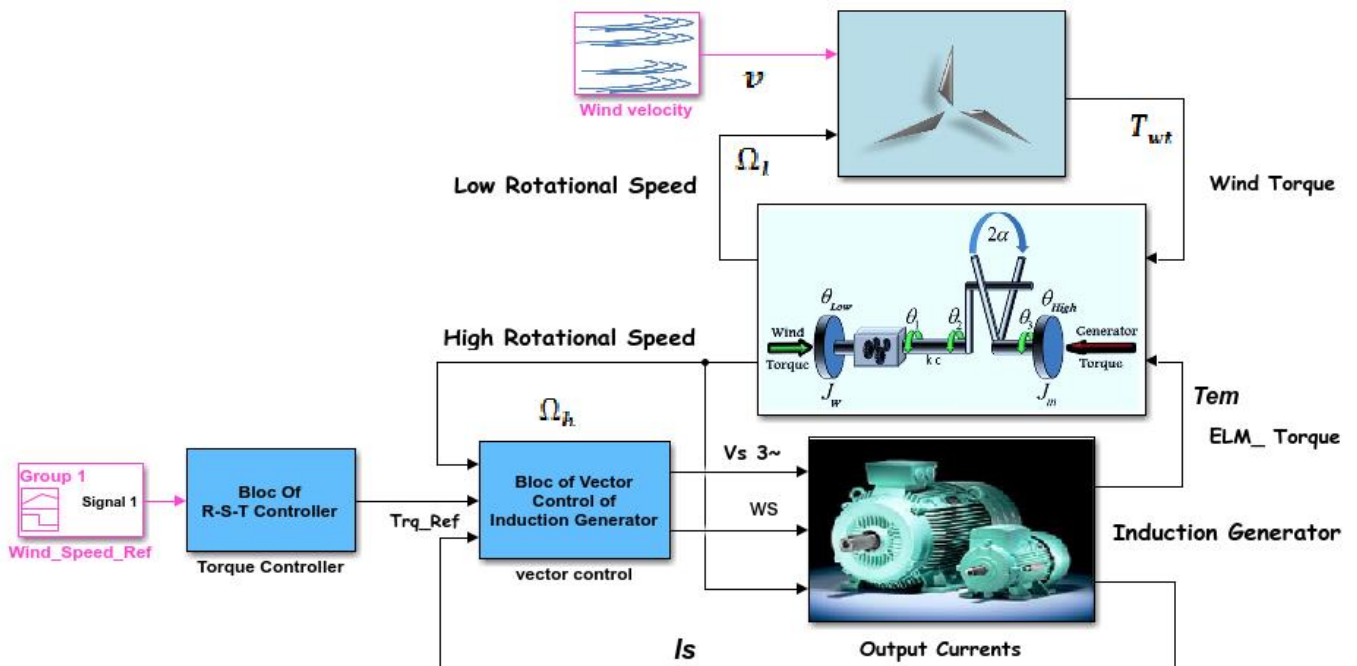


Fig. 1. Block diagram of the controlled wind turbine

2.1. Wind turbine aerodynamic modeling

The aerodynamic part models the extraction of mechanical power from energy in the wind. This part represents the physical rotor blade of the real wind turbine system. The mechanical power is then either fed directly to the electrical part or fed through the mechanical part to the electrical block. The output power of the wind turbine $P_{wt}[w]$ may be calculated from the following equation (Munteanu et al., 2018) :

$$P_{wt} = \frac{1}{2} \rho \cdot \pi \cdot R^2 \cdot v^3 \cdot C_p(\lambda) \quad (1)$$

In Eq. (1), $\rho[\text{Kg}/\text{m}^3]$ is air density, $R[\text{m}]$ is the blade length of a wind turbine, and $C_p(\lambda)$ is the power coefficient, versus tip speed ratio. The torque developed by the wind turbine may be expressed as follows:

$$T_{wt} = T_{wt}(\Omega_l, v)|_{\beta=\text{constant}} \quad (2)$$

where Ω_l is the low-speed shaft rotational speed and β is the pitch angle.

Then, it can be written as follows:

$$T_{wt} = \frac{P_{wt}}{\Omega_l} \quad (3)$$

According to Eq. (1), one obtains the following equation:

$$T_{wt} = \frac{1}{2} \rho \cdot \pi \cdot R^3 \cdot v^2 \cdot C_T(\lambda) \quad (4)$$

where $C_T = \frac{C_p}{\lambda}$ is the torque coefficient, v is wind speed, $T_{wt}[N.m]$ is wind torque, $T_{em}[N.m]$ is magnetic torque, $\Omega_l[\text{Rad}/\text{s}]$ is lowspeed, $\Omega_h[\text{Rad}/\text{s}]$ is highspeed, $T_{rq_ref}[N.m]$ is high-speed reference, $I_s[A]$ is stator current, $V_s[V]$ is stator voltage and $w_s[\text{Rad}/\text{s}]$ is stator frequency.

2.2. Drive train modeling

The mechanical part forms the connection between the aerodynamic part and the electrical part through torques T_{wt} and T_{em} and speeds Ω_l and Ω_h by the ratio N . The main component of the mechanical part is the gearbox. In this work, we consider coupling speed as a flexible speed; it means that the drive system of the wind turbine will be a three-mass system, as shown in Fig. 2.

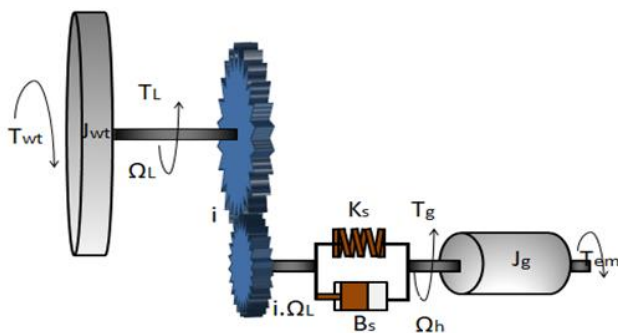


Fig. 2. Three-mass model of a wind turbine drive train

The motion equation is then given as follows:

$$T_{em} = J_g \dot{\Omega}_h + T_{int} \quad (5)$$

In Eq. (5), T_{int} and J_g are the internal torque and the high-speed shaft inertia $[kgm^2]$, respectively. With:

$$T_{int} = K_s \theta_d + b_s \Omega_d \quad (6)$$

$$\theta_d = N \theta_l - \theta_h \quad (7)$$

and:

$$\dot{\theta}_d = N \Omega_l - \Omega_h \quad (8)$$

According to Eqs. (5) and (6), one obtains the following:

$$T_{em} = J_g \dot{\Omega}_h + K_s \theta_d + b_s \Omega_d \quad (9)$$

where k_s is the shaft elasticity $[Nm/rad]$, b_s is the inner damping coefficient of the shaft $[kgm^2/s]$ and θ_d represents the difference in the angle of high-speed shaft θ_h and the low-speed shaft θ_l .

$$T_{wt} = J_{wt} \dot{\Omega}_l + N T_{int} \quad (10)$$

where J_{wt} is shaft inertia with low speed.

2.3. Electrical generator modeling

The electrical part based on induction generators represents the components responsible for converting the mechanical power to electrical power that can be fed into the power grid. In WECSs, the generator interacts with the drivetrain; hence, to this set of equations, the high-speed shaft Ω_h motion is usually added in the following form:

$$J_T \frac{d\Omega_h}{dt} = T_m - T_{em} \quad (11)$$

where T_m is mechanical torque and J_T is the equivalent inertia rendered to the high-speed shaft. The generator model is described as follows (Naik and Gupta, 2017):

$$\begin{cases} v_{ds} = R_s i_{ds} + \frac{d\lambda_{ds}}{dt} - \omega_s \lambda_{qs} \\ v_{qs} = R_s i_{qs} + \frac{d\lambda_{qs}}{dt} - \omega_s \lambda_{ds} \\ v_{dr} = R_r i_{dr} + \frac{d\lambda_{dr}}{dt} - (\omega_s - \omega_r) \lambda_{qr} = 0 \\ v_{qr} = R_r i_{qr} + \frac{d\lambda_{qr}}{dt} + (\omega_s - \omega_r) \lambda_{dr} = 0 \end{cases} \quad (12)$$

where subscripts 's' and 'r' refer to the stator and rotor side, respectively, and subscripts 'd' and 'q' refer to the dq-axis. The stator and rotor flux can be expressed as follows:

$$\begin{cases} \lambda_{ds} = L_s i_{ds} + L_m i_{dr} \\ \lambda_{qs} = L_s i_{qs} + L_m i_{qr} \\ \lambda_{dr} = L_r i_{dr} + L_m i_{ds} \\ \lambda_{qr} = L_r i_{qr} + L_m i_{qs} \end{cases} \quad (13)$$

where T_{em} can be calculated as follows:

$$T_{em} = \lambda_{qs} i_{ds} - \lambda_{ds} i_{qs} \quad (14)$$

2.4. Backlash model

Backlash can be modeled in many ways. Depending on the needed level of accuracy of the model, different choices can be made (Adlene and Abderrazak, 2018). The definition of backlash

relevant for this paper is defined as ‘the play between two physical parts which are supposed to move together and there is an amount of space between the parts’. For electromechanical systems, the growth of wear after a long operating period can engender a non-neglected backlash.

The modeling of this part consists of the following backlash model see (Fig. 1) (Fiegel, 2019):

$$\dot{\theta}_b = \begin{cases} \text{Max} \left(0, \dot{\theta}_d + \frac{k_s}{b_s} (\theta_d - \theta_b) \right), & \text{if } \theta_b = -\alpha \\ \dot{\theta}_d + \frac{k_s}{b_s} (\theta_d - \theta_b), & \text{if } |\theta_b| < \alpha \\ \text{Min} \left(0, \dot{\theta}_d + \frac{k_s}{b_s} (\theta_d - \theta_b) \right), & \text{if } \theta_b = \alpha \end{cases} \quad (15)$$

where θ_b represents the backlash angle, $\theta_b \leq |\alpha|$.

2.5. Bondgraph model of the wind turbine system

Bond graph is a graphical approach to modeling in which component energy ports are connected by bonds that specify the transfer of energy between system components. This formalism facilitates the construction of models that represent the dynamics of multi-domain systems.

The bond graph (BG) contains dissipative, accumulative and conversion elements and junctions. The elements are interconnected by bonds, which carry the exchange variables (general flow and effort) and allow an easy visualisation of the physical system topology and power flow. In addition, to use the BG tool for modeling purposes, its causal and structural properties are also used to study some control problems such as observability, controllability and input–output decoupling.

In this research work, we are interested to present the bond graph modeling of the energy conversion chain. Our goal is first to create a direct model (simulation) with wind speed as the input and rotor speed, electromagnetic torque and the power as outputs by maintaining the power coefficient at the optimum value.

2.5.1. Block diagram of the aerodynamic model part

The diagram model of the aerodynamic part in 20sim software is illustrated in Fig. 3. The wind speed can be considered as the averaged incident wind speed on the swept area by the blades.

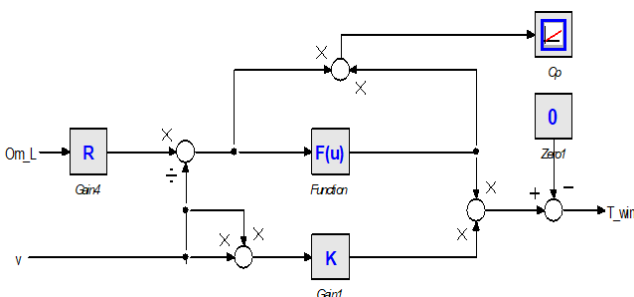


Fig. 3. 20-sim implementation of the aerodynamic model part

2.5.2. Bond-graph model of the drivetrain part

The bond graph implementation of the drivetrain part is shown in Fig. 4. The bond graph model consists of four 1-junctions and

one 0-junction. The 1-junction connected to the rotor inertia describes the rotor rotational speed. Since there are dynamics in between the rotor inertia and the generator inertia, they do not have the same speed: this is the reason for the 0-junction.

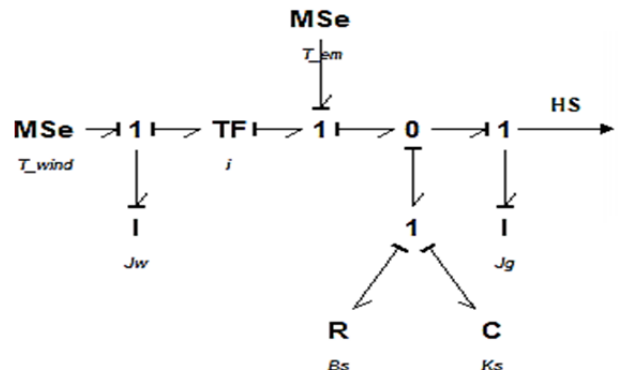


Fig. 4. Bond graph of the drivetrain

2.5.3. Bond Graph model of the electrical part

The bond graph of an induction generator using 20-sim software library is showing in Fig. 5.

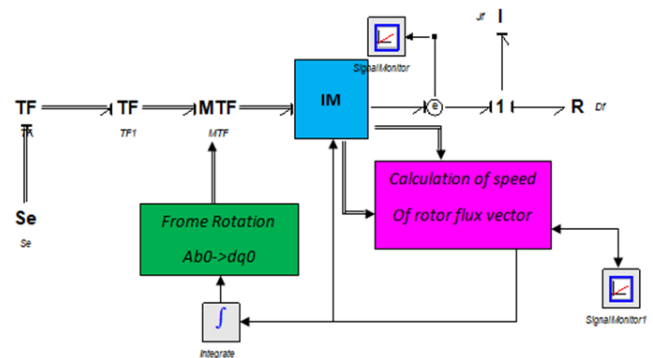


Fig. 5. Induction generator bond graph model

3. CONTROL DESIGN

To illustrate the performance of LQ control in order to eliminate the vibration problem caused by the backlash phenomenon in the wind turbine system, an LQ optimal control structure in the form of an RS controller based on the input–output approach is proposed. As mentioned in introduction, the optimisation is achieved by means of a rotational speed tracking loop based on the minimisation of the tip speed error, $\lambda_{opt} - \lambda(t)$.

3.1. Linear quadratic control of LQ formulation

The LQ control is based on the minimisation of the quadratic criterion which consists in weighting the variances of the control signal $u(k)$ and of $e(k + 1)^2$ the tracking error (Mokhtari and Marie, 2012). Let us consider in this study the tracking of a variable rotational speed reference. The identification of the wind turbine system with backlash gave us a transfer function as the following autoregressive–moving-average (ARMA) models form:

$$FTBO = G(z^{-1}) = \frac{Y(z^{-1})}{U(z^{-1})} = z^{-d} \cdot \frac{B(z^{-1})}{A(z^{-1})} \quad (15)$$

where: $G(z^{-1})$ is the open-loop transfer function with backlash, d is delay time, and $B(z^{-1})$ and $A(z^{-1})$ are the numerator and denominator of the system, respectively, with the following equations:

$$A(z^{-1}) = 1 + a_1z^{-1} + \dots + a_naz^{-na} \quad (16)$$

$$B'(z^{-1}) = b_1z^{-1} + \dots + b_nbz^{-nb} \quad (17)$$

By the Z inverse transformation of Eq. (15), we obtain the following:

$$A(z^{-1}) \cdot y(k) = B(z^{-1}) \cdot u(k) \quad (18)$$

$$y(k) = -a_1y(k-1) - \dots - a_nay(k-na) + b_1u(k-1) + \dots + b_nbu(k-nb-d) \quad (19)$$

Eq. (19) can write as follows:

$$y(k) = -\sum_{i=1}^{na} a_i y(k-i) + \sum_{j=1}^{nb} b_j u(k-j-d) \quad (20)$$

where y : is the system output (high speed: Ω_h) and u is the system control (electromagnetic torque: T_{em}), then we can rewrite Eq. (20) as follows:

$$\Omega_h(k) = -\sum_{i=1}^{na} a_i \Omega_h(k-i) + \sum_{j=1}^{nb} b_j T_{em}(k-j-d) \quad (21)$$

The simplest expression of the performance criterion given in (Mokhtari and Maria, 2012) is written as follows:

$$J = [e(k+1)]^2 + \beta \cdot \Delta u(k)^2 \quad (22)$$

where: J is the performance criterion, $\Delta u(k)$ is the increment of the system control, β is the weighting coefficient and $[e(k+1)]^2$ is the future error.

$$\text{With } e(k+1) = [y_{ref}(k+1) - y_{pr}(k+1)] \quad (23)$$

Then,

$$J = [y_{ref}(k+1) - y_{pr}(k+1)]^2 + \beta \cdot \Delta u(k)^2 \quad (24)$$

and $y_{ref}(k+1)$ is the reference speed (y_{opt}). $y_{pr}(k+1)$ is the prediction speed.

To calculate $y_{pr}(k+1)$, we give $d = 0$ and we use Eq. (19) as follows:

$$\begin{aligned} y(k) &= -[a_1y(k-1) + \dots + a_nay(k-na)] + b_1u(k-1) + \dots + b_nbu(k-nb) \\ &= -(a_1z^{-1} + \dots + a_naz^{-na}) \cdot y(k) + (b_1z^{-1} + \dots + b_nbz^{-nb}) \cdot u(k) \\ &= [1 - A(z^{-1})] \cdot y(k) + B(z^{-1}) \cdot u(k) \\ &= Z^{-1}A^*(z^{-1}) \cdot y(k) + Z^{-1}[Z^{-1}B^*(z^{-1}) \cdot y(k) + b_1] \cdot u(k) \\ &= A^*(z^{-1}) \cdot y(k-1) + B^*(z^{-1}) \cdot u(k-2) + b_1 \cdot u(k-1) \end{aligned} \quad (25)$$

with

$$A^*(z^{-1}) = -[a_1 + a_2Z^{-1} + \dots + a_naz^{-na+1}] \quad (26)$$

$$B^*(z^{-1}) = b_2 + a_3Z^{-1} + \dots + a_nbz^{-nb+2} \quad (27)$$

To obtain the prediction equation, replace k by $k+1$ in the Eq. (25).

$$y_{pr}(k+1) = A^*(z^{-1}) \cdot y(k) + B^*(z^{-1}) \cdot u(k-1) + b_1 \cdot u(k) \quad (28)$$

The derivative of Eq. (28) highlights the control variation $\Delta u(k)$, which gives the output predicted as follows:

$$y_{pr}(k+1) = [1 + A^*(z^{-1})] \cdot y(k) - A^*(z^{-1}) \cdot y(k-1) + B^*(z^{-1}) \cdot u(k-1) + b_1 \cdot \Delta u(k) \quad (29)$$

By replacing Eq. (29) in criterion J (24) we obtain the following:

$$J = \{y_{ref}(k+1) - [1 + A^*(z^{-1})]y(k) + A^*(z^{-1})y(k-1) - B^*(z^{-1})u(k-1) - b_1\Delta u(k)\}^2 + \beta \Delta u(k)^2 \quad (30)$$

To calculate the optimal variation of an order, it is enough to minimise the criterion J via this equation:

$$\frac{\delta(J)}{\delta(\Delta u)} = 0 \quad (31)$$

Then

$$\Delta u(k) = \eta \left(\begin{aligned} &y_{ref}(k+1) - [1 + A^*(z^{-1})]y(k) + \\ &+ A^*(z^{-1}) \cdot y(k-1) - B^*(z^{-1})\Delta u(k-1) \end{aligned} \right) \quad (32)$$

where:

$$\eta = \frac{b_1}{b_1^2 + \beta} \quad (33)$$

The control input value $u(k)$ to be applied at the current time is follows:

$$u(k) = u(k-1) + \Delta u(k) \quad (34)$$

3.2. The RST controller

The RST controller block implements a generalised predictive controller using a reference signal tracking polynomial representation. This type of control is based on the synthesis of a digital controller with two degrees of freedom. We can simplify Eq. (32) to give the LQ optimal control law as an RST controller illustrated in Fig. 6, and the transfer functions are given as follows:

$$R(z^{-1}) = \eta \{1 + a_1 + (a_2 - a_1)z^{-1} + \dots + (a_{na} - a_{na-1})z^{-na+1} - a_naz^{-na}\} \quad (35)$$

$$S(z^{-1}) = \left[1 + \eta \left(\begin{aligned} &b_2z^{-1} + b_3z^{-2} + \dots \\ &+ b_nbz^{-nb+1} \end{aligned} \right) \right] \cdot (1 - z^{-1}) \quad (36)$$

$$T(z^{-1}) = \eta \quad (37)$$

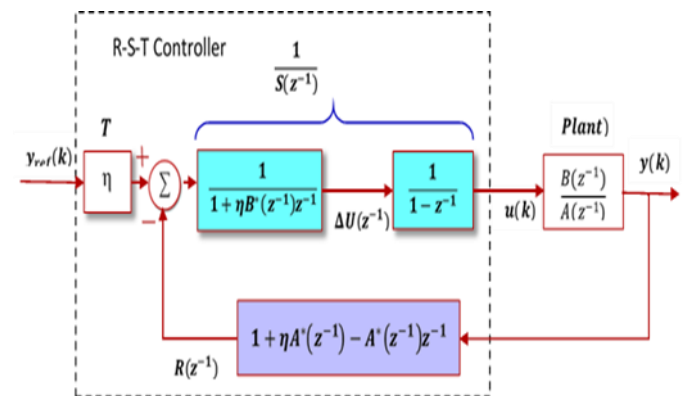


Fig. 6. LQ optimal control structure based on the RST form

4. RESULTS AND SIMULATION

In this section, the adaptive capability and robustness of the proposed LQ-RST algorithm to optimise the wind turbine energy conversion process in the presence of a vibration caused by the backlash fault is demonstrated. The overall model of the wind turbine system was simulated in 20sim software and MATLAB/Simulink/Sim Power Systems environment. The bond graph software 20 sim is object-oriented hierarchical modelling software. It allows users to create models using the bond graph, blockdiagram and equation models. Considering the block diagram illustrated in (Fig. 1), the model includes the wind turbine, induction generator, block of backlash fault and control blocks. The system parameters are presented in Table 1. Several scenarios with changes of backlash magnitude are considered in this study in order to examine the performance of the control system based on the LQ optimal control structure in the form of an RST controller. The asynchronous generator is assumed to have its own speed controller as well as vector controller.

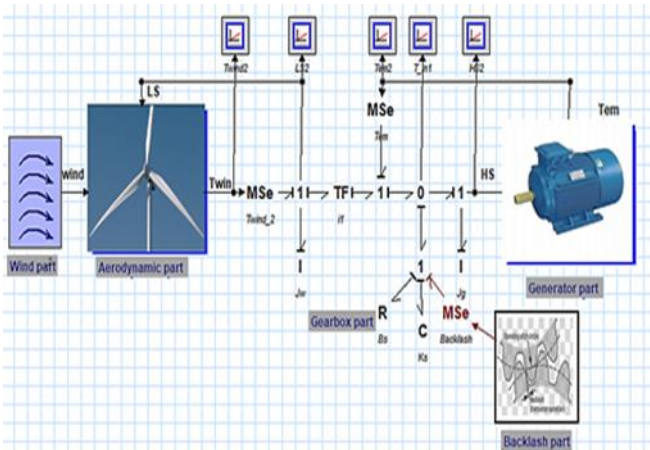


Fig. 7. Bond graph model of the wind turbine system

Tab. 1. Model parameters

Parameter name	Symbol	Value
Frequency	-	50Hz
Nominal power	Pn	6Kw
Multiplier ratio	l	6.25
Air density	P	1.25 kg/m3
Damping coefficient	Bs	2 Kg ^m 2/s
Number of pairs	P	2
Stator resistance	Rs	1.265 Ω
Rotor resistance	Rr	1.43 mΩ
Stiffness	Ks	75 N/m/Rad
Generator shaft inertia	Jg	0.01 kg/m ²
Inertia of wind turbine	Jwt	3 kg/m ²
Blade length	R	2.5 m
Mutual winding inductance	Lm	0.1397 H
Stator inductance	Ls	0.1452 H
Rotor inductance	Lr	0.1452 H
Max elect-magnetic torque	Tem_max	50 N/m
Stator voltage	Vs	220 V
Stator frequency	ω _s	100 π Rad/s

The following results are obtained by choosing the following values:

✓ R, S and T parameters of the control law are written as follows:

$$\begin{cases} R = -0.1235 + 0.127z^{-1} - 0.05002z^{-2} + 0.004843z^{-3} \\ S = 1 - 1.033z^{-1} + 0.04788z^{-2} - 0.01519z^{-3} \\ T = -0.041755 \end{cases}$$

✓ Backlash magnitude: $\theta_b = 0 \text{ rad}$, $\theta_b = 0.02 \text{ rad}$, and $\theta_b = 0.04 \text{ rad}$.

In order to assess the proposed control scheme, the simulation was executed according these scenarios:

4.1. Healthy system

This section presents the simulation results without a backlash fault in the wind turbine system. The simulation has been done using a bond graph and MATLAB/Simulink.

Case 01: Step responses for no controlled system

The results of a simulation are obtained with a constant wind velocity having an average speed of 7 m/s. The simulation model based on Fig. 7 presents the bond graph model of the wind turbine system and was constructed in 20-sim software.

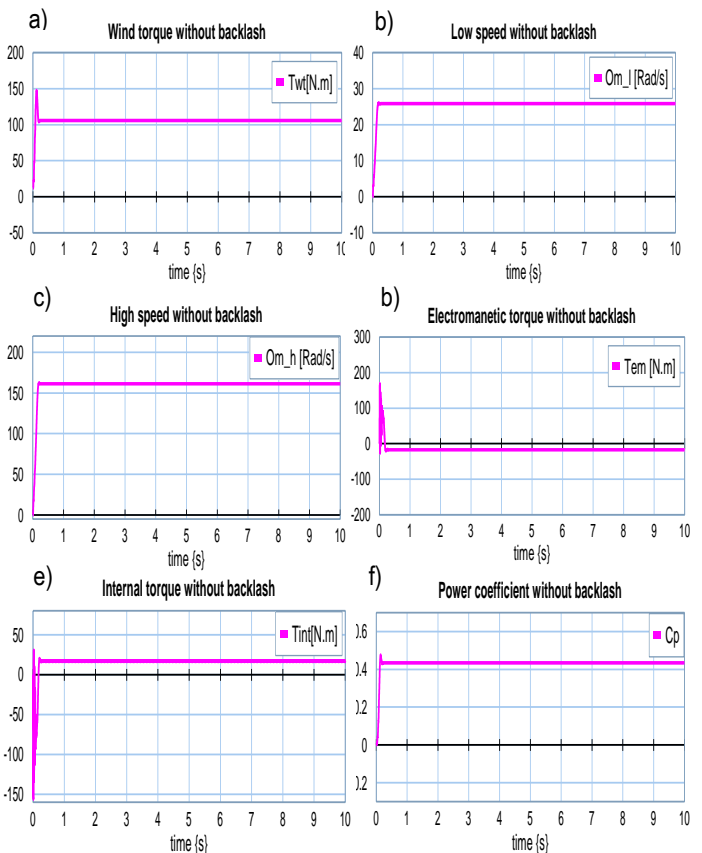


Fig. 8. Healthy system response with no controller (a) wind torque; (b) low speed; (c) high speed; (d) electromagnetic torque; (e) internal torque; (f) power coefficient

Fig. 8 depicts the system responses illustrated in Fig. 7 with zero backlash: (a) wind torque, (b) low speed, (c) high speed, (d) electromagnetic torque, (e) internal torque and (f) power coefficient. With regard to the instantaneous electromagnetic and internal torque (Fig. 8. d, e), we can indicate the presence of oscillations for a very short time at start up. (Fig. 8b and c) show the curve velocities of the multi-mass model. They have strong oscillations in the transient regime during 2s, and it then converted to its nominal speed at 157rad/s.

Case 02: Responses to the variable profile wind speed for the controlled system

To validate the proposed control system, a wind turbine system based on an induction generator is first tested in ideal conditions and driven to 140 rad/s in MATLAB/Simulink. Different step inputs of rotary speed for reference tracking were applied, and the dynamic responses for the LQ-RST controller are illustrated in Fig. 9.

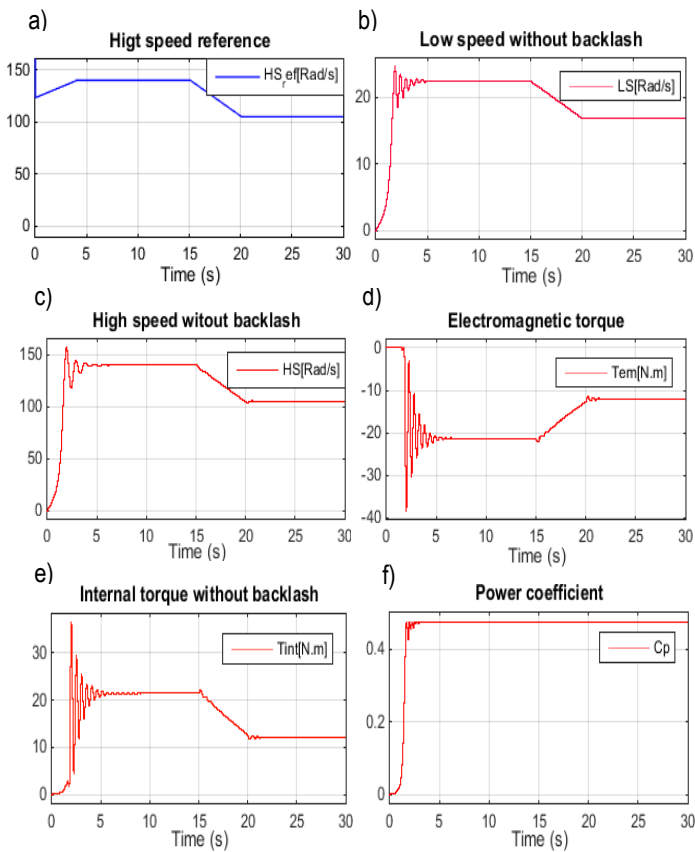


Fig. 9. Healthy system response with a controller. (a) speed reference; (b) low speed; (c) high speed; (d) electromagnetic torque; (e) internal torque; (f) power coefficient

Fig. 9a acts as a reference input for validation purposes and demonstrates the effectiveness of the proposed LQ-RST control algorithm even in the presence of a variable profile wind input. Fig. 9b–f show the performance of the proposed control; all figures show a better performance of the control law; the high velocity follows the reference given by the control and allows us to reduce the torque ripples. The command speed is increased linearly from 0 rad/s to 140 rad/s at $t = 5$ s. It is kept constant at

140 rad/s until $t = 15$ s, and decreased linearly to 120 rad/s at $t = 20$ s. Then, command speed is kept constant at 120 rad/s till $t = 30$ s. It can be seen from Fig. 9 b–f that the proposed method of control is able to track quickly the profile of the reference wind velocity. Nevertheless, it shows small oscillations at the time when the variation of the reference wind speed is applied.

4.2. Faulty system

In order to test the performance of the proposed controller (LQ-RST), the value of the backlash magnitude is doubled from 0.02 rad to 0.04 rad with different references tracking. Therefore, the controller should provide good control whatever the variation of the mechanical parameters is.

Case 01: Sinus responses

Fig. 10 a presents a sinusoidal input signal. The response of the system without backlash can be seen in Fig. 10 b. Simulations depicted in Fig. 11 a and b and Fig. 12 a and b illustrate the case with backlash ($\theta_b = 0.02rad$ and $\theta_b = 0.04rad$ respectively). All the waveforms of these figures present oscillations and nonlinearities caused by the backlash phenomenon. In these figures it is well seen that the system with backlash can efficiently affect the power quality.

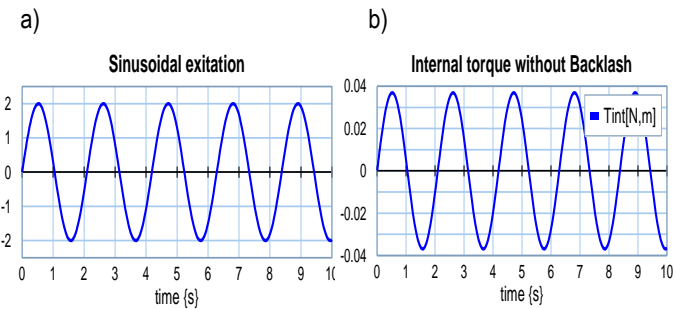


Fig. 10. Healthy response of no controller; (a) sinusoidal excitation; (b) internal torque

$\theta_b = 0.02rad$: To show the influence of the backlash fault on the system behaviour, we have begun with $\theta_b = 0.02rad$. Fig. 11a and b respectively show the simulated time responses corresponding to backlash angle (θ_b), backlash angular speed ($\dot{\theta}_b$) and internal torque T_{int} (see Eq. (6) and Eq. (15)). It is readily seen from these figures that these estimated variables present a cyclic sudden variation caused by the backlash phenomenon.

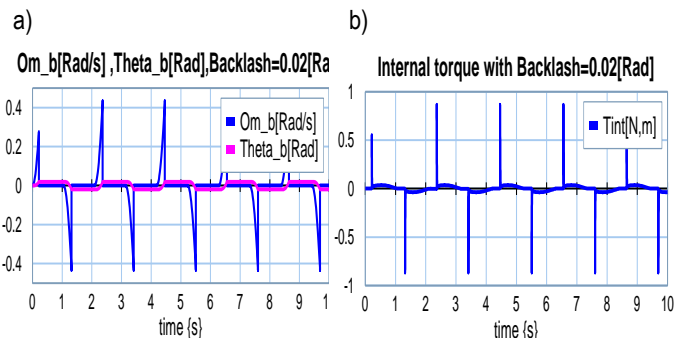


Fig. 11. (a) Backlash angle and backlash position; (b) internal torque

$\theta_b = 0.04rad$: However, in order to clearly show this influence, we have to amplify this phenomenon and introduce a fault at level 0.04 rad. Fig. 12a and b show the behavioral response of (θ_b) , $(\dot{\theta}_b)$ and internal torque T_{int} and the effect of this phenomenon on the dynamic response of the system. From the figures, we can conclude that the backlash has an important effect and high sensitivity on the mode operating WECSs.

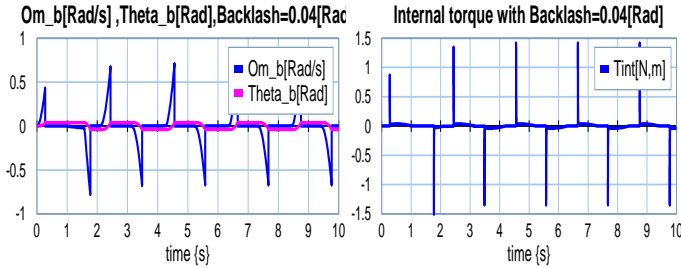


Fig. 12. (a) Backlash angle and backlash position; (b) internal torque

Case 02: Responses to the variable profile wind speed for the controlled system

Several scenarios with changes of magnitude of backlash are considered in this study in order to examine the performance of the proposed LQ-RST control algorithm. Measurements were repeated for the case with backlash $(\theta_b = 0.02rad$ and $\theta_b = 0.04rad$ respectively).

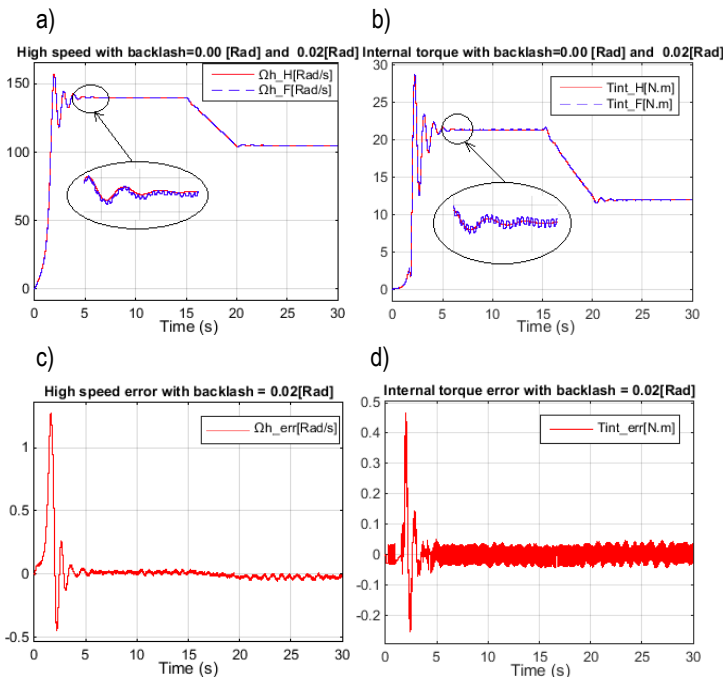


Fig. 13. Faulty system response with a controller: (a) high speed without and with backlash; (b) internal torque without and with backlash; (c) high speed error; (d) internal torque error.

$\theta_b = 0.02rad$: First, robustness tests are made with magnitude of backlash fault at 0.02 rad. The results of these tests are shown in Fig. 13 a and b. By analysing these figures, we can see that the backlash fault does not affect the performance of the operating mode system with a controller scheme. Nevertheless, they show a small oscillation even in the presence of time-varying variations in the profile of wind speed. In addition to this, strategy

'LQ-RST' proves to be the most significant in tracking the system states, for both lower and higher wind speeds, subjected to the variation of the wind speed. Fig. 13 c and d illustrate the residual errors between the healthy and the faulty system response.

$\theta_b = 0.04rad$: Last, robustness tests are made with a dead zone of magnitude at 0.04 rad. Similar results (see Fig. 14 a, b) can be achieved for the LQ-RST controller. These later demonstrate the effectiveness of the proposed control algorithm with evolution of the backlash fault. It is readily seen from Fig. 14 a and b and after zooming around at $t = 5$ s on different responses of the system (such as high speed, low speed, internal torque, etc.) that, we can easily show the oscillation caused by the disturbing torque. Larger variation is augmented and added to the dead zone, Fig. 14 a and b indicate that the LQ-RST controller is limited during this scenario. Fig. 14 c and d) illustrate the residual errors between the healthy and faulty system response.

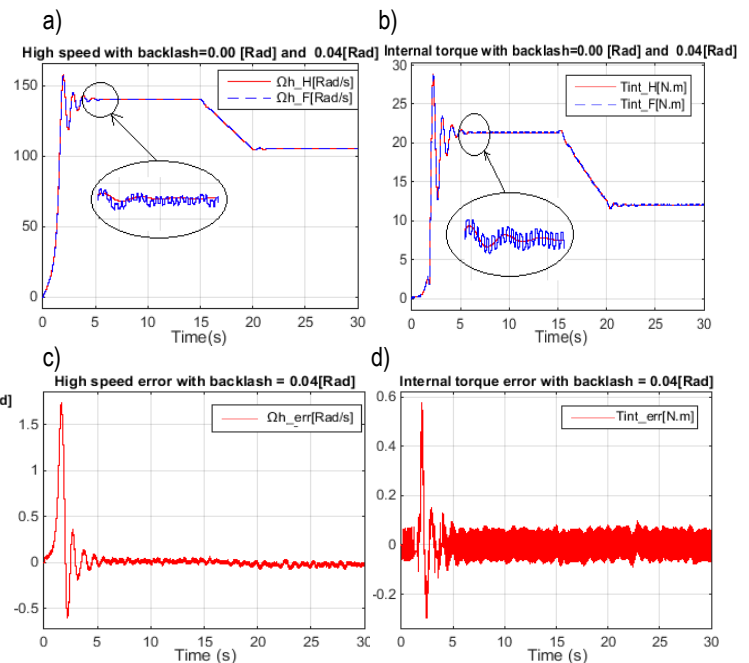


Fig. 14. Faulty system response with a controller; (a) high speed without and with backlash; (b) internal torque without and with backlash; (c) high speed error; (d) internal torque error.

Case 03: Responses to sequence wind speed for the controlled system

In this case, we have used a deterministic speed reference covering in steps the operating regimes corresponding to wind speeds from 6 m/s to 11 m/s with the same scenarios of case 2. Similar results (see Figs. 15 a–d, and Fig. 16 a–d) can be achieved for the LQ-RST controller. The efficiency of the LQ-RST controller is proved by means of numerical simulations applied on the wind turbine system with backlash. The LQ-RST Controller for the wind turbine system offers high robustness and fast dynamics. Changing the backlash magnitude approximately from 0.02 rad to 0.04 rad does not affect performance considerably.

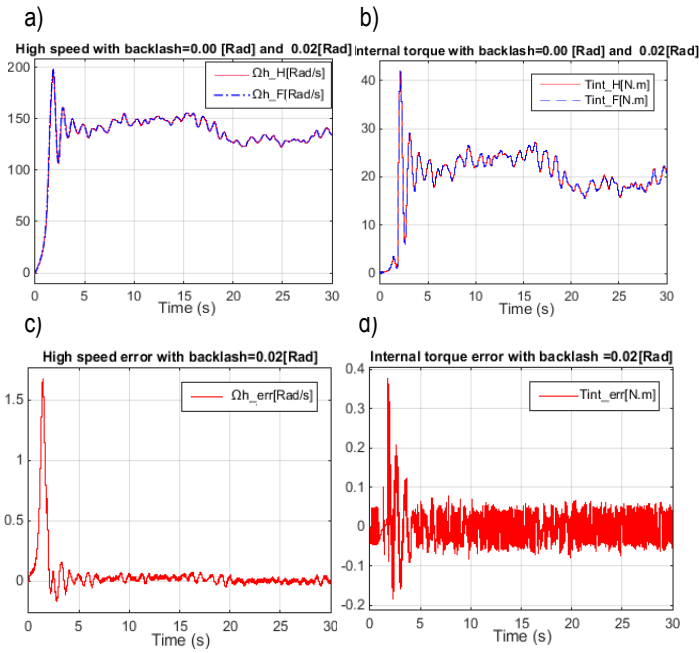


Fig. 15. $\theta_b = 0.02\text{rad}$: Faulty system response with a controller; (a) high speed without and with backlash; (b) internal torque without and with backlash; (c) high speed error; (d) internal.

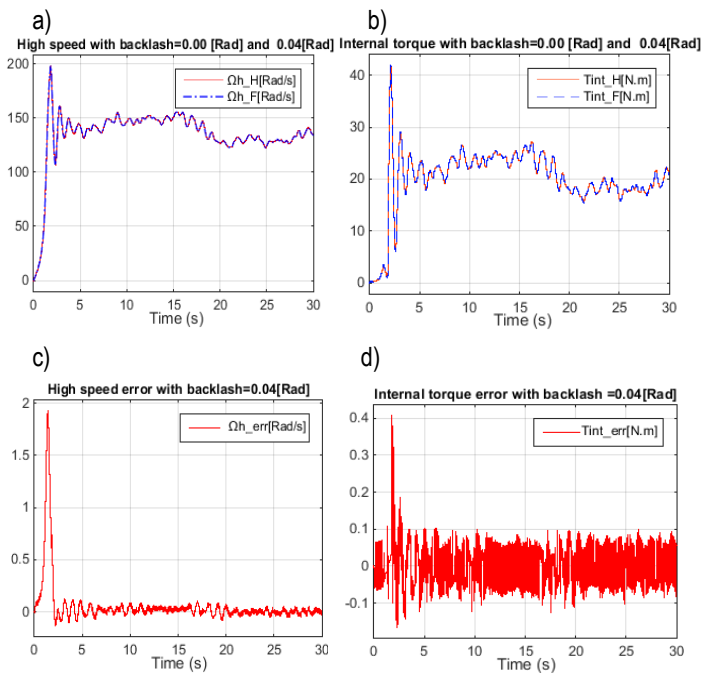


Fig. 16. $\theta_b = 0.04\text{rad}$: Faulty system response with a controller; (a) high speed without and with backlash; (b) internal torque without and with backlash; (c) high speed error; (d) internal torque error.

5. CONCLUSION


The purpose of this article was to control the high speed for a WECS with presence of backlash fault in the gearbox part. This is done by first making a BG model for a simplified WECS; the result of this simulation is then compared with that of the model produced with the MATLAB/ Simulink approach. The simulation results of the two approaches are almost the same with small

differences, which is why we continued the simulation with MATLAB/Simulink. Many scenarios have been carried out in order to validate the proposed control diagram. The influence of the backlash on the internal torque is clear especially in the excitation by a sinusoidal signal which directly affects the speed of the system and then the quality of energy; this is why we proposed the method of control based on the LQR-RST controller. The work presented demonstrates successful application of the LQR-RST controller to provide robust control under different faulty conditions of the gearbox.

REFERENCES

1. Adlene R., Abderrazak L. (2018), Study on the influence of backlash phenomenon on wind turbine power using bond graph approach, *J Braz. Soc. Mech. Sci. Eng.* 40, 91.
2. Amir R., other authors (2014), Effects of Floating Sun Gear in a Wind Turbine's Planetary Gearbox with Geometrical Imperfections, *Wind Energy*, 18(12), 2105-2120.
3. Cadiou J.C., M'Sirdi N.K. (1995), Modelization and Analysis of a System with Torque Transmitted through a Backlash, *9th world congress on the theory of machines and mechanisms, IFT.MM*, 2, 1467-1470.
4. Čulina I. (2011), Desing of mechanical assembly for inversingation of backlash effects in mechatronic systems, *Doctoral dissertation, Fakultet elektrotehnike i računarstva, Sveučilište u Zagrebu*.
5. Figel K. (2019), Backlash models for drivability simulation, 10.13140/RG.2.2.29154.79045.
6. Ganesh P.P., Senroy N., Kar I.N. (2018), Modeling and impact of gear train backlash on performance of DFIG wind turbine system, *Electric Power Systems Research*, 163, 356–364.
7. Gang T., Kokotović P.V. (1992), Adaptive Control of Systems with Backlash, *IFAC Proceedings Volumes*, 25, 87-93.
8. Guo-Qiang W., Shu-Nan W., Yu-Guang B., Lei L. (2013), Experimental studies on model reference adaptive control with integral action employing a rotary encoder and tachometer sensors, *Sensors*, 13(4), 4742–4759.
9. Lagerberg A., Egardt B. (2007), Backlash estimation with application to automotive powertrains, *IEEE Transactions on Control Systems Technology*, 15(3), 483–493.
10. Makosi C.A.M., Rinderknecht S., Binz R., Uphaus F., Kirschbaum F. (2017), Implementation of an open-loop controller to design the longitudinal vehicle dynamics in passenger cars, *SAE Technical Paper 2017-01-1107*.
11. Marton L., Lantos B. (2009), Control of mechanical systems with Stribeck friction and backlash, *Systems and Control Letters*, 58(2), 141-147.
12. Mohamed A.A., Xiangjie L., Di J. (2020), Design and implementation of partial offline fuzzy model-predictive pitch controller for large-scale wind-turbines, *Renewable Energy* 145, 981-996.
13. Mokhtari M., Marie M. (2012), Engineering Applications of MATLAB® 5.3 and SIMULINK® 3, *Translated from the French by Mohand Mokhtari, Michel Marie, Cécile Davy and Martine Neveu. Springer Science & Business Medi*.
14. Moradian K. (2014), Speed control of mechanical systems with backlash, *Indian J. Sci. Res*, 1(2), 94-99.
15. Munteanu B.A.I., Cutululis N.A., Caenga E. (2008), Optim. Control Wind Energy Syst. towards a global approach, *Springer Science & Business Media*.
16. Naik K.A., Gupta C.P. (2017), Fuzzy logic based pitch angle controller/or SCIG based wind energy system, *In 2017 Recent Developments in Control, Automation & Power Engineering (RDCAPE)* (pp. 60-65), *IEEE*.

17. **Odgaard P.F., Stoustrup J., Kinnaert M.** (2013), Fault-Tolerant Control of Wind Turbines: A Benchmark Model, *IEEE Transactions on Control Systems Technology*, 21(4), 1168-1182.
18. **Qikun S, Yan S, Renfu J, Peng S.** (2019), Design on Type-2 Fuzzy-based Distributed Supervisory Control with Backlash-like Hysteresis, *IEEE Transactions On Fuzzy Systems*, vol, no, pages.
19. **Ragheb A., Ragheb M.** (2010), Wind turbine gearbox technologies, *In Proceedings of the 1st International Nuclear & Renewable Energy Conference (INREC)*, 1–8.
20. **Ruderman M., Yamada S., Fujimoto H.** (2018), Backlash Identification in Two-Mass Systems by Delayed Relay Feedback, *Journal of Dynamic Systems, Measurement, and Control*, 141(6), pages.
21. **Ruderman M., Krettek J., Hoffmann F., Bertram T.** (2008), Optimal state space control of dc motor, *In Proceedings of the 17th world congress the international federation of automatic control. Seoul, Korea*, 5796–5801.
22. **Sami K., other authors** (2020), Maximum power extraction framework using robust fractionalorder feedback linearization control and GM-CPSO for PMSG-based WECS, *Wind Engineering*, vol, no, pages.
23. **Tao L., Zhang B., Feng Z., Zheng B-C.** (2014), Robust Control with Engineering Applications, *Mathematical Problems in Engineering*, vol, no, pages.
24. **Tomonobu S.** (2018), *Renewable Energy, Applied Sciences*, vol, no, pages.
25. **Yangshou X., Kang H., Fengwei X., Yong Y., Meng S., Hua Z.** (2019), Research on the Influence of Backlash on Mesh Stiffness and the Nonlinear Dynamics of Spur Gears, *Applied Sciences*, 9(5), 1029.
26. **Yonezawa H., other authors** (2019), Vibration Control of Automotive Drive System with Nonlinear Gear Backlash, *Journal of Dynamic Systems, Measurement, and Control*, 141(12), pages.
27. **Zhao X., Chen C., Liu J., Zhang L.** (2015), Dynamic Characteristics of a Spur Gear Transmission System for a Wind Turbine. In 2015 International Conference on Automation, *Mechanical Control and Computational Engineering. Atlantis Press*, vol, no, pages.
28. **Zhenxing L., Zhansheng L., Jingming Z., Guanghui Z.** (2017), Study on Interactions Between Tooth Backlash and Journal Bearing Clearance Nonlinearity in Spur Gear Pair System, *Mechanism and Machine Theory*, 107, 229-245.

Mohamed Arab:  <https://orcid.org/0000-0002-6535-9765>

Abederezak Lachouri:  <https://orcid.org/0000-0001-6718-4228>

Mohamed Kerikeb:  <https://orcid.org/0000-0002-1665-1356>

Lamine Mehennaoui:  <https://orcid.org/0000-0001-6337-6003>

DRIVING COMFORT ASSISTANCE SYSTEM CONSIDERING TWO SENSORS DATA

Stanimir KARAPETKOV*, Hristo UZUNOV* , Liliana INDRIE** , Zlatin ZLATEV*** 

*Technical University of Sofia, Faculty and College of Sliven, Sliven 59 Burgasko Shose Blvd 59, Bulgaria

**University of Oradea, Faculty of Energy Engineering and Industrial Management, Department of Textiles, Leather and Industrial Management, B.St.Delavrancea Str., no. 4, 410058, Oradea, Romania,

***Trakia university, Faculty of Technics and technologies, 38 Graf Ignatiev str., 8602, Yambol, Bulgaria

skarapetkov@yahoo.com, hvuzunov@gmail.com, liliindrie@yahoo.com, zlatin.zlatev@trakia-uni.bg

received 22 March 2020, revised 7 July 2021, accepted 12 July 2021

Abstract: In the present work, a system using data from two sensors located next to the driver and to the mass centre of the bus is proposed. Three degrees of discomfort have been used – comfortable, moderately uncomfortable and very uncomfortable. These levels are set out in the questionnaire. A survey was conducted. Respondents were selected between the ages of 14 and 65 and were divided into three age groups – adults, middle-aged and young. Accelerometer systems with MPU-6500 (TDK InvenSense Corp.) sensors are used. A correlation method (CORR) and sequentially improving estimation methods are used for feature selection, which significantly reduce the number of combinations of features obtained. Selected sensor data is entered into feature vectors. These vectors are reduced by principal component analysis. Predictive models have been created that take into account the age of passengers. The use of data from two sensors and separation of the passengers according their age, leads to an increase in the accuracy of predicting passengers discomfort level (DL) of up to 98%. These results can be used to evaluate and guide the vehicle driver in order to improve his driving style. In addition, the simplified interface does not distract the driver from the road conditions. The results obtained can lead to an improvement in the parameters of the transport process, which covers the interest of the carrier related to the efficient use of vehicles, and hence the reduction of fuel consumption and harmful emissions. However, it should be recommended that, when developing systems to ensure comfort of travel, adjustments should be made to suit the age group of passengers carried on public transport buses.

Key words: stated preference survey, predictive model, customer satisfaction, passenger comfort, passenger service, driver assistance system

1. INTRODUCTION

The deterioration of the comfort of traveling in vehicles is due to vibrations, noise and ambient temperature. Drivers' poor driving experience makes the public transportation system less attractive (Vrcan et al., 2011; HaoLiang et al., 2018).

The regulatory documents (ISO, 1978) mainly address the vertical vibration leading to a strong sense of discomfort in commuters. Research into the vertical stability of the passenger is also

the subject of scientific research. Improvements in train travel have been explored (Sharma et al., 2018), and also in sea and river passenger transport ships (Kim et al., 2014).

In Bulgaria, which is in the European Union, bus is one of the main methods of public transport in urban and interurban environments (Tsvetkova, 2017). From the available literature, there are known solutions related to attempts to improve travel comfort. Tab. 1 summarises the more commonly used methods for improving the comfort of public transport.

Tab. 1. Methods for improving the comfort of passengers in public transport vehicles

Method	Advantages	Disadvantages	Reference
Active seat suspension	It works individually for each passenger, feedback with different sensors.	Low stroke of the actuator, depends on the weight of the passenger, high cost of realisation.	Ikeda et al., 2018; Sikora, 2018
Active bus suspension	Long stroke of the actuator, built by serial bus manufacturers, feedback with different sensors.	Pneumatic or hydraulic pump with high power consumption is required.	Jurkiewicz et al., 2017; Long et al., 2018
Driver assistant systems	Opportunity for software realisation on a mobile phone.	The system is not active, it depends on the driver's level of experience.	Stoichkov, 2013

Driver-assisted systems have very good potential than the other two active suspension methods. They can be implemented on a mobile phone using the sensors of this device. They can also be applied to older bus models that do not have active suspension systems.

Solutions are known using the sensors available in the mobile phone. Combining their data gives better results than using an accelerometer alone. The advantage of these systems is that when one of the sensors fails, the operation of the system can continue with data from the other sensors. A major drawback of

the method is that such a method can only be used for a limited period of time after the failure of a major sensor in the system (Stoichkov, 2013).

The decision to use neural networks is made by car and mannequins (Kim et al., 2019). The disadvantage of this type of system is that it uses complex computational procedures and is suitable for operation in a controlled environment. It is necessary to propose a system that is suitable for real-world application of urban transport. The analysis made shows that the appropriate classification methods are those that use simplified calculation procedures, can be applied by technical means, and that can be placed directly on public transport buses because they speed up the calculation process and reduce the system response time.

It is not clear from the available publications whether the age of travellers is important for the comfort of travel. Such an analysis needs to be done.

The purpose of the article is to evaluate the possibility of improving travel comfort by using data from two sensor systems, depending on the age of the passengers.

2. MATERIAL AND METHODS

Iveco Poker Bus (FIAT-IVECO S.p.A.) is used. The bus has a total length of 7.5 m. Accelerometer systems with MPU-6500 (TDK InvenSense Corp.) sensors are used. The systems are mounted in protective housings. The connection between them is via Bluetooth communication. HC-06 modules are used. The module provides Bluetooth 2.0 connection at a speed of 2,400 bit/s. The first sensor system is located next to the driver and the second near the bus centre.

Fig. 1 shows a block diagram of the sensor system used. This scheme is applicable to both systems installed near the driver and to the centre of mass of the bus.

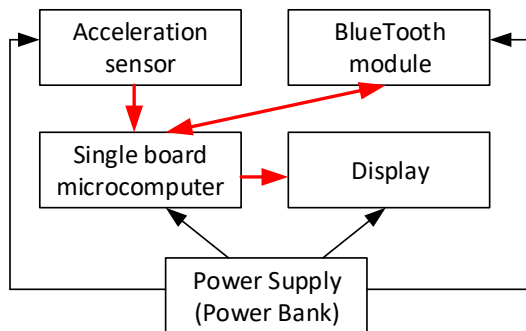


Fig. 1. Block-diagram of a measurement system

Fig. 2 shows a schematic diagram of the experimental layout, with the arrangement of the sensor systems used.

The designations of accelerations along the sensor-driver axes are: X, Y, Z (m/s²) – for linear accelerations; A, B, C (rad/s) – for angular accelerations. The axes of the sensor to the centre of mass of the bus are: X1, Y1, Z1 – for linear accelerations; A1, B1, C1 – for angular accelerations. The determination of the angular acceleration values on the rotary axes is calculated. This option is preferred because the gyroscopic sensor that is inserted into the MPU-6500 sensor has the disadvantage of obtaining a so-called ‘drift’ upon measurement (Li et al., 2019). The determination of the angular acceleration values is made by the following mathematical relations:

$$A = \text{atan}(Y, Z), \text{ rad/s} \quad (1)$$

$$B = \text{atan}(X, Z), \text{ rad/s} \quad (2)$$

$$C = \text{atan}(X, Y), \text{ rad/s} \quad (3)$$

These calculations are made for both sensor systems used.

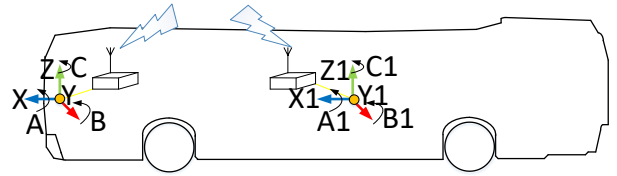


Fig. 2. Experimental setup – general view

Attempts were made in the light-part of day. Meteorological conditions are free of precipitation, clear, sunny weather, ambient temperature 17 °C and relative humidity 50%RH. Location of measurements are Tenevo Airport, Tundja Municipality, Bulgaria.

Based on the available literature (Smith et al., 2006), many data are needed and many people are interviewed to obtain objective results for travel comfort. Such analyses are only achievable under controlled and laboratory conditions with pre-prepared respondents. For this reason, the survey developed contains only disaggregated levels of discomfort. Three degrees of discomfort have been used – comfortable, moderately uncomfortable and very uncomfortable. These levels are set out in the questionnaire. The graphics used are with Creative Commons CC0 (<https://pixabay.com>).

A survey was conducted. Respondents were selected between the ages of 14 and 65, and were divided into three age groups – adults, middle-aged and young. Before completing the survey, a clarification is made as to what each degree of discomfort means, which should be noted after each manoeuvre.

The following methods have been used to select features describing the degree of discomfort (Su et al., 2017):

- Correlation method (CORR). Correlation dependence allows one to look for unknown links between features that describe discomfort. In the selection of features, those that have the least possible correlation with each other are sought;
- Method for selecting regression features by analysis of adjacent components (FSRNCA). The algorithm is suitable for selecting features for regression analysis;
- Method for ranking significant forecasting parameters (RELIEFF). The method is a selection function using the ReliefF algorithm for classification and the RReliefF algorithm for regression. This algorithm works well when evaluating the significance of characteristics for distance-based models;
- Weight averages obtained from the feature selection methods. The arithmetic mean of the weights of the features was used.

Principal Components (PCs) obtained by Principal Component Analysis were used to reduce the volume of feature vector data (Mladenov et al., 2015).

An initial model was used to describe the relationship between the main components and the degree of discomfort of the type:

The model coefficients are analysed, depending on the p-level value, for each of them. Non-informative coefficients are rejected by the model.

The residuals have been analysed (Tasev et al., 2011), which

are determined by the difference between the model values and the actual values.

The accuracy of the predictive models is estimated on the basis of statistical parameters. The coefficient of determination (R²), sum of squares of error (SSE) and root mean square error (RMSE) were used as the criteria for model evaluation.

The validation of the results obtained was done with data not used in the previous measurements. Mainly nonlinear manoeuvres are used – left and right turns, as well as reverse turns.

All data were processed at a level of significance $\alpha=0.05$.

3. RESULTS AND DISCUSSION

As a result of the calculations and analysis of results, the developed system is presented in general form. Selection methods for feature vectors by which passengers discomfort are predicted, depending on the age of the travellers. Predictive models have been developed. A system for indicating the degree of discomfort is proposed. Validation of the proposed system has been made. The results obtained are compared with those of the available literature.

Fig. 3 shows the sensor devices mounted next to the driver and to the centre of mass of the bus.

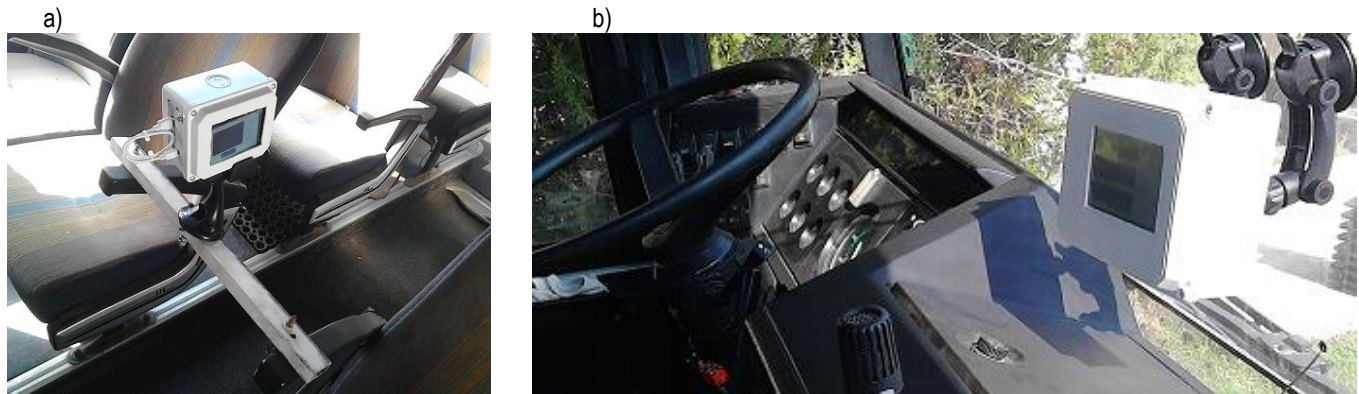


Fig. 3. Measuring devices – general view: (a) a measuring device installed near the mass centre of the bus, (b) a measuring device installed near the bus driver

Tab. 2 lists data for selected feature vectors. It can be seen that, by the RELIEFF method (6 features), the same traits were selected for all age groups according to which the degree of discomfort can be predicted. The highest number of traits were selected by the FSRNCA method (6–10 features), followed by the CORR method (4–7 features).

Tab. 2. Selected feature vectors

Age group	Method	Feature vector	Selected features
Old (O)	CORR	OFV1	X, Y, A, B, X1, B1, C1
	FSRNCA	OFV2	X, Y, A, B, C, X1, Z1, A1, B1
	RELIEFF	OFV3	Z, C, X1, Y1, Z1
MA	CORR	MFV1	C, Y1, A1, C1
	FSRNCA	MFV2	Y, A, C, X1, Y1, Z1, A1, C1
	RELIEFF	MFV3	Z, C, X1, Y1, Z1
Young (Y)	CORR	YFV1	Z, B, C, Y1, A1
	FSRNCA	YFV2	X, Y, Z, A, B, C, X1, Y1, Z1, C1
	RELIEFF	YFV3	Z, C, X1, Y1, Z1
Averaged (A)	CORR	AFV1	X, C, A1, C1
	FSRNCA	AFV2	X, B, C, X1, Z1, A1
	RELIEFF	AFV3	Z, C, X1, Y1, Z1

CORR, correlation method; FSRNCA, method for selecting regression features by analysis of adjacent components; MA, middle aged

Tab. 3 shows the results of preliminary analyses of passengers' discomfort, depending on the age of the respondents. Two

major components describe with sufficient accuracy over 95% of the variation in feature vectors. Results of averaged (A) travel comfort data are also presented. The use of average passenger discomfort data does not show sufficient accuracy to predict it. It is seen that the separation of the data by age groups shows an increase in the values of the coefficient of determination and the reduction of errors.

Tab. 3. PCR results for predicting passengers' discomfort

Feature vector	R ²	SSE	RMSE	Feature vector	R ²	SSE	RMSE
OFV1	0.95	1.06	0.29	YFV1	0.95	0.81	0.25
OFV2	0.98	0.49	0.19	YFV2	0.99	0.19	0.12
OFV3	0.95	0.59	0.29	YFV3	0.93	1.07	0.29
MFV1	0.94	1.39	0.33	AFV1	0.88	1.27	0.71
MFV2	0.96	1.04	0.28	AFV2	0.89	0.84	0.25
MFV3	0.94	1.38	0.33	AFV3	0.88	0.97	0.57

PCR, principal component regression; RMSE, root mean square error; SSE, sum of squares of error

The selected feature vectors, reduced by the principal component analysis method, were used to construct models for predicting the degree of discomfort for three age groups of travellers. After removing the insignificant coefficients from the base model that have $p\text{-Value} \gg \alpha$, it has been found that the relationship between travel discomfort and major components of the feature vectors can be described by the following models:

			R ² =0,98	
OFV2	$D = 2,31 + 0,99.PC1 - 0,72.PC2 - 0,01.PC1^2 - 0,55.PC2^2$		SSE=0,01	(5)
			RMSE=0,02	
			R ² =0,98	
MFV2	$D = 2,06 + 1,12.PC1 - 1,19.PC2 - 0,13.PC1.PC2$		SSE=0,04	(6)
			RMSE=0,02	
			R ² =0,98	
YFV2	$D = 2,08 + 1,06.PC1 - 1,51.PC2 - 0,04.PC1^2$		SSE=0,02	(7)
			RMSE=0,05	

Low standard error values are observed. The coefficients of all models are significant because the p-value is much less than the accepted level of significance $\alpha = 0.05$.

SSE and RMSE error values are low. The results show that the models obtained describe a significant part of the change in the degree of discomfort in travel, depending on the age group of travellers.

These estimates are not a sufficient criterion for evaluating the model. A residuals analysis needs to be done.

Residuals analysis shows that the models obtained are adequate. When analysing the residuals, there is a lack of systematic deviation of the actual data from the theoretical data, which is a sign of their normal distribution. The analysis of standardised coefficients shows that the first major component of the feature vectors has a significantly greater influence on the predictive power of the models.

Based on the models obtained, three degrees of discomfort have been defined, which can be used in driver signalling by visual indication. The display is divided into three levels – green, yellow and blue, depending on the level of discomfort. Fig. 4 shows the defined degrees of discomfort.

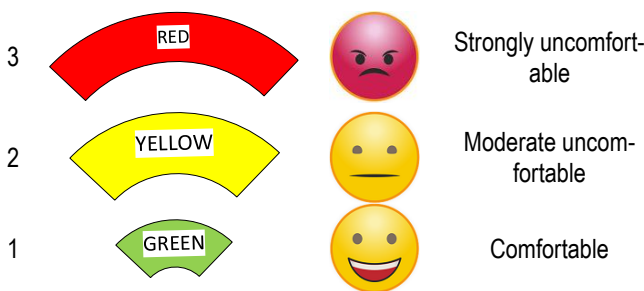


Fig. 4. Indication of the level of discomfort

Tab. 4. Results of system validation

M	V, km/h	M1, DL			M2, DL			M3, DL		
		40	50	60	40	50	60	40	50	60
O	S	1	2	3	1	2	3	1	2	3
	R	1	2	3	1	3	3	2	2	3
MA	S	1	1	3	1	1	3	1	1	3
	R	1	1	2	1	1	2	1	1	2
Y	S	1	2	3	1	2	3	1	2	3
	R	1	1	2	1	1	2	1	1	2

DL, discomfort level; MA, middle aged; M-manoevre; O, old; R, respondents; S, system; V-speed; Y-young

Tab. 4 shows the results of system validation. The following manoeuvres were performed at speeds of 40 km/h, 50 km/h and 60 km/h: M1-linear acceleration; M2-curvilinear acceleration; M3-curved slow-down acceleration. The levels of discomfort shown were obtained from a survey of respondents who participated in the previous stages of the survey. Three degrees of discomfort have been defined. The degree of discomfort reported by the system and those of the respondents was also reported. It can be seen that the degree of discomfort determined by the system and the respondents' answers coincide with a difference of up to 5%.

The results obtained confirm, supplement, and refine those reported in the available literature. The proposed model for predicting the degree of discomfort by Ivanov et al. (2019) can be used to predict the degree of discomfort with an accuracy of up to 87%. The models proposed in this paper, depending on the age of the respondents, increase this accuracy to 98%. The results presented by Ikeda et al. [8], where the authors evaluate the degree of discomfort in one respondent, mainly take into account the vertical vibration only. Kim et al. (2014) proposed a system using neural networks. Despite the many factors they used in their model, they achieved 70% accuracy only. Moreover, the neural network method used made their system slow and unsuitable for real-world public transport applications. Same problem also happened with Rekabdar et al. (2018). The system proposed in this paper eliminates this shortcoming by using simplified computing procedures that are suitable for use in a real public transport environment. The influence of the length of the vehicle is also taken into account in the present work. Regardless of the results obtained, which, to one degree or another, improve and complement the well-known travel comfort solutions, and research should continue towards the creation of a generalised model that takes into account the factors such as age of travellers, atmospheric, road conditions, and the particularities of the urban environment in which these systems are implemented. As demonstrated (Stoichkov, 2013), improving travel comfort and proper bus handling indirectly leads to a reduction in fuel consumption, prolongs the life of vehicles and also reduces harmful emissions to the environment.

4. CONCLUSIONS AND PROSPECTS FOR FURTHER RESEARCH

The results obtained in this paper confirm, supplement and improve the parameters mentioned in the available published literature.

Models have been obtained for predicting travel comfort, depending on the age of travellers. Separation of passengers into age groups has been found to improve the accuracy of prediction of the discomfort rate by up to 98%. Due to the large deviations of the averaged analytical models, it is not appropriate to use an averaged model when predicting travel comfort. This means that individual models must be designed for each age group.

In the present work, a three-level discomfort indication system is proposed. These results can be used to evaluate and guide the vehicle driver in order to improve his driving style. In addition, the simplified interface does not distract the driver from the road conditions. The results obtained can lead to an improvement in the parameters of the transport process, which covers the interest of the carrier related to the efficient use of vehicles by the reduction of fuel consumption as well as in reduction of harmful emissions. However, it should be recommended that, when developing systems to ensure comfort of travel, adjustments should be made to suit the age group of passengers carried by public transport buses.


REFERENCES

1. **Haoliang G., XiHui M., XiaoYong Y., Kai L.** (2018), Research on the influence of virtual modeling and testing-based rubber track system on vibration performance of engineering vehicles, *Engineering Review*, Vol. 38, No. 3, 288-295.
2. **Ikeda K., Endo A., Minowa R., Narita T., Kato H.** (2018), Ride comfort control system considering physiological and psychological characteristics: effect of masking on vertical vibration on passengers, *Actuators*, Vol. 7, 42, 1-13.
3. **International Organization for Standardization** (1978), Guide for the evaluation of human exposure to whole-body vibration, *ISO 2631*; ISO: Geneva, Switzerland.
4. **Ivanov A., Zlatev Z.** (2019), Development and research of information system elements for passengers drive comfort improvement, *Cybernetics and information technologies*, Vol. 19, No. 4, 101-115.
5. **Jurkiewicz A., Kowal J., Zajac K.** (2017), Sky-hook control and Kalman filtering in nonlinear model of tracked vehicle suspension system, *Acta mechanica et automatica*, Vol. 11, No. 3, 222-228.
6. **Kim D., Jeong M., Bae B., Ahn C.** (2019), Design of a human evaluator model for the ride comfort of vehicle on a speed bump using a neural artistic style extraction, *Sensors*, Vol. 19, 1-13.
7. **Kim J., Kim Y.** (2014), Time-domain analysis of passenger comfort on cruise ships under motion responses in waves, *Proceedings of the Institution of Mechanical Engineers, Part M: Journal of Engineering for the Maritime Environment*, Vol. 228, No. 4, 331-347.
8. **Li S., Gao Y., Meng G., Wang G., Guan L.** (2019), Accelerometer-based gyroscope drift compensation approach in a dual-axial stabilization platform, *Electronics*, Vol. 8, Art. 594, 1-12.
9. **Long L., Quynh L., Cuong B.** (2018), Study on the influence of bus suspension parameters on ride comfort, *Vibroengineering Procedia*, Vol. 21, 77-82.
10. **Mladenov M., Penchev S., Deyanov M.** (2015), Complex assessment of food products quality using analysis of visual images, spectrophotometric and hyperspectral characteristics, *International Journal of Engineering and Innovative Technology (IJEIT)*, Vol. 4, No. 12, 23-32.
11. **Rekabdar B., Mousas C.** (2018), Dilated convolutional neural network for predicting driver's activity, *21st International Conference on Intelligent Transportation Systems (ITSC)*, Maui, Hawaii, USA, November 4-7, 3245-3250.
12. **Sharma S., Kumar A.** (2018), Ride comfort of a higher speed rail vehicle using a magnetorheological suspension system, *Proceedings of the Institution of Mechanical Engineers, Part K: Journal of Multi-Body Dynamics*, Vol. 232, No. 1, 32-48.
13. **Sikora M.** (2018), Modeling and operational analysis of an automotive shock absorber with a tuned mass damper, *Acta mechanica et automatica*, Vol. 12, No. 3, 243-251.
14. **Smith D., Andrews D., Wawrow P.** (2006), Development and evaluation of the Automotive Seating Discomfort Questionnaire (ASDQ), *International journal of industrial ergonomics*, Vol. 36, 141-149.
15. **Stoichkov R.** (2013), Android smartphone application for driving style recognition, *Thesis, Institute for Media Technology*, Department of Electrical Engineering and Information Technology, Munich, Germany.
16. **Su W-H., He H-J., Sun D-W.** (2017), Non-Destructive and rapid evaluation of staple foods quality by using spectroscopic techniques: A review, *Critical reviews in food science and nutrition*, Vol. 57, No. 5, 1039-1051.
17. **Tasev G., Krastev K.** (2011), Exploration of mathematical model for optimization of frequency of diagnosis of the elements of machines, *Proceedings of The 11th International Conference, Reliability and statistics in transportation and communication*, Latvia, 115-119.
18. **Tsvetkova S.** (2017), Improving the quality of passenger transport in the city of Sofia by implementing intelligent transport systems, *Economic and Social Alternatives*, No. 4, 29-42, (in Bulgarian).
19. **Vrcan Ž., Siminiati D., Lovrin, N.** (2011), Design proposal for a hydrostatic city bus transmission, *Engineering Review*, Vol. 31, No. 2, 81-89.

Acknowledgement: This work was partially supported by the Bulgarian Ministry of Education and Science under the National Research Programme 'Healthy Foods for a Strong Bio-Economy and Quality of Life' approved by DCM #577 / 17.08.2018".

Hristo Uzunov:  <https://orcid.org/0000-0003-2229-2828>

Liliana Indrie:  <https://orcid.org/0000-0002-7094-4790>

Zlatin Zlatev:  <https://orcid.org/0000-0003-3080-5048>

THREE-DIMENSIONAL FUZZY CONTROL OF ULTRASONIC CLEANING

Volodymyr MORKUN[✉], Olha KRAVCHENKO[✉]

*Kryvyi Rih National University, 11, Vitaliy Matusevych Street, Kryvyi Rih 50027, Ukraine

morkunv@gmail.com, kravchenko@knu.edu.ua

received 3 September 2020, revised 12 July 2021, accepted 15 July 2021

Abstract: Consideration of ultrasonic cleaning as a process with distributed parameters enables reduction of power consumption. This approach is based on establishment of control over the process depending on fixed values of ultrasonic responses in set points. The initial intensity of radiators is determined using a three-dimensional (3D) interval type-2 fuzzy logic controller essentially created for processes with distributed parameters, as well as complex expert evaluation of the input data. The interval membership functions for the input and output data consider the space heterogeneity of ultrasonic cleaning. A rule base is formed, which is 2D and not dependent upon the number of input and output parameters. A model illustrating ultrasonic cleaning with a 3D interval type-2 fuzzy logic controller is designed. Comparative analysis of the output parameters of the proposed model and the traditional method indicates an increase in the energy efficiency by 41.17% due to application of only those ultrasonic radiators that are located next to the contamination.

Keywords: ultrasonic cleaning, 3D fuzzy interval type-2 logic, modeling, spatially distributed systems

1. INTRODUCTION

Effective cleaning guarantees both long-term exploitation of equipment and possibility of current maintenance. Ultrasonic cleaning is noted for higher efficiency and sustainability as it reduces the application of chemical solvents. Ultrasonic cleaning is based on the cavitation effect – implosion of bubbles resulting from the ultrasonic processing of a liquid. Consequently, energy that is capable of separating particles of dirt from the cleaned object is emitted. Issues related to enhancing the efficiency of ultrasonic cleaning are considered from two perspectives: as an investigation into parameters affecting a process in order to improve cavitation activity; and as establishment of control considering the peculiarities of ultrasonic cleaning. Cavitation intensity is not the same in different zones of an ultrasonic bath and depends on a number of factors. Space configuration of an ultrasonic bath, i.e., the size of the container, as well as the number and location of ultrasonic radiators, plays a major part in the process (Tangsopha and Thongsri, 2020). The frequency of insonation also affects cavitation distribution in space (Tangsopha et al., 2017). Temperature, intensity of processing, and oxygen content also influence the process, yet they only correct the intensity of cavitation in the ultrasonic bath without changing its distribution. While studying the parameters affecting cavitation, Xu et al. (2016) report the following dependencies: cavitation becomes unstable with long intonation, which is more vivid with greater capacity; increased gas content, capacity, and addition of a cleaning agent enhance cavitation, but on reaching an extreme value of these parameters, the cavitation activity falls. With relatively great capacity, cavitation increases with temperature, reaches its peak, and then drops. Besides affecting cavitation, these parameters are also interrelated: duration of insonation and high capacity influence temperature and gas content, while the latter depends on temperature. In other words, this is a complex physical process

with a great number of interrelated impact factors, the values of which change greatly at different points of a cleaning container.

Nigmatzyanov et al. (2019) present an attempt to consider the space distribution of cavitation by using an additional low-amplitude radiator to increase the efficiency of cavitation collapses in a remote zone of cavitation activity. Yet, this issue of automatizing cleaning considering the space distribution remains unsolved. Available systems of controlling ultrasonic cleaning are constrained either by time and expert evaluation regarding the need to continue the process or by assessment of the condition of the cleaning liquid including temperature, conductivity, and turbidity (Duran and Teke, 2018; Rahim et al., 2011). This leads to the fact that processing time – and consequently, power consumption – is not associated with the real contamination of a body. In other words, there arises a situation when insonation is related to the cleaned areas of a product. To avoid this, one should use an algorithm controlling ultrasonic cleaning, which will consider contamination of a body in terms of the body's separate areas. Assessing this condition through analysis of ultrasonic reflections in the bath is suggested because ultrasonic measurements provide high-quality and fast evaluation of space-distributed parameters (Porkuian et al., 2019, 2020; Morkun et al., 2015a). A three-dimensional (3D) interval type-2 (IT2) fuzzy logic controller, which is essentially created to control systems with distributed nonlinear parameters, is applied to the process of determining the establishment of a distributed controlling action (Li et al., 2007; Zhang et al., 2017).

2. PROBLEM DESCRIPTION

Let there be a system with distributed parameters describing the process of ultrasonic cleaning. Cleaning occurs due to m ultrasonic radiators located in set positions and set by intensity factors $u(z) = (u(z_1), u(z_2), \dots, u(z_m))$. The input parame-

ters are the measures in P space positions Z_1, Z_2, \dots, Z_p . Moreover, P and m are independent. Figure 1 depicts a bath for ultrasonic cleaning. Here, $\Delta x_z = (\Delta x_{z_1}, \Delta x_{z_2}, \dots, \Delta x_{z_p})$ goes to the system input and is the difference between the two latest measurements of the signal $\Delta x_z = |x_z^{(1)} - x_z|$ and $x_z = (x_{z_1}, x_{z_2}, \dots, x_{z_p})$, the value of the latest measurement. The intensity of the radiators is determined by the controller while analyzing the input parameters. The input parameters are measured by ultrasonic sensors that fix the reflection from the cleaned body in the set time intervals. It is necessary to establish control in such a way that cleaning is performed with minimum energy consumption considering the space distribution of dirt on the object. The space position is set by a 1D radial coordinate.

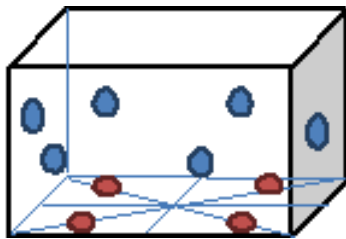


Fig. 1. Diagram of the ultrasonic cleaning bath with the sensors on its sides and the basic cleaning radiators on its bottom

To establish control of the set, a 3D IT2 fuzzy logic controller is used; its functioning algorithm is described in Section 3. Simulation of the controller functioning and comparison of its efficiency with the conventional method of cleaning is performed.

3. DEPENDENCY OF ULTRASONIC REFLECTIONS AND DEVELOPMENT OF CLEANING

Modeling ultrasonic cleaning (Figs. 2 and 3) applying k -wave (Treeby and Cox, 2010) reveals the dependency of the cleaning process and the ultrasonic reflections of a situational character. In other words, a signal can be affected by both dirt peeling, as seen in Fig. 2 (increased amplitude and reduced number of dispersed deviations), and the geometry of the cleaned sections (in Fig. 3, cleaning of the hole increases the dispersed deviations). For this reason, the following assumptions are used to determine the running of the process:

1. The process occurs as cleaning only, i.e., any change of a sensor signal indicates dirt peeling.
2. The sensor closest to the dirt peeling records the greatest change of a signal.

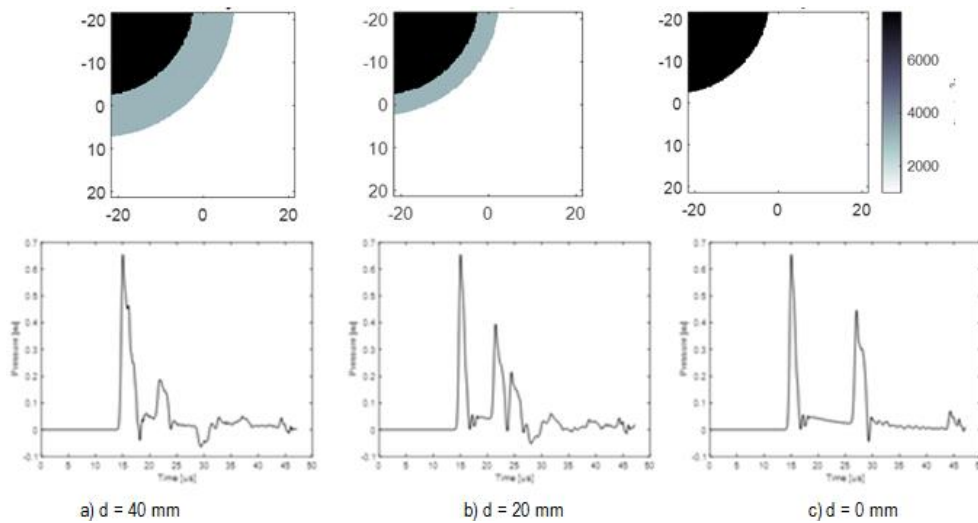


Fig. 2. Acoustic pressure during the processing of a body with contamination density $\rho = 3,100 \text{ kg/m}^3$, velocity of ultrasonic waves $c = 2,500 \text{ m/sec}$, and contamination thickness d (the cleaned body has $\rho = 7,800 \text{ kg/m}^3$ and the ultrasonic wave velocity $c = 5,170 \text{ m/sec}$) for sector of the circle

4. CONTROLLING ULTRASONIC CLEANING BY 3D IT2 FUZZY LOGIC CONTROLLER

Modern industrial advance calls for higher standards of energy efficiency and safety. Conventional methods of controlling systems with concentrated parameters cannot meet these standards, thus causing the necessity to use methods considering the space distribution of the system (Morkun et al., 2015b). The high complexity of mathematical models of these systems almost eliminates their practical application (Morkun and Tron, 2014a; Morkun et al., 2015c). To avoid complex and bulky mathematical models, training algorithms and expert experience are used (Morkun et al.,

2014b, 2015d). A 3D fuzzy logic controller is essentially created to control systems with distributed parameters (Li et al., 2007; Zhang et al., 2017). Expansion of the traditional fuzzy set by an additional space coordinate enables the processing of space data. When applying this controller to automatizing ultrasonic cleaning, space distribution of the system is used. The process is assessed by the changes and the "purity" of the ultrasonic responses in the cleaning container. Expert assessment of this parameter is quite variable. This problem is solved by applying an interval membership function enabling usage of expert assessment in the form of a range.

Thus, a combination of a 3D fuzzy logic controller (Li et al., 2007) and an IT2 fuzzy logic controller (Zadeh, 1975) serves as

the basis for a 3D interval fuzzy logic controller. It enables the establishment of control over ultrasonic cleaning with due regard

for its space distribution in the absence of clear expert assessment of the significance of changes in the ultrasonic response.

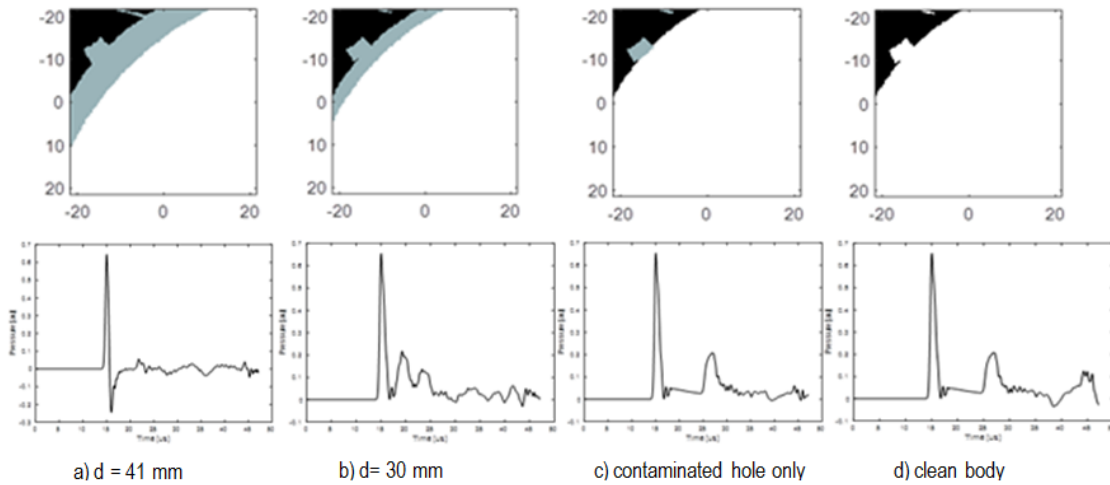


Fig. 3. Acoustic pressure during the processing of a body with contamination density $\rho = 3,100 \text{ kg/m}^3$, ultrasonic wave velocity $c = 2,500 \text{ m/sec}$, and contamination thickness d (the cleaned body has $\rho = 7,800 \text{ kg/m}^3$ and the ultrasonic wave velocity $c = 5,170 \text{ m/sec}$) for sector of the astroid

The membership function and the rule base

According to the problem description, the crisp inputs are $x_1(z)$ and $x_2(z)$, where $z = (z_1, z_2, \dots, z_p)$, denoting the changed ultrasonic responses in the latest cleaning cycle and the values of the latest indices of sensors, respectively. The crisp output indicates the intensity of functioning of the ultrasonic radiators in set positions $u(z) = [u(z_1), u(z_2), \dots, u(z_m)]$. The values of $x_1(z)$, $x_2(z)$ and $u(z)$ are normalized within $[0,1]$. All the variables have three linguistic marks: large (L), medium (M), and small (S). Considering the space distribution of ultrasonic cleaning, the upper and the lower membership functions of the input parameters appear as follows:

$$\underline{\mu}(x_i, z) = \exp\left(-\frac{((x_i - a)^2 + (|2|z - z_0| - 1| - 1)^2)}{\sigma_1}\right)$$

$$\bar{\mu}(x_i, z) = \exp\left(-\frac{((x_i - a)^2 + (|2|z - z_0| - 1| - 1)^2)}{\sigma_2}\right)$$

$$i = 1, 2, z = (z_1, z_2, \dots, z_p) \quad (1)$$

where $\underline{\mu}(x_i, z)$ and $\bar{\mu}(x_i, z)$ are the upper and lower values of the membership function, respectively; x_i is the crisp input; z is the radial input coordinate; a is the value of the linguistic mark with which the membership function acquires the maximum value: for large (L): $a = 1$; for medium (M): $a = 0.5$; and for small (S): $a = 0$, z_0 is the value of the spacious radial output coordinate, σ_1 and σ_2 are the parameters conditioned by the physical properties of both the cleaning container as well as the number of sensors and outputs and belong to the interval $[0,1]$; and i is the number of variables. Figure 4 shows a diagram for the medium linguistic mark (M) and the output $z_0 = 0.2$ and the small mark (S) and the output $z_0 = 0.5$ with $\sigma_1 = 0.1$ and $\sigma_2 = 0.2$. The graph indicates the maximum value in the space point closest to the output, and this corresponds to the linguistic mark.

For the output $u(z)$, the membership function is defined in the trapezoid-triangular form, as shown in Fig. 5. The membership function is 2D as the spatial impact is taken into account during the fuzzification of the input, while the output value is calculated depending on its space location.

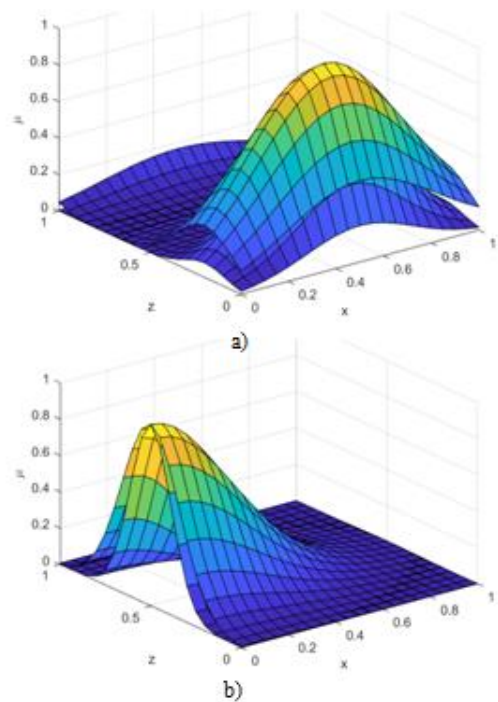


Fig. 4. Diagrams of the upper and lower membership functions: a) for the medium mark (M), for the output $z_0 = 0.2$; b) for the small mark (S), for the output $z_0 = 0.5$

The rule base (Table 1) considers the assumptions presented above: as change of a signal Δx_z is the major evidence of successful cleaning, it is considered more significant than the latest signal x_z conditioned not only by the contamination degree of a product, but also by its geometry and location in the container.

On the basis of the determined membership functions and the rule base, we describe the algorithm of the controller functioning based on the 3D IT2 fuzzy logic set (FS).

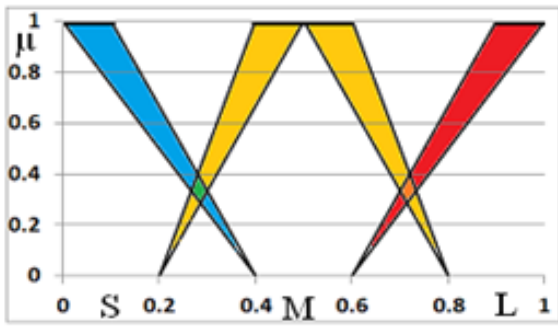


Fig. 5. Membership function for output $u(z)$. S – small, M-medium, L-large.

Tab. 1. Rule base (\tilde{L} - large, \tilde{M} - medium, and \tilde{S} - small)

$\Delta x_z / x_z$	\tilde{S}	\tilde{M}	\tilde{L}
\tilde{S}	\tilde{M}	\tilde{S}	\tilde{S}
\tilde{M}	\tilde{M}	\tilde{M}	\tilde{S}
\tilde{L}	\tilde{L}	\tilde{L}	\tilde{M}

5. THE 3D IT2 FS CONTROLLER

The concept of a 3D fuzzy set is introduced to enable consideration of the space distribution of complex physical and chemical processes (Li et al., 2007; Zhang et al., 2017). The controller based on this set is naturally created for processes with distributed parameters and can be applied to the controlling of ultrasonic cleaning. Expansion of the membership function in the given controller to reach the first interval results in changes of the input formation mechanism. Let us consider the operations within the

3D IT2 FS controller structure.

The structure of the 3D IT2 FS controller is similar to that of the basic one (Mamdani, 1974) with standard operations of fuzzification, the fuzzy logic output, and defuzzification (Fig. 6). Yet, availability of an additional space coordinate and intervals of the membership function call for their expansion. We provide all the controller operations for singleton fuzzification to simplify and contract them.

For the 3D fuzzy set, we determine the fuzzification of the crisp input X in the following way (Li et al., 2007):

$$\begin{aligned} \tilde{A}_{x_1} &= \sum_{z \in Z} \sum_{x_1(z) \in X_1} \frac{\mu_{x_1}(x_1(z), z)}{(x_1(z), z)}, \text{ where } \mu_{x_1}(x_1(z), z) = \\ &= \int_{u \in J_{x_1}} \left[\underline{\mu}_{\tilde{A}}(x_1(z), z), \overline{\mu}_{\tilde{A}}(x_1(z), z) \right] \frac{1}{u} \\ &\vdots \\ \tilde{A}_{x_N} &= \\ &= \sum_{z \in Z} \sum_{x_N(z) \in X_N} \frac{\mu_{x_N}(x_N(z), z)}{(x_N(z), z)}, \text{ where } \mu_{x_N}(x_N(z), z) = \\ &= \int_{u \in J_{x_N}} \left[\underline{\mu}_{\tilde{A}}(x_N(z), z), \overline{\mu}_{\tilde{A}}(x_N(z), z) \right] \frac{1}{u}, \end{aligned} \quad (2)$$

where u is the secondary variable, which is an interval for the membership function with the sets x and z ; J_{x_1}, \dots, J_{x_N} determine the interval of the membership function for the set x_1, \dots, x_N . In the case of ultrasonic cleaning, $\underline{\mu}_{\tilde{A}}(x_i(z), z), \overline{\mu}_{\tilde{A}}(x_i(z), z)$ correspond to $\underline{\mu}(x_i, z)$ and $\overline{\mu}(x_i, z)$ from Eq. (1), while $N=2$. Thus, the general fuzzification for two crisp inputs looks as follows:

$$\tilde{A}_x = \sum_{z \in Z} \sum_{x_1(z) \in X_1} \sum_{x_2(z) \in X_2} \frac{\mu_{x_1}(x_1(z), z) * \mu_{x_2}(x_2(z), z)}{(x_1(z), x_2(z), z)}, \quad (3)$$

where $*$ denotes a t-norm operation.

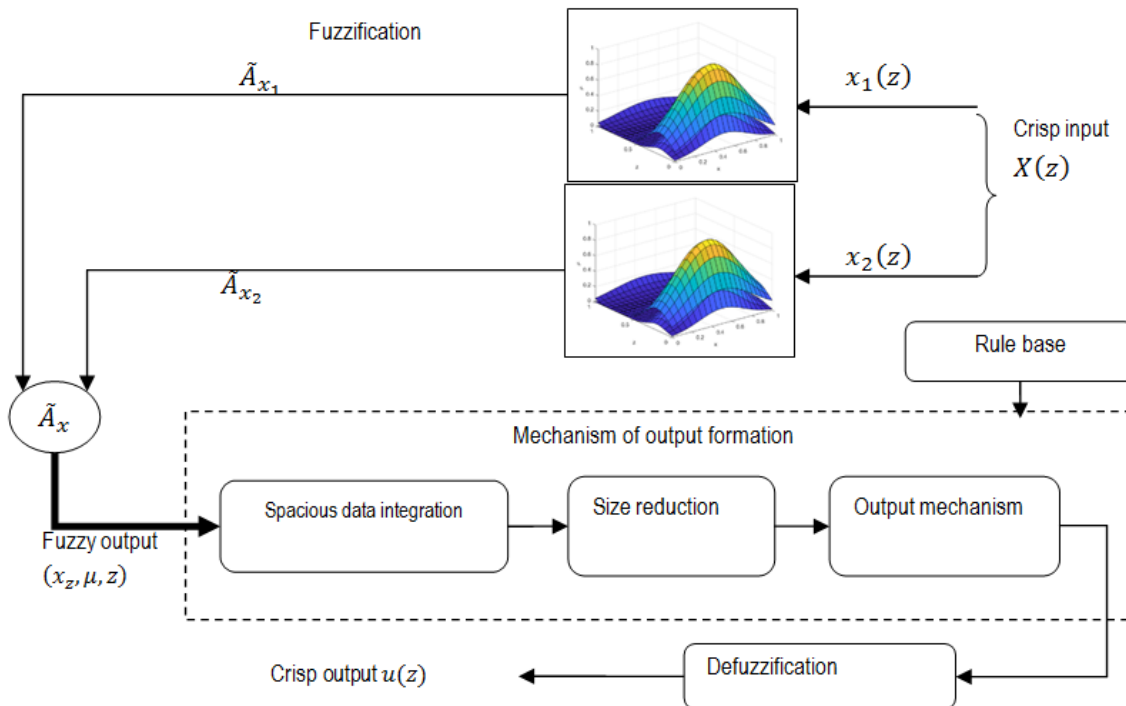


Fig. 6. The 3D IT2 FS controller

To establish control over ultrasonic cleaning, we define a t-norm as an intersection of sets, i.e., for \tilde{A}_{x_1} and \tilde{A}_{x_2} , we have:

$$\tilde{A}_{x_1} = \frac{1}{\bigcup_{\forall x \in X, z \in Z} [\underline{\mu}_{\tilde{A}_{x_1}}(x, z), \overline{\mu}_{\tilde{A}_{x_1}}(x, z)]}; \tilde{A}_{x_2} = \frac{1}{\bigcup_{\forall x \in X, z \in Z} [\underline{\mu}_{\tilde{A}_{x_2}}(x, z), \overline{\mu}_{\tilde{A}_{x_2}}(x, z)]}$$

$$\tilde{A}_{x_1} \cap \tilde{A}_{x_2} = \frac{1}{\bigcup_{\forall x \in X, z \in Z} [\underline{\mu}_{\tilde{A}_{x_1}}(x, z) \wedge \underline{\mu}_{\tilde{A}_{x_2}}(x, z), \overline{\mu}_{\tilde{A}_{x_1}}(x, z) \wedge \overline{\mu}_{\tilde{A}_{x_2}}(x, z)]} = \frac{1}{\bigcup_{\forall x \in X, z \in Z} [\min(\underline{\mu}_{\tilde{A}_{x_1}}(x, z), \underline{\mu}_{\tilde{A}_{x_2}}(x, z)), \min(\overline{\mu}_{\tilde{A}_{x_1}}(x, z), \overline{\mu}_{\tilde{A}_{x_2}}(x, z))]}$$

After fuzzification of the crisp inputs, the fuzzy logic output is established on the basis of the set rule base. According to Table 1, the l -th rule in the base can be written in the following way:

$$\tilde{R}^l: \text{If } x_1(z) \text{ is } \tilde{C}_1^l \text{ and } x_2(z) \text{ is } \tilde{C}_2^l \text{ then } u(z) \text{ is } \tilde{K}^l \quad (5)$$

where \tilde{R}^l is the l -th rule ($l = 1, 2, \dots, 9$); $x_1(z)$ and $x_2(z)$ are the input variables in different points of the space; \tilde{C}_1^l and \tilde{C}_2^l are the 3D IT2 FSs, and $u(z)$ is the controlling action. The next step is to reduce the 3D IT2 FS to conventional IT2 FS. With this, integration of spacious data, size reduction, and output establishment occur. Rule (5) can be written as the following fuzzy ratio:

$$\tilde{R}^l: \tilde{A}_1^l \times \tilde{A}_2^l \rightarrow \tilde{K}^l, l = 1, 2, \dots, 9 \quad (6)$$

The IT2 FS is obtained as a combination of the 3D IT2 FS at the input and application of the rule in the form of fuzzy ratios. Integration of space data results in transformation of the 3D fuzzy logic interval input \tilde{A}_x into the 3D set W^l which is an IT2 FS in

each point $x_z = [x_1(z), x_2(z)]$. The set W is an expanded composition of input sets. Figure 7 shows this composition for the singleton value. The expanded composition performed at the input set and the assigned sets of the l -th rule are presented by Li et al. (2007):

$$W^l_{\tilde{A}_x \circ (\tilde{C}_1^l \times \tilde{C}_2^l)} = \tilde{A}_x \circ (\tilde{C}_1^l \times \tilde{C}_2^l) \quad (7)$$

with the upper and the lower values of the membership function:

$$\underline{\mu}_{W^l} = \underline{\mu}_{\tilde{A}_x \circ (\tilde{C}_1^l \times \tilde{C}_2^l)}(x_z, z) = \sup_{x_1(z) \in X_1, x_2(z) \in X_2} [\underline{\mu}_{\tilde{A}_x}(x_z, z) * \underline{\mu}_{\tilde{C}_1^l \times \tilde{C}_2^l}(x_z, z)] = \sup_{x_1(z) \in X_1, x_2(z) \in X_2} [\underline{\mu}_{x_1}(x_1(z), z) * \underline{\mu}_{x_2}(x_2(z), z) * \underline{\mu}_{\tilde{C}_1^l}(x_1(z), z) * \underline{\mu}_{\tilde{C}_2^l}(x_2(z), z)] = \left\{ \sup_{x_1(z) \in X_1} [\underline{\mu}_{x_1}(x_1(z), z) * \underline{\mu}_{\tilde{C}_1^l}(x_1(z), z)] \right\} * \left\{ \sup_{x_2(z) \in X_2} [\underline{\mu}_{x_2}(x_2(z), z) * \underline{\mu}_{\tilde{C}_2^l}(x_2(z), z)] \right\} \quad (8)$$

$$\overline{\mu}_{W^l} = \overline{\mu}_{\tilde{A}_x \circ (\tilde{C}_1^l \times \tilde{C}_2^l)}(x_z, z) = \sup_{x_1(z) \in X_1, x_2(z) \in X_2} [\overline{\mu}_{\tilde{A}_x}(x_z, z) * \overline{\mu}_{\tilde{C}_1^l \times \tilde{C}_2^l}(x_z, z)] = \sup_{x_1(z) \in X_1, x_2(z) \in X_2} [\overline{\mu}_{x_1}(x_1(z), z) * \overline{\mu}_{x_2}(x_2(z), z) * \overline{\mu}_{\tilde{C}_1^l}(x_1(z), z) * \overline{\mu}_{\tilde{C}_2^l}(x_2(z), z)] = \left\{ \sup_{x_1(z) \in X_1} [\overline{\mu}_{x_1}(x_1(z), z) * \overline{\mu}_{\tilde{C}_1^l}(x_1(z), z)] \right\} * \left\{ \sup_{x_2(z) \in X_2} [\overline{\mu}_{x_2}(x_2(z), z) * \overline{\mu}_{\tilde{C}_2^l}(x_2(z), z)] \right\}$$

where $z \in Z$, the product $*$ indicates the t-norm operation (intersection of sets).

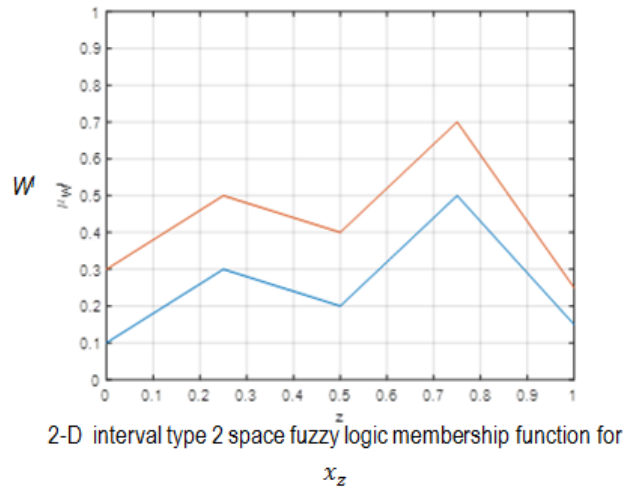
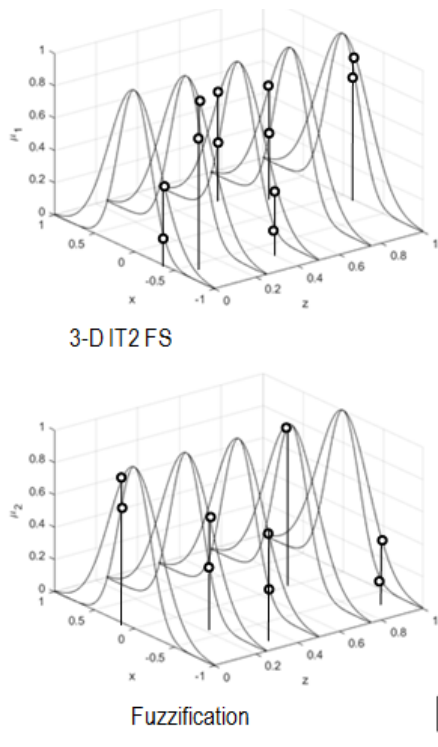


Fig. 7. Integration of space data for each crisp input $x_z = [x_1(z), x_2(z)]$

After integrating three-dimensionality, it is reduced by contracting the 3D data (x_z, μ, z) to the 2D form (x_z, μ) . Reduction

is performed by finding the maximum value, while the upper and the lower membership functions are determined as follows:

$$\underline{\mu}_{\varphi^l} = \max \underline{\mu}_{W^l} \quad \overline{\mu}_{\varphi^l} = \max \overline{\mu}_{W^l} \quad (9)$$

where $\underline{\mu}_{W^l}$ and $\overline{\mu}_{W^l}$ are the lower and the upper values, respectively, of the membership function;

The output consists of accumulation and typecasting. In accumulation, the upper and the lower boundaries of the membership function are determined as shown by Mendel et al. (2006):

$$\underline{\mu}_{\overline{B}}(u) = \max \left(\underline{\mu}_{\varphi^1}(u), \dots, \underline{\mu}_{\varphi^{N'}}(u) \right), \quad \overline{\mu}_{\overline{B}}(u) = \max \left(\overline{\mu}_{\varphi^1}(u), \dots, \overline{\mu}_{\varphi^{N'}}(u) \right), \quad \forall u \in U. \quad (10)$$

where N' is the number of production rules.

In compliance with the paper by Mendel et al. (2006), typecasting is performed by searching for the centroid of all production rules. It results in a collection of numbers with the maximum and the minimum values, i.e.:

$$C_{\overline{B}}(z) = \frac{1}{\{c_l(z), \dots, c_r(z)\}}, \quad (11)$$

where

$$c_l(z) = \min_{\forall \theta_i \in [\underline{\mu}_{\overline{B}}(u_i), \overline{\mu}_{\overline{B}}(u_i)]} \frac{\sum_{i=1}^n u_i \theta_i}{\sum_{i=1}^n \theta_i}, \quad (12)$$

$$c_r(z) = \min_{\forall \theta_i \in [\underline{\mu}_{\overline{B}}(u_i), \overline{\mu}_{\overline{B}}(u_i)]} \frac{\sum_{i=1}^n u_i \theta_i}{\sum_{i=1}^n \theta_i}$$

To find c_l and c_r , we use the formulae of the Karnik–Mendel iteration algorithm (Karnik & Mendel, 2001):

$$c_l(z) = \frac{\sum_{i=1}^l u_i(z) \overline{\mu}_{\overline{B}}(u_i) + \sum_{i=l+1}^N u_i(z) \underline{\mu}_{\overline{B}}(u_i)}{\sum_{i=1}^l \overline{\mu}_{\overline{B}}(u_i) + \sum_{i=l+1}^N \underline{\mu}_{\overline{B}}(u_i)}, \quad (13)$$

$$c_r(z) = \frac{\sum_{i=1}^r u_i(z) \underline{\mu}_{\overline{B}}(u_i) + \sum_{i=r+1}^N u_i(z) \overline{\mu}_{\overline{B}}(u_i)}{\sum_{i=1}^r \underline{\mu}_{\overline{B}}(u_i) + \sum_{i=r+1}^N \overline{\mu}_{\overline{B}}(u_i)}$$

Points r and l are determined iteratively by the Karnik–Mendel algorithm.

Defuzzification is reduced to a simple search for the mean value of the maximum and the minimum values after typecasting (Mendel et al., 2006):

$$u = \frac{c_r + c_l}{2}. \quad (14)$$

6. MODELING CONTROL BY THE 3D IT2 FS CONTROLLER

Ultrasonic cleaning is modeled by creating the ultrasonic pressure field with the assumption that the best cleaning occurs in zones with the largest values of acoustic pressure. Practical expediency of this assumption is confirmed by numerous experiments (Tangsopha et al., 2017; Tangsopha & Thongsri, 2020; Nigmatzyanov et al., 2019). The k -wave software device is applied to modeling, enabling the simulation of large-scale ultrasonic waves in the set period (Treeby & Cox, 2010; Treeby, et al., 2012; Morkun, et al., 2014).

As the space coordinate is actually single, we consider cleaning in a plane, i.e., sensors and radiators are in a single plane.

First, modeling without fuzzy logic control is performed. Four radiators of stable capacity are determined (Fig. 8a). The astroid with a single contaminated side is used as a cleaned product (Fig. 8b).

Contamination peeling is recorded when the acoustic pressure is $>50\%$ compared to the maximum. Experiments reveal that

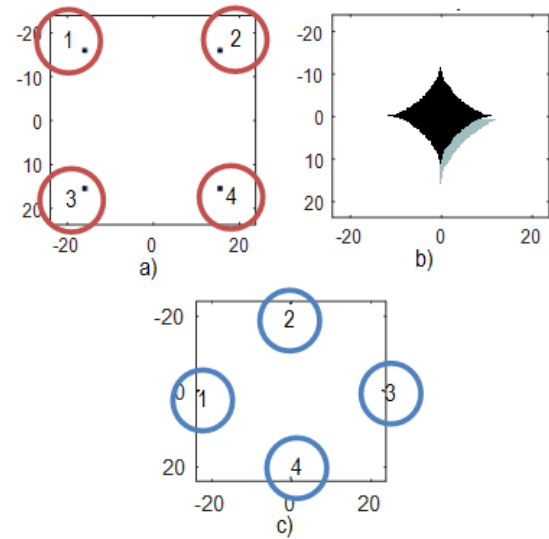


Fig. 8. Initial conditions of the experiment: a) location of the radiators; b) the view of the cleaned body; c) location of the sensors

complete cleaning covers five cycles. With that, all the radiators are engaged, and this stage corresponds to conventional ultrasonic cleaning.

While using fuzzy control, the initial conditions of the experiment remain the same. To assess the running of ultrasonic cleaning, four sensors are used, which are arranged as shown in Fig. 8c. The sensors are both ultrasound radiators and receivers. Changes of signals are assessed by the difference between the amplitudes of the latest signals, while the number of changes of the signal sign becomes the basis for assessing the “purity” of the signal. Initiation occurs as a result of the response after the initial ultrasonic radiation by the sensors. The sensors are set by space positions $z = [0 \ 0.25 \ 0.5 \ 0.75]$, while the coordinates of the radiators are $z_0 = [0.125 \ 0.375 \ 0.625 \ 0.875]$.

In the membership function (1), the following set values of the parameters $\sigma_1 = 0.1$ and $\sigma_2 = 0.2$ are used. After the initial processing according to the analysis of the maximum and the minimum values in each contamination point, the view of the cleaned object is obtained (Fig. 9).

The next step includes processing the body from all four basic radiators, followed up by ultrasonic assessment of the object’s condition.

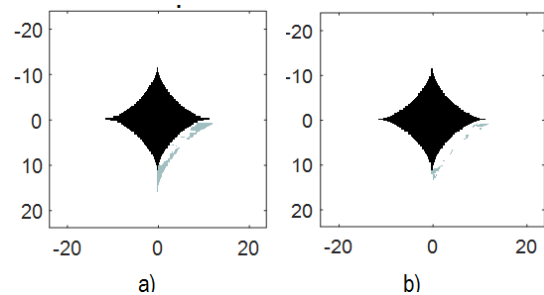


Fig. 9. View of the body after a) the first and b) the second cleaning cycles

Tab. 2. Input ($\Delta x, x$) and output (u) parameters in ultrasonic cleaning

Step number	Δx	x	u	Power saving, %
0	-	-	[1 1 1 1]	0
1	[0.2292 0.0598 1.0000 0.4948]	[1.0000 0.9167 0.6667 0]	[0 0.6051 1.0000 0.4161]	49.47
2	[0.0918 0.0026 1.0000 0.5896]	[1.0000 1.0000 0.5000 0]	[0 0.6253 1.0000 0.3537]	50.53
3	[0.2565 0.0084 1.0000 0.6364]	[1.0000 1.0000 0.3636 0]	[0 0.5488 1.0000 0.4900]	49.03
4	[0.1555 0.0104 1.0000 0.2768]	[1.0000 0.9091 0.2727 0]	[0 0.5159 1.0000 0.2104]	56.84
Total	[0 0 0 0]			41.17

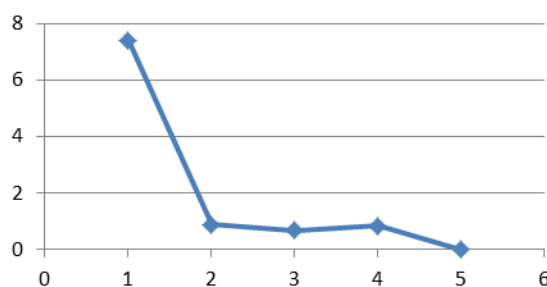


Fig.10. Reduction in the deviation vector module by the cleaning cycles

The normalized indices of the sensors obtained at Step 1 (Table 2) – change of the signal $\Delta x=[0.2292\ 0.0598\ 1.0000\ 0.4948]$ and the values of the latest measurements characterizing the degree of “purity” of the signal $x=[1.0000\ 0.9167\ 0.6667\ 0]$ – are in compliance with both the assumptions about the greatest change of the signal of the sensor closest to the contamination peeling and a great number of deviations in the sensors in close proximity.

After analyzing the sensor data by the controller in compliance with the above algorithm, the following normalized values of intensity for the radiators are obtained: $u=[0\ 0.6015\ 1.0000\ 0.2564]$ (Table 2).

The result obtained is relevant to the contamination pattern as it is located closest to three of the ultrasonic radiators. In the next stage, the intensity of each radiator is set with the amplification factor u . The result of the second cleaning cycle is shown in Fig. 9. The necessity to continue cleaning is determined by the module of the vector of signal deviations between the cycles. To complete cleaning, four cycles are required, besides the initial one. Fig. 10 depicts the reduction of the deviation vector module.

7. CONCLUSIONS

New methods of ultrasonic cleaning considering the space distribution of the process are developed. The described technology is based on the 3D IT2 fuzzy logic controller, which possesses a structure similar to the traditional one considering spatial and interval characteristics of the membership function. The membership functions considering the space impact of the input parameters are determined. A rule base that remains 2D and does not


depend on the number of sensors and outputs is designed. Assessment of cleaning is based on the difference between the ultrasonic reflections of the latest measurements and the number of dispersed deviations of the latest signal. The functioning algorithm of the described controller determines the amplification factor for each output normalized within $[0, 1]$. As some values are <1 , there is power savings of 41.17% for the ultrasonic cleaning process modeled herein.


REFERENCES

- Duran F., Teke M. (2018), Design and implementation of an intelligent ultrasonic cleaning device, *Intelligent Automation and Soft Computing*, 441-450.
- Karnik N., Mendel, J. (2001), Centroid of a type-2 fuzzy set, *Inform.Sci.*, 132, 195-220.
- Li H., Zhang X., Li, S. (2007), A Three-Dimensional Fuzzy Control Methodology for a Class of Distributed Parameter Systems, *IEEE Transactions on Fuzzy Systems*, 15(3), 470-481.
- Mamdani E. (1974), Application of fuzzy logic algorithms for control of simple dynamic plant, *Proceedings of the Institution of Electrical Engineers*, 121(12), 1585-1588.
- Mendel J. M., John R. I., Liu, F. (2006), Interval Type-2 Fuzzy Logic Systems Made Simple, *IEEE Transactions on Fuzzy Systems*, 14(6), 808-821.
- Morkun V., Morkun N., Tron V. (2015d), Model synthesis of nonlinear nonstationary dynamical systems in concentrating production using Volterra kernel transformation, *Metallurgical and Mining Industry*, 7(10), 6-9.
- Morkun V., Morkun N., Pikilnyak A. (2014a), Modeling of ultrasonic waves propagation in inhomogeneous medium using fibered spaces method (k-space). *Metallurgical and Mining Industry*, 6(2), 43-48.
- Morkun V., Morkun N., Pikilnyak A. (2014b), The adaptive control for intensity of ultrasonic influence on iron ore pulp, *Metallurgical and Mining Industry*, 6(6), 8-11.
- Morkun V., Morkun N., Tron V. (2015a), Distributed closed-loop control formation for technological line of iron ore raw materials beneficiation, *Metallurgical and Mining Industry*, 7(7),16-19.
- Morkun V., Morkun N., Tron V. (2015b), Distributed control of ore beneficiation interrelated processes under parametric uncertainty, *Metallurgical and Mining Industry*, 7(8), 18-21.
- Morkun V., Morkun N., Tron, V. (2015c), Identification of control systems for ore-processing industry aggregates based on nonparametric kernel estimators, *Metallurgical and Mining Industry*, 7(1), 14-17.
- Nigmatzyanov R. I., Kazantsev V. F., Prikhod'ko V. M., Sundukov S. K., Fatyukhin D. S. (2019), Improvement in Ultrasound Liquid Machining by Activating Cavitation Clusters, *ISSN 1068-798X, Russian Engineering Research*, 8, 699-702.
- Porkuian O., Morkun V., Morkun N. (2020), Measurement of the ferromagnetic component content in the ore suspension solid phase, *Ultrasonics*, 105, 106103.
- Porkuian O., Morkun V., Morkun N., Serdyuk O. (2019), Predictive Control of the Iron Ore Beneficiation Process Based on the Hammerstein Hybrid Model, *Acta Mechanica et Automatica*, 13(4), 262-270.
- Rahim A., Bardoshadi H. and Sarrafi S. (2011), Design and Manufacture an Ultrasonic Dispersion System, *Sensors and Transducers Journal*, 126(3), 52-63.
- Roohia R., Abedib E., Hashemi S. M. B., Marszałek K., Lorenzo J. M., Barbae F. (2019). Ultrasound-assisted bleaching: Mathematical and 3D computational fluid, *Innovative Food Science and Emerging Technologies*, 55, 66-79.
- Tangsopha W., Thongsri J., Busayaporn W. (2017). Simulation of ultrasonic cleaning and ways to improve the efficiency. *5th International Electrical Engineering Congress*, 8-10.

19. **Tangsopha W., Thongsri J.**, (2020), A Novel Ultrasonic Cleaning Tank Developed by Harmonic Response Analysis and Computational Fluid Dynamics, *Metals*, 10(335), 1-18.
20. **Treeby B. E., Jaros J., Rendell A. P., Cox B. T.** (2012), Modeling nonlinear ultrasound propagation in heterogeneous media with power law absorption using a k-space pseudospectral method, *Acoustical Society of America*, 131(6), 4324–4336.
21. **Treeby B.E., Cox T.** (2010), k-Wave: MATLAB toolbox for the simulation and reconstruction of photoacoustic wave fields, *Journal of Biomedical Optics*, 15(2), 021314.
22. **Xu H., Tu J., Niu F., Yang, P.** (2016), Cavitation dose in an ultrasonic cleaner and its dependence on experimental parameters, *Applied Acoustics*, 101, 179–184.
23. **Zadeh L.** (1975), The concept of a linguistic variable and its application to approximate reasoning, *Inform.Sci.*, 8, 199-249.
24. **Zhang X., Fu Z.-Q., Li S.-Y., Zou T., Wang B.** (2017), A time/space separation based 3D fuzzy modeling approach for nonlinear spatially distributed systems, *International Journal of Automation and Computing*, 15, 1-14.

The authors express their sincere gratitude to Kryvyi Rih National University for support in conducting this research.

Volodymyr Morkun:  <https://orcid.org/0000-0003-1506-9759>

Olha Kravchenko:  <https://orcid.org/0000-0003-0667-2695>

HAND GUIDING A VIRTUAL ROBOT USING A FORCE SENSOR

Radovan GREGOR^{*} , Andrej BABINEC^{*} , František DUCHON^{*} , Michal DOBIŠ^{*} 

^{*}Faculty of Electrical Engineering and Information Technology, Institute of Robotics and Cybernetics, Slovak University of Technology (STU) in Bratislava, Ilkovičova 3, SK-812 19, Bratislava, Slovakia

radkog@gmail.com; andrej.babinec@stuba.sk; frantisek.duchon@stuba.sk; michal.dobis@stuba.sk

received 14 April 2021, revised 18 July 2021, accepted 20 July 2021

Abstract: The research behind this paper arose out of a need to use an open-source system that enables hand guiding of the robot effector using a force sensor. The paper deals with some existing solutions, including the solution based on the open-source framework Robot Operating System (ROS), in which the built-in motion planner MoveIt is used. The proposed concept of a hand-guiding system utilizes the output of the force–torque sensor mounted at the robot effector to obtain the desired motion, which is thereafter used for planning consequential motion trajectories. Some advantages and disadvantages of the built-in planner are discussed, and then the custom motion planning solution is proposed to overcome the identified drawbacks. Our planning algorithm uses polynomial interpolation and is suitable for continuous replanning of the consequential motion trajectories, which is necessary because the output from the sensor changes due to the hand action during robot motion. The resulting system is verified using a virtual robot in the ROS environment, which acts on the real Optoforce force–torque sensor HEX-70-CE-2000N. Furthermore, the workspace and the motion of the robot are restricted to a greater extent to achieve more realistic simulation.

Keywords: hand guidance, force–torque sensor, motion planning, industrial robot, Robot Operating System

1. INTRODUCTION

According to the International Federation for Robotics (IFR; <https://ifr.org/free-downloads/>, 2020), in 2018, >400,000 new industrial robots were installed in the manufacturing sector. The annual increase in this parameter was 6%, which—at the end of 2018—increased the "population" of industrial robots to 2,439,543 pieces. The dominant segments are the automotive, electronics, metalworking, plastics, and food industries. Such growth is also due to new technologies that make it easier to work with robots for nonprofessional users. One of these technologies is power–torque control, which allows robots to provide "touch" and enables users to work with the robot at the level of manual guidance. This technology makes it possible to create robotic applications more efficiently and in a significantly accelerated manner.

The following standards apply in particular to industrial robots' work in cooperation with humans:

- a) International Organization for Standardization (ISO) 10218 – 1 Robots and robotic devices - Safety requirements for industrial robots. Part 1 Robots.
- b) ISO 10218 – 2 Robots and robotic devices - Safety requirements for industrial robots. Part 2 Robot systems and integration and technical standard.
- c) ISO technical standard (TS) 15066 – Robots and robotic devices - Collaborative robots.

The first standard describes the requirements and guidelines for safe design, protective measures, and information for industrial robot usage. It describes the basic risks associated with robots and describes the elimination or adequate reduction of risks. The second standard deals mainly with the integration and installation of industrial robots into cells or production lines. This standard is a continuation of the first one; it is much more detailed, and it speci-

fies the requirements for individual elements of the robotic system. The technical standard TS 15066 describes the safety requirements for the integration of collaborative robotic applications. Collaborative robotic systems differ from standard industrial ones in that the operator may work close to the robotic system. Simultaneously, the robot does not limit its activities in any way and can thus come into physical contact with the human operator.

Human–robot collaboration can have the following four modes:

- Safety-rated monitored stop;
- Hand guiding;
- Speed and separation monitoring; and
- Power and force limiting.

This paper focuses on the area of hand guiding of robots. Our research is unique in that it provides an open-source solution based on a relatively inexpensive force–torque (FT) sensor. The goal of our research is to point out the possibilities of using low-cost reusable solutions when hand guiding the robot effector, which is a better solution than using a teach pendant in the process of teaching robotic paths. An example of such use can be tracking of an uneven path with many via points when using a teach pendant, which could be more time-consuming. In this research, we have also focused on the fluency and safety of the robot's motion during the hand-guiding process so that it is more ergonomic for an operator. The algorithms were tested on the virtual robot model KUKA KR16. It is an industrial robot that is not intended for use outside a cage, but during the teaching process, its maximum speed is limited to the safe value; thus, hand guiding is allowed.

The paper is organized as follows. Section 2 demonstrates the current state of the art and defines the uniqueness of our solution. Section 3 describes the hardware and software components used

in this work and the methodology. Section 4 shows how the data from the FT sensor were processed. Sections 5 and 6 show the visualization of the whole process and the configuration of the solution, respectively. Section 7 describes the implementation of our solution since the existing path planning system is unsuitable for our purpose. Section 8 presents the results of the experiments and the verification of the whole solution.

2. RELATED WORKS

According to Matheson et al. (2019), in the field of human-robot collaboration (HRC), robots with technologies corresponding to power- and force-limiting operating modes are primarily used, but the number of applications of standard industrial robots using hand-guiding and speed-monitoring modes is also increasing. Manual guidance is a representative functionality of cooperative robots, which allows unqualified users to interact with and program robots more intuitively than while using a teach pendant (Safeea et al., 2017). Such functionality is made possible mainly by sensing the forces and torques.

Loske and Biesenbach (2014) describe a typical implementation of an FT sensor integrated for hand guiding into an industrial robot's control. The article includes a SI-130-10 sensor integrated with a KR 16-2 robot. Functional applications, such as hand guiding, hand-guiding motion learning, and sensor-guided motion, have been demonstrated. The results show the need to configure such a sensor, especially with reference to gravity. The article also demonstrates the much higher efficiency of the robot's learning for the required movements and points in space.

Reyes-Uquillas and Hsiao (2021) analyze manual guidance control using an FT sensor. They propose an adaptive admittance law that can adjust the parameters of the FT sensor to modify robot compliance in critical areas of the workspace, such as near and on-configuration singularities, joint limits, and workspace limits, for a smooth and safe operation. This demonstrates the further usefulness of FT sensors in manual guidance and advanced control methods.

In another paper (Safeea et al., 2019), the authors deal with a robot's precise manual guidance at the level of the end effector when navigating around obstacles. An FT sensor is used to manually guide the robot, while the compliant robot's body is used to detect contact with an obstacle. Thus, the solution proves the possibility of using the FT sensor for manual guidance even with more-expensive compliant robots, such as the KUKA iiwa. Another method of precise manual guidance with an expensive compliant robot is demonstrated by Safeea et al. (2017). In this case, FT sensing is used directly from the joints of the robot itself.

Massa et al. (2015) analyze the various possibilities of manual robot guidance. For example, various admittance/impedance control methods or the use of different learning methods for this type of guidance are given. The authors show that a key aspect of robot programming is for the operator to consider the robot as a reduced-mass tool. The result is an ability to intuitively learn how to use a robot, even for an operator who has no experience with robotics. The article also excellently demonstrates the possibility of using an FT sensor for this purpose. Simultaneously, the authors focus on gravity compensation during manual guidance of the robot using an FT sensor.

Jamone et al. (2014) describe the use of a six-axis FT sensor on a humanoid robotic arm. In this case, the FT sensor was used to detect the internal and external forces acting on the robotic

arm. The article also presents the control strategies for a robotic arm without knowledge of the environment. A similar system is also addressed by Jo et al. (2013), whereby a robotic arm is used to grasp objects. It is equipped with FT sensors with gravity compensation, and the control is designed based on torque-to-velocity transformation using FT sensors.

Peng et al. (2021) have presented a robotic assembly methodology for the manufacture of large, segmented composite structures. A robot wrist-mounted FT sensor enables gentle but secure panel pickup and placement. Human-assisted path planning ensures reliable collision-free motion of a robot with a large load in a tight space. This work demonstrates the versatility of sensor-guided robotic assembly operations in a complex end-to-end task using the open-source Robot Operating System (ROS) software framework.

A very interesting way of using an FT sensor is presented by Zhao et al. (2020). In their work, the peg-in-hole approach for a six-parallel-legged robot is proposed. An FT sensor is used to plan the trajectory in real time to mate the peg and the hole.

Lee et al. (2016) and Zhang et al. (2019) deal with hand-guiding learning as a more suitable alternative for the learning of industrial robots rather than learning with a teach pendant. However, these authors do not suggest manual guidance using an FT sensor but rather a sensorless guiding method based on torque control on the robotic arm's motors. This method depends on the robot's exact dynamic model, which is not always available (especially in the case of commercial manufacturers). Moreover, commercial manufacturers of robotic systems may not allow new robot control methods to be implemented. Current FT sensors can extend such functionality on a commercially available robot and quickly detect forces and torques. At the same time, the price of FT sensors has dropped dramatically recently. An example of such an innovative sensor is given in a previous work (Noh et al., 2016). An example of a similar sensor, which is used in our research, is the Optoforce sensor (<https://www.coden.org/blog/finalist-optoforce-hungary-sensors-for-the-internet-of-things/>, 2015). Optoforce is a young innovative spin-off company that has already been bought by OnRobot (<https://www.crunchbase.com/organization/optoforce>, 2020), with renaming of the original sensor as HEX FT sensor (<https://onrobot.com/en/products/hex-6-axis-force-torque-sensor>, 2021).

FT sensing has great applications not only in hand-guiding of robots but also in other controls, as demonstrated by Safeea et al. (2019), Jamone et al. (2014), and Jo et al. (2013). Furthermore, in the Strategic Research Agenda for Robotics in Europe 2014–2020 (https://www.eu-robotics.net/cms/upload/topic_groups/SRA_2020_SPARC.pdf, 2020), emphasis is placed on sensor-based safety systems to enhance human-robot interaction, multiple degrees of freedom, tactile feedback, and physical human-robot interaction. The technology that would lead to these goals is described in this strategic document as the compliant control of a complex mechanical structure with visual and tactile perception of human interaction to produce intuitive physical interfaces. This is exactly what hand guiding of a robot using a force sensor fulfills.

FT sensors can be used effectively in various applications with industrial robots, but they are also often used as safety sensors. This is demonstrated, for example, in the article by González et al. (2021). The authors demonstrate an advanced teleoperation and control system for industrial robots in order to assist the human operator to perform tasks such as sanding, deburring, finishing, grinding, polishing, and so on. An FT sensor mounted on the robot

end effector is utilized as a safety indicator to stop the motion of the robot system when the sensor measurements are abnormally large.

As mentioned earlier, in our research, we use the Optoforce sensor, specifically, the HEX-70-CE-2000N version. The sensor is composed of a system of three three-axis hemispherical sensors. The sensors are inserted between two cylindrical aluminum plates with a diameter of 70 mm. The range of measured forces varies depending on the measurement axis. The highest measurable value of the force is in the F_z axis. The manufacturer specifies its value at 2000 N. At certain pressures in the F_z axis, the silicone forms a protective layer around the sensors to prevent damage. As a result of the flexible properties of silicone, the sensors can withstand a maximum possible overload in one axis of up to 200% of the specified nominal value without permanent damage. When obtaining data from the sensor, we used a reading frequency of 100 Hz, while the maximum possible frequency is 1 kHz. This sensor is characterized by high resolution, the possibility of use with various robots, and a relatively low price. There is also a package for this sensor in the ROS environment (<https://github.com/shadow-robot/optoforce>, 2020), used in the presented research.

The advantages of our solution compared to the solutions described earlier are the following:

- The solution is developed using several open-source modules in ROS. These include the following standard packages:
 - MoveIt - motion planning framework designed primarily for trajectory planning and inverse kinematics calculation based on selected algorithms;
 - Gazebo - a simulation environment that allows simulating the dynamics of a robot;
 - ros_control and ros_controllers - set of software packages for the use and development of robot controllers; and
 - RViz - a three-dimensional visualization tool.
- Considering that open-source modules are used, the solution is easily extensible and scalable, which is not the case with the closed proprietary systems described earlier.
- The solution can be easily and quickly implemented on various robots – from standard industrial robotic arms through power-sensitive robots to mobile manipulators. This advantage is also made possible by the use of ROS.
- Based on the force acting on the sensor, a planning process is periodically started, which generates the currently required trajectory for the robot effector. In contrast, rescheduling and exchanging the trajectory takes place smoothly in terms of position and speed without interruption of movement.
- Trajectory planning is constantly monitored so that a plan that would cause a fundamental change in arm configuration (e.g., from the elbow up to elbow down) is not triggered. These changes can occur either near a configuration where a joint is approaching a constraint or close to singular configurations. Such a plan is assessed as risky, and its execution is suspended.

3. COMPONENTS AND METHODOLOGY

When implementing the solution of manual robot guidance based on an FT sensor, the ROS framework was used, enabling the design and verification of robot control algorithms without the need for physical connection of the robot. The advantage of this solution is that the same implementation can be redirected to a

real robot's control. The ROS acts as an interconnection element between the systems.

The control algorithms were verified on the model of the industrial manipulator KUKA KR16, which consists of models of individual parts of the robot provided in stereolithography (STL) file format, and their kinematics is defined using the unified robot description format (URDF). These models and the URDF are available in ROS-Industrial, which contains experimental packages for KUKA manipulators, including the `kuka_kr16_support` package (<https://www.crunchbase.com/organization/optoforce>, 2020). Other important components are MoveIt, ros_control, Gazebo, and RViz; the necessary configuration files for these components are described later in the "Configuration" section.

To integrate the Optoforce sensor into the system, an optoforce package was used, which contains an ROS node for operating the FT sensor (<https://github.com/shadow-robot/opto-force>, 2020). As shown in Section 4, the sensor measurements suffer from noise, drift, and bias; therefore, the acquired data need to be preprocessed. The force and torque vectors are then computed from the processed sensor measurements.

To perform a robot motion corresponding to the applied force, motion planners have been utilized. The input to the motion planner is usually the current and final pose of the robot effector. Therefore, we need to determine the position vector \mathbf{p} of the desired point in the robot workspace to which the robot effector will be moved. Assuming that the position vector is expressed in the effector's coordinate system, it can be computed by a simple proportional reduction of the force vector \mathbf{F} using the proportional constant k_p according to Eq. (1).

$$\mathbf{p} = k_p \mathbf{F} \quad (1)$$

Such a point can be regarded only as an auxiliary point, and there is no need to completely achieve this position during robot motion. However, the magnitude of the position vector may be used to determine the desired speed of the robot effector during hand guidance; in this context, the safety of the operator must be ensured by limiting the speed. The value of the proportional constant $k_p = 0.002 \text{ m/N}$ was determined experimentally.

Initially, in our research, the planning process was performed using the MoveIt framework, which is described in Section 7.1; however, we find this approach to be unsuitable. Therefore, the new planning method described in Section 7.2 was implemented.

4. SENSOR DATA PREPROCESSING

To interconnect the Optoforce sensor with the ROS platform, installing the Optoforce driver was necessary (<https://github.com/shadow-robot/optoforce>, 2020). The driver uses the pySerial library to retrieve data from the sensor via the Universal Serial Bus. The data frequency is set to 100 Hz by default. During initialization, the configuration parameters are read, including coefficients for conversion from device-specific units to newtons and newton-meters. When started, the driver publishes messages to a topic called `optoforce_0`. The messages are in the ROS format called `geometry_msgs/WrenchStamped`. The data message contains the force and torque vectors' coordinates acting on the sensor in the sensor coordinate system, which is aligned with the tool0 system. Tool0 is defined in the URDF description of the robot as the coordinate system of the effector.

Before the sensor data can be used, the sensor must be calibrated. A series of experiments were performed to determine the

calibration parameters. As an example, the calibration of the sensor in the Z-axis is described. The sensor was placed such that the gravitational force acts only in the opposite direction of its axis. At zero static load, a zero-output value is assumed, and at a load of 1 kg, an output value of -9.806 N is assumed. Table 1 shows the average output values for the indicated number of samples.

Tab. 1. Evaluation of the uncalibrated sensor output

Number of samples	Used weight, kg	Theoretical output, N	Maximum acquired output, N	Minimum acquired output, N	Average acquired output, N	Average deviation, N
7,898	1	-9.806	-4.0094	-5.8962	-5.2917	3.0885

Figure 1 shows that the sensor values fluctuate significantly under static load. Another measurement lasting longer at zero load revealed that the identified deviation is accompanied by drift, as evidenced in Fig. 2. Based on the measurements, the functionality was approximated by a first-order polynomial, as follows:

$$f(x) = 0.26924x + 2.923 \quad (2)$$

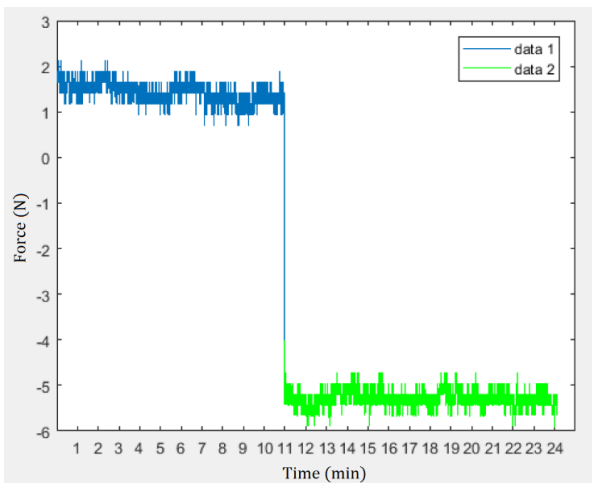


Fig. 1. Fluctuation of the sensor outputs at zero and nonzero static loads

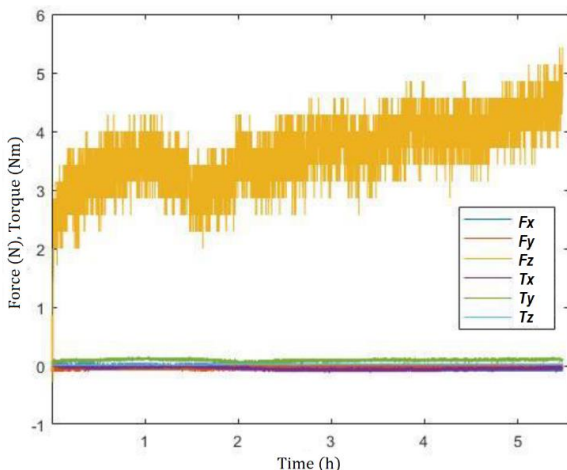


Fig. 2. Experiment revealing the drift of the sensor output value

Tab. 2. Measuring the transfer characteristic

Measurement number	Used weight, kg	Gravitational force, N	Acquired output, N	Measurement error	
				Absolute, N	Relative, %
1	1.00	9.806	28.412	18.606	189.70
2	1.97	19.317	60.51	41.193	213.20
3	4.38	42.95	123.12	80.17	186.00
4	10.09	98.942	315.6	216.658	218.9
5	20.40	200.042	638.15	438.108	219.00

Based on the other measurements listed in Table 2, the transfer characteristic between the actual and measured data was interpolated, as in Eq. (3).

$$f(x) = 3.218x - 5.633 \quad (3)$$

Using this relationship, the average relative error dropped to 5.65%. Calibration had to be done for the other axes similarly.

5. VISUALIZATION OF PROCESS

The KUKA KR16 robot model was visualized in the RViz environment. The magnitude and direction of the force acting on the Optoforce sensor, located on the sixth axis of the robot, are used to determine the new point to which the robot is moving. This point's position vector expressed in the effector coordinate system is represented by a red arrow starting from the center of the tool0 coordinate system (Fig. 3). The visualization of the vector is dynamic, depending on the actual force applied to the sensor.

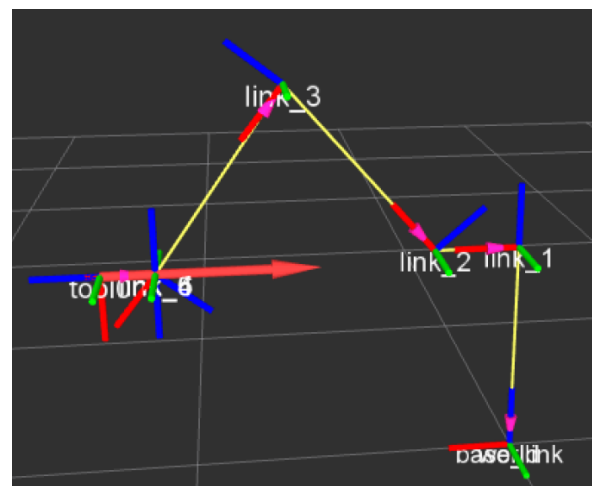


Fig. 3. Visualization of the KUKA KR16 robot model in the RViz environment with the position vector of the point to which the robot is moving

For detailed visualization of the data from Optoforce, the tool from the ROS Qt (RQt) framework that monitors the topic of optoforce_0, was used. The output is the time-dependent data shown

in Fig. 4. In the RViz environment, the results are reconstructed from the detected force and torque components and visualized with an arrow as the force and torque vectors using the WrenchStamped module (Fig. 5).

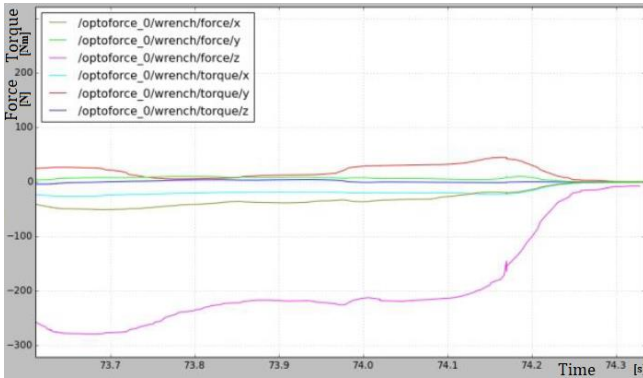


Fig. 4. Visualization of data from Optoforce by monitoring the topic of optoforce_0

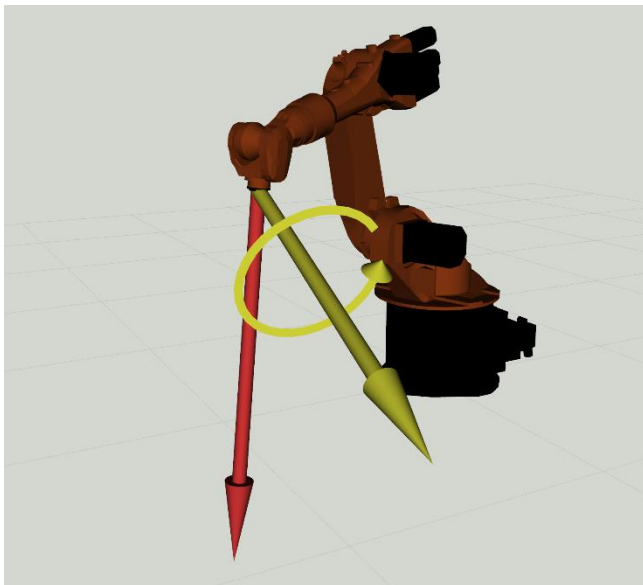


Fig. 5. Force and torque vectors reconstructed from the detected force and torque components

6. CONFIGURATION OF SOLUTION

The kinematic model of the KUKA KR16 industrial manipulator is described in the URDF format. This model needs to be extended with the manipulator's dynamic properties, such as weights, centers of gravity, and moments of inertia of all moving parts of the robot. These values are approximately calculated in the computer-aided design (CAD) software based on the geometry and material properties. They are then exported to the URDF format via the SolidWorks to URDF (SW2URDF) plugin.

An example of the modified parameters for link 1:

```
~/catkin_ws/src/kuka/robots/kuka.urdf
...
2 <inertial>
3 <origin rpy="0 0 0" xyz="0 0 0"/>
4 <mass value="21.654"/>
// default value: 2 kg
```

```
5 <inertia ixx="0.5521" ixy="0.046477"
ixz="0.28985" iyy="0.81346"
iyz="0.050687" izz="0.71343"/>
// default values: 0.01 Kg*m^-2
6 </inertial>
...
```

For the correct simulation in Gazebo, it is important to add information about the URDF structure into the <transmission> part. This part defines the relationship between drives and joints. Since the Movelt tool is also used for trajectory planning, in addition to the URDF, it is necessary to create a Semantic Robot Definition Format (SRDF) file that describes the mutual collision positions of individual robot arms, virtual joints, planning groups, fixed joints, and other parameters related to the movement and interaction of the robot with the environment. This file is created by the Movelt Setup Assistant, which provides a graphical interface for configuration. The default algorithm from the Kinematics and Dynamics Library (KDL) is used to calculate the inverse kinematics, and the Open Motion Planning Library (OMPL) is used for trajectory planning as it includes the RRTConnect algorithm, which is selected as a planner for Movelt. Later, in our proposed planning method, a linear interpolation is used between the individual transition points located on the calculated planned trajectory.

To link Movelt and Gazebo, a JointTrajectory controller is used. This controller is defined in a configuration file in Yet Another Markup Language (YAML) format, where the proportional-integral-derivative (PID) parameters of the positioner and the frequency of publishing the joint status are defined. In Fig. 6, an rqt_graph of the connection between the controller and Gazebo can be seen.

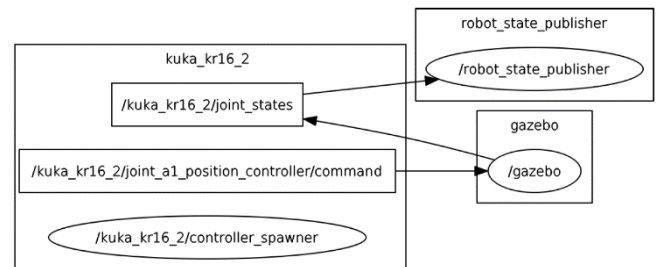


Fig. 6. Rqt_graph showing the connection between the controller and Gazebo

7. IMPLEMENTATION

The article compares two approaches. The first is the use of all available packages and the planning of robot movements using the Movelt planner. This approach's disadvantage is that the robot always stops after the trajectory is completed to start planning a new movement. The second approach assumes the implementation of an own planning algorithm, which eliminates this problem, and the planned trajectory is modified while the robot is moving.

7.1. Planning with Movelt

After configuring the system, a node was created with an algorithm to control the manipulator's movement. The controller accesses the data from the sensor by retrieving messages from the topic optoforce_0. Based on this, it is possible to create a result-

ant vector of the applied force, which defines the desired direction of movement of the robot's endpoint. Subsequently, we can determine the position vector of the point to which the robot effector is moved. Since the planner works with the coordinates relative to the robot's base coordinate system, the coordinates of the position vector of the target position are transformed into the base coordinate system. The orientation of the effector is changed similarly. Based on the resulting torque vector acting on the sensor, the effector's required orientation is also calculated as a proportional reduction of the torque vector. Using the `moveit::planning_interface::MoveGroup` class and its `getCurrentPose()` method to get the current position of the effector, the effector's current position is acquired. The request to plan a new trajectory must contain the target position and orientation (ROS message `geometry_msgs::Pose`), which is sent to MoveIt using the `plan()` method, and the output is the new trajectory. The trajectory is formed by a series of waypoints that have all the joint positions explicitly specified. The resulting trajectory is then sent to a controller that controls the position of the joints.

7.2. Planning with the proposed algorithm

The disadvantage of the `move_group` node is that further planning and control are possible only after the current task is completed. Therefore, the `move_group` node waits until it receives information from the server about reaching the goal. This results in the robot stopping at each point determined by the computed position vector. By using the `FollowJointTrajectory` motion service, it is possible to obtain smoother movements. This control system implements a method for replacing a part of the planned trajectory. It allows rescheduling of the trajectory and launching of a new plan at a specific time. When we send a new message of the type `trajectory_msgs/JointTrajectory`, the controller joins the trajectories at time t^* specified in the new message's header. At t^* , the controller switches from the previous trajectory to follow the new trajectory as depicted in Fig. 7.

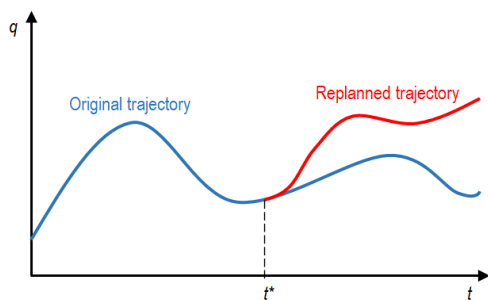


Fig. 7. Principle of the joint trajectory switching

It is important to ensure that the positions and velocities at time t^* are the same for both trajectories. For this purpose, the call to the `query_state` service is used, which provides the information about the current trajectory's future positions and velocities at the requested time (Joint Trajectory Action Controller, Official webpage ROS Documentation, 2020).

The planning algorithm can then use different interpolation techniques to generate a joint path from the current position and velocity at time t^* to an auxiliary position given by the position vector \mathbf{p} calculated using Eq. (1). In our case, we used interpola-

tion based on a cubic polynomial. It is then needed to specify the constraint conditions, which are the initial and final positions of the joints $\mathbf{q}(t_0)$ and $\mathbf{q}(t_f)$, as well as the initial and final velocities in the joints $\dot{\mathbf{q}}(t_0)$ and $\dot{\mathbf{q}}(t_f)$, to ensure that the positions and velocities at time t^* are the same for the current and the replacing trajectories. The acceleration will not be limited in any way, so we anticipate that there will be a step change in the acceleration when switching from one trajectory to another. However, the controller in the robot's joints can handle this step change without major problems. Based on the limiting conditions and the requirement of the cubic shape of the polynomial, we can compile a set of equations for one joint, as in Eq. (4), which can be rewritten into a matrix shape, as in Eq. (5) [24]. The polynomials' coefficients can then be calculated according to the equations in Eq. (6), which were derived from Eq. (5). The trajectory for each joint of the manipulator is formulated likewise.

$$\begin{aligned} q(t_0) &= a_0 + a_1 t_0 + a_2 t_0^2 + a_3 t_0^3 \\ \dot{q}(t_0) &= a_1 + 2a_2 t_0 + 3a_3 t_0^2 \\ q(t_f) &= a_0 + a_1 t_f + a_2 t_f^2 + a_3 t_f^3 \\ \dot{q}(t_f) &= a_1 + 2a_2 t_f + 3a_3 t_f^2 \end{aligned} \quad (4)$$

$$\begin{bmatrix} q(t_0) \\ \dot{q}(t_0) \\ q(t_f) \\ \dot{q}(t_f) \end{bmatrix} = \begin{bmatrix} 1 & t_0 & t_0^2 & t_0^3 \\ 0 & 1 & 2t_0 & 3t_0^2 \\ 1 & t_f & t_f^2 & t_f^3 \\ 0 & 1 & 2t_f & 3t_f^2 \end{bmatrix} \cdot \begin{bmatrix} a_0 \\ a_1 \\ a_2 \\ a_3 \end{bmatrix} \quad (5)$$

$$a_0 = q_0 \quad a_2 = \frac{3(q_f - q_0) - (2\dot{q}_0 + \dot{q}_f)(t_f - t_0)}{(t_f - t_0)^2} \quad (6)$$

$$a_1 = \dot{q}_0 \quad a_3 = \frac{-2(q_f - q_0) + (\dot{q}_0 + \dot{q}_f)(t_f - t_0)}{(t_f - t_0)^3}$$

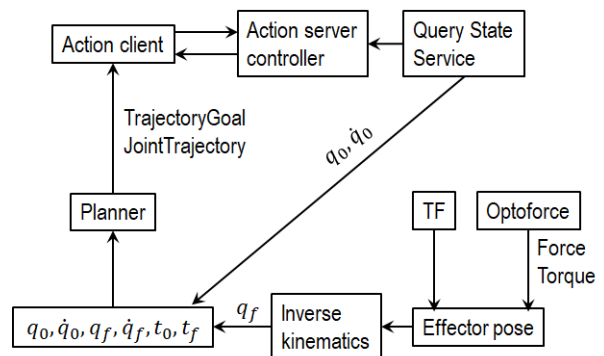


Fig. 8. Block diagram of the proposed system with continuous replanning procedure reacting on sensor readings

We obtained the initial position and velocity of the planned trajectory from the `query_state` service. The initial time of the planned trajectory will therefore be $t_0 = t^*$. For safety reasons, the final speed $\dot{q}(t_f)$ is set to 0 ms^{-1} . However, during the continuous planning process, the robot will not stop because the next new planned trajectory will overwrite the current trajectory after time t^* , and the zero speed requirement is delayed. The joints' final positions must be calculated using inverse kinematics from the position vector \mathbf{p} of the target position obtained from the data from the force sensor, as shown in Fig. 8. To calculate the inverse

kinematics in MoveIt, there is a dedicated setFromIK() method in the RobotState class.

7.3. Increasing the security of the solution

Since the planned trajectories are created from linear sections to ensure their unambiguity, there may be sudden undesirable changes in the arm's configuration (see Fig. 10) near the singularity or joint limit. Therefore, it is necessary to limit the resulting solution. If the arm configuration reaches such a position that one of the joints approaches the limit of its range (Fig. 9), then the new planned position in the original configuration would not be achievable. It would be necessary to rotate one or more joints into another overall arm configuration. From the point of view of manual guidance operation, this movement would be dangerous. Therefore, a new node has been created to monitor and limit potentially dangerous configuration changes.

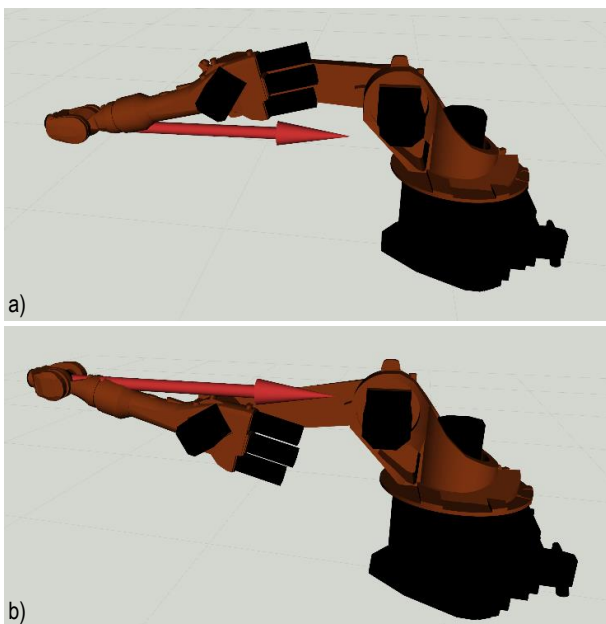


Fig. 9. Two different arm configurations for the same effector position: (a) elbow up; (b) elbow down

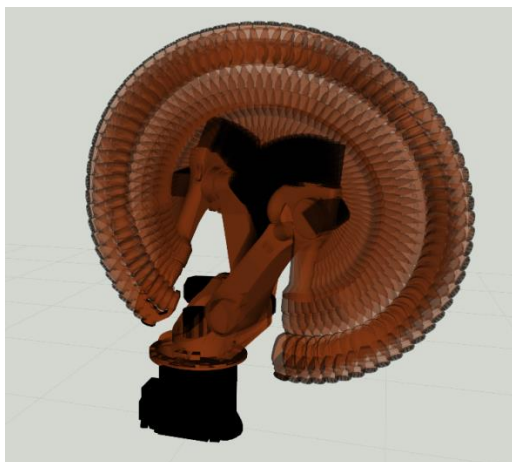


Fig. 10. Displaying a change in the configuration of the arm, which is forced by the need to rotate the first joint by 360° during the execution of MoveIt

Furthermore, it is also necessary for a more realistic simulation to limit the space in which it is possible to plan future target positions. We limited the planning space by adding collision objects, through which the planned trajectory must not pass. Thus, a floor was created on which the robot is placed, and the workspace of the robot was also partially limited, which is further shown in Fig. 17.

7.4. Teaching the path of a robot by guidance

The teaching process is simple and is performed during manual navigation. Whenever the arm stops because no force is applied to the sensor, its current position and orientation in the Cartesian system can be written to the file (these points are shown in Fig. 11 under the label data 2). When teaching is complete, all memorized positions and orientations are uploaded to the ComputeCartesianPath service. This will create additional extra positions, which can be seen as data 1 in the same image. The entire trajectory is then planned as one continuous movement.

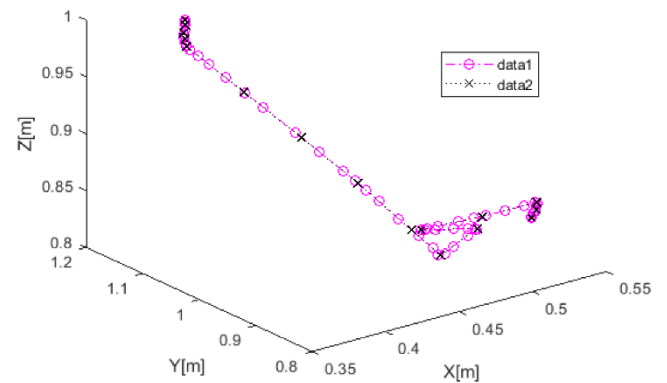


Fig. 11. Points written to a file during the manual navigation (data 2) and extra points created by ComputeCartesianPath service (data 1)

8. EXPERIMENTS

During the experimental verification of the solution, it was first necessary to verify whether it is possible for MoveIt to enter the desired target positions based on calculation of the position vectors of these points from the force vector. It was also necessary to verify what positioning error occurs with this solution. In Fig. 12, an arrow with blue label shows the position vector pointing from the tool coordinate system, obtained from the resultant force vector. This vector points to the desired target position. The cusped line with orange label represents the planned motion trajectory with the individual nodal points. The endpoint of the manipulator moves along the orange trajectory. The inaccuracy of the reached target position compared to the planned one was 0.1 mm, which is an acceptable deviation when manually guiding the robot via the FT sensor.

Subsequently, the sequential planning of trajectories was verified using MoveIt while pressure was applied to the sensor in the desired direction. The planned trajectory for the new calculated point was prepared immediately after completing the execution of the previous plan. The chart in Fig. 13 shows the shortcoming of this method, as the robot stops every time it passes the appropriate trajectory.

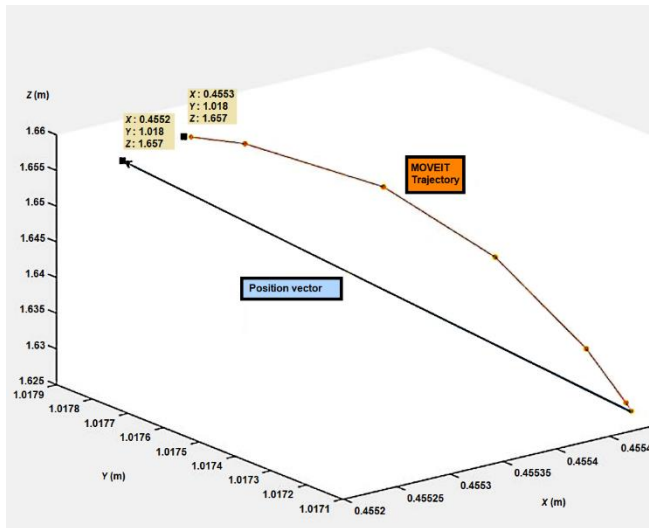


Fig. 12. Position vector pointing from the tool coordinate system to the desired position of the effector (arrow with blue label), and the planned trajectory with its via points (cusped line with orange label)

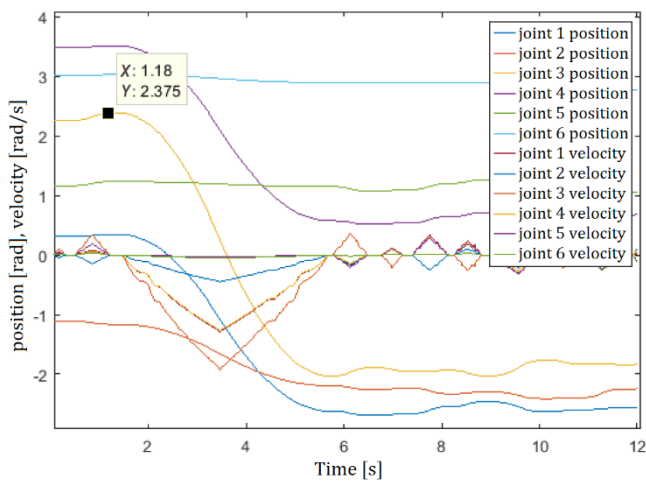


Fig. 13. Triangle-like lines represent speeds in the joints. It is obvious that the robot will stop between the individual plans

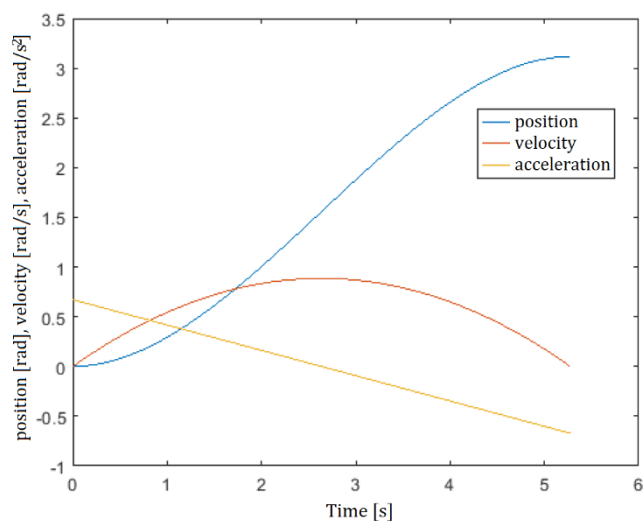


Fig. 14. Basic experiment to verify the implementation of polynomial interpolation performed on one joint. The output of the algorithm is the desired trajectory for the position, speed, and acceleration

The proposed algorithm eliminates these unwanted stops and provides smooth transitions between successive trajectories. First, verification of the algorithm was performed on one of the joints. The joint trajectory planning based on polynomial interpolation works as expected. The limiting conditions in this experiment were determined as follows: initial joint position $q(t_0) = 0$ rad, final joint position $q(t_f) = 3.11723$ rad, and the initial and final joint speeds $\dot{q}(t_0) = 0$ rad/s and $\dot{q}(t_f) = 0 \frac{\text{rad}}{\text{s}}$, respectively. In Fig.14, we see the resulting desired trajectories for the position, speed, and acceleration.

To verify the algorithm's functionality with continuous trajectory replanning, an experiment was created with smooth switching of planned trajectories. We can use the same trajectory planned in the previous experiment, and additionally, we request a switch to the new trajectory at time $t^* = 1.84$ s. We send a request to the query_state service with a timestamp equal to t^* . The response is the future value of the position $q(t^*) = 0.882$ rad and speed $\dot{q}(t^*) = 0.807$ rad/s. We use these values as the initial limiting conditions for generating a new desired trajectory. For safety reasons, we set the final limiting condition for speed to $\dot{q}(t_f) = 0$ rad/s. During normal manual guidance, the value of the final joint position in the new trajectory is given based on the inverse kinematics from the point in space to which the position vector (computed from the acting force) is directed. In other words, the trajectories are replanned periodically, and application of some amount of force causes changes in the limiting conditions used in the polynomial interpolation. For this experiment's purpose, however, we consider the joint's target position to be the value $q(t_f) = 0$ rad. The resulting desired trajectory is shown in Fig. 15. A new trajectory is created by combining the two plans, where there is no interruption of movement in position or speed, but the movements follow each other smoothly. We can see in Fig. 15 that before the moment of 1.84 s, the values with index "1" are valid, and after this moment, the values with index "2" are valid. The original values of the first trajectory after time $t^* = 1.84$ s are shown in dashed lines. With a cubic trajectory, the acceleration change is not continuous, but the controller can regulate this step change.

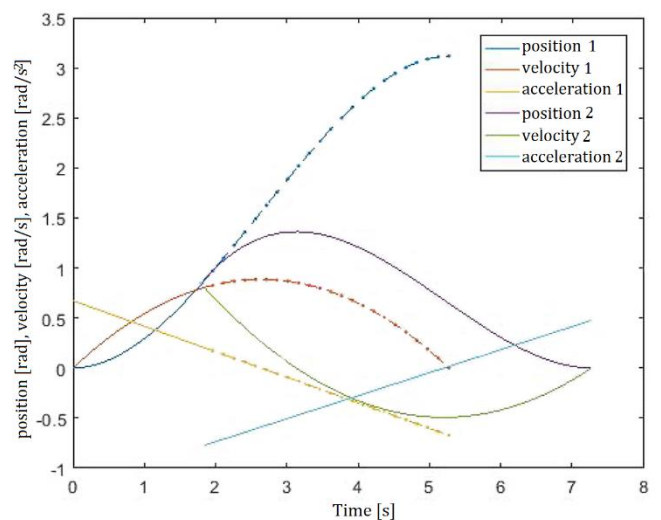


Fig. 15. Verification of the algorithm's functionality with continuous desired trajectory replanning

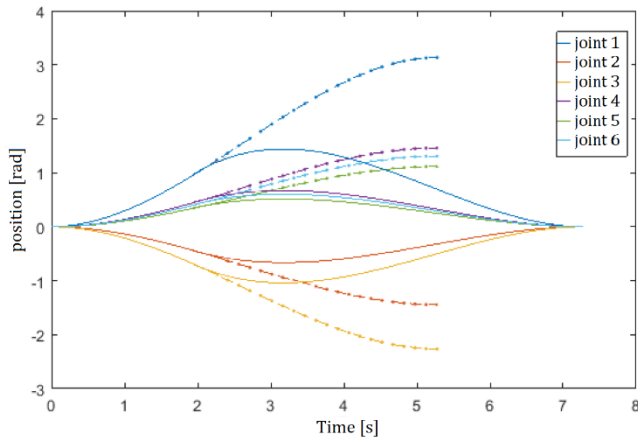


Fig. 16. Continuous trajectory replanning simultaneously in all six degrees of freedom of the robotic manipulator

A similar experiment was performed to smoothly switch to new desired trajectories simultaneously in all six degrees of freedom of the robotic manipulator. The result is shown in Fig. 16.

Finally, the additional space constraints of the robot were also verified. If the robot is manually guided by a sensor to move, such a planned trajectory that will pass through collision objects does not apply, and the robot stops. Fig. 17 shows in red the force vector that acts on the robot via the FT sensor in the effector's coordinate system and forces it to collide with the floor. However, this plan was assessed as dangerous, and therefore no collision occurred.

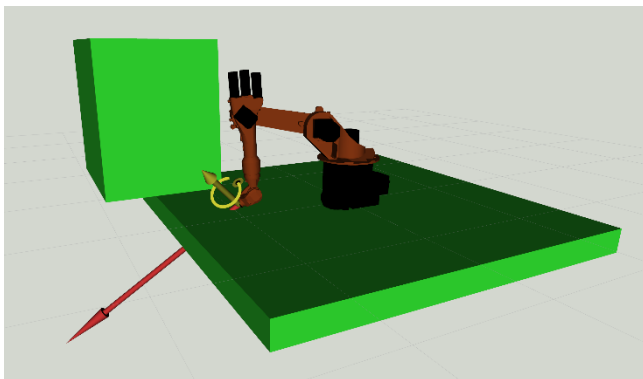


Fig. 17. The environment where the space constraints of the robot were verified

9. CONCLUSION

This article presented the implementation of the Optoforce HEX-70-CE-2000N sensor into the ROS framework for use in manual robot guidance. It was also shown that the sensor needs to be properly calibrated. In the ROS environment, the robot controllers were set so that the control of the robot endpoint also considers the influence of external forces measured on the Optoforce sensor. These are reconstructed as the force and torque vectors from the detected forces in all degrees of freedom. This work verifies the algorithm of motion planning of the virtual manipulator's effector based on the action of forces and torques on the force sensor using the basic settings of the MoveIt framework. This method of motion planning proved to be insufficient for the needs of the robotic effector's manual guidance because the robot

is stopped after the execution of each scheduled partial trajectory. Therefore, our research was focused on the design and verification of a robot motion planning algorithm that uses polynomial interpolation and allows the continuous merging of subplans, which is necessary for online manual guidance. Experimental verification of the solution shows a smooth connection between the original and the new plans. The required trajectory is obtained without a step change in position and speed. To bring the simulation closer to reality, the selected implementation's basic spatial and speed limitations were added to the solution. At the same time, this increased the solution's safety, which is very important in manual guidance.

In future work, we will focus on optimizing the planning system to accelerate responses to changes in force concerning ergonomics for the operator. The system supervising the appropriate selection of the inverse kinematics solution will also be optimized to eliminate random selection and ensure the calculation of the solution taking into account the robot's current configuration. One of the options that will be verified in connection with this problem is the IKFast solver. Finally, the proposed system will be deployed and verified on a real robot.

REFERENCES

1. **Jamone L., Fumagalli M., Natale L., Nori F.** (2014), Control of physical interaction through tactile and force sensing during visually guided reaching, *2014 IEEE International Symposium on Intelligent Control (ISIC)*, 1360-1365.
2. Experimental Packages for KUKA manipulators with ROS-Industrial (2020), https://github.com/ros-industrial/kuka_experimental
3. **González C., Solanes J.E., Muñoz A., Gracia L., Gírbés-Juan V., Tornero J.** (2021), Advanced teleoperation and control system for industrial robots based on augmented virtuality and haptic feedback, *Journal of Manufacturing Systems*, 59, 283-298.
4. **Jo J., other authors** (2013), Grasping force control of a robotic hand based on a torque-velocity transformation using F/T sensors with gravity compensation, *IECON 2013-39th Annual Conference of the IEEE Industrial Electronics Society*, 4150-4155.
5. Joint Trajectory Action Controller, Official webpage ROS Documentation (year), http://wiki.ros.org/robot_mechanism_controllers/JointTrajectoryActionController
6. **Lee S.-D., Ahn K.-H., Song J.-B.** (2016), Torque control based sensorless hand guiding for direct robot teaching, *IEEE/RSJ International Conference on Intelligent Robots and Systems (IROS)*, 745-750.
7. **Loske J., Biesenbach R.** (2014), Force-torque sensor integration in industrial robot control, *15th International Workshop on Research and Education in Mechatronics (REM)*, 1-5.
8. **Massa D., Callegari M., Cristalli C.** (2015), Manual guidance for industrial robot programming, *Industrial Robot: An International Journal*, 42(5), 457-465.
9. **Matheson E., Minto R., Zampieri, E.G., Faccio M., Rosati G.** (2019), Human-Robot Collaboration in Manufacturing Applications: A Review, *Robotics*, 8(4), 100.
10. **Noh Y., Bimbo J., Sareh S., Wurdemann H.** (2016), Multi-axis force/torque sensor based on simply-supported beam and optoelectronics, *Sensors*, 16(11), 1936.
11. **Peng Y.C., Chen S., Jivani D., Wason J., Lawler W., Saunders G., Wen, J.** (2021), Sensor-Guided Assembly of Segmented Structures with Industrial Robots, *Applied Sciences*, 11(6), 2669.
12. **Reyes-Uquillas D., Hsiao, T.** (2021), Safe and intuitive manual guidance of a robot manipulator using adaptive admittance control towards robot agility, *Robotics and Computer-Integrated Manufacturing*, 70, 102127.


13. **Safeea M., Béarée R., Neto P.** (2017), End-effector precise hand-guiding for collaborative robots, *Iberian Robotics conference*. Springer, Cham, 595-605.
14. **Safeea M., Bearee R., Neto, P.** (2017), End-effector precise hand-guiding for collaborative robots, *Iberian Robotics conference*, 595-605, Springer, Cham.
15. **Safeea M., Neto P., Béarée R.** (2019), Precise hand-guiding of redundant manipulators with null space control for in-contact obstacle navigation, *IECON 2019-45th Annual Conference of the IEEE Industrial Electronics Society*, 693-698.
16. **Spong M., Hutchinson S., Vidyasagar M.** (2005), *Robot modeling and Control*, 1st Edition. Wiley.
17. **Zhang S., Wang S., Jing F., Tan M.** (2019), A sensorless hand guiding scheme based on model identification and control for industrial robot, *IEEE Transactions on Industrial Informatics*, 15(9), 5204-5213.
18. **Zhao Y., Gao F., Zhao Y., Chen, Z.** (2020), Peg-in-Hole Assembly Based on Six-Legged Robots with Visual Detecting and Force Sensing, *Sensors*, 20(10), 2861.
19. <https://github.com/shadow-robot/optoforce>, (2020)
20. <https://ifr.org/free-downloads/>, (2020)
21. <https://onrobot.com/en/products/hex-6-axis-force-torque-sensor>, (2021)
<https://www.code-n.org/blog/finalist-optoforce-hungary-sensors-for-the-internet-of-things/>, (2015)
22. <https://www.crunchbase.com/organization/optoforce>, (2020)
23. https://www.eu-robotics.net/cms/upload/topic_groups/SRA2020_SPARC.pdf, (2020)


This publication was created with support under the Operational Program Integrated Infrastructure for the project "Robotized cell for intelligent welding of small volume production (IZVAR)", code ITMS2014+: 313012P386, cofinanced by the European Regional Development Fund.

The authors also gratefully acknowledge the contribution of the Slovak Research and Development Agency under the project APVV-17-0214 and the contribution of the Scientific Grant Agency of the Slovak Republic under the grant 1/0754/19.

Radovan Gregor:  <https://orcid.org/0000-0002-9498-6768>

Andrej Babinec:  <https://orcid.org/0000-0001-5550-2583>

František Duchoň:  <https://orcid.org/0000-0003-4140-9737>

Michal Dobiš:  <https://orcid.org/0000-0002-2453-212X>